New Frontiers in Collisionless Reconnection: Exploring Magnetosphere-Relevant Reconnection with Experiments and Custom Kinetic Simulations

by

Samuel M. Greess

A dissertation submitted in partial fulfillment of

the requirements for the degree of

Doctor of Philosophy

(Physics)

at the

UNIVERSITY OF WISCONSIN–MADISON

2022

Date of final oral examination: 9 December 2022

The dissertation is approved by the following members of the Final Oral Committee:

Jan Egedal, Professor, Physics
Cary Forest, Professor, Physics
John Sarff, Professor, Physics
Carl Sovinec, Professor, Engineering Physics

NEW FRONTIERS IN COLLISIONLESS RECONNECTION: EXPLORING MAGNETOSPHERE-RELEVANT RECONNECTION WITH EXPERIMENTS AND CUSTOM KINETIC SIMULATIONS

Samuel M. Greess

Under the supervision of Professor Jan Egedal

At the University of Wisconsin-Madison

Magnetic reconnection is a ubiquitous phenomenon throughout the universe, but in terms of proximity, its occurrences at the day-side magnetopause and in the magnetotail are the instances that are closest to Earth both spatially and in importance to human life. At the day-side magnetopause, the solar magnetic field reconnects with the magnetic field of the Earth; these reconnected field lines move to the magnetotail, bringing solar wind plasma with them. Further reconnection at the magnetotail leads to the transfer of these energized particles into the Earth's upper atmosphere. Usually, the result of these incursions is only the ethereal beauty of the auroras (borealis and australis); however, larger quantities of incident plasma can and have had devastating effects on terrestrial and space-based electronic systems. Predicting these geomagnetic storm events depends on an understanding of both how and when large quantities of plasma and magnetic flux are emitted from the Sun (also a reconnection-based event) and how long it will take for these particles to enter the Earth's atmosphere via the magnetopause and magnetotail reconnection processes. To that end, in addition to satellite missions created to measure *in situ* activity, experiments and simulations here on Earth are studying reconnection in the relevant parameter regimes, particularly in plasmas whose collisionality is low enough to mimic the space environment. One such experiment is the Terrestrial Reconnection EXperiment (TREX), which is based at the University of Wisconsin-Madison as a partner of the Wisconsin Plasma Physics Laboratory (WiPPL) collaborative research facility. TREX is designed to access the kinetic regime, which is typified by thin current layers, anisotropic pressure distributions, and fast reconnection. In

conjunction with TREX, the newly developed Cylindrical VPIC (Vectorized Particle-in-Cell) code from Los Alamos National Laboratory has been used to simulate TREX in manner that preserves the experiment's cylindrical symmetry while optimizing computational efficiency. Different modified versions of the basic TREX VPIC setup have been successfully used to confirm and complement experimental findings, as well as to investigate plasma regimes the experiment cannot (presently) reach and to model different proposed TREX drive coil geometries. This thesis will present work from both the TREX laboratory and TREX VPIC simulations, with an emphasis on comparing the measured properties of reconnection in both scenarios and demonstrating how these data align with theoretical predictions about the kinetic reconnection parameter regime. Significant background to the construction and operation of TREX, Cylindrical VPIC, and relevant portions of the WiPPL facility will also be included.

Acknowledgments

No one accomplishes anything alone. I would be remiss if I did not extend my whole-hearted thanks to the teachers, researchers, professors, students, and administrative staff at each and every academic and scientific institution I have been fortunate enough to attend or work with. These include, in chronological order, KIVA Elementary School, Mohave Middle School, North High School and its fantastic International Baccalaureate program staff, Carnegie Mellon University, the University of Michigan, Princeton University and the Princeton Plasma Physics Lab, Los Alamos National Laboratory, and most of all, the University of Wisconsin-Madison.

While (nearly) everyone I could thank is technically included in that list, there are more than a few people who deserve to be mentioned by name. They are the following:

Thank you to all the other current and former TREX, Jan-group, and BRB-related students who helped me collect the data that makes up the bulk of this thesis and/or proofread sections of it ahead of my defense- Alex Millet-Ayala, Rachel Myers and her pet snake Alfie[1], Paul Gradney, Cameron Kuchta, Sue Kim, Harsha Gurram, Blake Wetherton, Roger Waleffe, and Douglass Endrizzi. Alex gets an additional shout-out for being far and away the person who has volunteered the most of their time to assist me in data collection, sacrificing not only regular work hours but multiple holidays and weekends.

A quick thank you to Ethan Peterson, who both provided me with the Overleaf template I used to write this thesis and figured out how to fix it when it suddenly started to log almost

[1]Alfie is the only pet who came to the lab and met me in the flesh. Sorry Alex, seeing your lizards and cats over Zoom doesn't count. I did also meet Joe's dog, Gimli, but that was always outside of the lab.

100 errors simultaneously.

Another quick thank you to Katariina Nykyri, who selflessly volunteered to evaluate my Introduction from the perspective of an actual space physicist before she had even met me in person.

Thank you to all the BRB and WiPPL engineering staff, particularly to Alex Squitieri and John Wallace for their work on TREX. An extra special thank you to Mike Clark, who was my mentor and supervisor when I first started working in the BRB lab in the summer of 2014.

Thank you to our main collaborators at Los Alamos National Laboratory, specifically Bill Daughton, Ari Lê, and Adam Stanier. A special thank you to Adam for helping me through the arduous process of adapting my thinking to include simulation work after I spent so long working exclusively in experiments with unscaled SI units, and to Bill for helping me understand part of the underlying physics of the Lower Hybrid Drift Instability.

Thank you to my committee members, Cary Forest, John Sarff, and Carl Sovinec. Thanks specifically to Cary for being the mastermind behind the BRB and creating such an excellent environment to foster the growth of experimental space plasma physics as a field, to John for running (in conjunction with Karsten McCollam) the Plasma Group Talk program which was an essential introduction to scientific presenting that I greatly appreciated, and to Carl for putting up with all my questions during his Waves and Instabilities course and for all the excellent feedback on my thesis draft. A slightly-related thank you to Ellen Zweibel, who wasn't able to be on my defense committee but was in my prelim exam and who encouraged me to look more into the Lower Hybrid Drift Instability.

A big thank you to Joe Olson, who has been the foundation upon which much of TREX and this thesis' experimental data was based. Joe's skill and ease in the laboratory belie the difficulty and occasional danger of the work he so often undertakes. He can just as easily design and build a major experimental upgrade all on his own as he can teach a near-neophyte how to do it themselves; furthermore, his compassion and understanding in the face of any mistakes they may make has been invaluable in keeping his colleagues

encouraged and engaged throughout their long years of graduate research. I would not be 1/8 the experimentalist I am today without his tutelage.

Of course, as gigantic thank you to my advisor, Jan Egedal, for guiding me through my career in Wisconsin. Not only is he the evil genius behind TREX, he has an ability to manage students, classes, and other research projects that borders on the supernatural. Thank you Jan in particular for pushing me out of my comfort zone; without your assistance, insistence, and occasionally frank (but fair!) criticism, I doubt I ever would have written a paper, made a presentation, or even started working on TREX simulations with Los Alamos. I am profoundly grateful to have had Jan as an advisor. Jan, tak for alt!

Outside of academia, I'd like to thank all my family members for their support throughout this lengthy process, even though they all insist that they have no idea what I do. This includes Andrew (Dad), Wendy (Mom), Rachel, Edwinna (Grandma), Bruce, Martha, and Mary Lu. Their encouragement and love have made all the difference whenever I've been at or near my lowest points on this long road.

Finally, last but certainly not least, I need to give a very special and specific thank you to someone without whom this thesis would not exist, in the most literal sense. When I began to focus on writing around early 2022, I was paralyzed by the apparent enormity of the task that lay ahead of me. I could not begin to decide where to start or what to say, and with each passing day with little or no significant output, my anxiety and feelings of failure only grew. The only way I was able to begin writing and continue on through until now is by the selfless intervention of the one person I felt comfortable speaking to about how much of a quagmire I was in. That person is Emily Lichko. Not only did Emily teach me about "burnout" (so I could understand that I wasn't some kind of freak graduate anomaly), she took time out of her schedule multiple times a week to help me plan my writing process and address my concerns about different sections or chapters. Emily did this all of her own initiative with no clear benefit to herself. Emily, I cannot thank you enough. This written thesis is as much a product of your kindness as it is one of my writing. Thank you for being an amazing friend and teaching me the physics-graduate-student-equivalent of how to SSDGM.

Definitions

BRB	Big Red Ball vacuum vessel at the Wisconsin Plasma Physics Laboratory (WiPPL)
CME	Coronal Mass Ejection - when a massive magnetized bubble of plasma erupts from the corona via magnetic reconnection
IMF	Interplanetary Magnetic Field - the magnetic field that fills the heliosphere, whose large scale structure is that of the Parker spiral.
LaB_6	Lanthanum Hexaboride - an elemental compound used in emissive cathode construction on the BRB and PCX.
MHD	Magnetohydrodyamics - a fluid model description of plasma dynamics.
MPDX	Madison Plasma Dynamo Experiment - the original name of the BRB.
TREX	The Terrestrial Reconnection EXperiment
WiPPL	Wisconsin Plasma Physics Laboratory (WiPPL)
CAD	Computer-aided design [software]

Table of Contents

List of Figures

List of Tables

Chapter 1

Introduction and Background

1.1 Magnetic Reconnection

The Sun's magnetic field is a key driver of many of the plasma phenomena that are observed at the solar surface, like the expulsion of coronal mass ejections (CMEs) or high-energy flare events. The solar plasma, like any magnetized plasma, is constrained to move along the Sun's magnetic field lines, which often begin and end in the Sun itself; an example of this can be seen in Figure 1.1, where the ejected plasma loops back down to the solar surface.

However, large quantities of plasma can and do escape the immediate solar environment despite their magnetization. This is accomplished through a process known as magnetic reconnection, where the twisted field lines "pinch" together, break, and then "reconnect" in a new geometry that is no longer tied to the solar surface. The resulting "island" of magnetic field and plasma can now travel away from the Sun as components of the interplanetary magnetic field (IMF) and the solar wind (respectively). A simplified version of this process is drawn in Figure 1.2.

Reconnection can also take place when the solar wind encounters the Earth's magnetosphere[1]. When the directions of the IMF and Earth's magnetic field oppose each other,

[1]Indeed, reconnection occurs in many locations in the universe in both natural and experimental contexts; however, the forms of reconnection described in the text proper are those most relevant to this thesis.

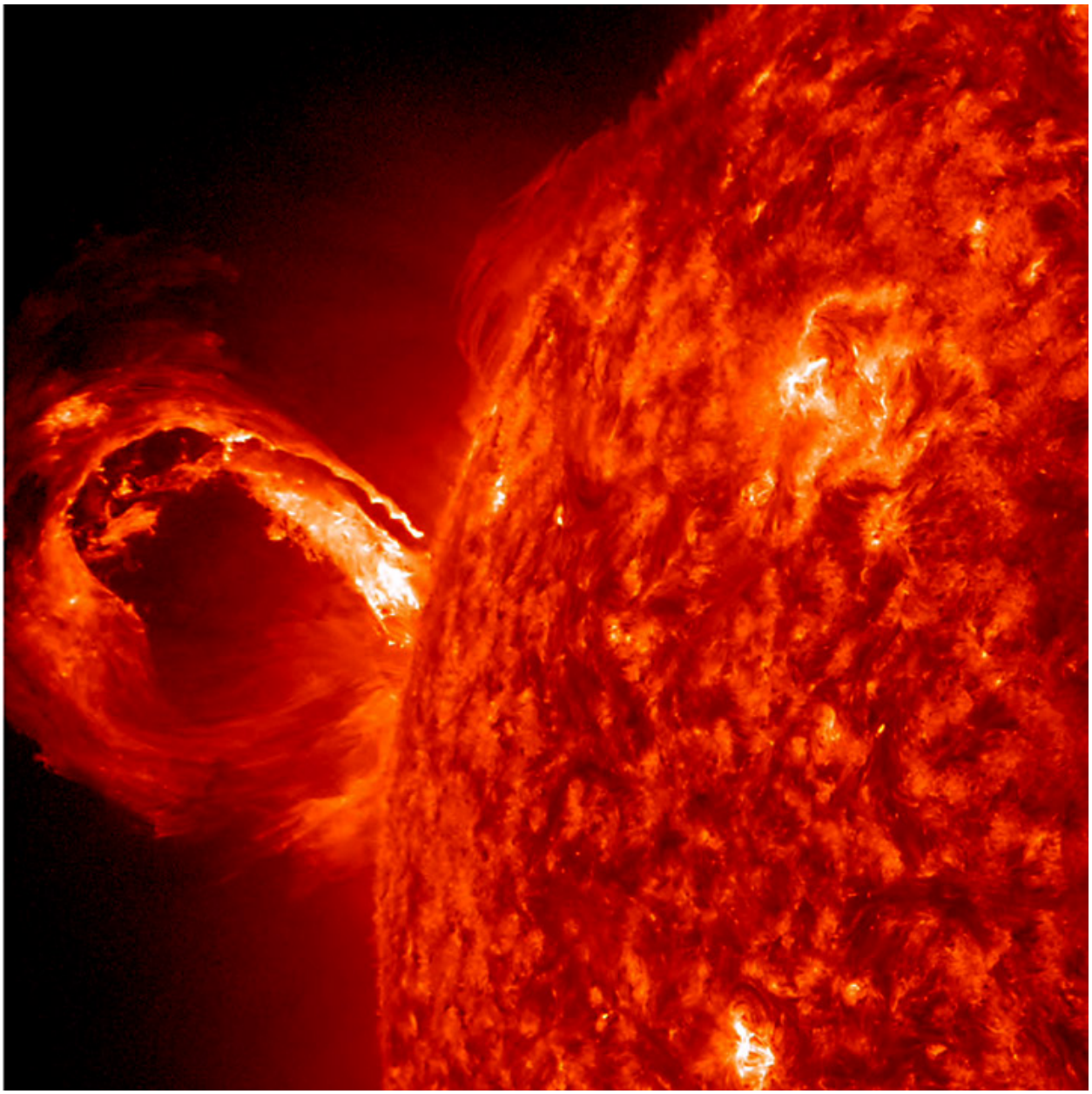

Figure 1.1: A coronal mass ejection leaving and then looping back into the surface of the Sun along the Sun's magnetic field lines. Image recorded by the Solar Dynamics Observatory (SDO) in extreme ultraviolet light on 1 May 2013 (from sdo.gsfc.nasa.gov).

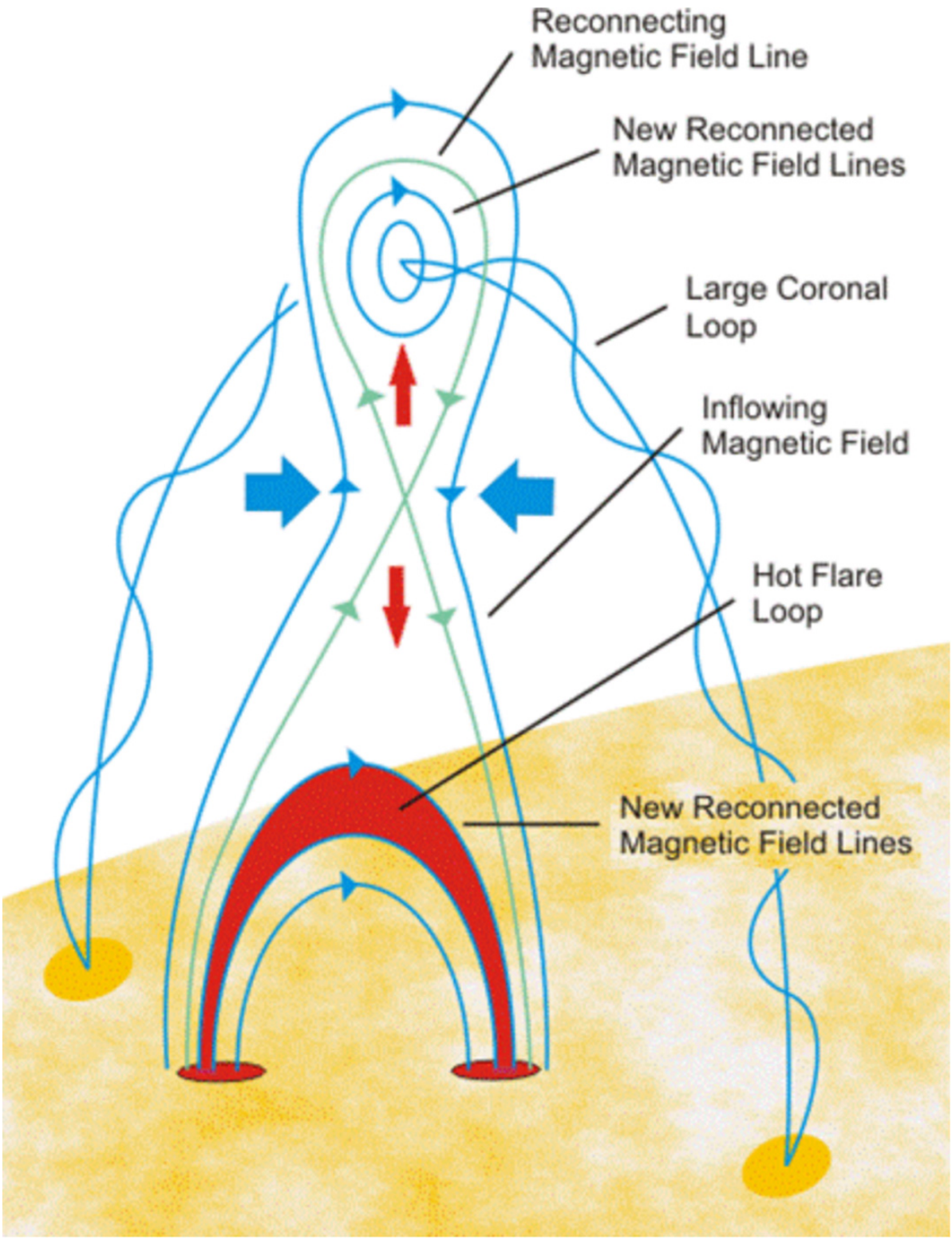

Figure 1.2: An illustration of how magnetic reconnection allows magnetized plasmas to leave the Sun's surface in the form of CMEs. Image courtesy NASA's MMS Mission Gallery.

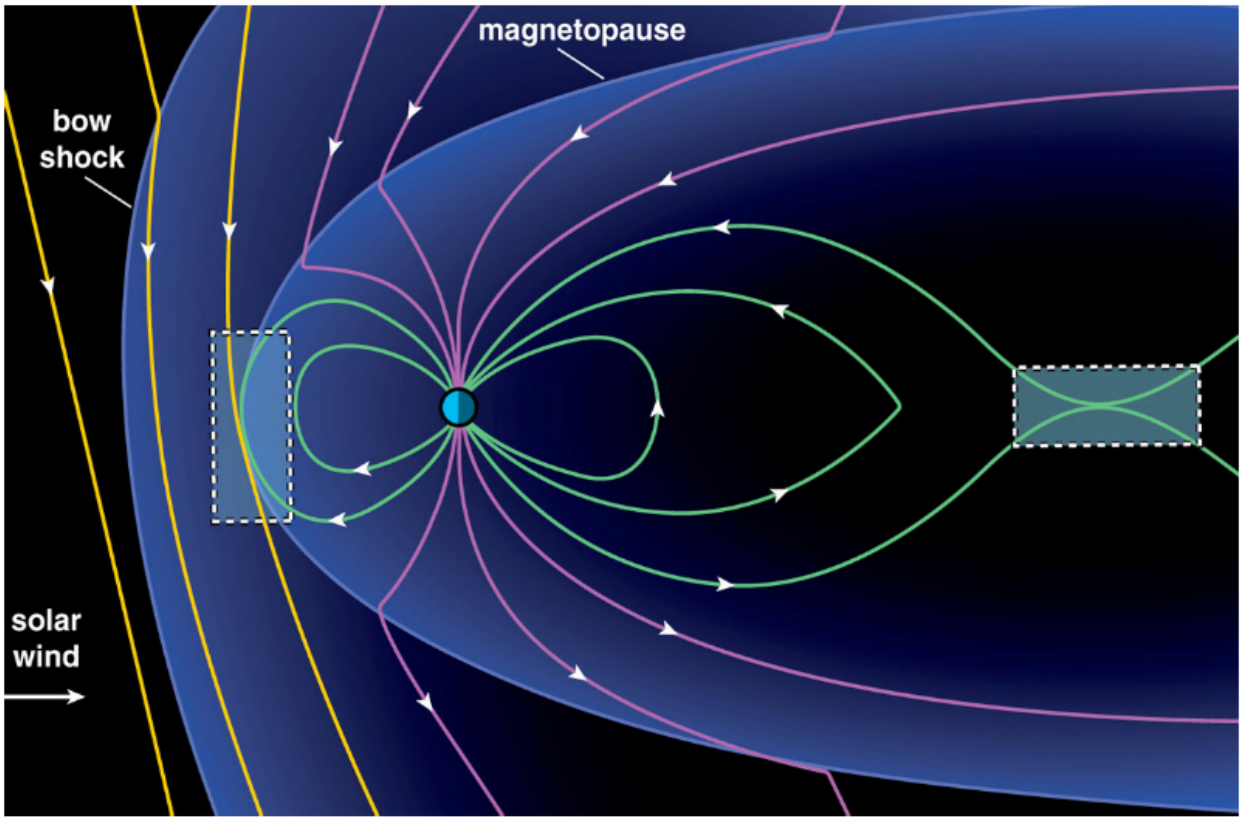

Figure 1.3: The interaction between the solar wind and the Earth's magnetic field. Two separate areas are highlighted - one at the dayside magnetopause and the other in the magnetotail. Image reproduced from Burch et al. [1].

reconnection between the two occurs at the dayside magnetopause (left rectangle in Figure 1.3); the resultant field lines are then pushed over the magnetic poles to the Earth's magnetotail, where they reconnect again (right rectangle in Figure 1.3). This process eventually allows the transit of both solar and magnetosphere plasmas into the Earth's atmosphere, particularly at the magnetic poles- this is the cause of the polar auroras (borealis in the north, australis in the south).

An example of these auroras is shown in Figure 1.4. While undeniably beautiful, the effect masks the potential for serious damage to human civilization; in the rare cases where the space weather processes behind the auroras become more energetic and violent, events known as "geomagnetic storms" can occur. The rapid magnetic fluctuations that characterize these storms can induce loop currents and power surges that destroy electrical equipment,

resulting in blackouts or communications failures. Notable examples of this include the Carrington Event of 1859, which destroyed telegraph lines and stations across Europe and North America, and the 1989 Québec Geomagnetic Storm, which caused a nine-hour blackout in the eponymous Canadian province and was briefly misinterpreted as a communications attack from the Soviet Union. The reconnection process is important to understanding the potential damage a geomagnetic storm can cause; not only is reconnection responsible for allowing large bursts of solar plasma and magnetic flux to leave the Sun's surface and enter the Earth's magnetic environment, but the process itself is a source of energization for the incident particles. This is because reconnection is responsible for converting energy stored in a magnetic field into particle kinetic and thermal energy, in addition to rearranging the field's topology. The study of magnetic reconnection is a crucial component of understanding the connection between the Sun and the Earth and the possible dangers that this connection presents to civilization.

1.2 Ohm's Law and Reconnection

In an ideal limit, a plasma is modeled as a perfectly conducting fluid with no source of electrical resistance and thus no mechanism of magnetic diffusion. These qualities are expressed in the Ideal Ohm's Law:

$$\mathbf{E} + \mathbf{v} \times \mathbf{B} = 0\,, \tag{1.1}$$

which can be derived from the momentum balance equation of the plasma's electrons. Here, $\mathbf{E}$ is the electric field, $\mathbf{B}$ is the magnetic field, and $\mathbf{v}$ is the macroscopic flow velocity[2], which is taken to be equivalent to the ion fluid velocity $\mathbf{v_i}$ [2]. From an analysis of Eq 1.1, it can be concluded that the plasma is in a "frozen-in" state, where the particles are inseparable from any magnetic field lines they lay along. This status is also referred to as the "frozen flux"

[2]All terms are taken to be in the laboratory frame, as opposed to the plasma's frame. In the plasma's frame, $\mathbf{v} = \mathbf{0}$ and thus Eq 1.1 simplifies to $\mathbf{E} = \mathbf{0}$

Figure 1.4: A photograph of the Aurora Borealis over the Pacific Northwest of the United States taken by astronauts aboard the International Space Station in January 0f 2016. Image credit to NASA and the ESA.

limit, where "flux" refers the the magnetic flux function, defined as:

$$\Psi = \int_{\mathbf{S}} \mathbf{B} \cdot d\mathbf{S}\,, \tag{1.2}$$

where S is some arbitrary surface. Taking the time rate of change of this parameter and applying Stokes' Theorem, the "frozen" (e.g., unchanging) quality of the flux in this limit becomes evident:

$$\begin{aligned} \frac{\mathrm{d}\Psi}{\mathrm{d}t} &= \int_{\mathbf{S}} \frac{\partial \mathbf{B}}{\partial t} \cdot d\mathbf{S} + \oint \mathbf{B} \cdot (\mathbf{v} \times d\mathbf{r}) \\ &= -\int_{\mathbf{S}} \boldsymbol{\nabla} \times (\mathbf{E} + \mathbf{v} \times \mathbf{B}) \cdot d\mathbf{S} = 0\,. \end{aligned}$$

This is clearly a problem for reconnection; if the magnetic flux through some arbitrary surface cannot be changed, then field lines cannot break and reconnect through the cancellation of some opposing field component. As such, for reconnection to occur, something must force the plasma out of the ideal limit, resulting in the right-hand-side (RHS) of Eq 1.1 becoming nonzero. Several different mechanisms have been established that could conceivably provide this non-ideal behaviour; these mechanisms define different types or "regimes" of magnetic reconnection, which are explained below.

1.2.1 Sweet-Parker

The first mechanism proposed as a means of breaking the frozen-in condition was electrical resistivity η and an associated current density $\mathbf{J}$, which updates Eq 1.1 to:

$$\mathbf{E} + \mathbf{v} \times \mathbf{B} = \eta \mathbf{J} \,. \tag{1.3}$$

A now-famous and basic physical model for reconnection based on electrical resistance is the Sweet-Parker model [3], which envisions reconnection occurring in a thin current layer situated between two inflows that are still in the ideal limit. These two inflows have identical properties save for oppositely-directed magnetic fields and inflow velocities. An example of this may be seen in Figure 1.5. Here, the field lines in the inflows move in toward the resistive current layer where they able to diffuse, cancel each other, reconnect and be expelled into the outflow. The size of the current layer is defined by its width-over-length aspect ratio of δ/L.

The magnitude of the inflow electric field E_{in} can be described in terms of the inflow speed, v_{in}, using Eq 1.1:

$$E_{in} = v_{in} B_{in} \,.$$

The electric field in the current layer, E_{layer}, can be found from Eq 1.3 using the fact that the magnetic field cancels inside the layer:

$$E_{layer} = \eta J \,.$$

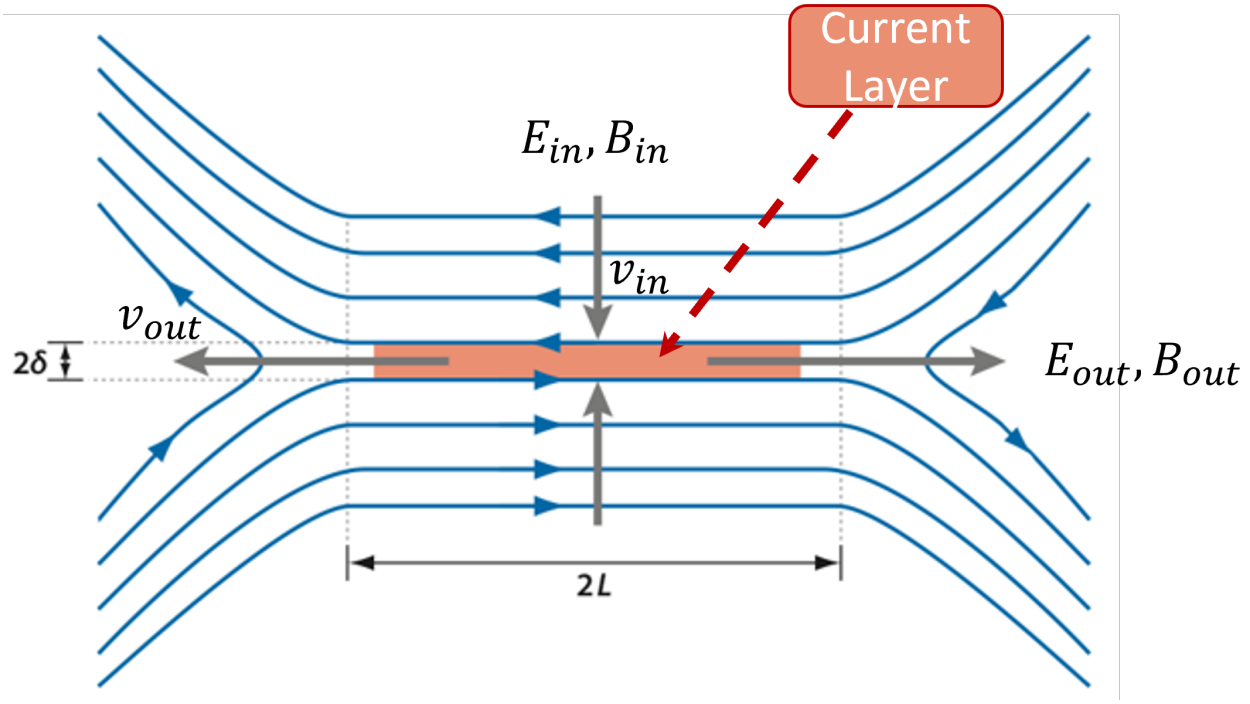

Figure 1.5: Standard Sweet-Parker reconnection current layer. Reproduced from Zweibel and Yamada [4] with some modifications.

Now, the induced electric field in the inflow must be balanced by the diffused electric field in the layer; otherwise, the smooth flow of field lines into and out of the diffusive current layer could not be maintained and the steady reconnection process would not be sustainable. This means that the two electric fields derived above must be equal to each other, resulting in

$$E_{in} = E_{layer} = v_{in} B_{in} = \eta J \, .$$

By applying Ampère's law in a loop around the current layer from one inflow to the other, we can evaluate the magnitude of the current density:

$$2L(B_{in}) + 2\delta(0) + 2L(B_{in}) + 2\delta(0) = (2L)(2\delta)\mu_0 J$$
$$\rightarrow J = B_{in}/(\mu_0 \delta) \, .$$

This in turn allows us to find an expression for the inflow speed in terms of the resistivity of the layer and its width:

$$v_{in} = \eta/(\mu_0 \delta)\,.$$

The maximum possible ouflow speed, v_{out}, can be determined by evaluating the limit of the magnetic pressure of the inflow being fully converted into the outflow's kinetic energy density:

$$\frac{1}{2} n m_i v_{out}^2 = \frac{B_{in}^2}{2\mu_0}\,,$$

where n is the particle density and m_i is the ion mass. This equation shows that the maximum outflow speed is equivalent to the Alfvén speed of the inflow, $v_A = B_{in}/\sqrt{\mu_0 n m_i}$. Finally, incompressibility and particle continuity mean that the relation $v_{in} L = v_{out}\delta$ must hold. Combining this with our results for the inflow and outflow speeds, we reach this result for the rate at which Sweet-Parker reconnection proceeds:

$$\frac{v_{in}}{v_{out}} = \frac{\delta}{L} = \left(\frac{\eta}{\mu_0 L v_A}\right)^{1/2} = S^{-1/2}\,,$$

where S is the Lundquist number, the ratio of the speed at which magnetic perturbations advect through a plasma vs the speed at which they diffuse out from a plasma. This immediately presents a problem for the applicability of the Sweet-Parker model: the rate of reconnection is slower as the plasma environment becomes less resistive. Reconnection events observed at the surface of the Sun can occur on timescales on the order of minutes to hours; however, with Lundquist numbers in astrophysical environments measured in excess of 10^{10}, the timescale of a Sweet-Parker reconnection event would be on the order of months or longer. Clearly, electrical resistance alone is not enough to facilitate reconnection on the timescales that are observed in natural high-S (highly conductive) environments[3].

[3]It should be noted, however, that a slightly-modified form of the Sweet-Parker model that takes compressibility, effective resistivity, and the downstream plasma pressure into account has been verified by laboratory experiments [5, 6]. Furthermore, natural plasma environments can occur at Lundquist numbers low enough ($S \lesssim 10^4$) to be (theoretically) well-modeled by Sweet-Parker; protostellar disks tend to exist in this limit [7].

1.2.2 Further Ohm's Law terms

A more generalized form of Ohm's Law can be constructed from the electron momentum balance equation:

$$\mathbf{E} + \mathbf{v} \times \mathbf{B} = \eta \mathbf{J} + \frac{\mathbf{J} \times \mathbf{B}}{ne} - \frac{\boldsymbol{\nabla} \bullet \mathbf{P_e}}{ne} + \frac{m_e}{ne^2} \frac{\mathrm{d}\mathbf{J}}{\mathrm{d}t}, \tag{1.4}$$

where $\mathbf{P_e}$ is the electron pressure tensor and the macroscopic velocity $\mathbf{v}$ can be related to the electron fluid velocity by the relation $\mathbf{v_e} = \mathbf{v} - \mathbf{J}/ne$ [2]. These additional terms come in to play when the MHD single-fluid approximation fails; when the scale size of the reconnection region is smaller than the ion skin depth $d_i = c/\omega_{p,i}$ (where $\omega_{p,i}$ is the ion plasma frequency), the flows of the ions and electrons are uncoupled. There are other possible terms that can contribute to the total electron momentum equation, but the ones included in Eq 1.4 are the most relevant for most applications, including those that will be described in this thesis. Reconnection systems (experimental, simulated, and natural) that are able to include these terms are characterized as "fast" reconnection, as they allow rates significantly larger than those permitted by the Sweet-Parker derivation. As such, it is these terms that draw the most attention in this thesis and similar works that focus on reconnection models with rates comparable to those observed in nature.

1.2.3 Two-Fluid

In the context of reconnection, the first new term in Eq 1.4 is known as the Hall term, representing the electric field contribution due to the cross between the magnetic field and the Hall currents. The Hall currents are the result of the differential motion between the ions and electrons at or below the ion kinetic scale (i.e., $\delta \leq d_i$). The formation of these currents is demonstrated in Figure 1.6. The ions begin to diffuse as they enter the ion diffusion region (gray), but the electrons remain magnetized until they enter the smaller electron diffusion region (orange). The difference between the ion and electron paths (where the ions have "cut

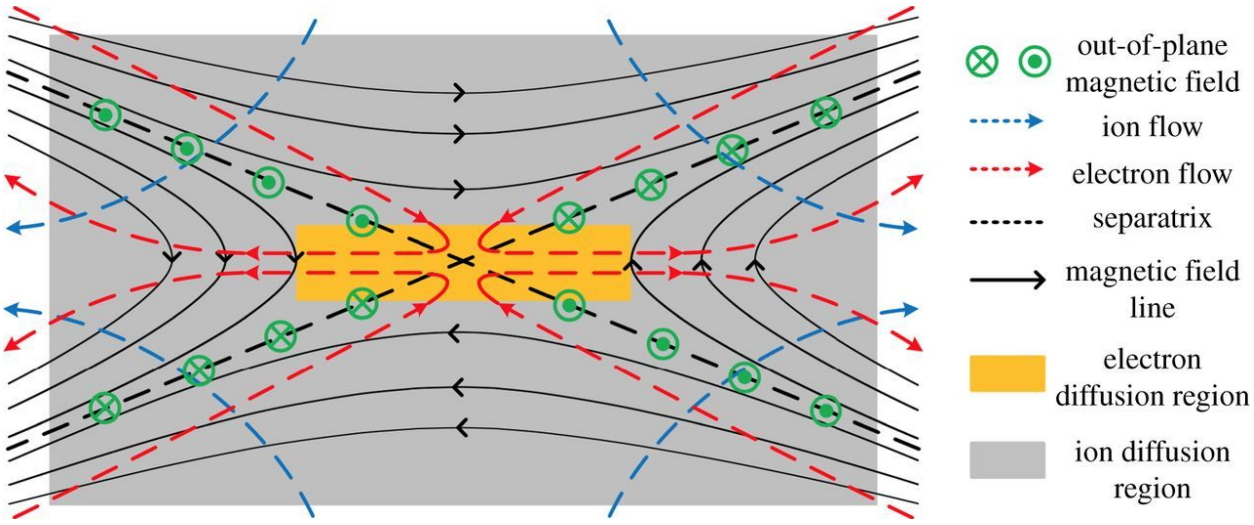

Figure 1.6: A two-fluid regime reconnection layer with visible Hall quadruple magnetic field. Reproduced from Zweibel and Yamada [4]

the corner", so-to-speak) results in four separate current loops- these are the Hall currents, and they generate the quadrapolar Hall magnetic field. The existence of this Hall quadrapole in experimental or simulation data is a fast method of verifying that a given reconnection scenario takes place at sub-ion scales.

1.2.4 Kinetic

At even smaller scales (approaching the electron skin depth $d_e = c/\omega_{p,e}$, where $\omega_{p,e}$ is the electron plasma frequency), the final two terms in Eq 1.4 can become significant factors contributing to the total reconnection electric field. The most notable of these is the pressure-tensor-divergence term[4], which becomes stronger as the electron pressure becomes more anisotropic.

Pressure anisotropy can develop only when the collisionality of the plasma is low enough. The general process is as followed, and is modeled in Figure 1.7: the expansion of the

[4]The final term, the electron inertia, can also contribute. That said, an analysis of the normalized form of Ohm's Law shows that this term scales as the divergence of the pressure tensor term multiplied by a factor of $(d_e/\delta)^2$, where δ is the scale size of the system [8]. The work presented in Chapter 7 of this thesis will show that $\delta \approx 2 - 3d_e$, meaning that the inertial term is expected to be smaller than the pressure tensor term by a factor of $4 - 9$.

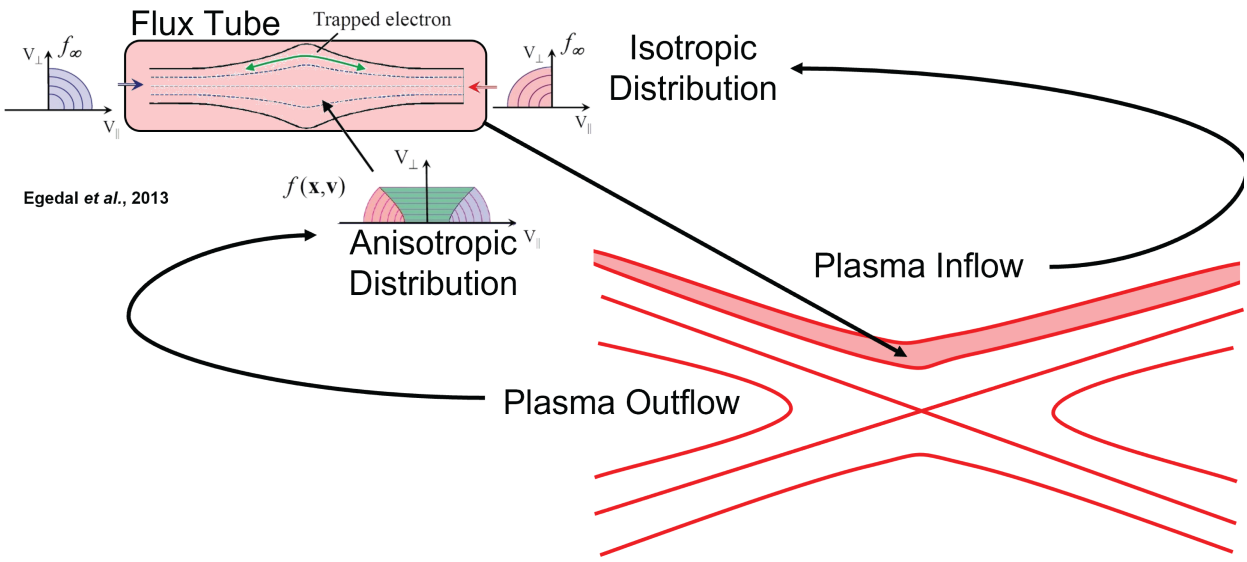

Figure 1.7: The generation of anisotropic pressure in low-collisinality reconnection. Reproduced in part from Egedal et al. [11].

inflowing flux tubes lowers the density of the (still-magnetized) electrons without affecting the (now unmagnetized) ions. To maintain quasi-neutrality, a parallel[5] electric field develops, mitigating the electron density decrease. This field accelerates the electrons in the parallel direction; if the collisionality is sufficiently low, the electrons can be accelerated enough to increase their pressure in the parallel direction ($p_{\parallel}$) while the pressure in the perpendicular direction ($p_{\perp}$) remains unaffected. The result of this is an anisotropic electron distribution function that looks like it has been "stretched" out in the $v_{\parallel}$ direction of the $v_{\perp}$ and $v_{\parallel}$ phase space. This pressure anisotropy leads to a growth in the gradients of several off-diagonal terms of the electron pressure tensor $\mathbf{P_e}$, yielding the increased importance of the $\boldsymbol{\nabla \cdot \mathbf{P}_e}$ term in Eq 1.4[6].

[5] In here and in most circumstances related to reconnection, parallel and perpendicular are defined relative to the direction of the reconnecting magnetic fields.

[6] The exact process leading from the $p_{\parallel} > p_{\perp}$ anisotropy generated in the inflow to the large spatial differentials in specific off-diagonal pressure tensor components is outside the scope of this thesis. Until recently, this mechanism was demonstrated in numerical simulations [9] but did not have a comprehensive theoretical derivation. This has changed due to advances in computing power allowing detailed kinetic simulations at realistic ion-to-electron mass ratios, as explained by Egedal et al. [10].

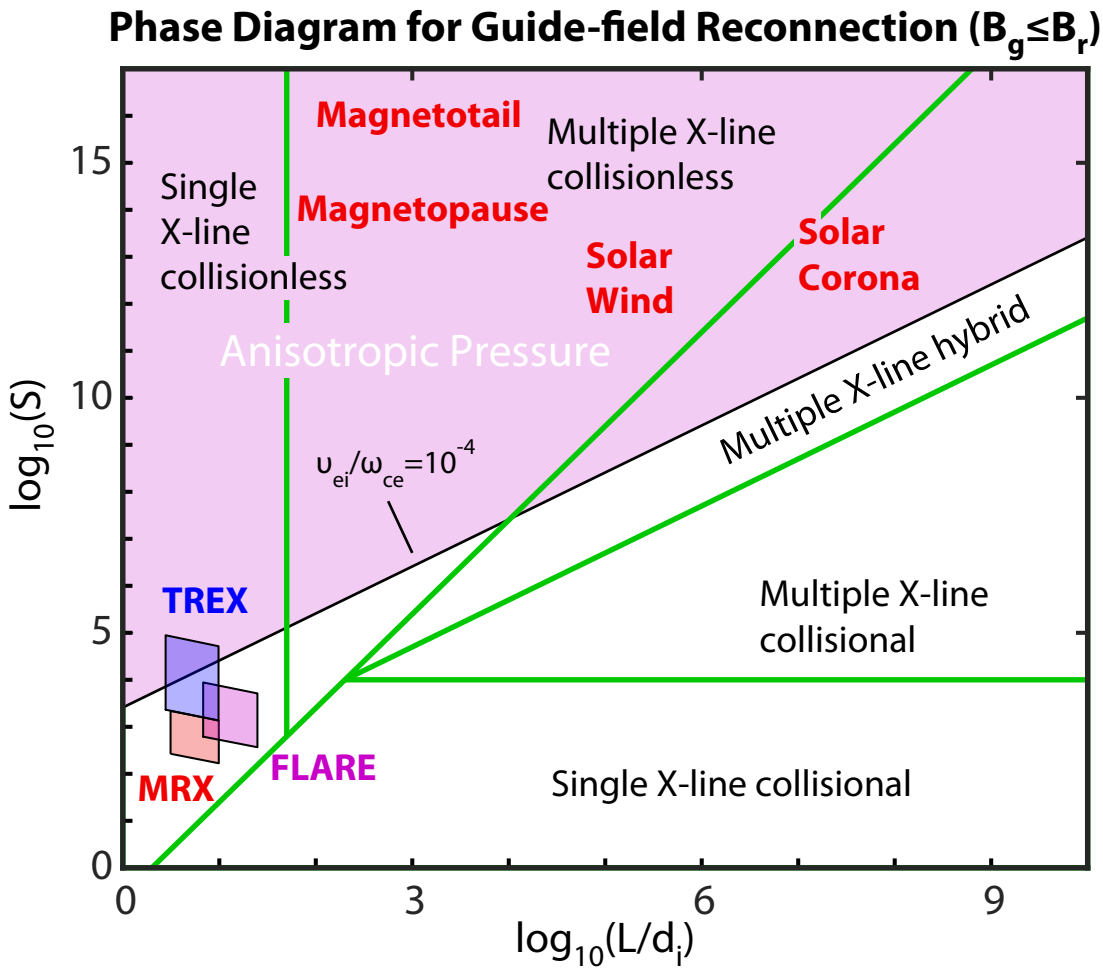

Figure 1.8: Phase diagram for different regimes of magnetic reconnection in the approximately antiparallel case (where the guide field, B_g, is smaller than the reconnection field, B_r). At large enough values of the Lundquist number (S), experiments can reach into the "collisionless" regime which allows for the development of pressure anisotropy; this becomes possible despite the relatively small size of experimental plasmas, compared to their extraterrestrial counterparts. The construction of this phase space is based on the work done in Ji and Daughton [7], Daughton and Roytershteyn [12], and Lê et al. [13].

1.3 TREX Motivation and Objectives

The relative importance of the different terms in Eq 1.4 varies depending on the scale size of the reconnection system and the extent to which the plasma's magnetic field can rearrange itself through diffusion vs. advection; consequently, the various "regimes" of magnetic reconnection (defined by which physical mechanisms are dominant in breaking the frozen-in

condition) can be characterized in a phase space defined by the system size (L/d_i) and the Lundquist number (S) [12]. The result of this calculation is the widely-used reconnection phase diagram, a version of which is shown as Figure 1.8. Here, we can see that many naturally-occurring solar-system plasmas are found in the shaded region where anisotropic pressure distributions can develop[7]. This region is defined by the following simulation-defined inequality:

$$\frac{\nu_{ei}}{\omega_{c,e}} \lesssim 0.1 \frac{m_e}{m_i} \tag{1.5}$$

where ν_{ei} is the local electron-ion collision frequency [13]; effectively, this means that the timescale of the electron collisions must be longer than the timescale of an electron's transit through the reconnection region. Equation 1.5 can be rewritten in the form of Fig. 1.8 phase-space as the following:

$$S \gtrsim 10\epsilon \frac{m_i}{m_e} \frac{L}{d_i} \tag{1.6}$$

where $\epsilon = L_{SP}/L \approx 1$, the ratio of the traditional Sweet-Parker layer length to the actual layer length (taken to be of order unity) [13]. This relation is fortuitous for plasma experimentalists: while space-scale plasmas are (by definition) too large to be recreated on Earth and are generally much more conductive than those that can be generated in terrestrial laboratories, the reconnection regime relevant to these plasmas (where pressure anisotropies can develop) can still be accessed at attainable values of L/d_i and S. This is the motivation behind the creation and design of the Terrestrial Reconnection EXperiment (TREX)- by optimizing the plasma density and magnetic field strength to levels that will place the experiment in the lower left corner of the pressure anisotropy domain, the properties of reconnection in a space-relevant context can be studied in a laboratory environment. The majority of this thesis will focus on efforts to construct and upgrade TREX to push further into this parameter space as well as attempts to verify the dominance of the pressure tensor term of Ohm's Law in breaking the frozen-in condition and to demonstrate that the rate at which reconnection

[7]Higher-density plasmas, such as those used in fusion research or observed in some accretion disks, are typically outside of this region; these labels have been omitted from the diagram as they are not relevant to the work presented in this thesis.

occurs is suitably "fast"[8]. In conjunction with these laboratory datasets, this thesis will also detail the implementation and evolution of a particle-in-cell code (VPIC) as a simulated model of TREX itself.

1.4 Thesis Outline

This thesis will be presented in the following order:

- Chapter 2 will explain the construction and workings of the BRB, or Big Red Ball, the vacuum vessel that TREX operates in as part of the WiPPL (Wisconsin Plasma Physics Laboratory) collaborative research facility.
- Chapter 3 will detail TREX's first (publication-producing) experimental run, roughly corresponding to the years 2015 and 2016. This run resulted in the observation of plasmoid formation within TREX [15], owing to the intricately-constructed magnetic flux array probe.
- Chapter 4 explores the TREX configuration that ran in 2017. This run introduced substantial hardware upgrades but was hindered by probe construction difficulties; this set the stage for the following year's run campaign.
- Chapter 5 describes TREX's 2018 run campaign, which built on the successful hardware upgrades from the previous year with a new probe construction paradigm that greatly improved probe efficiency and standardization relative to past TREX probes. It was data from this campaign that motivates the work in the next three chapters.
- Chapter 6 is an introduction to the particle-in-cell code known as Cylindrical VPIC, which has been used extensively to simulate the TREX experimental geometry. This newly-created code (courtesy of Los Alamos National Laboratory) facilitated TREX

[8]Much of this process was also covered in detail in Olson [14], with some emphasis on parts of this endeavor that will not be examined here.

simulations in 2D and 3D that were instrumental in the data analyses that make up the next two chapters.

- Chapter 7 details the analysis of the width of the TREX reconnection layers in both simulation and experiment, as well as the relevance of the width in the context of Ohm's Law and the observation of the likely Lower Hybrid Drift Instability in these datasets. This chapter is essentially a reproduction of Greess et al. [16].
- Chapter 8 describes the evaluation of the reconnection rate in simulations of TREX and compares them to the experimental results found in Olson et al. [17]. This chapter is essentially a reproduction of Greess et al. [18].
- Chapter 9 is the conclusion of this thesis, wherein the main points and findings will be summarized.

In addition, this thesis contains several appendices:

- Appendix A gives additional information about the probes used in the different experimental iteration; specifically, it details the magnetic flux array used successfully to measure the data shown in Chapter 3, the attempted magnetic flux array and subsequent prototype Bdot probes that were tested in tandem with the hardware upgrades described in Chapter 4, and finally some engineering specifics relating to the T_e probe introduced in Chapter 5.
- Appendix B is an extended look at some of the technical aspects and intricacies of TREX VPIC, including a listing of the relevant user-defined inputs and detailed calculations of the various code and computational timesteps.
- Appendix C contains additional information relating to the data collection and analysis processes of Chapter 7.
- Appendix D gives more information on the Lower Hybrid Drift Instability, including its physical basis and some of the properties used to identify it in Chapter 7.

Portions of appendices A, B, and C are specifically written in the context of providing engineering and programmatic details that may be helpful to future researchers who find themselves in positions similar to that of the author, in the hopes that some of the challenges that went into reaching the final conclusions of this thesis will be understood and overcome.

Chapter 2

The Big Red Ball at the Wisconsin Plasma Physics Laboratory

The Big Red Ball (BRB) is a 3 meter spherical vacuum vessel, part of the Wisconsin Plasma Physics Laboratory (WiPPL), which itself is a DOE collaborative user facility operating out of Madison, Wisconsin. The Big Red Ball, so-named due to its shape and its covering of red-painted insulation, is the vessel in which all TREX experiments have been performed. A photograph of the outside of the BRB with associated peripheral coils and various probes can be seen in Figure 2.1

The BRB was initially called the Madison Plasma Dynamo Experiment (MPDX), when it was conceived and built in the late 2000s and early 2010s. Its original purpose was to use a ring cusp confinement method (see Section 2.2) and a novel method for stirring the plasma [19] to induce flow-driven MHD instabilities at astrophysically-relevant parameters, allowing investigation into the physics of laminar and turbulent plasma dynamos [20]. While much of this functionality was verified by Weisberg et al. [21], the wide versatility of the MPDX vessel in regard to the customizability of its hardware and its confined yet unmagnetized plasma bulk eventually led to its designation as the BRB facility [22].

The BRB is well suited to studying both basic plasma processes as well as phenomena relevant to a wide variety of space and astrophysical systems. In addition to hosting TREX

and our various magnetic reconnection experiments, published results from work on the BRB include topics such as ambipolar diffusion across field lines [23], the magneto-rotational instability [21], the Parker spiral [24], and the formation of collision-less shocks [25].

This chapter will present an overview of the BRB, specifically in regard to its engineering and general physical parameters. The vacuum vessel itself will be discussed in Section 2.1, followed by a summary of the geometry and properties of the vessel's cusp confinement configuration in Section 2.2. Section 2.3 will explain the construction and use of the BRB's external Helmholtz coil, which is an essential part of the various TREX experiments. The next Section, 2.4, will deal with the two plasma sources on the BRB that were used for TREX, namely the cathodes used in earlier configurations (subsection 2.4.1) and the plasma guns used for later configurations (subsection 2.4.2). Finally, this chapter will conclude with a brief overview of the generalized process of probe use and construction for the BRB (Section 2.5) and the various control systems used to manage BRB experiments (Section 2.6). The contents of this chapter are focused on aspects of the BRB that are or have been useful for TREX, but not on elements that are unique or purpose-built for TREX; for TREX-specific hardware, see the following chapters.

2.1 Vacuum Vessel

The BRB is a spherical aluminum vacuum vessel covered in insulating spray foam. The foam, which insulates the vessel and mitigates potential condensation issues, is painted red, resulting in the vessel's name. The aluminum cast is approximately 1.5 inches thick with an inner diameter of 3 m. The wall of the casting includes embedded cooling channels through which water is pumped. The wall also includes multiple cutouts of different sizes, shapes, and locations to allow access for diagnostics and hardware. Specifically, the BRB has nearly two hundred 3 inch circular ports, sixteen 16.5 inch circular ports, and twelve large rectangular ports ("boxports"), many of which are visible in Figure 2.1. The base pressure of the vessel, 5–10 $\times$ 10^{-7} Torr, is maintained using two 2000 L/min turbomolecular pumps, two 1000

L/min turbomolecular pumps, and two 4000 L/min cryogenic pumps.

Geographically, the BRB is oriented such that its equator extends from North to South with poles at the East and West. Magnetically-speaking, the geographically Western-most pole is the Northern (N) pole, and the hemisphere containing that pole is known as the N hemisphere[1]. The N hemisphere rests on rollers that allow it to separate from the S hemisphere. This opening facilitates the installation of larger hardware (see Figure 2.2); this process is further aided by two overhead cranes, one of which is mounted to the ceiling of the lab space one floor above the BRB and accessible via a large rectangular cutout in the floor. Depending on the hardware being installed and the number of personnel on-hand, the turn-around from vacuum-break to sealing the vessel and pumping back down can take as little as a single day.

2.2 Confinement

The interior surface of the vacuum vessel is lined with several thousand SmCo rare earth magnets (3.8 cm×2.5 cm×5.0 cm) with $B \sim 0.3$ T at their surface. These are installed in 36 axisymmetric rows, which are visible in Figure 2.3. The rings are separated by 5° each and are embedded with alternating polarity, such that the entire wall forms a high-order multipolar magnetic field. These magnets are shielded from the plasma with alumina tiles; the remaining interior is covered by alumina spray.

This confinement configuration has been demonstrated in Cooper et al. [20], as shown in Figure 2.4. The top two plots show how the plasma density and temperature fall off as distance from the wall decreases, while the bottom plot shows (in addition to linear cuts from the top two plots) that the wall's magnetic field falls off rapidly as distance from the wall increases. There is very little overlap between the region where the plasma exists up to the

[1] A common way to contextualize these directions within the BRB lab-space is to use the nearest cross streets: Charter St, which goes North and South, and University Avenue, which is a one-way street going from East to West. The N hemisphere [magnetic] is the one closest to Charter St. The equator of the BRB runs parallel to Charter. See this map of Sterling Hall on the UW-Madison campus for details.

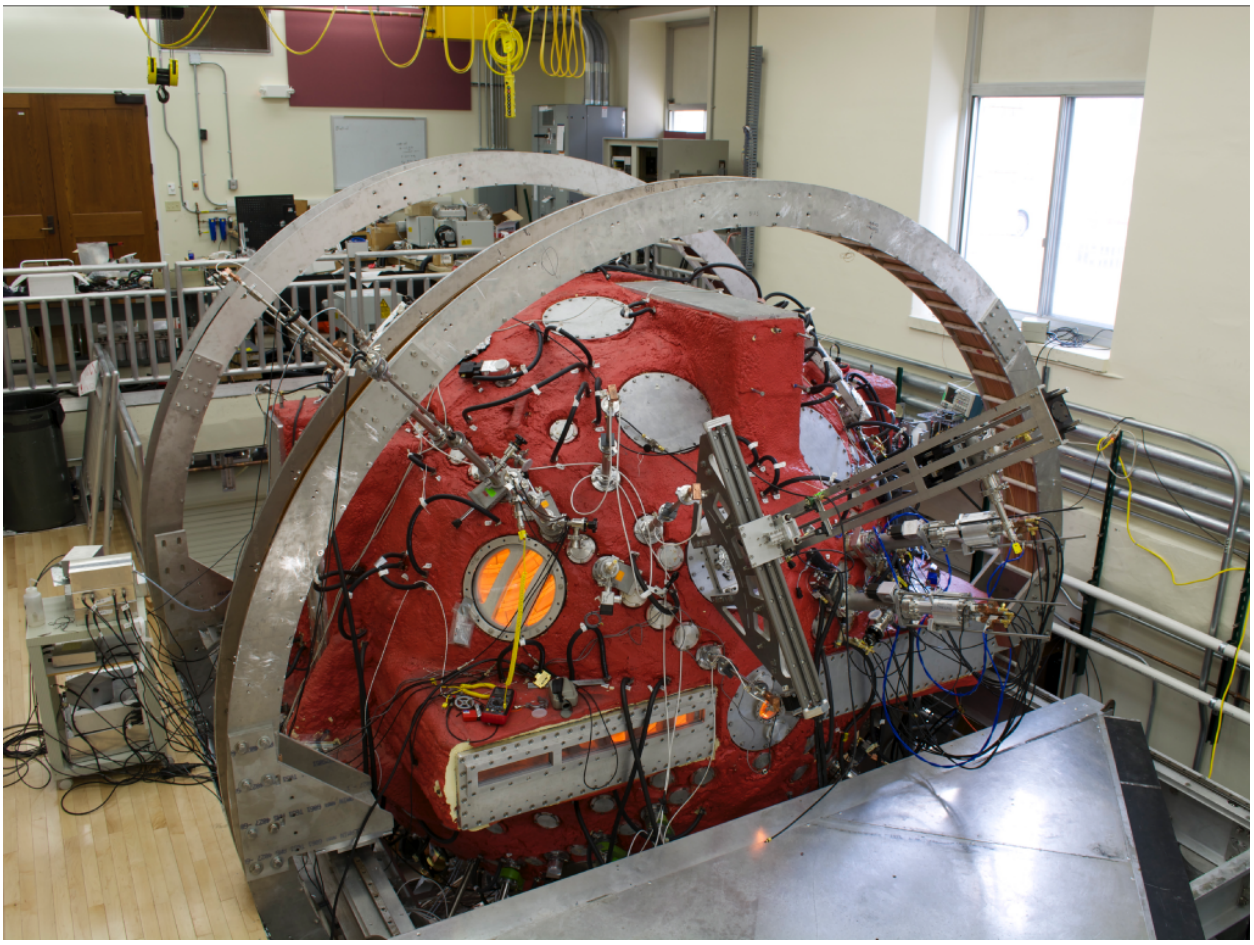

Figure 2.1: The BRB (Big Red Ball) at WiPPL.

wall and the region where the magnetic field from the wall exists. This gap between the plasma and the wall's magnetic field means that the plasma is both confined and unmagnetized. This is one of the main advantages of the BRB - different magnetic configurations can be implemented inside the device without disrupting the overall confinement.

2.3 Helmholtz Coil

The construction and installation of the external Helmholtz Coil on the BRB was completed toward the end of the summer of 2014. While this timeframe places most of the construction process outside the scope of this dissertation, some of the work done on the coils (particularly

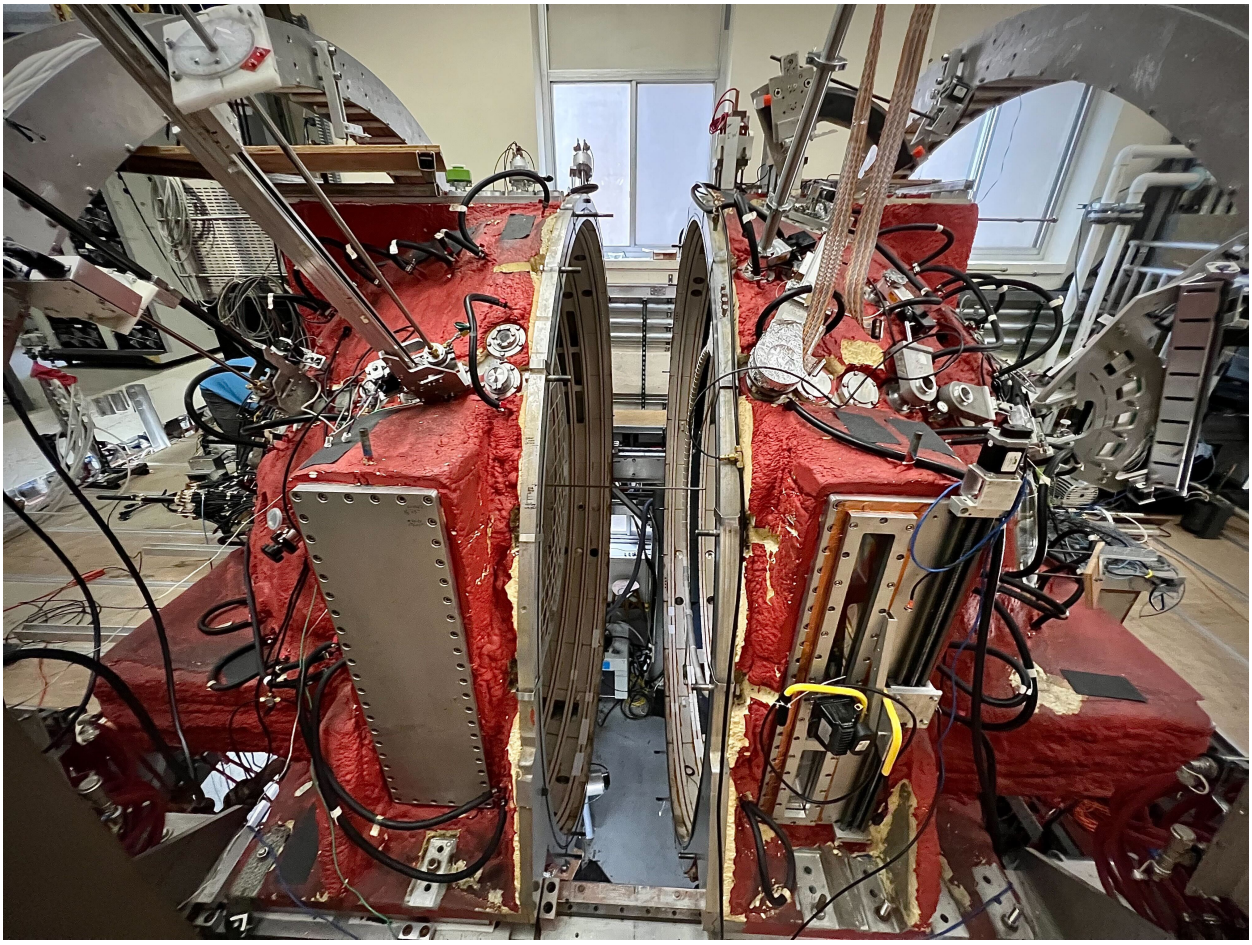

Figure 2.2: The BRB split open to facilitate hardware installation.

with respect to the inter-winding electrical connections and cooling system) was done by the author, and as such will be detailed in this section, along with a basic overview of the coil and its functionality. A more in-depth explanation of the coil's construction and operation may be found in Olson [14].

A Helmholtz coil is a particular geometry of electric currents that is implemented in many different experimental contexts to create nearly-uniform magnetic field through a large volume. A Helmholtz coil configuration is created when two identical coils of radius R_H are placed coaxially, such that the separation between them is also equal to R_H. By summing the contributions from each individual coil, the total on-axis magnetic field magnitude is

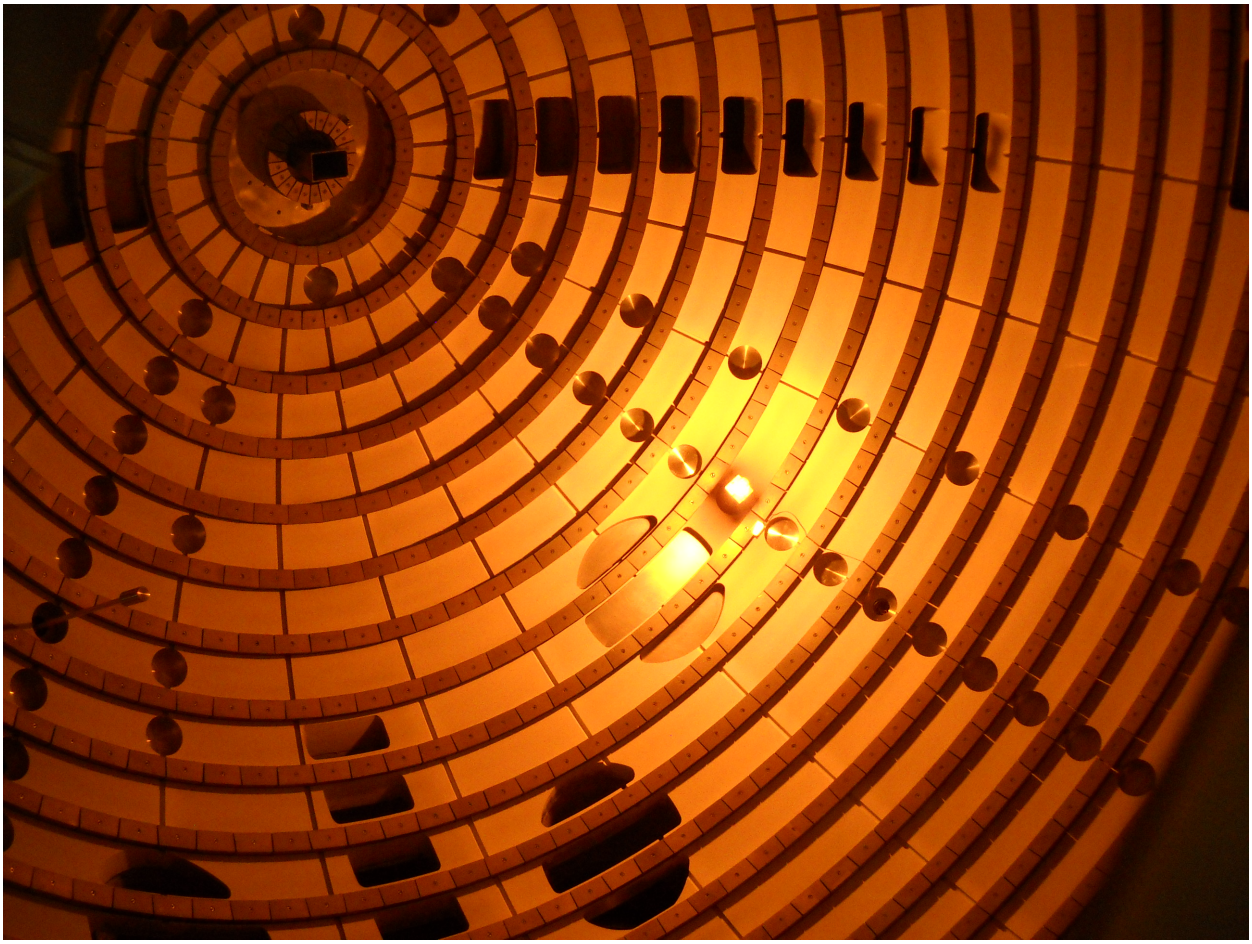

Figure 2.3: Concentric permanent magnetic rings inside the BRB.

found to be

$$B_H = \left(\frac{4}{5}\right)^{3/2} \frac{\mu_0 I_{tot}}{R_H} \tag{2.1}$$

where I_{tot} is the total current through an individual coil; if a coil has N turns and I current per turn, then $I_{tot} = NI$. The full analytical result for the off-axis field can be derived using elliptical integrals of the first and second kind; details on this analysis may be found in Olson [14]. The direction of the Helmholtz field can be varied, depending on how the Alpha power supplies (described below) are connected. For a usual TREX experiment, the background Helmholtz field points from the Northern pole to the Southern pole; in the usual TREX analyses, this is taken to be the $-\hat{z}$ direction.

A schematic of the BRB Helmholtz coil's physical parameters may be found in Figure 2.5(a).

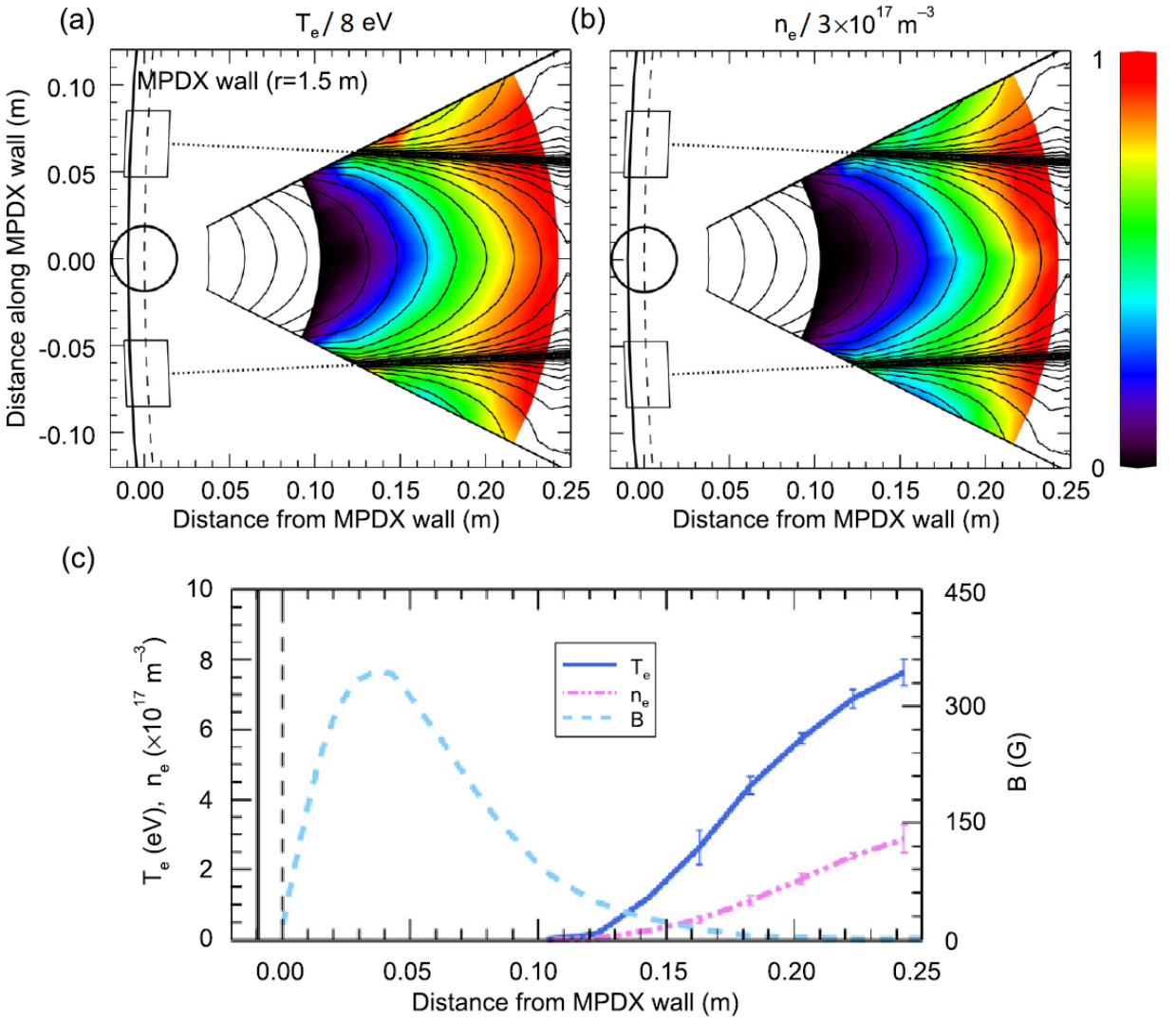

Figure 2.4: Measurements of plasma temperature (a) and density (b) near the wall of the BRB, demonstrating the plasma confinement properties of the embedded magnet rings in Fig. 2.3. The black lines are contours of the magnetic field. (c) shows the profiles of B, T_e, and n_e along a radial cut through the profiles in (a) and (b). Figure reproduced from Cooper et al. [20].

Due to the physical constraints of the BRB vessel, the coil configuration is not technically that of a "true" Helmholtz coil; the separation between the coils (2.32 m), slightly larger than the coil radius of 2.03 m. A comparison of the BRB coil's field with a "true" Helmholtz field is shown in Figure 2.5(b); while there is a difference in the overall magnitude of the field inside the vessel, the relative uniformity of the field through the regions of greatest interest for TREX ($R < 1$ m and $|Z| < 1$ m) has not been significantly changed.

Each of the two coils on the BRB was constructed from 88 total turns of water-cooled copper conductor. An example of this conductor - extruded copper with a square cross-section and central hole for water flow - can be seen in Figure 2.6(a). These conductors are insulated with a Daglas glass and polyester blend that provides 600V of electrical insulation. The process of winding these conductors is explained in further detail in Olson [14], but the roller assembly used to uncoil the conductor from its spool and wind it onto the Helmholtz coil frame is included here in Figure 2.6(b). Each frame is wound with 16 individual loops of 5.5 turns of a single continuous conductor. To connect these loops together, the ends of each loop were de-insulated and bent away from the frame before being clamped and brazed together to establish an electrical connection. These conductor ends were also fitted with brass hose nozzles to facilitate their connections to the water cooling system via the manifolds directing water through each loop. These two types of connections can be seen in Figure 2.6(c) and (d)[2].

The two coils are connected to a system of large power supplies known as the "Alphas," named for their company of manufacture (Alpha Scientific). The Alphas are water-cooled and capable of outputting a maximum continuous output of 800A at 194V. Based on this maximum, the Helmholtz coils can generate a maximum field of 282 G at the center of the vessel. More detail about the Alpha power supplies may be found in Olson [14].

[2]It is [some of] these connections that were the writer's most substantive contribution to the permanent BRB hardware; they are something he is exceptionally proud to have assisted with in his very first months in Madison, back in 2014.

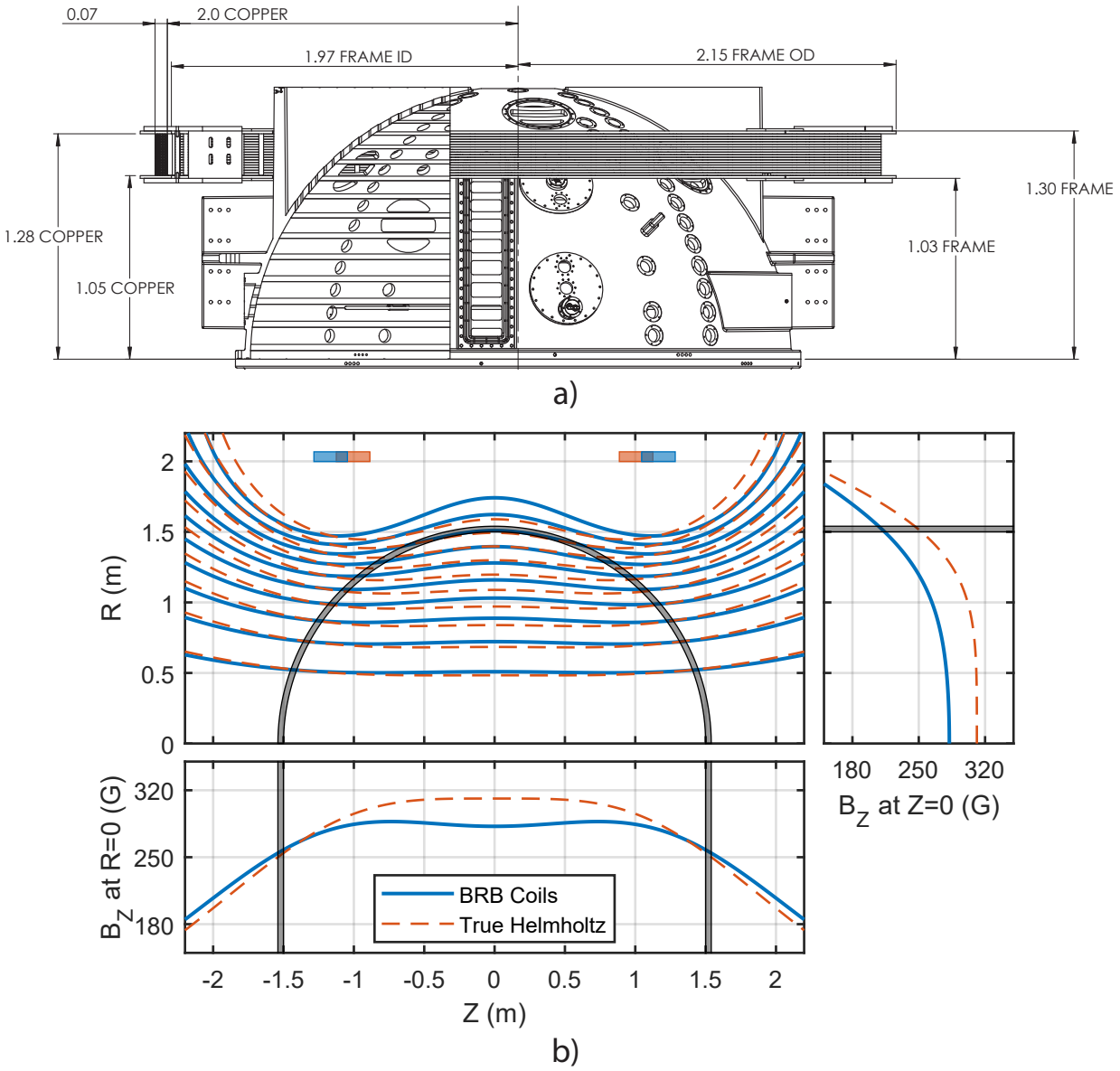

Figure 2.5: The BRB Helmholtz coil. (a) shows an engineering diagram of one hemisphere of the BRB and its associated coil, showing the positions and dimensions of the coil windings and housing relative to the BRB's poles and equator. (b) shows profiles of the BRB Helmholtz coil (blue) compared with a "true" Helmholtz coil (orange), where the coil separation would be exactly equal to the coil radius. Though the BRB's coil placement disqualifies it from being a technically "true" Helmholz setup, the deviation in the shape of the field from a "true" Helmholtz field is negligible inside the boundaries of the BRB vessel (shown in gray). Reproduced from Olson [14].

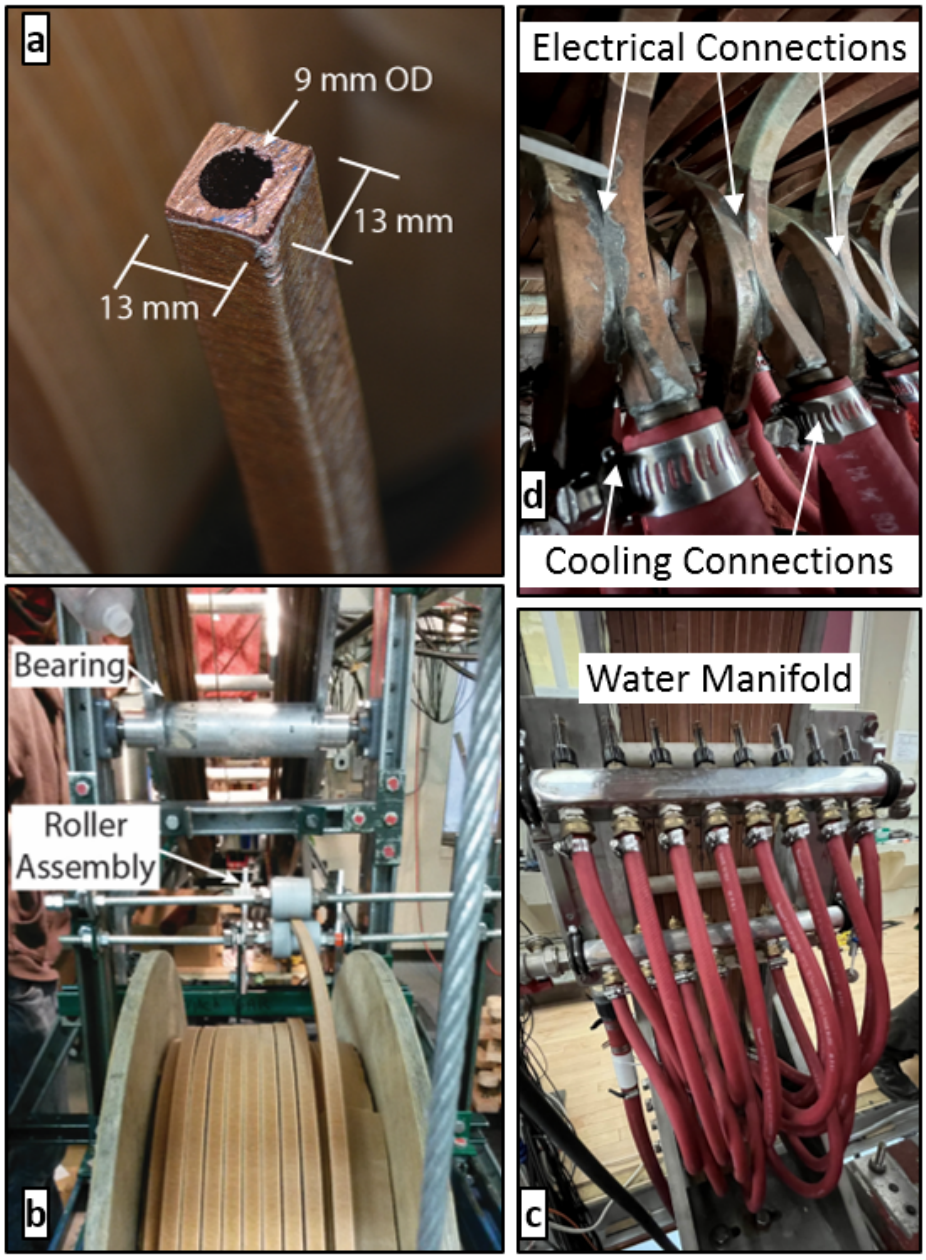

Figure 2.6: (a) Closeup picture of the copper conductor used for the Helmholtz coil wrapped with fiberglass insulation. The hollow center allows for the coils to be water-cooled while in operation. (b) As the conductor comes off the spool, it runs through a roller assembly that helps straighten and align the copper before winding onto the coil frame. (c) Water cooling manifold on the inner side of the western coil. The red tubing connects the water supply to the different conductor segments. (d) Electrical connections between different conductor segments. These soldered connections combine the distinct wound conductor loops into a single continuous electrical loop. Partially reproduced from Olson [14].

2.4 Plasma Sources

While several different plasma sources can and have been used on the BRB, this section will describe the two sources most relevant to TREX. Specifically, the cathodes were used for TREX runs up through 2016; starting in 2017, the plasma guns became the main TREX plasma sources.

2.4.1 Cathodes

The emissive cathodes consist of a lanthanum hexaboride (LaB_6) tip (a 3cm by 7cm cylinder) which is radiatively heated by an internal graphite filament to $\sim 1300°C$. Electrons emitted from these cathodes are drawn to a separate anode; the relative electrical bias between these two tips results in electrons being accelerated up to several hundred eV. These electrons both ionize the surrounding gas and heat the resultant plasma. LaB_6 is a commonly used filament for industrial hot cathodes due to its low work function, large current output, and durability. The cathodes on the BRB were initially designed to heat and stir the plasma of the original MPDX experiment; more detail on their construction and operation can be found in Weisberg [26]. While the standard BRB cathode circuits use a switching power supply to run in steady-state, this proved incompatible with TREX's large applied Helmholtz field; as such, a separate discharge circuit was implemented to circumvent this difficulty. Further detail about the design an operation of this circuit may be found in Olson [14].

2.4.2 Plasma Guns

The plasma guns are an array of "washer" guns, so-named because they contain an arc chamber made of alternating molybdenum and boron nitride washers. At opposite ends of this arc chamber sit a cathode and an anode; when appropriately biased, these generate an arc across the chamber that ionizes any neutral gas that has been pumped into the chamber's volume. The resultant plasma then expands out of the gun's nozzle and into the BRB vacuum vessel at the relative sound speed. A diagram of a single washer gun can be seen on the right

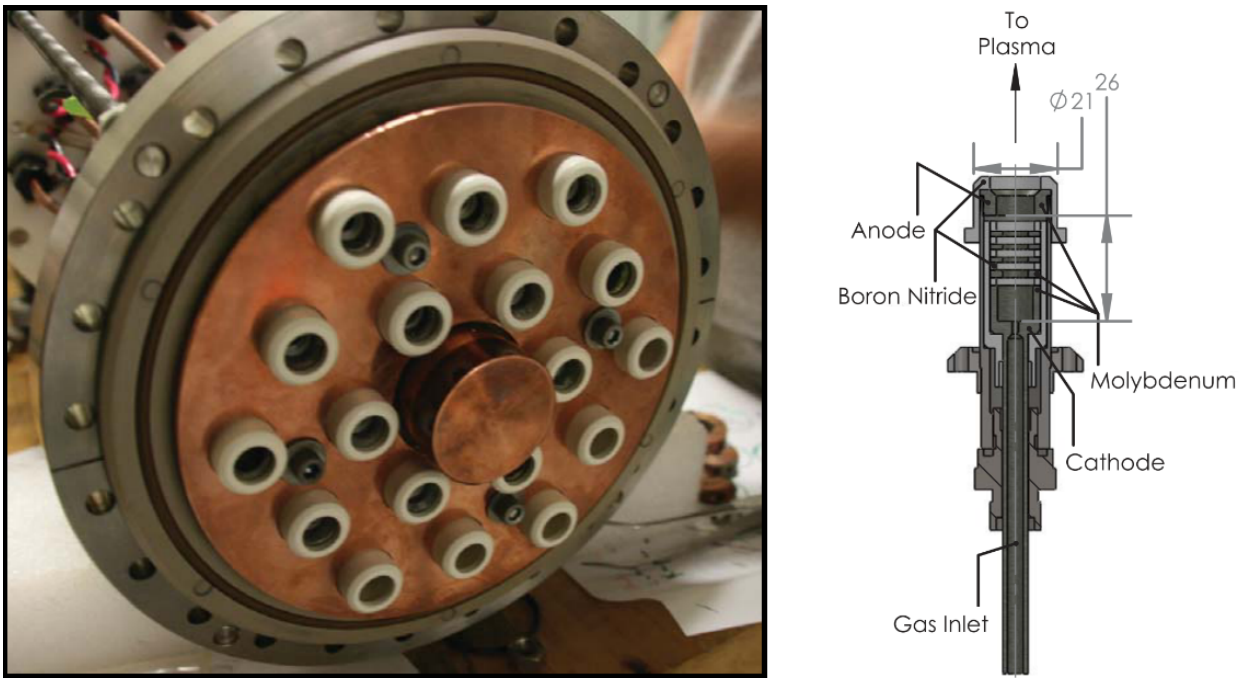

Figure 2.7: (left) The plasma-facing side of the plasma gun array. This group of guns is located on the BRB's northern pole. (right) Schematic of an individual gun. Both images reproduced from Brookhart [27]

half of Figure 2.7. 18 of these washer guns are arranged in a hexagonal pattern, visible on the left side of Figure 2.7; together, these form the plasma gun array.

The guns are powered by a set of custom-made pulse forming network (PFN), one for each gun of the array. Ionization in the arc chamber begins with an initial voltage spike of > 500V from the PFNs, which then transitions into a near-constant output of 1kA and ~ 100V. These current and voltage measurements are tracked and recorded as part of the dataset for each experimental shot. The resultant data traces can be used as a quick confirmation of the success of the plasma generation and thus the validity of a given experimental shot (as shown in Figure 2.8(a) and (b)).

The gun arrays were initially designed for use on the Madison Symmetric Torus [28] and were later adapted or duplicated for use in the Rotating Wall Machine Experiment, the Line-Tied Reconnection Experiment, and the Pegasus experiment [29]. More detailed descriptions of the construction and functionality of the plasma gun array may be found in

Brookhart [27] and Endrizzi [30].

While the plasma guns have generally proven superior in their durability and ease of use relative to the cathodes (such that all TREX experiments from 2017 through the present use them exclusively), they are not without their disadvantages. The arcing and ionization process can fail [necessitating the *ex tempore* checking of the current traces, as in Figure 2.8(b)], and over time the washers degrade and their material is ablated into the BRB volume (see Figure 2.8(c)). Regardless, their functionality in aggregate has been instrumental for TREX's recent experimental successes.

It should be noted that the location of the plasma gun array (at the BRB pole aligned with the central axis) means that plasmas generated by the guns tend to be denser at smaller values of R (i.e., closer to the central axis). This is not necessarily a drawback, as many of the reconnection types being investigated in TREX (such as that at the dayside magnetopause) involve density asymmetry, but it should be kept in mind. The degree of asymmetry can be controlled by the strength of the Helmholtz field being applied while the guns are in operation; stronger fields will collimate the plasma more tightly along the BRB's axis.

2.5 General Probe Construction

While future sections will explain the individual probe construction processes (or, more specifically, the actual measurement-taking portions of a probe), this section will detail the generalized probe geometries that are most often used in the BRB. These details relate to spatial coverage, support, position tracking, and quality of the vacuum seal; all of these issues must be taken into considering when designing a probe for use on TREX or any other BRB experiment.

Most (but not all) TREX probes are designed to be installed and removed while the BRB vessel is pumped down to vacuum. Furthermore, probes are generally expected to be able to take measurements in the center of the vessel, necessitating that the length of the probe-shaft from the measurement area to the box outside the vessel be on the order of a few

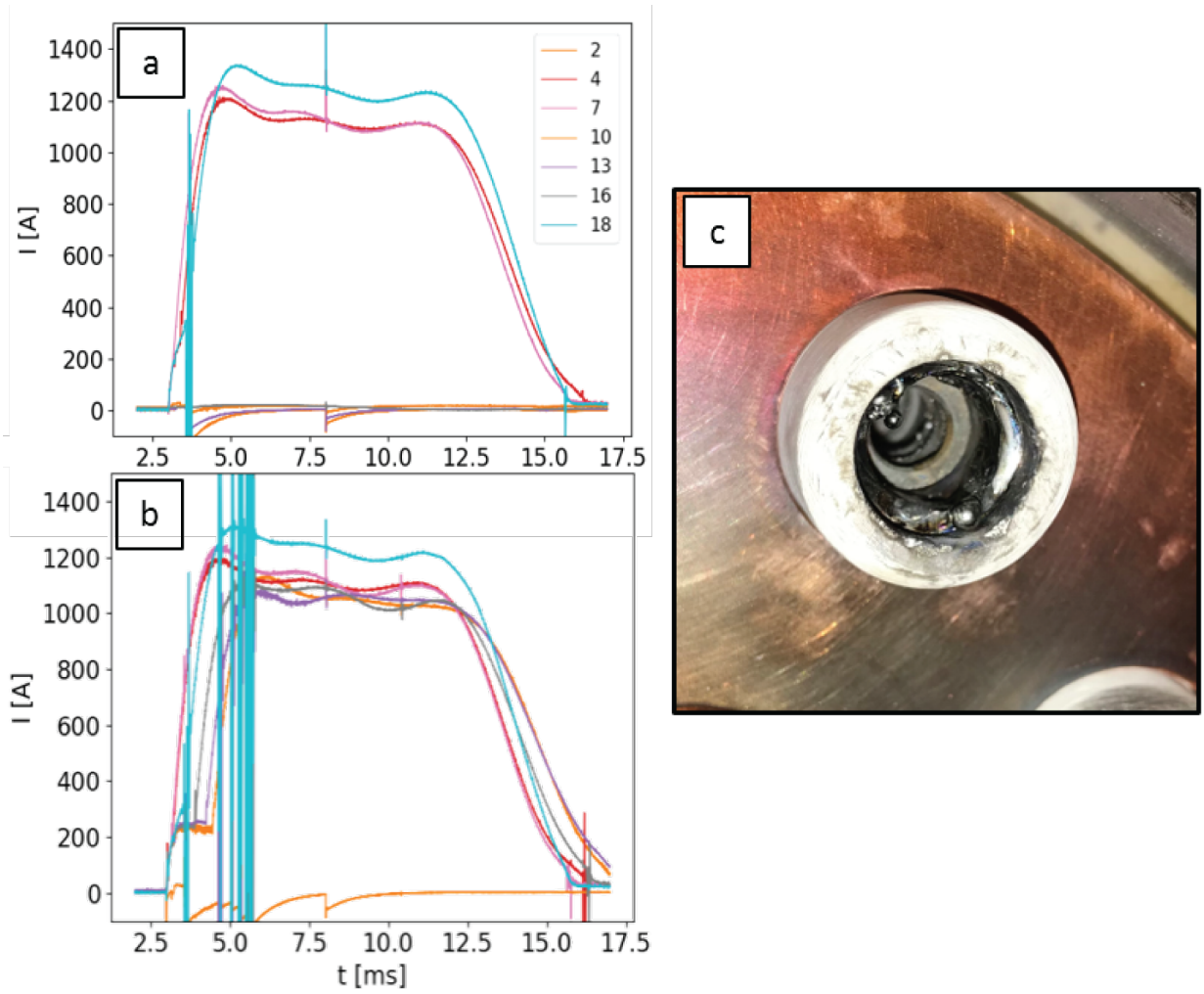

Figure 2.8: (a) and (b) are traces of the current through the plasma gun PFNs as seen in the control room during regular running of the experiment. (a) shows a good shot with three guns set to run (the rest are turned off and thus have signals set to 0 aside from noise pickup), while (b) shows an example of a shot with six guns, where four of them have failed (in this case, gun 18 [blue] experienced significant sputtering and guns 13, 6, and 2 experienced a notable delay in their start up time. Gun 10 is not turned on; the typical 0-trace has been corrupted by the significant noise pickup from the other gun malfunctions). (c) shows an example of how the plasma guns can degrade with time - the gun anode has melted and reformed into multiple beads of metal around the apeture. Image reproduced in part from Endrizzi [30].

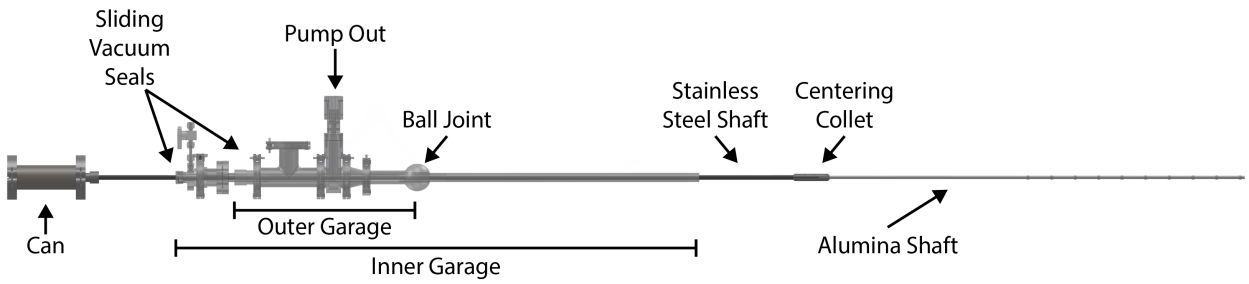

Figure 2.9: Generalized diagram of the standard probe construction for use on the BRB. The telescoping design allows the probe tip to reach deep into the BRB. Some probes can be inserted and withdrawn without breaking the BRB's vacuum; this depends on the relative sizes of the garages and the shafts. Image reproduced from Olson [14].

meters. These two considerations necessitate the usage of a double-telescoping garage design, which when fully retracted can house the probe outside of the BRB vessel but when fully extended can reach the targeting measurement area. An example of such a setup is shown in Figure 2.9. The actual measurement portion of the probe is encased in the (plasma-facing) alumina tube, which is mated to a stainless steel shaft; this shaft protects the probe wiring as it extends from the alumina up to the can, where it is connected to a vacuum-sealed electrical feedthrough. The output of this feedthrough is then connected to the probe's associated racks as needed. The stainless steel shaft is enclosed by the two concentric telescoping garages, which are equipped with sliding vacuum seals to allow for probe movement without breaking vacuum.

To connect a probe to the vacuum vessel, the fully-retracted probe is physically attached at the tip-side end of the outer garage to one of the BRB's (closed) external ports. A vacuum system is then connected to the pump out output on the outer garage and the probe interior is pumped down to vacuum. The BRB port is then opened and the probe is now part of the vessel's vacuum system. If the probe is leak-proof, it can now be pushed and pulled along the telescoping garages' axis. Various stops are used along different portions of the stainless steel shaft and the inner garage to prevent the probe from extending too far.

Probe positioning can either be done by hand or through the use of a properly calibrated motorized probe stage system; the latter case is particularly useful for probes that will be

moved to many different locations throughout an experimental campaign. Linear movement stages are easily clamped to the probe's outer garage while the stepper motor is attached to the stainless steel probe shaft; the motor's movement is set via Labview (see Section 2.6, below) which sends and receives signals from the stage's associated Galil motor controller.

The BRB also has the option of installing probes on a sweep stage that combines the motion of a linear stage with an angular extent of $\pm 30°$, giving the probe coverage area through a $2D$ wedge rather than along a single linear cord[3]. Probes attached to these stages need to be built with an additional ball joint at the tip-side end of the outer garage (shown in Fig. 2.9). A generalized view of the sweep stage setup is given in Figure 2.10.

2.6 Control Systems

The various control systems used to operate TREX (or indeed, any experiment on the BRB) have been constructed through years of work, wherein graduate students and research scientists have built on each other's contributions to create a workable (if at times finicky) network of programs, interfaces, and devices. A full description of all of these systems and their workings are far outside the scope of this dissertation; what follows is simply a list of the different components or processes and a short description of their part in the operation of the experiment, to be used as a quick reference for someone who may be involved with TREX's experimental operation but not intimately familiar with the intricacies of control systems. More detailed information about the variety of control systems may be found in any prior BRB/MPDX theses, with a particular emphasis on Olson [14] and Weisberg [26].

2.6.1 Labview

The experimental operator interface is designed using the LabView software, creating a single Virtual Instrument (VI) that controls many of the TREX experimental parameters from the

[3]However, unlike linear stages that can be installed on almost any probe at any port location, sweep stages are limited to installation on one of the fourteen $16.5''$ ports

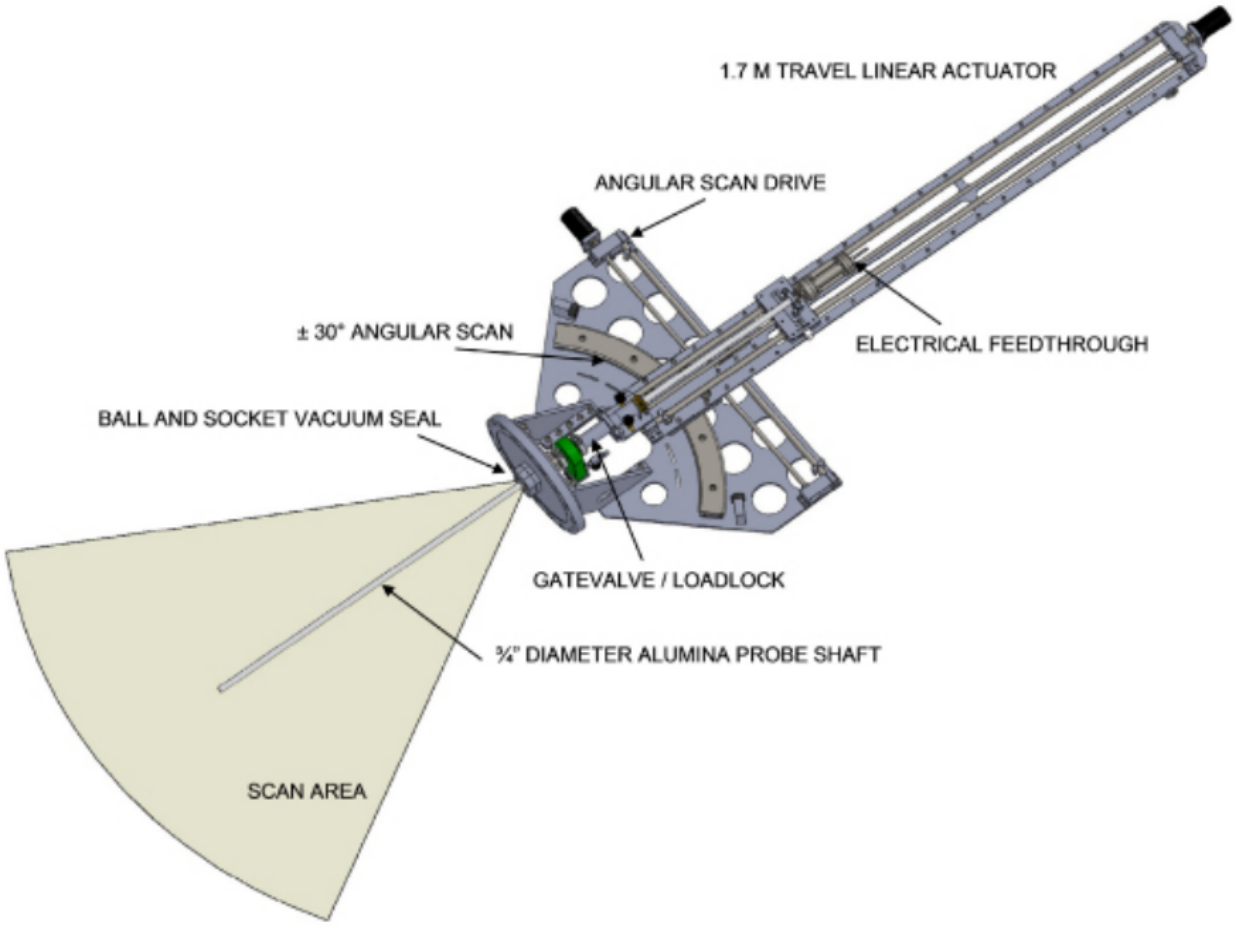

Figure 2.10: Diagram of the BRB probe sweep stage, which allows probes to measure a $2D$ area inside the vessel, rather than just a single linear chord segment. Image reproduced from Olson [14].

safety of the BRB control room. Most typically, the TREX VI is used to send trigger pulses to various switches and digitizers, control the size of the drive potential and Helmholtz field used to induce reconnection, set the locations of any probes attached to a motor control, and to set a shot to operate with a plasma or in a vacuum. LabView is a program created by National Instruments that uses block diagrams, pre-programmed VI subroutines, and visual programming to facilitate the production of customized laboratory control interfaces.

2.6.2 cRIO

The cRIOs (compact RIO, where RIO is an industry-typical acronym for reconfigurable input/output module) are two National Instruments systems that interface directly with LabView. In TREX, they are used to execute LabView commands that specify the size of the capacitor bank drive potential and the strength of the Helmholtz field.

2.6.3 Trigger Systems

The BRB trigger control system uses a field-programmable gate array (FPGA) to send trigger pulses through fiber optic cables to various control boxes and digitizers through the lab area. The trigger systems offer up to 24 channels of "slow" triggers with 1 ms resolution and up to 32 channels of "fast" triggers with 1 µs resolution; these fast triggers are a secondary system set by a primary trigger input. The fast triggers are specifically useful for pulsed-power applications like TREX.

2.6.4 MDSplus and Digitizers

Data signals taken from TREX probes are digitized at or near the probe output. As the type of digitizer and speed of digitization used has varied between different TREX campaigns and different TREX probes, more detail about a specific digitizer setup will be given in each of the relevant sections of the following chapters. After a given shot, the data is uploaded to a remote database using MDSplus, a software that allows users to create and manage databases and data structure hierarchies. This data is easily accessed remotely (from within the WiPPL internal plasma network or by way of an approved remote IP address) and can be downloaded for local analysis.

Chapter 3

TREX 2015-2016

TREX 2015-2016 was the earliest iteration of TREX that produced published results[1]. While the author was a part of this version of TREX, particularly with respect to the construction and testing of the experiment's main magnetic diagnostic, the flux array, most of the results and construction of this experiment were covered in detail by previous thesis work. As such, this chapter will provide a brief introduction to this version of TREX and the resulting data. A deeper investigation of this experiment may be found in Olson et al. [15] and Olson [14]. For the main portion of this thesis' focus, please see Chapters 4 (for the hardware) and 5 (for the data collection). For further information on the theory and design behind the magnetic flux array used to obtain the results detailed in this chapter, see Appendix A.

3.1 Coil Geometry & Plasma Source

A 3D CAD view of the TREX geometry may be seen in Figure 3.1, which also includes an insert of a theoretical reconnection layer and the associated magnetic field lines. The drive coils, shown in magenta, are included, as are the magnetic flux array (red and black; coverage area shaded gray in the theoretical layer insert) and the sweep stage (blue) which held this

[1] An earlier version that began running in fall of 2014 but was unsuccessful in generating useful reconnection data. As it was technically from a time before the author of this thesis was a part of the TREX research group, it will not be covered in any further detail in this document.

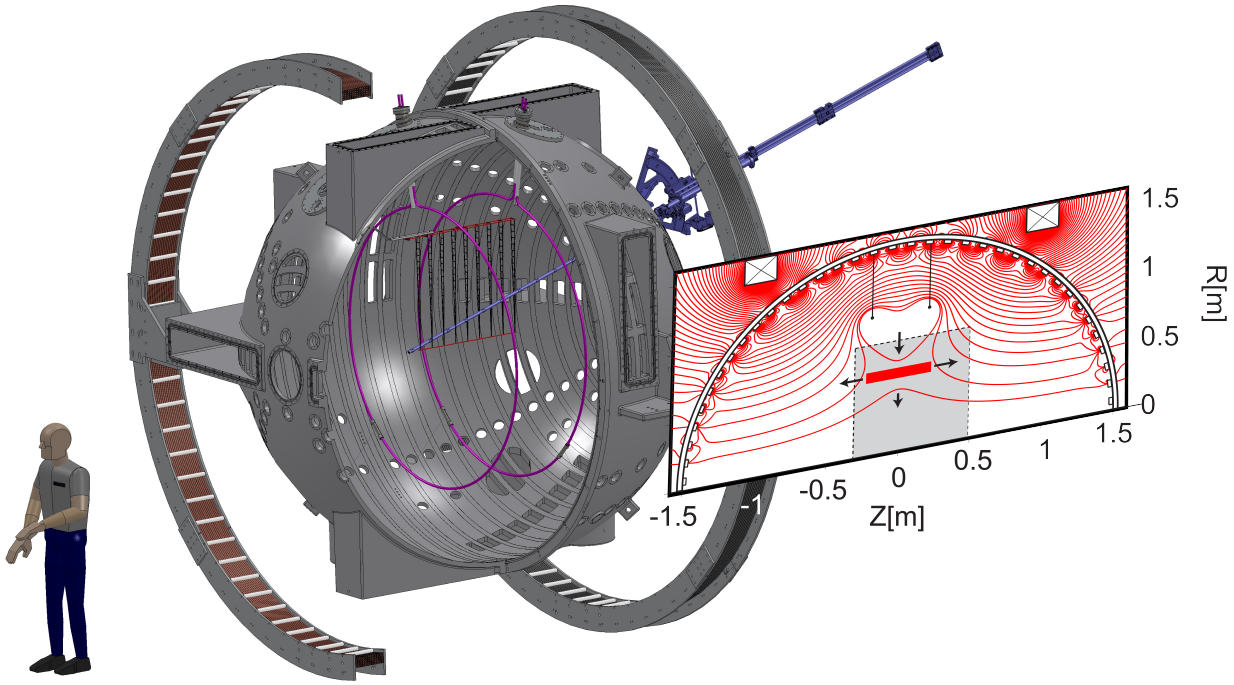

Figure 3.1: TREX setup for the 2015-2016 runs, with an insert showing a theoretical field line distribution. Reproduced from Olson [14].

TREX version's temperature probe array.

The 2015-2016 TREX drive consisted of two coaxial 1.8 m diameter coils located at $Z = \pm$ 0.2 m. The coils were constructed in-house out of two separate conducting tubes: an inner tube made of copper and an outer tube made of aluminum. These two conductors were part of separate circuits with separate capacitor banks; they were kept isolated from each other with Teflon tubing. The plasma-facing surfaces of the coils were sprayed with alumina (aluminum oxide) paint to protect and insulate them from the experimental plasma; this coating can be seen in Figure 3.2, which shows one of the drive coils after installation into the BRB. Note also the two anchor clamps circled in yellow; these were connected to the coils after their installation. The clamps are attached to thick wires that attach to the walls of the BRB. These were a necessary addition to correct the angular alignment of the drive coil. While it was intended that the coils would be rigid enough to remain in place

after installation, unexpected torques on the coil leads led to them twisting in place. The outer conductor was used to transmit a "heating" pulse into the ambient plasma volume, after it had been generated by the LaB_6 cathodes (see Section 2.4.1 for more information on these plasma sources). The heating pulse consisted of three different ringing currents through the outer conductor that was used to heat and homogenize the background plasma before the actual reconnection experiment began. An example of the capacitor potentials and coil currents associated with these heat pulses may be seen in Figure 3.3(b) and (c). For more information on the effect of the heating pulses, see Olson [14]. The inner conductor of the drive coils was used to transmit the actual "drive" of the reconnection experiment into the plasma volume. This drive current creates a magnetic field to oppose the field of the external Helmholtz coil, creating our reconnection region. As the drive through the coils grows in magnitude over time, the reconnection layer is pushed down from underneath the drive coils toward the central axis of the BRB. A theoretical example of the field lines and reconnection layer generated by such a configuration may be seen in the insert of Figure 3.1, and sample values for the potential and current through the drive circuit may be seen in Figure 3.3(d) and (e).

Further engineering displays from the TREX control room are shown in the rest of Figure 3.3. The current drawn from the cathodes is shown in (a); the cathodes remain on until the start of the heating pulses. The density of the ambient plasma is shown in (f); this data comes from the BRB interferometer. While timing and spatial considerations preclude the interferometer's use in evaluating the TREX plasma density immediately around the reconnection layer, it remains useful for understanding the general background profile.

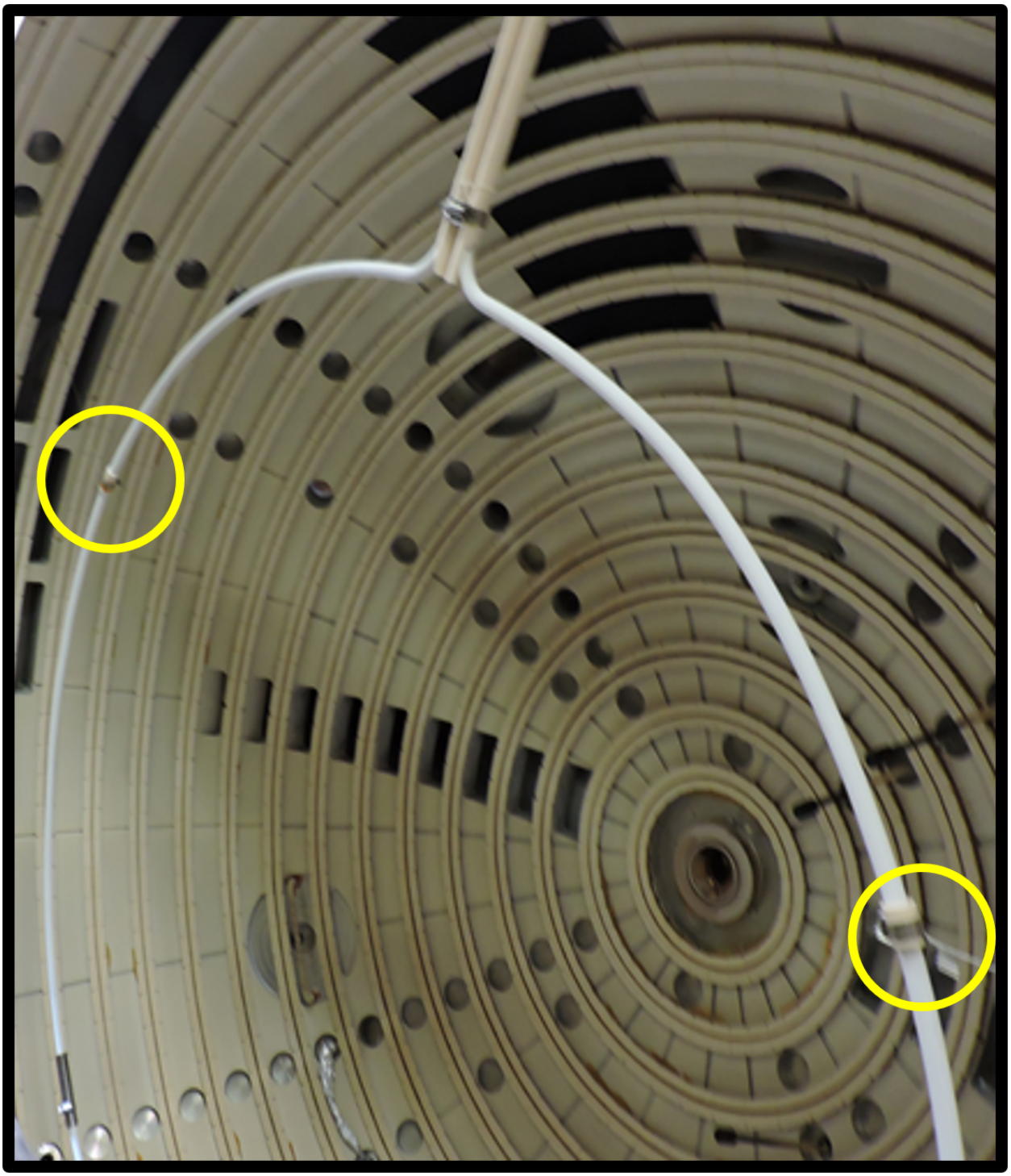

Figure 3.2: A drive coil from the TREX 2015-2016 run, after being installed in the BRB. The two anchor clamps have been highlighted by yellow circles.

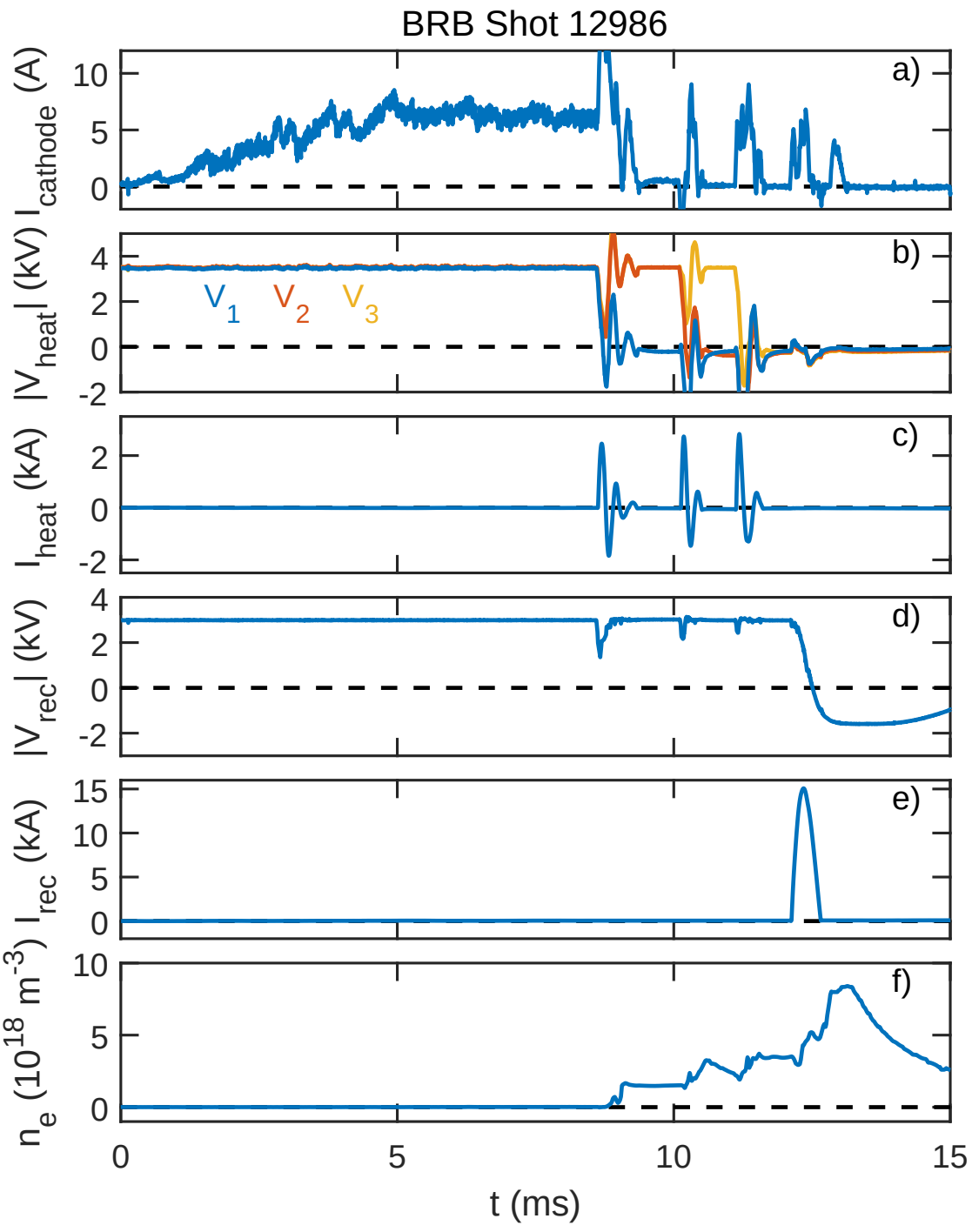

Figure 3.3: Standard TREX control room outputs from the 2015-2016 runs. Includes the cathode discharge (a), the potential and current through the heater circuit (b and c, respectively), the potential and current through the drive coil circuit (d and e, respectively), and the measured density profile from the interferometer. Reproduced from Olson [14].

3.2 Results

3.2.1 Example Magnetic and Electric Field Data

An example of the processed data from the flux array (see Appendix A) is shown in Figure 3.4. The raw signals have been scaled and integrated to produce the B_Z, J_ϕ, V_{loop}, and E_ϕ quantities, where E_ϕ is equivalent to E_{rec} and V_{loop} is its path-integration, the loop voltage. The black lines are contours of the flux function Ψ, which map to the magnetic field lines. The layer is clearly visible as an X-point and a current layer that moves down to lower values of R as time progresses. It is from plots like these that the main conclusions of TREX's 2015-2016 run were reached; these are described below.

3.2.2 Plasmoids

The most notable result to come from TREX 2015-2016 and the flux array was the observation of magnetic islands, otherwise known as plasmoids [15]. The breaking of laminar reconnection current layers into plasmoids has been demonstrated as one possible mechanism for arriving at reconnection rates much faster than the Sweet-Parker rate [31]. Two examples of plasmoids being generated and then ejected from the reconnection current layer are viewable in Figure 3.5(a)-(f); plasmoids are ejected from the reconnection region due to the magnetic tension in the downstream field lines, taking a substantial portion of the current density with them. Current density can build up again to pre-plasmoid levels, but at this point the layer will again be vulnerable to plasmoid growth. This process is clearly shown in Fig. 3.5(g); after the first plasmoid is formed and ejected, the current layer is almost extinguished. The island's size and location is marked by the 'X' for the outer edge of the island and an 'O' for the center of the island[2]. Fig. 3.5(h) shows the effect the islands have on the absolute reconnection rate (E_{rec}). The formation of the plasmoid corresponds to a stagnation in the reconnection rate, but its ejection occurs in tandem with a large increase in the rate. Effectively, the plasmoids

[2]Plasmoids are also identified as O-points, in contrast to the standard reconnection X-point.

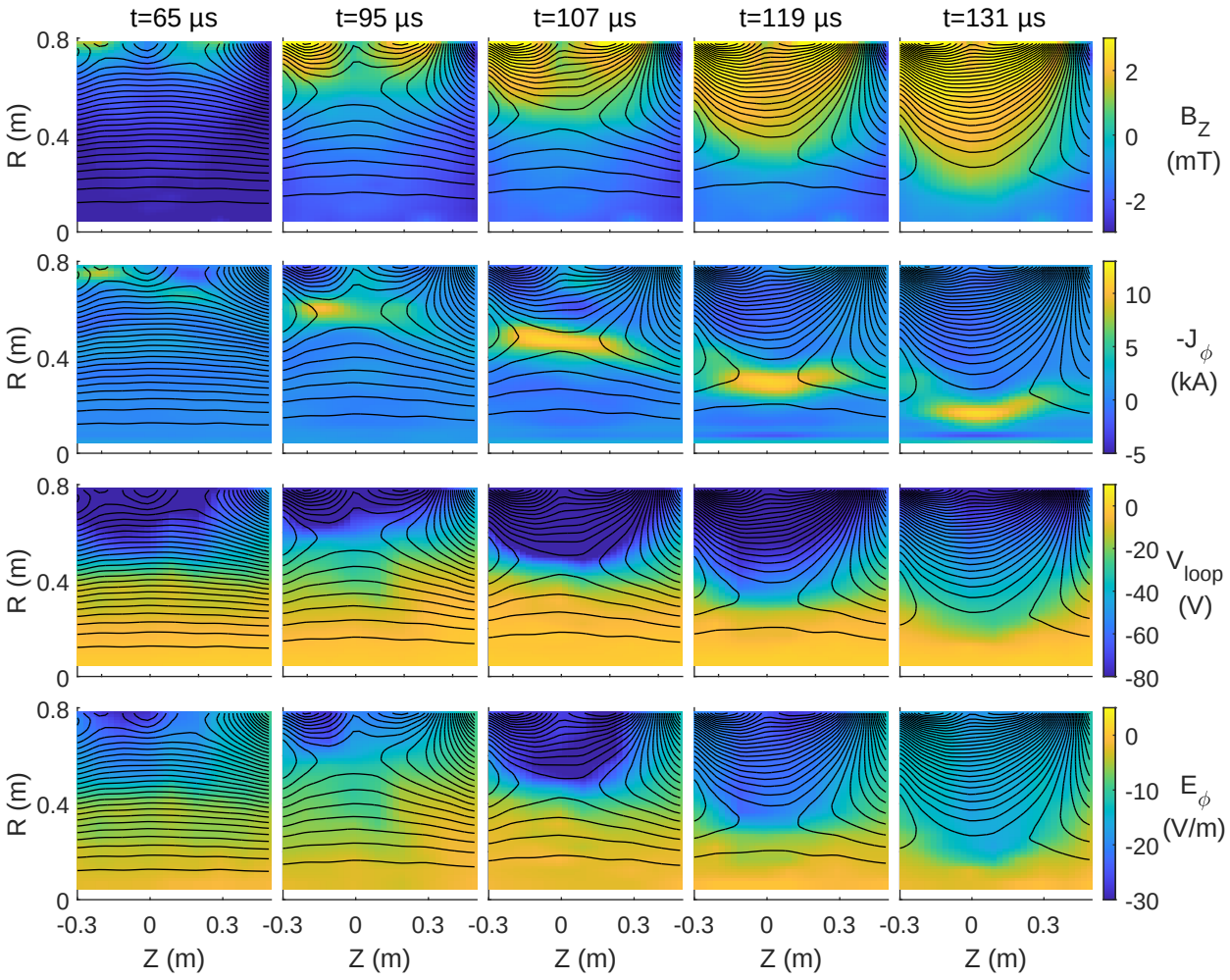

Figure 3.4: Processed data from the flux array, showing the evolution of the reconnection region with respect to time. All of this data came from a single experimental shot; frames like these can be combined into videos.

are large collections of magnetic flux; when they form, the reconnection rate is lower because incoming flux is "trapped" by the island, but when the plasmoid is ejected the amount of flux leaving the reconnection region is greatly increased compared to what can typically transit through a laminar current layer. This explosive behaviour is in agreement with previous simulations [32].

What's most notable about TREX's plasmoid observations is how commonly they occur (or indeed, the fact that they occur at all) in the context of theoretical predictions about when plasmoid-mediated reconnection can occur. Recalling the phase space diagram discussed in

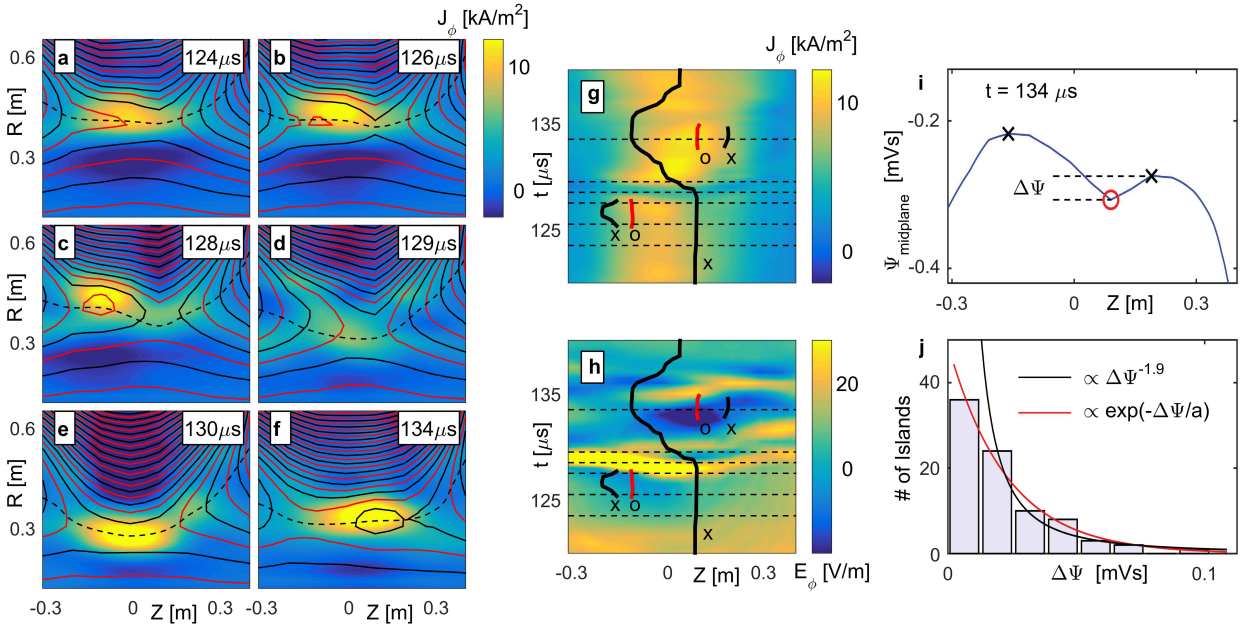

Figure 3.5: Plasmoid observations in flux array data from TREX. Subplots (a) through (f) show the out-of-plane current density with contours of the flux function, which map to the magnetic field lines. A plasmoid is seen forming in (b) and is ejected by (d) 3μs later; a second plasmoid has formed by the time of frame (f). In (g) and (h), the flux array data from plots (a)-(f) is re-plotted to show their time evolution. The lines marked 'O' and 'X' show the paths of the O-points and X-points, respectively. This data is used to create plot (i), where the size of a plasmoid is measured. All the measured plasmoid sizes are binned into groups in the final subplot, (j). Two potential fits to the size of the plasmoids (or "islands") are given; the black fit excludes the bin for the smallest islands, on the assumption that that bin's count may not be accurate because it's missing plasmoids that are smaller than the spatial resolution of the flux array cells.

Section 1.3 (partially reproduced here in Figure 3.6), the derived critical Lundquist number $S_{crit} = 10^4$ represents the low-end cutoff below which collisional plasmoid reconnection cannot occur (represented by the horizontal blue line separating the "single X-line" and "multiple X-line" collisional sections) [33]; furthermore, the lower limit for the size of simulated collisionless reconnection systems is "$L/d_i \approx 50$" (shown as the vertical blue line separating the "single X-line" and "multiple X-line" collisionless sections) [32, 34]. TREX 2015 operates below both these cases, in what should be the "single X-line collisionless" regime (indicated by the green oval). This, in conjunction with results from other reconnection experiments that are also shown in Fig. 3.6 (red ovals) [35, 36, 37], represents a clear divergence between

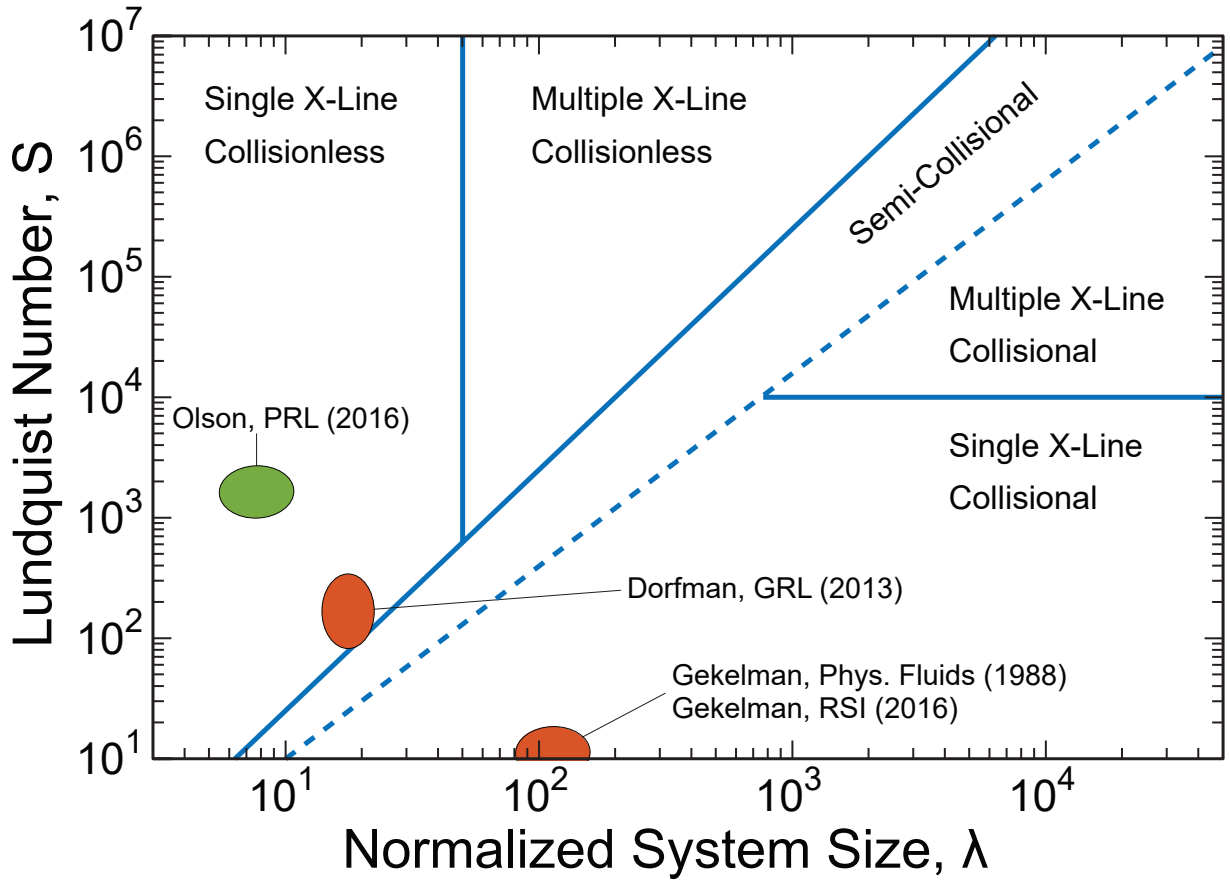

Figure 3.6: Reconnection phase diagram, similar to Figure 1.8. This version of the diagram is accurate to data measurements taken in TREX 2015-2016. Notably, the calculated values for TREX (the green oval) do not reach any of the theoretical multiple X-line regions of the diagram, despite TREX's observations of magnetic islands. Partially reproduced from Olson et al. [15] and Olson [14].

experimental observations and theoretical predictions [15].

3.3 Difficulties & Necessary Upgrades

While TREX 2015-2016 represented both the first fully successful sustained experimental run in the TREX group and the first publication of TREX data [15], it also brought a number of design issues to light that needed to be addressed. Several of these are listed here:

The Drive Coils: there were multiple issues with the drive coils that precluded them

Figure 3.7: Scorch marks and arcing craters on the TREX 2015-2016 drive coils. The alumina coating was insufficient as an insulator. In addition to the visible damage, arcing to the coils also exerts a torque on the drive coil, which contributed to the eventual snapping of one of the TREX coil anchor wires.

from being used indefinitely. First, the alumina paint used to insulate the coils from the plasma was not a permanent barrier to the plasma. As the paint wore away, the coils became scorched and pock-marked from both the plasma itself and the electrical arcs leading to the coil surface. An example of a region of one of the drive coils showing significant damage may be seen in Figure 3.7. Furthermore, the coils had to be anchored with several *ad hoc* clamps and wires (circled in Fig. 3.2) to keep them aligned with each other and the Helmholtz coils. These wires were burned away as more and more experimental shots were taken, and the increase in arcing events as the alumina wore away increased the torques exerted on the coils. Eventually, one of these wires snapped and its associated coil jerked out of alignment, ending the 2015-2016 experimental run. The next iteration of TREX would need sturdier coils with stronger insulation and better anchoring.

The Drive Circuit: during TREX 2015-2016 the measured loop voltage at the drive coils

indicated that for any given experimental shot, a significant portion of the potential charged up in the drive capacitor banks was lost along the twisted-pair transmission lines. In order the maximize the amount of the drive potential that was injected into the plasma, a new transmission line system needed to be designed. Furthermore, a new capacitor bank was needed in order to drive magnetic fields strong enough to increase the experimental Lundquist number into the phase-space where anisotropic pressure distributions can develop in the reconnection region (see Fig. 1.8).

The Plasma Source: a new, higher density plasma source would allow TREX to reach larger scaled system sizes on the standard reconnection phase diagram (Fig. 1.8), allowing for investigations to proceed deeper into previously unexplored reconnection parameter spaces. Additionally, the timing scheme necessary to coordinate the cathode discharges with the heating pulses and reconnection drive was onerous and a common point-of-failure; a new plasma source that could avoid these issues would simplify the experimental process considerably.

The Flux Array: Further detail about the engineering difficulties relating to the flux array may be found in Appendix A.1.4. Regarding the impact of the array's design on the plasmoid measurements described above, the size of the array cells acted as a minimum cutoff to the measurement's spatial resolution. This was demonstrated during the statistical analysis of the plasmoid sizes and frequencies as shown in Fig. 3.5(j); while the plasmoid size could be measured (Fig. 3.5(i)), there remained the possibility that the number of plasmoids in the smallest size bin was artificially deflated by virtue of being too small to be have their structure resolved by the array cells. This meant that the size vs. frequency relation of the plasmoids had either an exponential or a power law scaling, depending on whether or not the number of islands measured in the smallest bin could be trusted; this ambiguity could potentially be avoided with smaller array cells. Thus, a new array design would ideally have a finer cell distribution over each row's length.

All efforts to implement the hardware upgrades will be addressed in the next chapter; attempts to upgrade the probes are addressed in Appendix A, Sections A.2 and A.3.

Chapter 4

TREX 2017

Following some of the difficulties encountered in prior TREX runs (see the previous chapter), the TREX drive was redesigned before the run campaign that began in the early months of the year 2017. While a full explanation of the theory and construction of the new drive system is beyond the scope of this thesis, this section will begin with a brief introduction to the main upgrades. These hardware upgrades were generally successful and carried over into TREX 2018 (Chapter 5), where the main bulk of the experimental data used in this thesis' primary conclusions was recorded. In contrast, the main diagnostic upgrades, namely the second generation flux array (Section A.2) and the initial $\dot{B}$ triple probes (Section A.3), were not carried on into future TREX runs, and have thus been relegated to Appendix A. Further information may also be found in Olson [14].

The new drive system consists of three main parts, all of which are represented in the circuit diagram shown in Figure 4.1. These three parts and their appropriate sections are as follows: the new drive capacitor bank (Section 4.1), the new transmission lines (Section 4.1.1), and finally the new internal drive coils (Section 4.2).

TREX 2017 also switched from using the emissive cathodes to generate the background plasma density to the plasma gun array; the properties of the guns have been explained in Section 2.4.2.

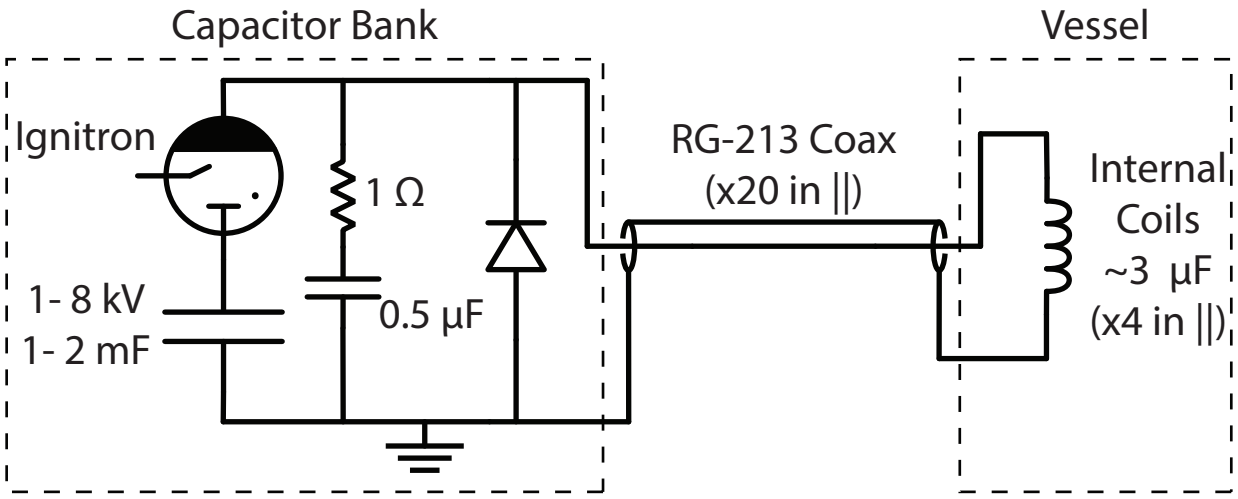

Figure 4.1: The upgraded TREX drive circuit, consisting of three main parts: the new drive capacitor bank, the new transmission lines, and the new internal drive coils. Image reproduced from Olson [14].

4.1 Drive Capacitor Bank

The new capacitor bank (seen in Figure 4.2) is designed to provide a total of 1 or 2 mF of capacitance, depending on whether one or both sets of three parallel 330 μF capacitors are attached to the drive circuit[1]. The bank also includes a high-voltage ignitron that acts as a switch to discharge the bank when triggered, a flyback diode to prevent the sinusoidal "ringing" of a typical LRC circuit, and an RC snubber that mitigates switching noise from the ignitron; these elements can all be seen schematically in Fig. 4.1. The entire bank is sealed inside a box made of phenolic, acrylic, and DMD paper sheeting. In standard operation, the bank provides a discharge of up to 8 kV for a peak current of ~ 35 kA through each of the four drive coils.

[1]This adaptability ended up becoming useful in 2022, when undetected water leaks caused by heavy rain caused the cap bank to partially explode, destroying two of the capacitors in one set of three. That set was quickly removed and the cap bank was able to continue operating in the 1 mF configuration for several hundred more shots before further damage to the bank necessitated it be shut down until full repairs were made.

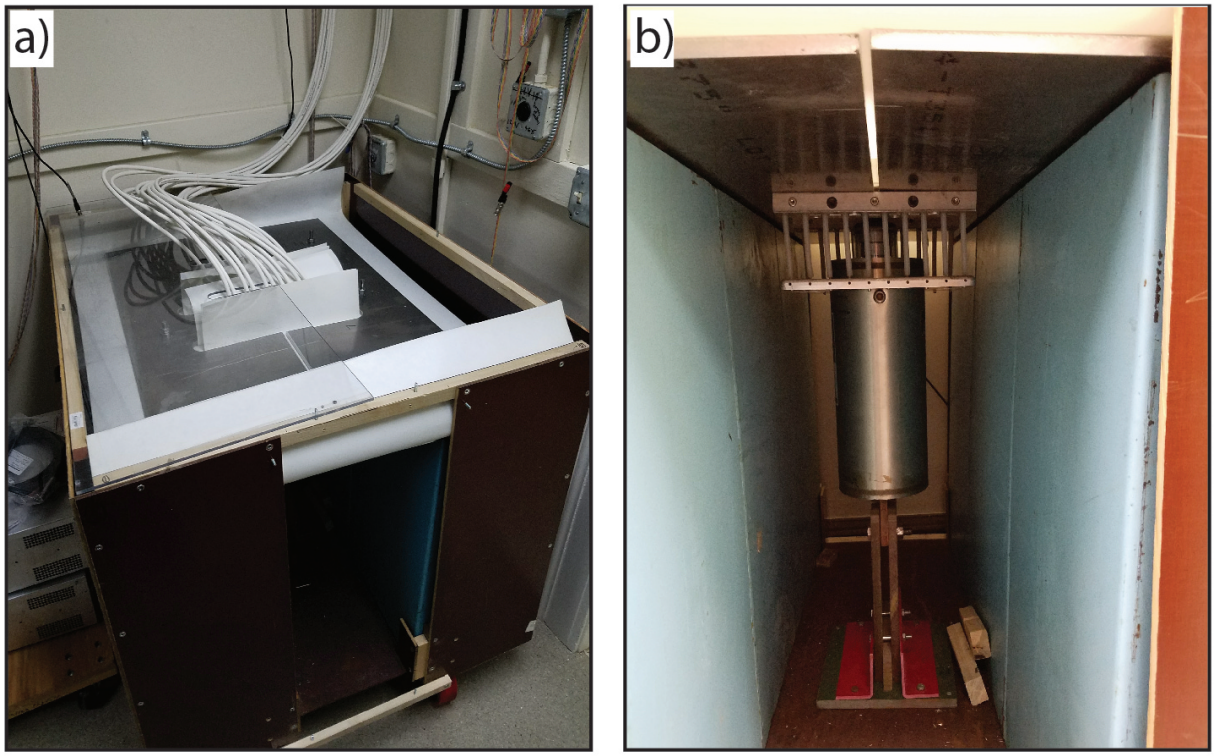

Figure 4.2: (a) The upgraded TREX capacitor bank, consisting of two sets of three 330 µF capacitors connected in parallel and sealed inside an insulating box made of phenolic and acrylic. The TREX transmission lines are the white cables exiting the top of the bank; they pass through a pipe in the ceiling into the BRB lab room. (b) Inner view of the capacitor bank. The two sets of capacitors are shown on either side of the image (light blue). The central device is the ignitron, which acts as the switch that discharges the capacitors when given the command input from the BRB control room VI. Both images reproduced from Olson [14].

4.1.1 Transmission Lines

The previous TREX transmission lines consisted of $\sim 50\ ft$ of twisted pair cable extending from the capacitor bank to the drive coils. While easy to assemble, this configuration resulted in significant inductive losses; the calculated inductance of these cables was found to be ~ 14 µH, which accounted for about 75% of the drive circuit's total inductance. To remedy this, new transmission lines were constructed using 20 separate RG-213 coaxial cables in parallel. As with the prior transmission lines, these cables ran from the capacitor bank (visible in Fig. 4.2(a) as the white cables coming out the top of the bank), through a metal

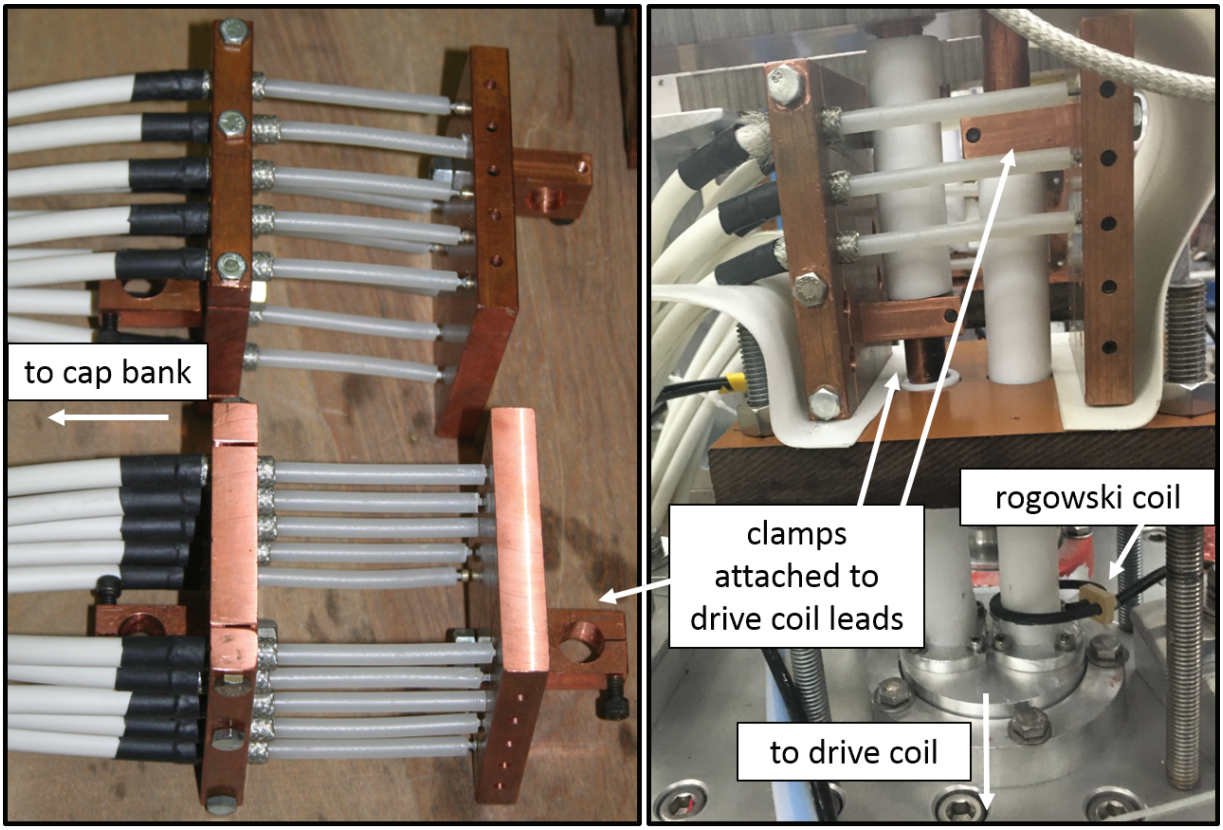

Figure 4.3: The upgraded transmission lines used starting with the TREX 2017 run. On the left: two of the clamps used at the end of the line to connect to the drive coils. The line is made of RG-213 coaxial cables connected in parallel. The copper clamp at the coil side of the transmission line splits the cables into their core and shield components. On the right: An example of how the transmission lines are clamped to a drive coil lead. The drive coil leads extend out the top of the BRB through a vacuum seal and are held in place with a thick phenolic plate. The leads on either end of the coil are held apart from each other and covered with additional Teflon tubing to prevent shorting. Rogowski coils are placed around one of the leads for each coil, allowing the coil current to be measured in the control room.

pipe into the BRB laboratory, and then up along the southern Helmholtz coil while enclosed in a flexible metal shield before being connected to the drive coil leads on top of the BRB to complete the drive circuit (clamp connections visible in Figure 4.3). The nominal inductance of RG-213 is 77 nH/ft, giving a total transmission line inductance of ~ 0.2 µH, or less than 1.5% of the prior value.

4.2 Drive Coils

As detailed previously (see Section 3.3), the main issues under consideration for the redesign process of the drive coils was the need to physically withstand both repeated plasma exposure and the torsion forces that resulted from the intense magnetic field pulses. The concentric aluminum and copper tubes of the previous coils were replaced with a hard drawn copper pipe, which was surrounded by PTFE (Teflon) tubing to provide electrical insulation and then covered by interlocking alumina ceramic cones to provide a high-temperature-resistant plasma-facing surface. The coils were held in place using a series of aluminum clamps that had been sprayed with alumina paint and baked in a vacuum oven to minimize potential outgassing into the BRB vacuum; the clamps on the bottom of the coils were supported by quartz glass-covered stainless steel rods anchored to the bottom of the BRB. A panoramic view of the drive coils may be seen in Figure 4.4. The new coil setup consisted of the four 92 cm radius primary drive coils and two smaller heating coils meant to act in a manner similar to the heating pulses used in prior TREX runs (see Section 3.1); however, after the TREX plasma sources were upgraded from the emissive cathodes to the plasma guns, this heating mechanism was no longer used. These coils were kept in place for the remainder of the run but were not reused in subsequent installations. For more information on the technical dimensions of the coils and their construction process, see Olson [14].

Figure 4.4: Panoramic view of the new TREX drive coils (left is up, right is down - descriptions of this image will assume that it has been turned properly) after they've been installed in the BRB but before the vessel is closed and pumped down. The new coils are enveloped a shield made of interlocking alumina cones. Pictured are the four main drive coils (larger coils in the middle) and two of the smaller heater coils (far left and far right) which were eventually removed after the adoption of the plasma gun sources (see Section 2.4.2. Also visible is the second magnetic flux array (more information in Section A.2).

4.3 Conclusions

While TREX 2017 was a disappointment in terms of its intended primary diagnostic (the second generation flux array, see Section A.2), the other upgrades implemented from the prior TREX runs proved to be very effective. The coils were well-protected from the plasma environment, were not subject to arcing, and showed no signs of yielding to any applied torques. The plasma guns proved to be a reliable and much more easily-controlled mechanism for generating background plasma. Especially notable was the extremely robust and efficient upgrade to the TREX drive circuit, which minimized drive failure events and significantly improved TREX's ability to inject stronger fields into the plasma. All of these upgrades would be carried over into TREX 2018 with little or no change. Finally, the many prototype $\dot{B}$ probes (see Section A.3) were invaluable in assessing the needs with respect to probe design for TREX 2018; it was these next generation probes (described in the following chapter) that finally bore the data that constitutes the majority of this thesis.

Chapter 5

TREX 2018

As stated at the end of the previous chapter, TREX 2018 used many of the same hardware systems that compromised TREX 2017. The only major hardware change was the removal of the drive coil closest to the BRB south pole from the circuit, such that the drive field was injected from three coils rather than four[1]. The main difference going into 2018 was the removal of the second generation flux array[2] and the shift in focus to the use of $\dot{B}$ probe arrays. The following chapter will deal almost exclusively with the probes used in TREX 2018, including both the different $\dot{B}$ probe arrays and the temperature and density Langmuir probe array. Some expository engineering information regarding the operation of the Langmuir probe array is included in Appendix A, in Section A.4.

For the main results of TREX 2018, see Chapters 7 and 8. Much of TREX 2018's experimental campaign happened concurrently with the development of TREX VPIC; for more information on this process, see Chapter 6 and Appendix B.

[1] For more information on why this was done, see Section 6.4.1.
[2] Good riddance!

5.1 Fast Magnetic Probes

5.1.1 B Dot Probe Basics

$\dot{B}$ probes, also known as Mirnov coils, Faraday pickup loops, flux probes, etc., are simple plasma diagnostics that rely on Faraday's Law of Induction to measure the changes in a magnetic field through the probe's cross-sectional area. The probe consists of some number of loops N of a conductor enclosing a small area A; a time-changing magnetic field component parallel to the normal vector of A will generate an EMF around the loop. This can be measured as a potential difference V across the leads of the conductor:

$$V = -\frac{\mathrm{d}\Psi_B}{\mathrm{d}t} = -NA\frac{\mathrm{d}B}{\mathrm{d}t}\,. \tag{5.1}$$

This in turn allows the magnetic field component normal to A to be calculated:

$$B(t) = -\frac{1}{NA}\int_{t_0}^{t_f} V(t)\mathrm{d}t\,. \tag{5.2}$$

where t_0 is some initial time when the field value is known and t_f is the time when the field value is desired.

The leads of a given $\dot{B}$ loop are connected to digitizer channels such that the potential values at each lead can be read as the experiment proceeds. Two channels are used per probe - one for each lead - to minimize common-mode noise (CM):

$$V = V_1 - V_2 \propto \left(\frac{\dot{B}}{2} + CM\right) - \left(-\frac{\dot{B}}{2} + CM\right) = \dot{B}\,. \tag{5.3}$$

A sample circuit diagram of a basic $\dot{B}$ probe is shown in Figure 5.1. The diagram includes voltage divides at each end to keep the signal measurements within the digitizer's acceptable input range (generally ± 1 V). Probe calibration is based on careful measurement of probe cross-sectional areas and comparisons between measured magnetic fields with known vacuum

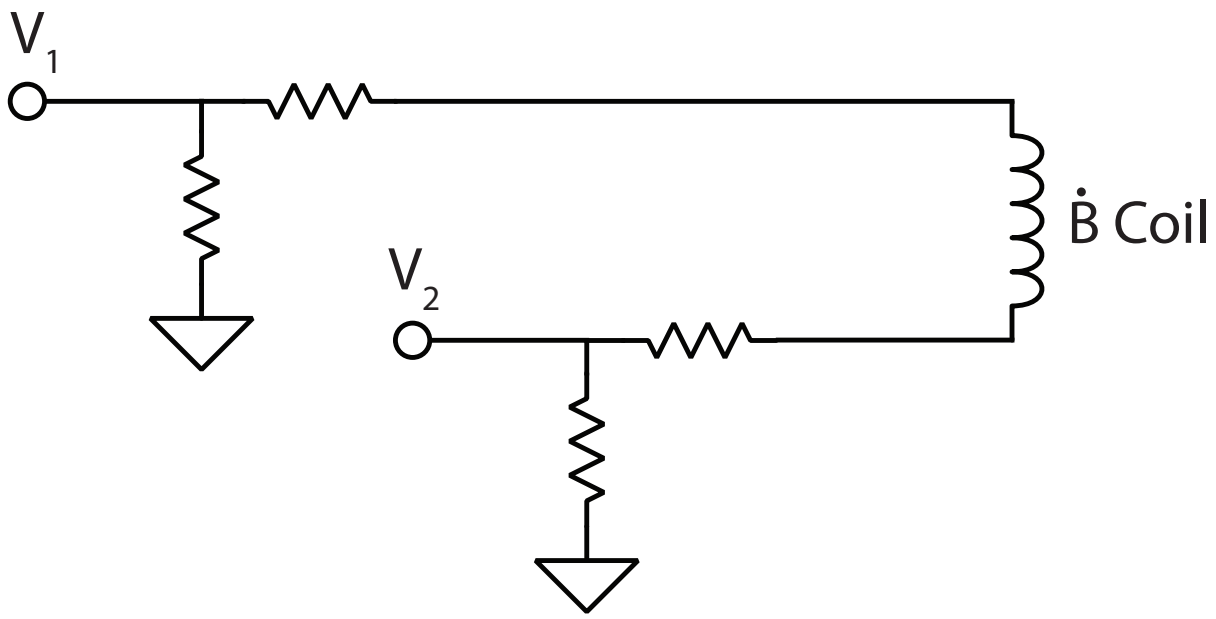

Figure 5.1: Schematic of the technique using two ground referenced digitizer inputs, V_1 and V_2, to take a differential measurement of a single $\dot{B}$ probe. Reproduced from Olson [14].

fields.

5.1.2 Individual Triple Probes

The fast magnetic probes, also known as the $\dot{B}$ (Bdot) probes, are an improved design over the various magnetic probe iterations (see Section A.3). Physically, these probes are formed from twisted pair wire wrapped around a $3D$ printed resin mold that contains pathways for three orthogonal directions of $\dot{B}$ measurement. Each individual direction consists of two separately-wound oppositely-directed coils (a natural consequence of using prefabricated twisted pair wire) that allows for the subtraction of common-mode noise[3]. The 0.003 *in* enameled pre-twisted magnet wire was hand-wound around the three grooves in the resin mold and secured in-place using superglue. The terminations of these wound pairs was then

[3]This is distinct from the basic $\dot{B}$ probe design of TREX 2017 (detailed in Section A.3), where the common-mode noise was eliminated by assigning one digitizer channel to each probe lead for a total of two channels per probe. In this case, one probe lead is assigned to the digitizer input and the other is assigned to the digitizer ground; this puts both leads of one probe loop on one channel while its paired loop goes on a second channel. The process for subtracting the common-mode noise is revised accordingly.

hand-soldered into an accompanying customized PCB with surface mount 100 Ω resistors. These resistors both reduced the effect of internal capacitance of the windings and impedance-matched the twisted pair leads going from the board to the probe box to reduce transmission line effects. This in turn served to improve the frequency response of the probes over the prior configurations. The PCBs themselves were glued to $3D$ printed resin spacers, designed to interface with the resin probe forms and provide a standardized probe spacing. The use of $3D$ printed resin molds was intended to standardize the probe construction process and probe cross-sectional area, rather than rely on the variable sizes of the prior hand-made $\dot{B}$ probes. The forms are roughly cylindrical with a diameter of 3.5mm and a length of 17mm. The coil along the probe's axis (local z direction) has a smaller cross-sectional area than the other two coils (local x and y), but were wound with an additional number of turns to make up for the difference. The specific number of turns varied depending on the desired frequency response of the probes (see below).

One of the principal elements considered in the redesign of the $\dot{B}$ from 2017 to 2018 was improving the frequency response of the probes. As stated in Section A.3, the probe measurements from 2017 indicated that the layer passed the probes at speeds in excess of 50 $\mathrm{km\,s^{-1}}$; with a probe size on the order of ~ 5 mm, the fine layer structure of a current layer would be interpreted by the probe as a signal with a frequency of ~ 10 MHz. This in turn meant that the natural L/R timescale of the $\dot{B}$ probe circuit needed to be increased to keep the assumption of a linear relationship between V_{probe} and $\dot{B}$ valid. Along with the previously-described modifications to the $\dot{B}$ probe construction process, this was achieved by lowering the number of windings in a given probe to reduce the probe loop's inherent inductance. This decrease had to be balanced with the coinciding decrease in the strength of the measured signal.

After testing the frequency response of different winding numbers, it was decided that for probes being digitized at 10 MHz, the x and y direction loops would have 3 turns each while the z direction loops would have 5 turns each (the larger number compensating for the z direction's lower cross-sectional area). While ideally all probes would operate at as

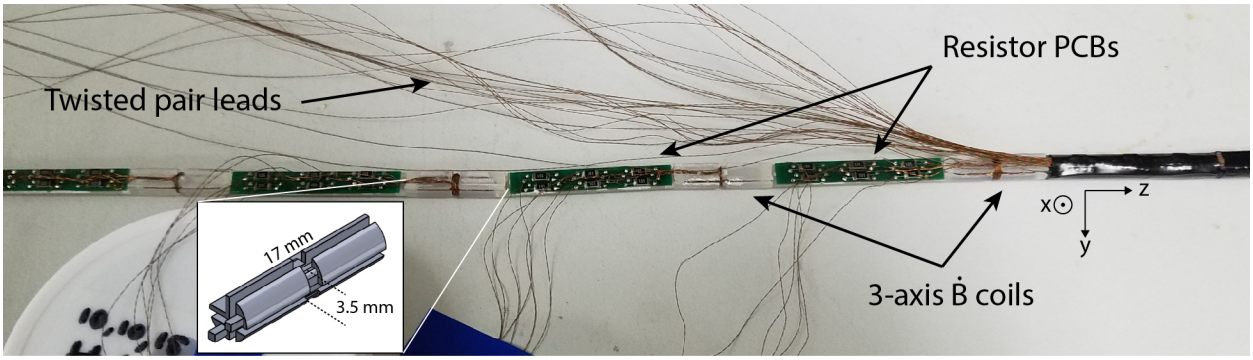

Figure 5.2: The $\dot{B}$ probes during construction. The actual probes (white) are three-axis $3D$ printed resin forms meant to mimic the shape and features of the previously-used LEGO probe frames. The twisted pair wire is hand-wound around the grooves in each of the three directions. Each wire is then terminated at the resistor PCBs (green) where a 100 Ω surface mount resistor is placed to reduce the internal capacitance of the probe and match the twisted pair wire's nominal impedance to improve the frequency response (see Fig. 5.3, below). The twisted pair leads then travel from the PCB to the box-end of the probe array. The PCBs were themselves mounted on $3D$ printed resin spacers that were designed to attach to the three-axis resin forms, providing a uniform, well-defined separation between each individual probe. After the probes were wound and the wires were connected, the probe length was wrapped in thin Teflon sheeting to hold the wiring in place. The positions corresponding to the PCBs were then wrapped in thin copper foil to reduce noise, and then the entire probe length was sealed with heat-shrink (right side of the image). The completed probe structure was inserted into a closed ceramic tube as part of the standard BRB probe construction explained in Section 2.5.

high a frequency as possible for optimal resolution of the current layers, the TREX digitizers progressively lose usable channels as their sampling frequency increases. As such, it was decided that a second set of "slower" $\dot{B}$ probes would also be constructed, to allow some digitizers to operate at 2 MHz with increased probe capacity. These probes were wound with 10 turns in the x and y directions and 15 turns in the z direction.

The frequency testing of the probes was done using a small, single-turn Helmholtz coil connected to a function generator which drove the field in the coil over a range of frequencies. The potential across the Helmholtz coil and the potential measured across the probe were both fed into an oscilloscope and compared in their amplitude and phase. Some of the results of this analysis can be seen in Figure 5.3. Crucially, the end of linearity in the probes occurs

at or above the Nyquist frequency limit of the digitizers[4].

It should be noted that the anticipated frequency associated with a thin layer passing the probes at the larger end of driven speed of the reconnection layer ($\sim$ 10 MHz) is higher than both our probe's Nyquist frequency and the linearity cutoff in their frequency response, even for our fastest probes. This means that features of the thinnest features of the reconnection current layers may not be completely resolved by the probes. This effect will become important when discussing the layer width measurements in Chapter 7.

5.1.3 Linear Probe

The linear probe (so-named because of the three probe arrays, it's the only one whose probe-shaft is completely straight) consists of 15 separate double-wound $\dot{B}$ triple probes. Ten of these ($\#1-3,5,7,9,11,13-15$) are "slow" probes and the remaining five ($\#4,6,8,10,12$) are fast probes. The probe's area of coverage spans $\sim$ 1 m, while the entire probe (including the stainless steel shaft) spans $\sim$ 3 m, allowing it to reach deep into the BRB. This probe was installed through a boxport at $R = 40$cm and was parallel to the machine's Z-axis. This probe could be scanned through different values of Z. The linear probe array's layout can be seen in Figure 5.4(a); this probe's position is shown in green in both plots of Figure 5.5.

5.1.4 Shepherd's Hook Probe

The shepherd's hook probe (commonly called the hook probe; so-named because its probe shaft contains a rounded $\angle 90$ bend like a shepherd's crook, such that the probe array's central axis is perpendicular to the probe shaft's central axis) is an array eleven probes, six of which (odd-numbered) are "slow" and the remaining are "fast". This probe array originally had three additional probes on the box-end, but these were broken during final assembly due to difficulties inserting the completed probe array into the ceramic tube used to shield

[4]The Nyquist frequency is half of the sampling rate; it is the highest frequency signal that can be measured at that rate without aliasing. Aliasing means that a given measurement cannot distinguish between two potential waveforms with different frequencies; the measurement can indicate one waveform or the other, leaving the true frequency of the signal being measured ambiguous.

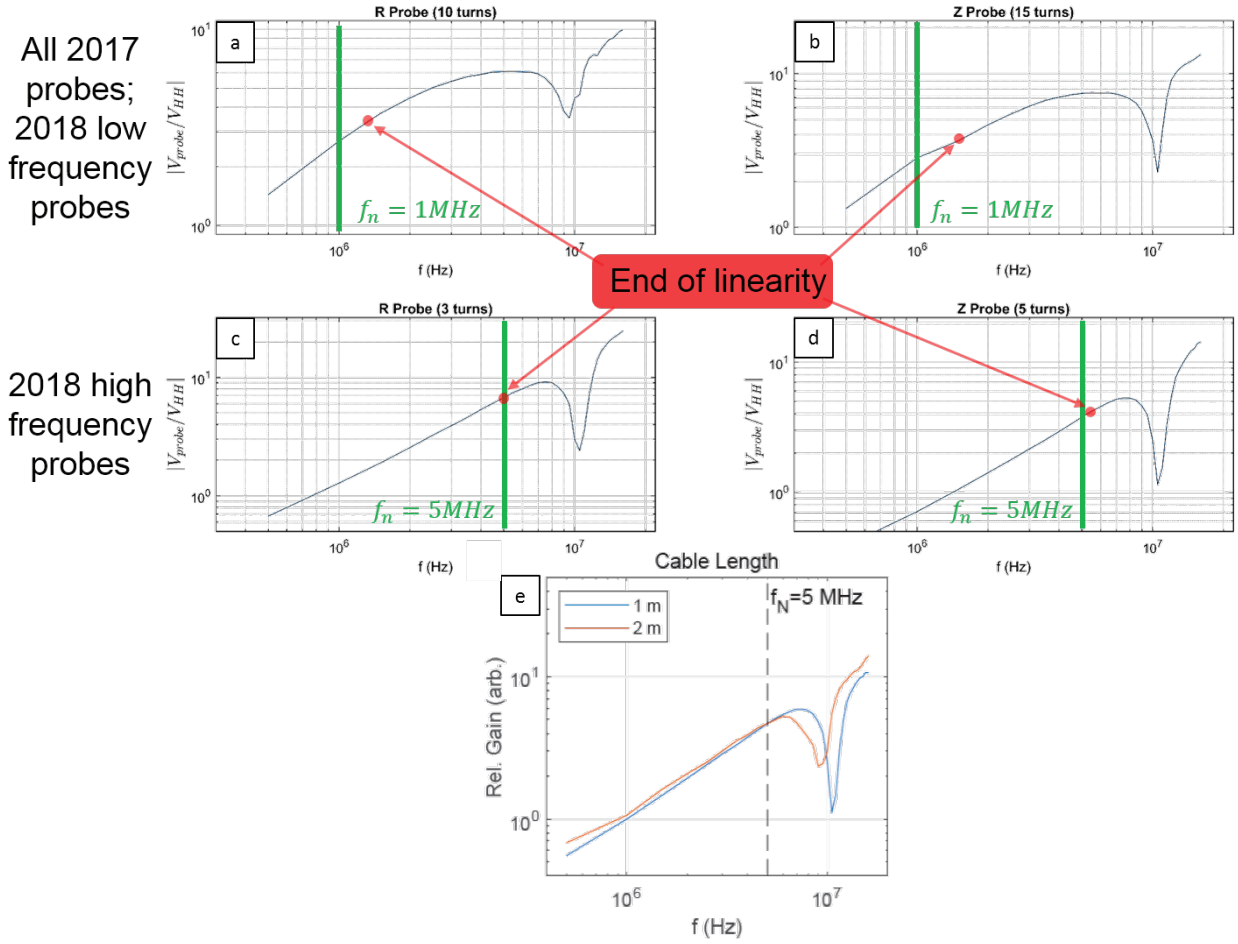

Figure 5.3: Frequency response analysis of the 2017 and 2018 $\dot{B}$ probes. The top row ((a) and (b)) show the frequency response of the "slow" probes from 2018 and all the probes from 2017; the signal begins to dampen just above the Nyquist frequency of 1 MHz (corresponding to our digitization frequency of 2 MHz). The new high frequency probe design had to be adjusted to keep the end of linearity at or above the new Nyquist frequency (half of the anticipated digitization frequency of 10 MHz); the second row of plots ((c) and (d)) demonstrate that this was successful. The bottom plot (e) demonstrates how the length of the twisted pair leads from the probe to the digitizer can affect the dampening rate and the location of the anti-resonance; moving the digitizers as close as feasibly possible to the probes will minimize this distortion. Plot (e) has been reproduced from Olson [14].

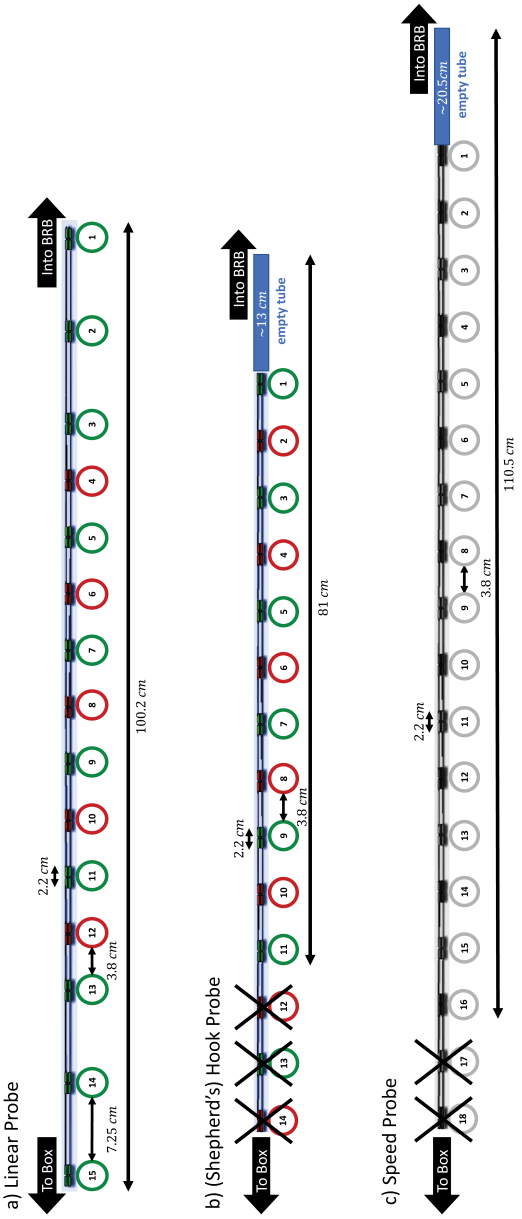

Figure 5.4: Schematic of the three $\dot{B}$ probe array constructions. The green probes are "low" frequency (2 MHz digitization rate) while the red probes are "high" frequency (10 MHz digitization rate). Gray probes are "slow" and only record data along one direction (where the area normal is parallel to the machine's Z direction). Fast and slow probes were alternated as a compromise between our limitations in both spatial and time resolution. Note that for the hook probe and speed probe, difficulties in inserting the finished probe array into their ceramic tubes resulted in the breaking of several box-end probes (marked with Xs) and an empty space between the tip of the ceramic and the tip of the probe array (noted as the blue cylinders). Other individual loops or probes were occasionally found to be broken over the course of the experimental run, but these were comparatively minor issues that were fixed in the probe evaluation codes.

it from the plasma. This also resulted in an empty space between the sealed end of the ceramic tube and the innermost triple probe (#1). Taking these issues into account, the hook probe array has a measurement length of about 68 cm. The hook probe entered the vessel at $Z = -25$ cm and could be scanned to different values of R from the central axis ($R = 0$ cm) up to just underneath the drive coils ($R = 90$ cm). The probe could also be rotated up to $\angle 180$, allowing the probe tip[5] to reach from $Z = -95$ cm to $Z = 45$ cm. Note that special care had to be taken when moving and rotating this probe to ensure it did not collide with other internal hardware. The hook probe array's layout can be seen in Figure 5.4(b); this probe's position (top) and scan area (bottom) is shown in cyan in both plots of Figure 5.5.

5.1.5 Speed Probe

The speed probe (so-named because it is used to track the position and speed of the layer as it moves from under the coils toward the BRB's central axis) is an array of 16 "slow" probes. Contrary to the other two probe arrays, these probes only record data in one direction (i.e., they aren't functioning as triple probes), such that only the (machine's) Z-directed component of the change in magnetic flux is measured. This probe array also had difficulties in the process of inserting it into its ceramic tube, resulting in the loss of two additional box-end probes and an empty space between the sealed end of the ceramic tube and the innermost probe (#1). The functional measurement region of the array extended from the innermost probe at $R =\sim 0$ cm out to $R =\sim 90$ cm. The probe array is aligned with the BRB's $Z = 0$ cm line owing to two bends in the stainless steel probe shaft that move the probe away from the (nonzero) Z value of its port. The speed probe array's layout can be seen in Figure 5.4(c); this probe's position is shown in blue in both plots of Figure 5.5.

[5]The physical tip, not the probe measurement area; the difference between these two is about 13 cm.

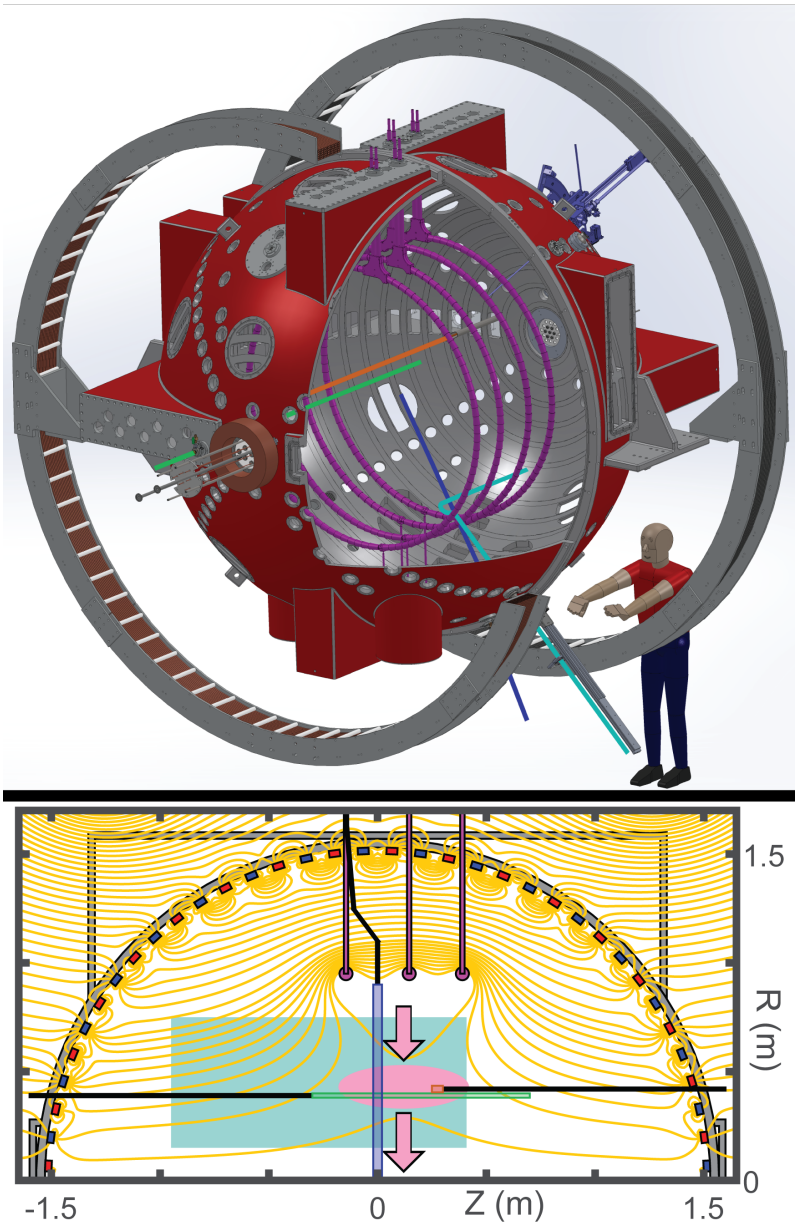

Figure 5.5: Top: A CAD drawing of this iteration of TREX installed on the BRB. The drive coils are in magenta. The probes (and their probe shafts) are color coded: cyan for the hook probe, blue for the speed probe, green for the linear probe, and orange for the temperature probe. Bottom: A cross-section of the top half of the TREX vessel showing a theoretical example of the typical experimental geometry. The magnetic field lines are shown in goldenrod. The reconnection region (pink) is driven down from the drive coils to the central axis, as indicated by the arrows. The probes are also shown, with similar colors to the top plot (the probe shafts are uncolored in this instance). The operating region through which the hook probe can be scanned is shown as the cyan rectangle. Note that this is a compressed representation of TREX's cross-section; all the probes are shown in this image even though they are located at different values of the toroidal angle ϕ.

5.1.6 Speed Measurement

The speed probe array is used to track the path of the layer as it moves through different values of the R coordinate. It does so by measuring the magnetic features of the reconnection layer (such as the maximum value of $\dot{B}_z$) at each of the individual probe locations at a specific value of R and comparing the time at which they occur. An example of this process in three different reconnection shots in hydrogen plasma is shown in Figure 5.6. While the full layer path over the entire radial extent of the speed probe array can be determined, typically only layer paths and speeds around locations of interest (such as $R = 40$ cm, near the linear probe) are considered. Over a small enough range of R, the layer path can generally be modeled as linear for simplicity; however, this assumption can break down for layer paths measured at the edges of the speed probe.

5.2 Temperature Probe

The T_e probe, so-named because it measures the temperature of the plasma, is an array of 16 separate Langmuir probe tips, each of which are electrically isolated from each other and can be set at a different bias potential. A Langmuir probe is a common type of plasma diagnostic used to calculate a plasma's temperature and density based on how much current a biased probe tip draws from the plasma. A full explanation of the physics of Langmuir probes, their operation, and their construction is far beyond the scope of this thesis; what follows is a highly abridged summary of this information. Complete details on the TREX Langmuir probe arrays may be found in Olson [14]. The current drawn to a biased probe tip in a plasma is related to the bias potential the probe tip is held at, the plasma potential, the plasma density, and the electron temperature. Through several simplifying assumptions, this relation can be analytically derived; its form is that of a nontrivial, negatively-diverging exponential function that is transcendental in the electron temperature. By varying the probe tip's potential bias through multiple reproducible shots, the measured probe currents can

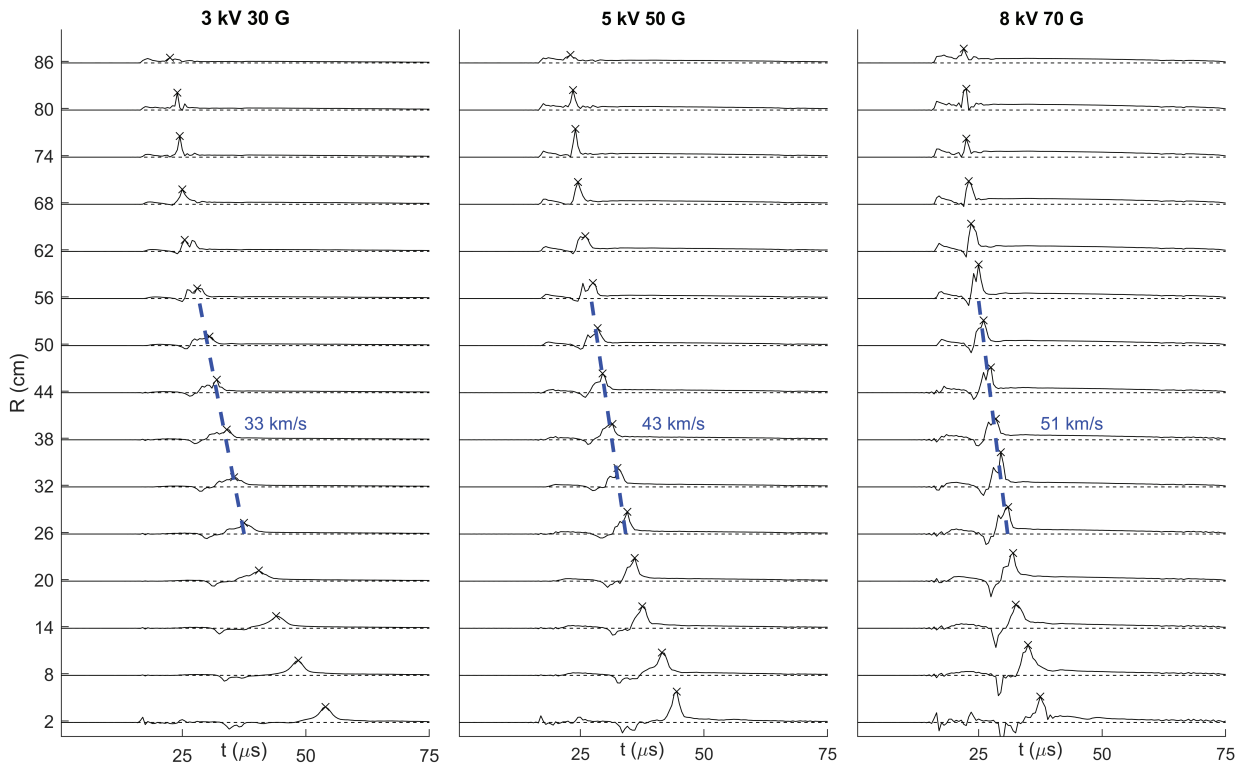

Figure 5.6: Three examples showing how the speed of the layer is calculated. In each of these three shots the raw $\dot{B}_z$ signals measured by each individual probe in the speed probe array is shown at each probe's R location. The maxima of the signals (analogous to the maximum intensity of the reconnection current layer) are marked with Xs. By taking the time the maxima occurs for each R value, the path of the layer can be found. To evaluate the speed, typically the maxima around a given point of interest (such as $R = 40$ cm are used to find a linear fit for the layer position. Examples of these fits and their associated speeds (slopes) are shown in blue. Values here have been rounded to the nearest cm and km s^{-1} for clarity.

be used to construct an IV curve based on the model, but this method requires many shot repetitions at many different probe biases to collect all the data necessary to characterize the curve. To avoid this issue, the TREX T_e probe uses an array of Langmuir tips each set at a different bias, such that the entire IV curve for a given probe location can potentially be found from a single shot, assuming that the tip biases are appropriate for the plasma conditions. This tip array can be seen in Figure 5.7. In addition to the Langmuir tips, the T_e probe includes its own $\dot{B}$ triple probe which is used to contextualize the probe's position relative to the passing reconnection current layer. The process of operating the T_e probe

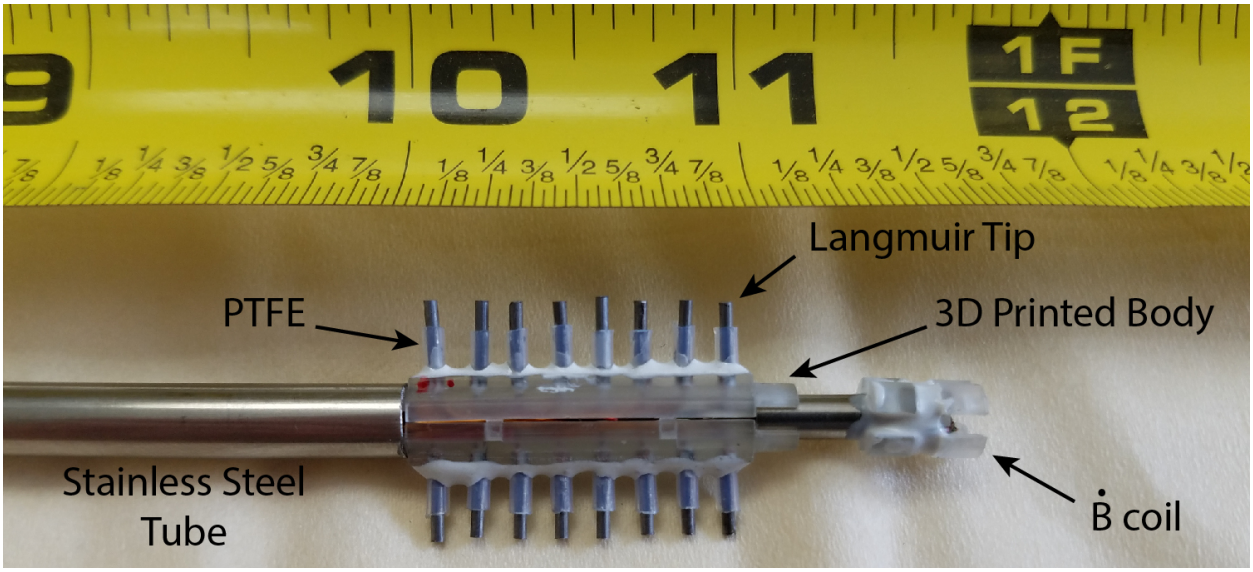

Figure 5.7: The upgraded multi-tip Langmuir T_e probe. Image reproduced from Olson [14], where more information about this probe's construction process and operation may be found.

during an experiment is nontrivial[6]. The data recorded by the probe must be monitored through the run to ensure that it is valid; in addition to a potential malfunction, it is entirely possible for the probe to report measurements that appear valid but are in fact unreliable due one or more aspects of the probe being run in a way that violates the assumptions necessary to complete the IV curve calculation. This can result in a significant loss of time if unnoticed[7]. To combat this possibility in future potential runs, some of the raw data output from the T_e is reproduced in Section A.4 in Appendix A. For more information on the operation of this probe, please see Olson [14]. The T_e probe's position is shown in orange in Fig. 5.5; it is located at $R = 40$cm and enters at the boxport opposite of the linear probe (green) and can be moved to different values of the Z coordinate as desired.

[6]Compare with the $\dot{B}$ probes which passively take measurements without the need for user input aside from their digitizer trigger.

[7]This is known from experience.

5.3 Jogging Method and Current Measurement

The TREX probes record data as a function of time. As the reconnection layer is pushed down from beneath the drive coils toward the central axis ($R = 0$), the features of the layer are recorded by the probes they pass, resulting in a data set that shows when in time a given layer feature appears at the probe's location. However, many of our analyses are dependent on understanding the spatial extent of these features; as such, a method to convert this time-indexed data into position-indexed data needs to be employed. This analysis, known as the "jogging method", employs an extension of the Taylor hypothesis, which states that the time between two features in in a moving medium can be translated into a distance between these two features using the medium's speed, on the assumption that the "pattern" formed by these features is essentially fixed in the medium's frame [38]. In other words, if we assume that the geometry of the layer does not change in the time it takes for our entire region of interest to pass a probe, then it is valid to use the measured speed of the layer in that vicinity to directly convert time measurements into distance measurements. This assumption, originally devised to apply to turbulent eddies in a moving fluid, is commonly extended to spacecraft data and other experimental plasma systems [39]. The Taylor hypothesis is one of the simplifying assumptions used to turn the $\dot{B}$ probes' measurements in the Z direction into values for the reconnection current layer J_ϕ. Starting from Ampère's law in a plasma:

$$\mu_0 \mathbf{J} = \nabla \times \mathbf{B} \quad ,$$

the ϕ component of the equation in a cylindrical geometry is

$$J_\phi = \frac{1}{\mu_0} \left(\frac{\partial B_r}{\partial z} - \frac{\partial B_z}{\partial r} \right) \quad .$$

By assuming translational symmetry in the Z direction, we can eliminate the $\partial/\partial z$ term[8]. The Taylor hypothesis lets us assume the following relation:

$$\frac{\partial}{\partial r} = \frac{\partial}{\partial t}\frac{\partial t}{\partial r} = \frac{1}{u_r}\frac{\partial}{\partial t} \quad ,$$

where u_r is the radial speed of the layer, measured from the speed probe array. This gives us our standard relation for determining the reconnection current density from our measured $\dot{B}$ signals:

$$J_\phi = -\left(\frac{1}{u_r \mu_0}\right)\frac{\partial B_z}{\partial t} \quad . \tag{5.4}$$

5.4 Sample Data Profiles

An example of the data taken in a given TREX parameter set by our hook probe array and T_e probe are shown in Figure 5.8. The hook probe data is taken from multiple separate shots where the hook probe is moved to different R positions, such that the jogging method is not used to determine the radial position of different layer features (though it is still a part of the J_ϕ calculation). The T_e, in contrast, is taken from a single experimental shot at a single R position, and thus does use the jogging method to convert the time signals to position measurements (shown in the lower horizontal axis of the T_e probe plot). All coordinates shown in this figure (R' and Z') are taken to be distances measured from the center of the reconnection layer, rather than machine coordinates; regardless, the cylindrical directions remain the same between the "primed" and "unprimed" (layer coordinates vs machine coordinates) systems. This plot is an example of some of the data that can come from the probes that have been described earlier in this section; more detailed analyses of the actual results in plots like these will be given in future sections.

[8]This term can actually be calculated from probe data, but is invariably very small.

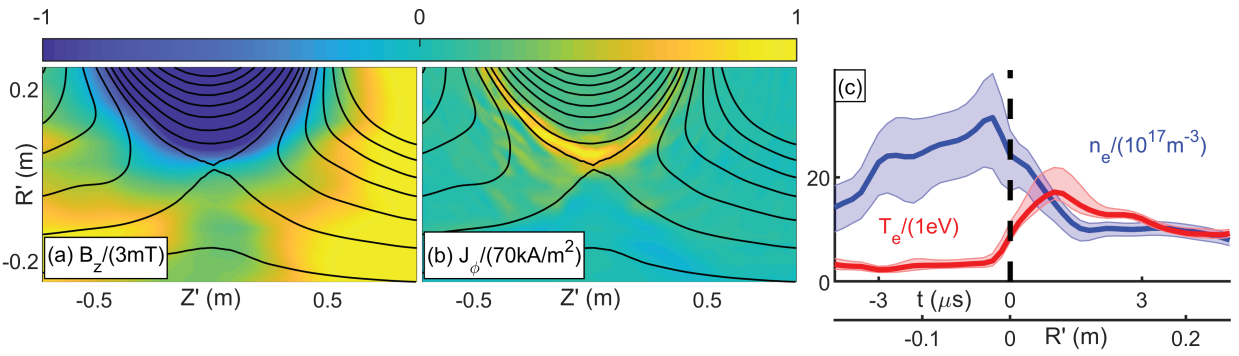

Figure 5.8: Example of experimental data. Plots (a) and (b) show the data from the hook probe recorded in a scan including 34 different probe positions covering the cyan region in Fig. 5.5. The black lines are contours of the flux function, Ψ, which map to the magnetic field lines. (a) shows the reconnecting magnetic fields, and (b) shows the out-of-plane current layer. (c) shows data from the T_e probe (orange in Fig. 5.5(b)); the shaded regions represent the 95% confidence interval for the values of density and temperature based on the fit of the probe's IV curve. The lower R' side of the layer is closer to the plasma sources and thus has a higher density than the other side of the layer. There is a jump in the plasma temperature when the layer passes the probe. The data in (c) is compiled using the jogging method to convert the time signal into a measurement of the R'-coordinate. The R' and Z' coordinates are versions of the regular machine R and Z coordinates but re-centered on the layer's location. This figure initially appeared in Greess et al. [16].

5.5 Conclusion

TREX 2018 took the successful hardware improvements of the 2017 run and used them to their full advantage by establishing a new probe construction standard that facilitated data collection in a manner that was both highly resolved and minimally perturbative to the plasma. Data from this run will be extremely useful in developing TREX VPIC simulations as detailed in the next chapter, as well as providing the backbone for the layer width and reconnection rate findings presented in Chapters 7 and 8, respectively.

Chapter 6

VPIC

Simulations have long provided invaluable insight into the physics of different plasma regimes, including those relevant to the low-collisionality environment of the Earth's magnetopause and the TREX experiment [40, 12, 41, 42, 13, 43][1]. However, most if not all of these analyses are performed using geometries that are not comparable to TREX. TREX's cylindrical symmetry is a defining aspect of the experiment; the driven magnetic field pushes the plasma density radially inward and creates a cylindrical current sheet. Until the recent invention of Cylindrical VPIC[2], it was not feasible to simulate TREX with codes that are optimized for low-collisionality plasmas (e.g., PIC codes) while maintaining the crucial cylindrical symmetry- to do so would necessitate a full 360° simulation domain, which would be excessively expensive in terms of computation time. Cylindrical VPIC bypasses this issue; now, cylindrical symmetry is preserved even in the 2D limit. What follows is an introduction to PIC codes in general (Section 6.1), succeeded by a description of the process of creating a basic TREX initialization deck for running different TREX simulations (Section 6.2) and an explanation of the complexities involved in translating between simulation units and experimental (SI) units (Section 6.3). This chapter will conclude with an overview of some early results from Cylindrical VPIC simulations of TREX (6.4) as a lead-up to VPIC's use

[1] Literally any paper by Ari Lê.

[2] Courtesy of Adam Stanier at Los Alamos National Laboratory (currently without an official release).

in evaluating TREX data in the next two chapters. Additional information on VPIC and TREX VPIC may be found in Appendix B.

6.1 VPIC Theory

Particle-In-Cell (PIC) codes are used to run simulations that retain the kinetic-scale physics of low-collisionality plasmas; while comparatively expensive in terms of computational power, PIC codes can study the types of physics that are lost when using a more simplified fluid model. While there are many different implementations of the standard PIC idea, the code used to model TREX is VPIC (Vector Particle-In-Cell), a code created as Los Alamos National Laboratory [44, 45, 46]. VPIC has been optimized to minimize data motion between processors, leaving more processing time allotted for the actual simulation calculations. Prior to this work, VPIC has been successfully used to model a wide range of kinetic plasma environments, including reconnection [45, 40], laser-plasma interactions [47], and heating mechanisms in the solar wind [48]. The workings of VPIC are similar to those of other PIC codes and is covered in-depth in Bowers et al. [49]. What follows is a brief explanation of the mathematical model that defines the VPIC process, which is represented in the simplified graphic seen in Figure 6.1.

The initialized simulation domain, consisting of whatever groups of particles and fields that have been specified for a given run, is divided into smaller areas (or volumes, depending on the dimensionality) called cells by a set of grid-lines. Within each cell, the total number of particles, their net charge, and their net velocity are used to calculate a current density associated with the cell, of the form:

$$\mathbf{J} = \sum_s \int d\mathbf{u} q_s c \gamma^{-1} \mathbf{u} f_s \quad . \tag{6.1}$$

where f_s is the instantaneous phase-space distribution of species s, with q_s being the charge of species s, and $\gamma = \sqrt{1+u^2}$ is the relativistic factor.

These net values are then used to calculate updates to the initialized electromagnetic fields, which are defined along the lines of the grid that defines the cells. VPIC does this by solving relativistic Maxwell-Boltzmann equations in a linear background medium,

$$\left[\frac{\partial}{\partial t} + \gamma^{-1}\mathbf{u} \bullet \nabla + \frac{q_s}{m_s}\left(\mathbf{E} + \gamma^{-1}\mathbf{u} \times \mathbf{B}\right) \bullet \nabla\right] f_s = \left.\frac{\delta}{\delta t}\right|_{\text{coll}} f_s \tag{6.2}$$

$$\frac{\partial \mathbf{B}}{\partial t} = -\nabla \times \mathbf{E} \tag{6.3}$$

$$\frac{\partial \mathbf{E}}{\partial t} = \epsilon^{-1}\nabla \times \mu^{-1}\mathbf{B} - \epsilon^{-1}\mathbf{J} - \epsilon^{-1}\sigma\mathbf{E} \tag{6.4}$$

$$\nabla \bullet \mathbf{B} = 0 \tag{6.5}$$

$$\nabla \bullet \mathbf{E} = \rho/\epsilon \tag{6.6}$$

where m_s is the mass of species s, ϵ and μ here denote the permittivity and permeability of the background plasma (respectively), and σ is the background conductivity. The collisionality term $\left.\frac{\delta}{\delta t}\right|_{\text{coll}} f_s$ may be set as desired or removed entirely.

These new fields along the gridlines then have their values interpolated down to the locations of each particle, allowing the particles' positions to be updated based on the forces that they experience from the new fields:

$$\frac{d\mathbf{r}}{dt} = c\gamma^{-1}\mathbf{u} \tag{6.7}$$

$$\frac{d\mathbf{u}}{dt} = \frac{q_s}{m_s c}\left[\mathbf{E} + c\gamma^{-1}\mathbf{u} \times \mathbf{B}\right] \quad . \tag{6.8}$$

After the particle positions and velocities are updated, new values for the net current density in each cell can be calculated, and the process begins again. This cycle repeats until the simulation is terminated. One key difference between the standard VPIC codes detailed in the references above and the simulations used to model TREX is that the TREX models a relatively new implementation of VPIC that uses a cylindrical coordinate geometry in place of the standard Cartesian system. Cylindrical VPIC operates in a very similar manner to Cartesian VPIC, but it is useful in modeling TREX because it allows simulations to preserve

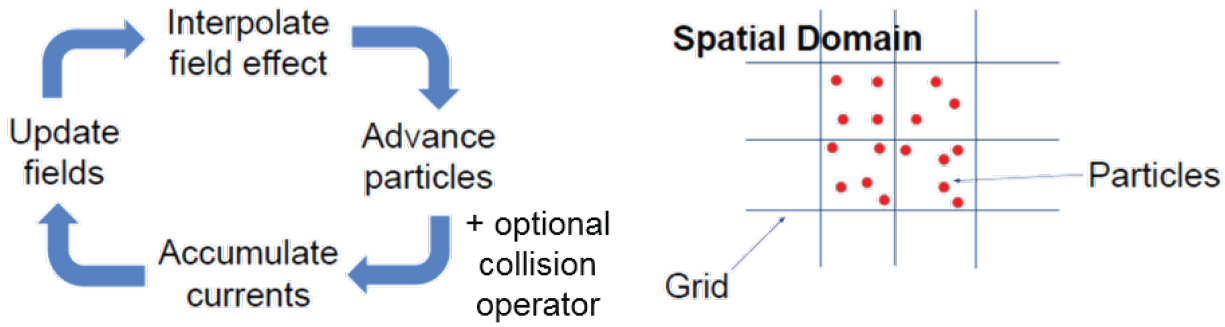

Figure 6.1: The basic process of VPIC. A simulation domain (right) starts with particles (red) with some given initial charge and velocity distribution and some initialized field geometry whose value is calculated along the grid lines that divide up the domain. Starting at the bottom of the process loop (left), the net charge and velocity of each grid cell is determined by summing the contributions of each particle in the cell. This yields the current and charge densities throughout the domain, which are in turn used to calculate the new electromagnetic fields along the grid lines. Next, these field values are interpolated down to the individual particle locations and are used to update the particles' momentum, after which they are advanced to their new position after a timestep passes. At this point, the process begins again. There is also an optional collisional operator step that can be applied as part of the particle advancement step. Figure reproduced in part from Lichko [48].

TREX's cylindrical symmetry with greater computational efficiency[3]. One consequence of the new coordinate system is that the size of a cell varies with respect to the value of the radial coordinate R; as R decreases, the cells get smaller and smaller, leading to an increase in time spent moving data between cells (and by extension, processors) and a decrease in the overall efficiency of the code. Furthermore, the simulation currently cannot reach $R = 0$; some small value of R must be chosen to be the simulation's minima to avoid introducing a singular point. This choice of R will be detailed further below.

[3]If we wanted to preserve TREX's cylindrical symmetry in a Cartesian simulation, we would need to simulate the entire 360° ϕ domain of the experimental volume [e.g., all of it]. With Cylindrical VPIC, the symmetry of the simulation is preserved for any given subset of the toroidal angle used to define it, even if the value of ϕ is so small that the domain is essential 2D in the (R, Z) plane. This saves considerable computational time compared to the Cartesian alternative.

6.2 Initial TREX Setup

Simulations of reconnection typically start with one of several standardized geometries, like the Harris sheet in a periodic bounding box [50]. However, the goal of studying the TREX experiment depends on recreating the BRB and TREX geometries and initial conditions in the domain of the simulation; due to differences between the scaling of experimental units (SI) and code units (unit-less quantities scaled by reference plasma parameters), this conversion between the two fields can be nontrivial. What follows is a brief explanation of the different steps that went into deciding on our standard TREX initialization deck, on which most TREX simulations are based.

6.2.1 Boundary Conditions

The default boundary conditions for both fields and particles in VPIC is periodic; while the TREX model keeps this true for the toroidal direction ϕ, this is not the case for the R and Z boundaries. In the (R, Z) plane, the simulation domain is rectangular (the BRB wall and embedded magnets are not included in the simulation) extending from $Z = \pm 1.5$ m and up to $R = 3$ m from some small but nonzero minimum R value[4]. Both the Z boundaries and the upper R boundary are set as conducting boundaries for the electric and magnetic fields, essentially approximating a metallic wall[5]. The properties of the lower R bound, typically at $R = 0.05 - 0.1$ m, are slightly more difficult to conceptualize. In TREX, the reconnection current layer takes the form of a cylinder aligned along the vessel's central axis; as the drive ramps up, the cylinder is compressed into a thinner and thinner cylinder, until all sides of the layer reach the central axis of the BRB at the same time and bounce off of each other. To reproduce this effect and prevent the high-density core of the initial plasma background from "falling" out of the simulation domain, the low R boundary is also given the attributes

[4]The TREX simulation deck starts by setting up several parameters (including the R and Z) in SI units, before converting them to simulation units.

[5]However, in contrast to a metallic wall, these boundaries are also set to reflect particles to keep them in the system. In VPIC, the boundary conditions for electromagnetic fields are set independently from those of the particles.

of a conducting surface that reflects particles.

6.2.2 Initial Density Profile and Pressure Balance

The next step in constructing the TREX VPIC deck is determining the initial conditions that best match the experiment. The first parameter that was matched was the experimental density, determined at several values of the R coordinate using one of the TREX temperature probes. These points were fit to the following decreasing exponential:

$$N_e(R) = N_{0,SI} e^{N_{scale,SI} R^2} + N_{1,SI} \tag{6.9}$$

where $N_{0,SI} = 3.3547 \times 10^{18}$ 1/m^3, $N_{1,SI} = 2.4121 \times 10^{17}$ 1/m^3, and $N_{scale,SI} = -10.252$ 1/m^2 and the value of R is in SI units[6]. This profile may be seen in Figure 6.2(a) in SI units and in (b) for code units. This analysis also assumed that the electron temperature T_e is 5 eV and the ion temperature T_i is 1 eV at $R = 0.5$ m (before the reconnection process has begun). The first initialized magnetic profiles was simply a constant field equal to the applied Helmholtz field B_{HH}. While this did not actually model the initial field in the experiment, where the plasma density impedes the field from fully penetrating the experimental volume, it was initially assumed that the difference would have a minimal effect in the simulation. This however turned out to have been incorrect; this field configuration and the consequent imbalance between the magnetic and kinetic pressures launched waves from the low R regions of the domain toward the high R regions, potentially disrupting and delaying the formation of the reconnection layer underneath the drive coils at $R = 0.92$ m. To compensate, the following initial magnetic profile was implemented:

$$B_Z(R) = \sqrt{2\mu_0 \left[B_c - \left(N_e(R) q_e \left(T_e + T_i\right)\right)\right]} \tag{6.10}$$

[6] see Appendix B for information on how this formula is converted to code units.

where q_e is the elementary charge, $N_e(R)$ is Eq 6.9, and B_c is the following constant:

$$B_c = \frac{B_{HH}^2}{2\mu_0} + q_e \left(T_e + T_i\right) N_{1,SI} \tag{6.11}$$

All temperature values are taken to be in eVs. This profile is plotted in Figure 6.2(c), and the resultant pressure profile in subplot (d). While the sum of the magnetic and kinetic pressures is not constant even after this modification, the difference has been more than halved and the direction of the imbalance has been swapped from what it would be without the modified magnetic field profile. These changes mean that any pressure waves that begin as soon as the simulation starts are both smaller and heading away from the region where the reconnection layer is forming, such that their effect is no longer notable. Some work was done into completely smoothing the pressure curve by adding in a drift electron velocity, but it became clear that any improvements would be minimal compared to the amount of time it would have taken to properly implement.

6.2.3 Particle Emission

While the initial density profile does have a strong inverse dependence with the R coordinate, the density in the experiment is never measured as going to 0. However, when early VPIC TREX runs were analyzed, it became apparent that the expanding "bubble" of flux being injected at the drive coils was pushing all of the ambient plasma out of the area, resulting in reconnection with density on one side and a vacuum on the other. This is not the case in the experiment; for example, the density profile in Figure 5.8 shows that while the density above the layer is lower than the density below, it is certainly nonzero. To solve this, particle emission was incorporated into the area around the drive coils. During a simulation, particles with thermal velocities matching those of the initial plasma profile were continuously injected at points around (but slightly offset from) the drive coil locations. This is thought to be an experimental analogue for the ionization that likely occurs around the drive coils, particularly at the miniature reconnection sites between the coils that have outflows in the

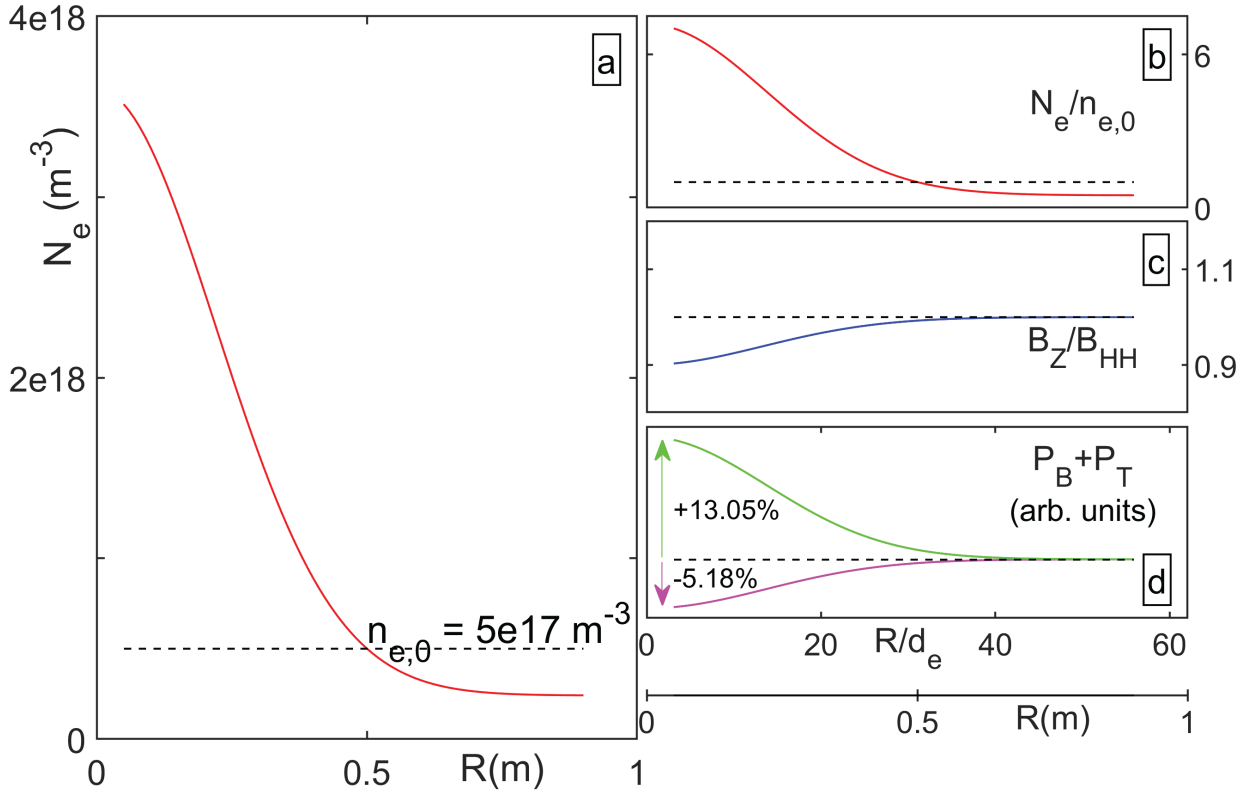

Figure 6.2: TREX VPIC initial density, magnetic field, and pressure balance profiles. The standard initialized density profile (a) is based on density measurements in TREX from late 2017-early 2018, fitted to a decreasing exponential. (b) shows the profile in initialized code units, where the density is normalized by $n_{e,0}$, its value at $R = 0.5$ m. (c) shows the updated initial magnetic field profile in initialized code units, where the field is normalized by B_{HH}, the Helmholtz field. While the first implementations of TREX in VPIC assumed that at the start of a shot, the Helmholtz field was constant through the simulation domain, but this led to an imbalance between the magnetic and kinetic pressures that created large wave structures in the initial plasma that could affect the reconnection. Plot (d) shows two separate pressure totals, one with a constant magnetic field (green) and the other with the modified magnetic field profile (magenta). While neither total pressure is constant at small R, the modified version is closer to equilibrium and the resulting wave structures are much smaller. Furthermore, the unmodified version generates waves moving from small to large R because $P_{smallR} > P_{largeR}$; waves moving in this direction at the start of the simulation can disrupt the formation of the reconnection layer. Conversely, the modified version has its pressure imbalance in the opposite direction, resulting in a wave that is moving in the opposite direction and unlikely to affect the formation of the layer. All plots in code units have their R scale shown in both SI units and in number of electron skin depths d_e. Values in these plots will change as changes to the initial parameters are made; this figure demonstrates the standard case and should not be taken as definitive of all simulations' initializations.

$\pm R$ directions. The particle emission functionality was designed at Los Alamos National Laboratory specifically for use with the TREX VPIC setup; a full explanation of how the emitter works (a nontrivial process) is beyond the scope of this thesis. The amount of density injected by these emitters is set as part of the simulation's input deck; this value does not have an obvious physical analogue, so matching effect of this emission parameter to the particle density measured in the experiment in the injected drive flux side of the reconnection layer was done through a process of trial and error.

6.2.4 Current Drive

The ramping drive current injected through the drive coils in TREX was modeled in VPIC by placing ramping simulation currents at the locations corresponding to the drive coils. In TREX, the drive current takes the form of a decaying sinusoidal, owing to the drive's properties as an LRC circuit[7]. However, the majority of our reconnection measurements take place just as the drive current is beginning to ramp up, as the LRC timescale of the drive circuit is much larger than the experimental timescale; this allows the drive current to be approximated as linearly increasing over these scales (see Figure 6.3).

In VPIC, the drive current begins at 0 and begins increasing with a constant value for $\dot{I}$, whose value is input manually into the simulation deck depending on what type of experimental drive is being modeled. Several measured values for $\dot{I}$, taken from experimental drive current measurements at different parameter sets, are shown in Table 6.1 with their corresponding drive potential and the Helmholtz field values that typically accompany them[8]. These values can be used directly in VPIC or linearly interpolated to provide the desired current drive.

[7]The current trace measured through the coils does not appear sinusoidal due to the flyback diodes, which prevent the circuit from ringing. If these diodes were removed (as they have been in some cases), the behaviour of the current would clearly be that of a decaying sinusoid.

[8]These values are customary to (1) get a (very) rough matching between the driven magnetic field and the background (Helmholtz) magnetic field and (2) make some of our most standard shot parameter groups easier to remember. These field values can be changed without necessarily needing to alter the associated $\dot{I}$ value.

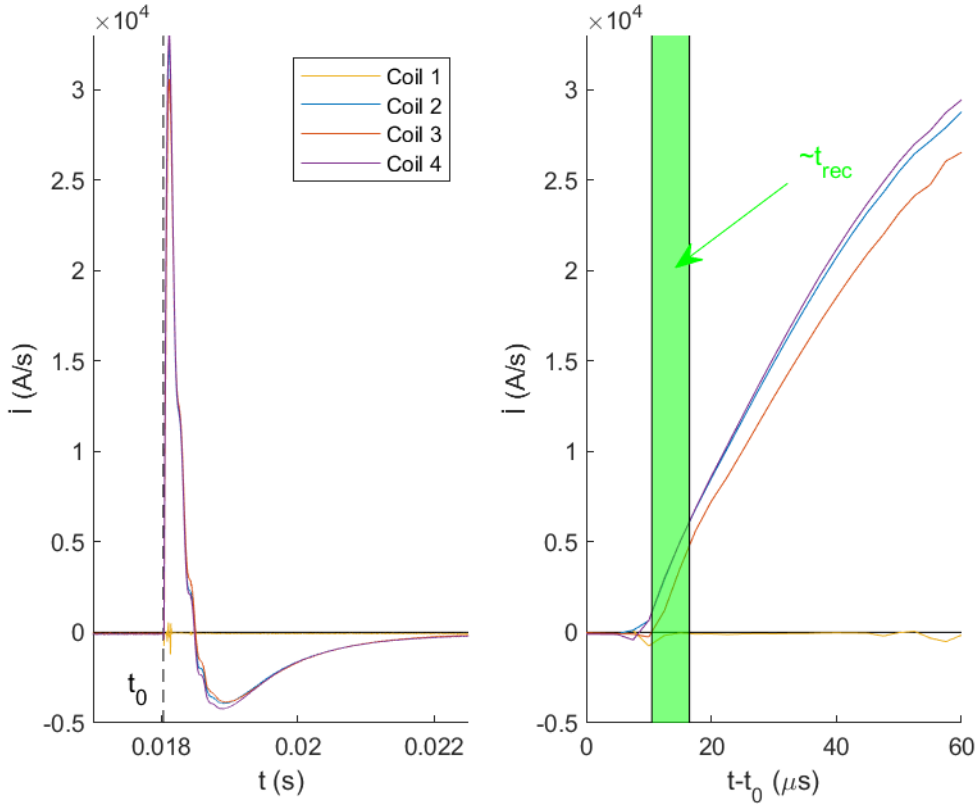

Figure 6.3: The TREX 2018 drive currents. The full drive current is shown on the left, with the time where the discharge starts marked as t_0. A zoomed-in version of this plot is shown on the right, where the timescale has been re-scaled relative to t_0 and is now given in µs. While the shape of the full drive pulse is sinusoidal, over the timescale where the reconnection occurs (approximately the green region) the pulse is approximately linear. This is the form used to model the drive in VPIC.

Drive Potential (kV)	Helmholtz Field (G)	Approximate coil $\dot{I}$ value ($\mathrm{kA\,s^{-1}}$)
1	30	87365
3	30	2.734×10^5
5	50	4.4514×10^5
7	70	6.2818×10^5

Table 6.1: Typical experimental run parameters and their equivalent approximate values for $\dot{I}$ through a drive coil; this value is used to scale the injected drive current in the TREX simulations.

6.2.5 Collisionality

Collisions in VPIC are implemented with a Monte-Carlo collision operator for binary Coulomb collisions [51]. Collisions are optional in TREX-VPIC simulations, but when they are included they are based on the expected value of the standard reference collision frequency:

$$\nu_{ei,0} = \frac{n_{e,0} \ln \Lambda q_e^4}{6\sqrt{2}\pi^{3/2}\sqrt{m_e}(q_e T_e)^{3/2}\epsilon_0^2}$$

where $n_{e,0}$ is the SI density at $R = 0.5$m, $\ln \Lambda$ is the Coulomb logarithm (≈ 10), and q_e, m_e, and T_e are the electron charge, mass, and temperature, respectively. This value is rescaled to code units and then applied to calculate the expected frequencies for electron-electron, electron-ion, and ion-ion collisions, each of which have their own flag so they can be individually turned off or on. Additionally, the code timestep frequency at which the full collision operator in Eq 6.2 is applied can be adjusted, rather than defaulting to always being applied or never being applied. Collisions occur between pairs of particles within the same cell, conserving momentum and energy. The cumulative effect of the collisions leads to approximately 90° of scattering over one collision time ($1/\nu_{ei,0}$).

Regardless of the specifics of how the collisions are modeled, testing done in TREX-VPIC through a range of collisionalities have shown that there is very little distinction between simulations with no collisions and those with realistic collision rates. Unless otherwise stated, most VPIC results presented in this thesis do not include collisionality.

6.3 Matching Experimental Units to Simulation Units

While TREX VPIC simulations are designed around mimicking TREX experimental parameters, VPIC itself runs in so-called "code units", which are dimensionless values based on natural electron units ($d_e = c = w_{pe} = 1$, where these terms are the electron skin depth, the speed of light, and the electron plasma frequency, respectively) and on normalized data values based on some of the initial experimental inputs (for more on these initialization

values, see Appendix B). Thus, if VPIC results are to be compared with TREX experimental results, some method of conversion between the two unit systems is necessary. Unfortunately, this process is nontrivial. At the start of the unit conversion process one might naively assume that it would be sufficient to simply reverse the initialization processes that turn the starting TREX setup into the starting VPIC setup; for example, if the initialized magnetic fields are scaled by B_{HH}, the applied Helmholtz field, one might simply need to take any magnetic field output from later time-steps in the simulation and multiply them by B_{HH}. This, however, would not be sufficient; as the conditions in the simulation evolve with time, the necessity of keeping to the electron scale and holding several different dimensionless values to constant, potentially non-physical values for numerical tractability (e.g. the mass ratio or the plasma to cyclotron ratio - again see Appendix B) means that **local** values for evolving data types do not maintain their initialized scaling. To circumvent this effect, we use a dimension scaling technique originally devised to match PIC results to observations from MMS as described in Egedal et al. [52]. In this analysis, all unit conversions are reduced down to expressions composed of two free parameters and assorted physical constants. While the basis of these free parameters (identified as "α"s) can be changed to fit different available data measurements, we chose to use the electron density and electron temperature values, α_n and α_T, respectively, due to the comparatively large experimental uncertainties in the temperature and density measurements relative to those of other collected data (i.e., all those that come from our magnetic probes). These two parameters are defined as

$$\alpha_n \equiv \frac{n_{e,TREX}(\mathrm{m}^{-3})}{n_{e,VPIC}} \qquad \alpha_T \equiv \frac{T_{e,TREX}(\mathrm{J})}{T_{e,VPIC}}$$

where the VPIC values of both n_e and T_e are the standard code output units. These values can be found by comparing the experimentally-derived profiles of n_e and T_e to their VPIC equivalents; the α values are whatever number the VPIC profiles (or, more likely, portion of the profile- see below) need to be multiplied by to match their experimental counterparts. An example of this is shown on the left half of Figure 6.4; here, the VPIC profiles of n_e and

T_e have been scaled by the α values to roughly match the experimental profiles.

After α_n and α_T have been established, they can be used to calculate α values for other parameters based on the dimensionless scales that the simulation holds constant [52]. For this thesis, the two most-used conversions are as follows:

$$\alpha_B = \sqrt{\mu_0 \alpha_n \alpha_T} \equiv \frac{B_{TREX}(\mathrm{T})}{B_{VPIC}} \qquad \alpha_J = q_e \alpha_n \sqrt{\frac{\alpha_T}{m_e}} \equiv \frac{J_{TREX}(\mathrm{A/m^2})}{J_{VPIC}}$$

where μ_0, q_e, and m_e are SI values for the vacuum permeability, electron charge, and electron mass, respectively. Notably, these scale values can differ from the initialized scalings by as much as 25%[9].

Unfortunately, this matching process for determining α_n and α_T also involves a level of ambiguity - different portions of a density or temperature profile may require different scalings to equal their experimental analogues. There is no single "correct" way this decision of appropriate scaling can be made; for the work detailed in this thesis, multiple different matching paradigms were tested before a single one was selected (as detailed in Fig 6.4). Furthermore, these simulations vary from those used to establish this analysis method in Egedal et al. [52] in that the upstream environment is not constant; the nature of the TREX simulations means that the properties of the plasma upstream of the reconnection region are highly time dependent. This is in spite of the fact that the initialization of the TREX simulations is well defined.

An example of this issue is demonstrated in the right half of Fig 6.4, where the profiles for β_e when the layer is located at $R \sim 0.4$m have been calculated for a VPIC simulation and two separate TREX experiments. This simulation was initialized to match the fields, densities, and pressure balances of a standard 8kV70G experiment, but by the time the simulation has evolved enough to reach times that are physically interesting, the β_e profile has evolved to such a degree that it now more closely resembles that of a 5kV50G experiment.

[9]For the case shown in Fig 6.4, the starting magnetic fields were scaled by $B_{HH} = 70G$; the calculated value for α_B is only 77.68% of this initial scale.

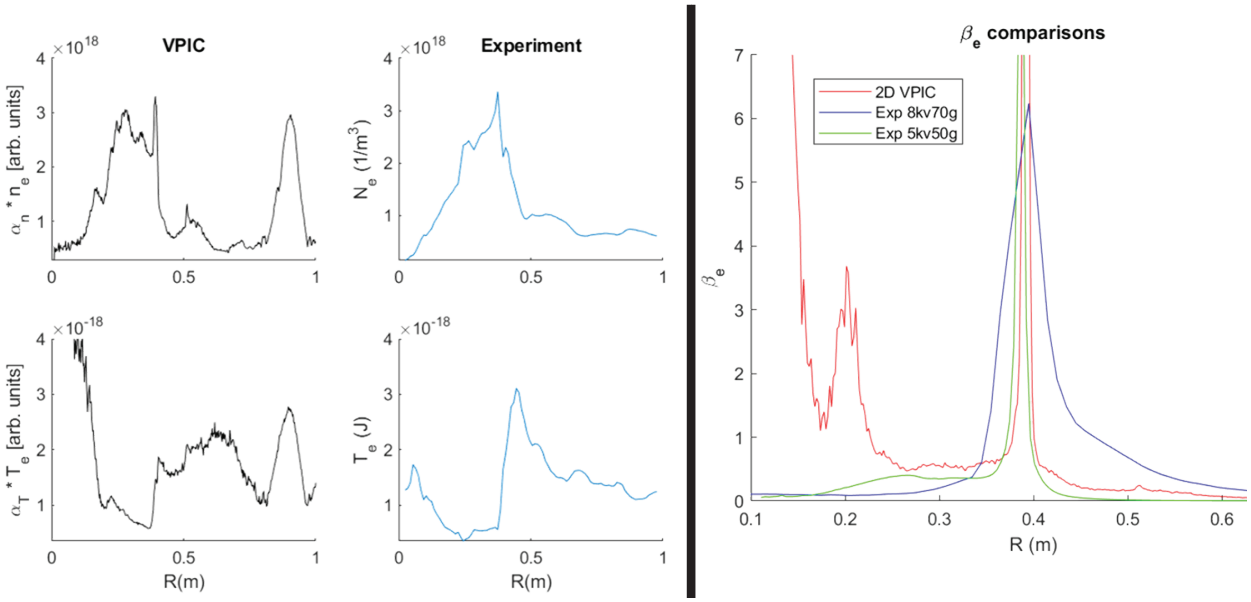

Figure 6.4: VPIC-to-SI unit matching procedure, based on Egedal et al. [52]. Left side: VPIC outputs for density (left-top) and temperature (left-bottom) are scaled by some constant until they "match" the measured profiles in the TREX experiment (right-top and bottom). These constants are the α_n and α_T values used in the conversion calculation. These plots are all taken from a time when the current layer is at $R \sim 0.4$m. Whether or not the "matching" between the plots is good is a matter of some ambiguity, as there is no clearly defined region where the matching should be established. In this case, the α values were chosen such that the average values on either side of the density/temperature peak are roughly equal; this choice was made to reflect the level of certainty available for data taken with the T_e probe (where data trends are generally taken to be more reliable than individual spikes) and to match the process used to select density values to calculate the layer width scales (where data is specifically taken on either side of the layer - see Chapter 7 and Appendix C). This ambiguity is true for any simulation output aside from the initialization, where the density and temperature profiles have been set based on experimental data and the scale constants are well defined (see Figure B.1 and Section 6.2.2). Right side: attempts to match the electron β profile between simulations and two different experimental runs. The simulation was initialized as a standard 8kV70G run, but the β_e profile when the layer is at $R \sim 0.4$m more closely matches the profile calculated from an experimental shot at 5kV50G. This further demonstrates the difficulty in trying to recreate a specific experimental scenario in VPIC - even though the initial field and density profiles have been created to match the measured experimental starting point for a given setup, this does not necessarily translate to a simulated output that is easily compared to the experiment at some later time.

Parameter	Experiment	VPIC
Mass Ratio (m_i/m_e)	1836+	$400 - 1836$
Temperature Ratio (T_e/T_i)	at least 5	$2.5 - 25$
Average Initial Plasma β	$\sim 10^{-2} - 10^{-1}$	$10^{-2} - 10^{-1}$
Magnetic Field Strength	$10 - 100\ G$	$10 - 100\ G$
(R, Z) size	1.5 mby3 m	$\sim$ 193 by $399 d_e$
ϕ size	360°	$0° - 60°$ so far

Table 6.2: Comparison of typical experimental parameters to typical simulation parameters. Specific cases may vary outside these values; these cases will be noted as they occur.

There is no known solution to this discrepancy[10]; this imbalance must be taken into account as an inherent source of uncertainty when comparing time-evolved simulation data with their experimental counterparts.

6.4 General VPIC Results

This section will describe some of the general VPIC runs and results, as opposed to the more detailed analyses that will be featured in the following chapters (specifically Chapters 7 and 8). Part of simulating TREX with VPIC involves a guess-and-check framework for testing different simulation features (for example, collisionality, particle emission, coil geometry, boundary conditions, initialization parameters, etc). Aside from the most extreme cases, VPIC runs tend to fall within a general range of parameters, which are listed in Table 6.2 with their experimental analogues.

6.4.1 Early VPIC Result: Coil Number

One of the first tangible results of TREX simulations of VPIC was the "preemptive" verification of the change in TREX 2018's standard run geometry compared to what it was in 2017. TREX VPIC simulations began in early 2018, and the initial results of the four-drive-coil

[10]Short of being able to initialize a simulation at a physically interesting point in time and running it backward, which if possible is certainly nontrivial.

runs repeatedly showed the formation of a stable magnetic island between the centermost coils. This was unexpected, as the results of TREX 2017 (also with four coils, see Chapter 4) showed no such island. However, while TREX 2018 was set to have the same coil geometry, the second version of the magnetic flux array (see Section A.2) that was present in 2017 had now been removed. When TREX 2018 eventually started, initial magnetic results showed the formation of a stable magnetic island, just as VPIC had predicted; the conclusion was that the flux array in 2017 had been a significant enough perturbation to prevent the island equilibrium state. Following this result, one of the outer TREX drive coils was removed from the circuit, leaving a three-drive-coil configuration; experimental data and simulations using this setup immediately showed a return to the standard reconnection layer geometry. A summary of these geometry changes and their associated simulation and experimental data may be viewed in Figure 6.5.

6.4.2 2D VPIC

2D simulations are the most commonly run versions of the VPIC-TREX model; while the cylindrical geometry is preserved, the toroidal angle ϕ has been eliminated[11]. 2D simulations with a mass ratio of 400 are more-or-less the standard starting point when beginning an investigation; mass ratios of this order are large enough to preserve most of the physics that occur at realistic mass ratios [42] while keeping the computational time reasonable (on the scale of $4 - 12$ hours, not including queue time). These simulations are usually run on one of the supercomputers available to workers at Los Alamos National Laboratory (LANL), typically on the Snow, Badger, or Grizzly computer clusters (all of which can be accessed remotely). One typical 2D simulation result is pictured in Figure 6.6. Here, the code units of the domain and the out-of-plane current density have been converted back to SI values. The black and magenta lines represent contours of the magnetic flux function Ψ (see Section

[11]Technically, there is still a nonzero value of ϕ, but it very small ($\leq 5°$); combined with the periodic boundaries at the limits of ϕ that are standard in all TREX simulations, the simulation domain is effectively two dimensional.

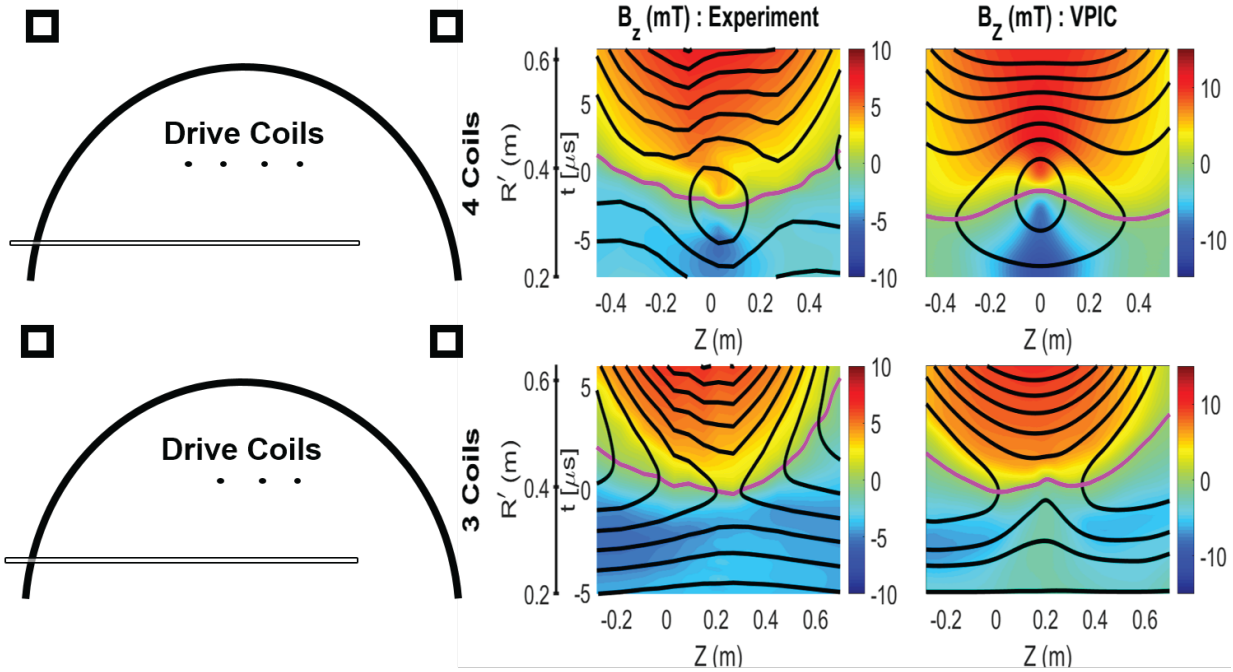

Figure 6.5: Early VPIC results were used to modify the geometry of the TREX setup in early 2018. Originally the 2018 run was set to begin as it did in 2017 with four drive coils, but without any form of the flux array. VPIC simulations of this setup run before TREX 2018 started up showed the formation of a large, stable magnetic island between the centermost two coils (top right). This was unexpected; the four coil experimental campaigns in 2017 consistently showed a standard reconnection layer (e.g., without the stable island). When the first results from TREX 2018 were found, they revealed a similar stable island (top middle). The conclusion reached was that the flux array used in TREX 2017 had provided enough of a perturbation to the plasma to break this island up. To solve this issue, the leftmost (southernmost in BRB coordinates) coil was removed from the drive circuit (but left inside of the vacuum vessel for convenience). The resultant plasmas reverted back to a standard reconnection layer geometry (bottom middle), which matched with similarly modified VPIC simulations (bottom right).

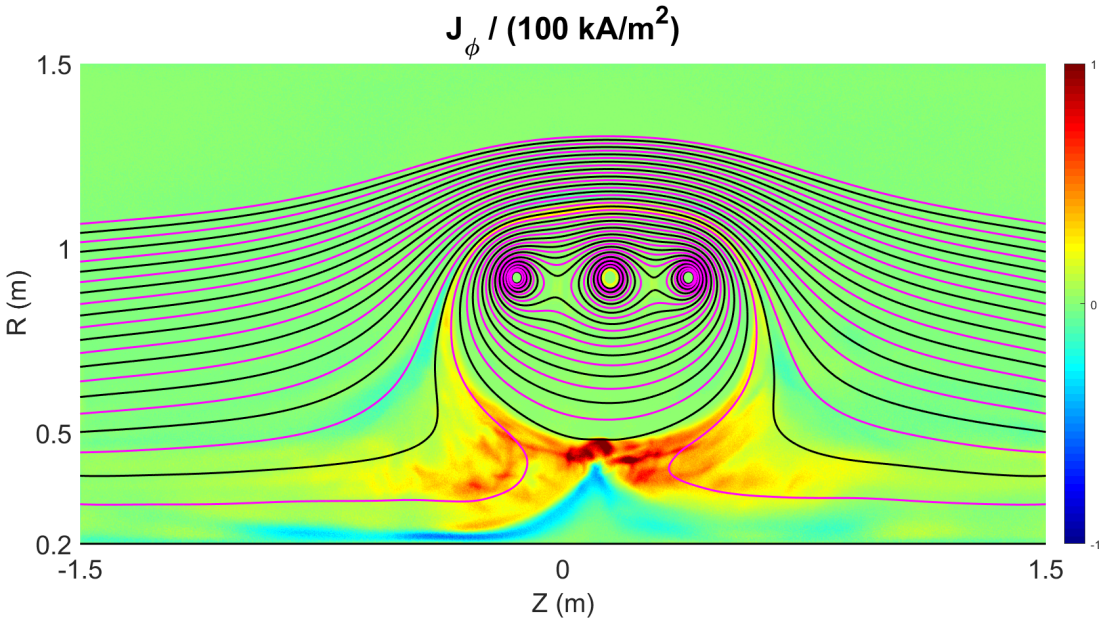

Figure 6.6: A frame from a typical 2D VPIC run, showing the out-of-plane current layer (the ϕ direction) and the contours of the magnetic flux function which map to the magnetic field lines. VPIC results of this nature are often edited into movies demonstrating the behaviour of the reconnection layers.

A.1.1), which map to the magnetic field lines in the RZ plane. The reconnection region and the reconnection current layer are clearly visible. Note how the minimum value of R is 0.2m due to the minimum R limitation described in Section 6.2.1.

6.4.3 3D VPIC

As one would expect, a TREX VPIC run that includes a nontrivial toroidal dimension is much more computationally expensive than a simple 2D run. As a consequence, the main 3D run used in TREX VPIC publications and in this thesis was run on the CORI supercomputer at the National Energy Research Scientific Computing Center (NERSC). This 3D run, with mass ratio $m_i/m_e = 400$, has an angular extent of 60° and thus appears as a "wedge", equivalent to 1/6 of the total toroidal extent of the physical BRB vessel. The toroidal boundaries are periodic (as they are in 2D). An example of several different timeframes of this run is shown in Figure 6.7, where the evolution of the reconnection current layer is clearly visible

from both the "front" view ((a), (c), and (e)) and the "side" view ((b), (d), and (f)). The colorscale in these plots also varies the opacity of a given cell, such that cells with lower total current densities are transparent. Further analysis of this run will be detailed in the following chapter.

6.4.4 Experimental and Simulation Comparison

A full comparison of the magnetic geometry of the reconnection region between the experiment, 2D VPIC, and 3D VPIC is shown in Figure 6.8. In this figure, all units and values have been scaled in an attempt to directly compare the experimental and simulation results. As referenced in Section 6.3, this analysis was nontrivial and involved the comparison of multiple different scaling and calibration paradigms before a decision was made. Broadly speaking, the magnetic geometries are consistent between the three scenarios: for example, each shows an out-of-plane current layer ((g), (h), and (i)) along the separatrix rather than extending out into the exhaust as a jet and each plot of the out-of-plane magnetic field ((d), (e), and (f)) shows the characteristic Hall quadruple, where the higher-density (lower R) side of the configuration has stronger magnetic magnitudes. Further analysis of the similarities and differences between experiment and 2D/3D VPIC will be given in the following chapters.

6.5 Conclusion

TREX VPIC uses the newly-created cylindrical implementation of VPIC to simulate the TREX experimental domain in a manner that is relevant to TREX parameters, maintains TREX's defining cylindrical symmetry, and operates with greater computational efficiency than was previously possible. Results from TREX VPIC simulations have been used to analyze, contextualize, and motivate the acquisition of TREX experimental data; these processes will be detailed in the following chapters.

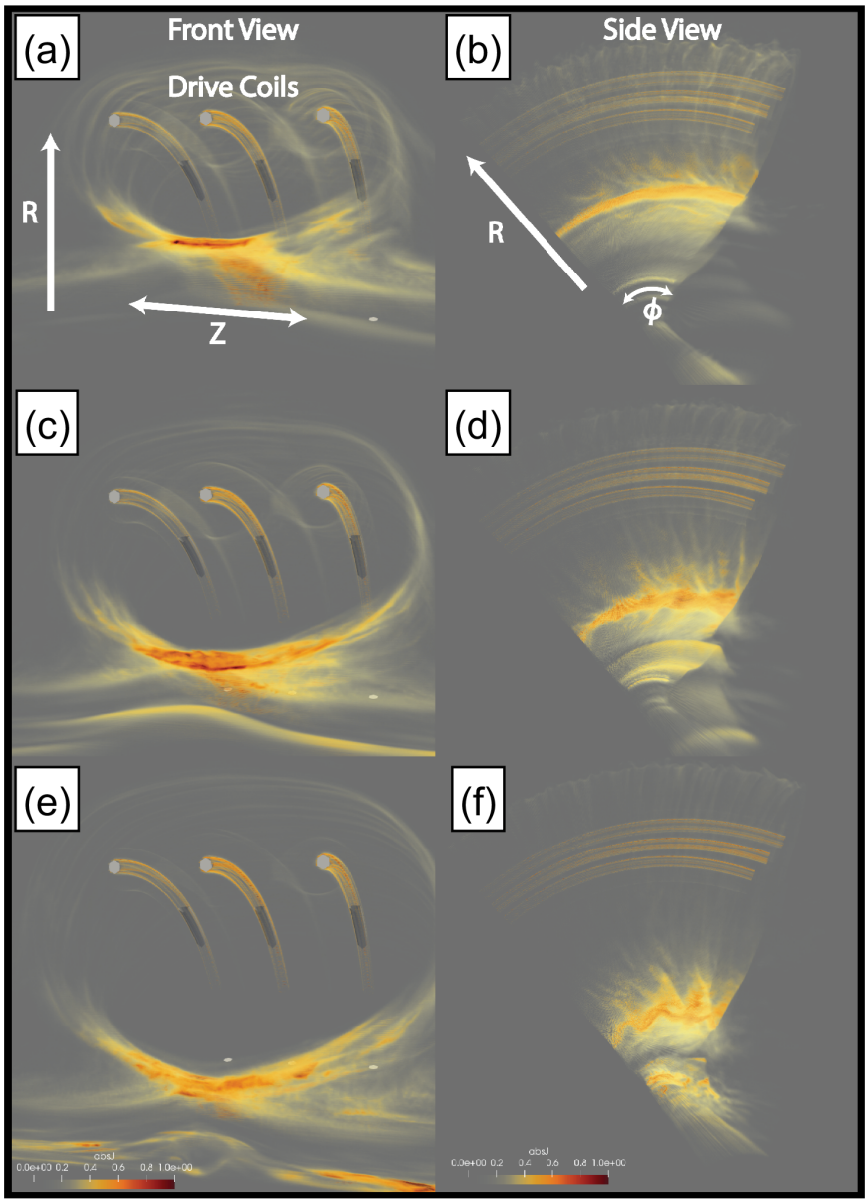

Figure 6.7: Multiple frames of a 3D run of the TREX simulation. This simulation has a mass ratio of 400 and a toroidal extent of 60° with periodic boundaries in the toroidal (ϕ) direction. Shown here are three different time outputs, viewed from the front and from the side. The colorscale of these plots shows the total current density in code units; the colormap is indexed by opacity as well as color, such that lower current density in a region causes that region to be more transparent. In each pair of timesteps ((a) and (b), (c) and (d), (e) and (f)), the reconnection current layer is the most obvious feature and shows a distinct time dependence in its geometry (see Section 7.2.2). The drive coils are also visible due to the particle emission around the coil surfaces.

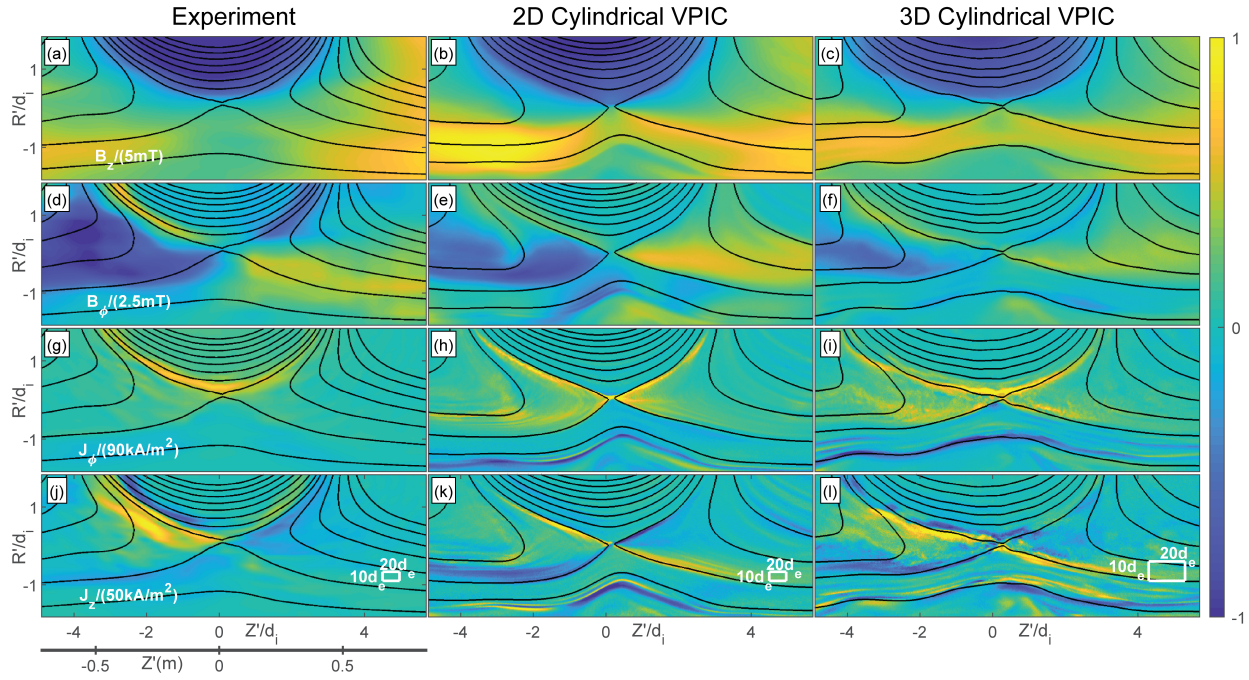

Figure 6.8: Comparison of TREX experimental data from a scan of the hook probe (cyan in Fig. 5.5(b)) with cylindrical VPIC runs in both 2 and 3 dimensions. The 2D run is at full mass ratio, and the 3D run is at a mass ratio of 400. The 3D run plots show data taken from a single value of ϕ. Each row of plots for a different magnetic feature shows contours of the magnetic flux function ψ in black. Each row has been scaled relative to the same magnitude, shown in the leftmost plot of each row. (a-c) compare the in-plane (B_z); (d-f) show out-of-plane (B_ϕ) magnetic fields. (g-i) show the out-of-plane current density (J_ϕ); (j-l) show the in-plane (J_z) current structures.

Chapter 7

Reconnection Layer Width

7.1 Introduction and Background

This chapter will be covering the results from Greess et al. [16], barring some information about the reconnection rate that has been moved to the next chapter. Within this chapter, several of the basic details of the TREX experiment and the TREX VPIC simulations will be repeated for the sake of clarity; similarly, some figures that were shown in earlier chapters will be reproduced here. Additional information regarding the curved probe measurements shown in Figure 7.5 and the density selection process used to determine the electron skin depths used in Figure 7.6 may be found in Appendix C. Background information on the Lower Hybrid Drift Instability mentioned in Section 7.2.2 may be found in Appendix D.

7.1.1 Kinetic Reconnection and the Layer Width

Although reconnection often governs the global dynamics of plasma systems, the reconnection process occurs in localized electron diffusion regions (EDRs), where the motion of the electron fluid decouples from the magnetic field, breaking the frozen-in law of magnetohydrodynamics. The origin of this process in the collisionless regime, where conventional resistive friction is absent, remains controversial. For example, laminar kinetic models predict that the EDRs are characterized by intense current layers with widths as narrow as the kinetic scales associated

with the electron orbit motion [53, 50]. In other models, the scattering of electrons by electric field fluctuations associated with high-frequency instabilities is proposed to widen the current layers and enhance the anomalous transfer of momentum from the electrons to the ions [54, 55, 56].

Significant insight into reconnection physics is provided by fully kinetic numerical models. In 3D configurations it has been argued that turbulence can cause local suppression of the effective conductivity [57, 58, 59], but other simulation studies have reported these effects are relatively small in both low-β parameter regimes [60] relevant to solar physics and for higher-β regimes with asymmetric layers relevant to the magnetosphere [61, 62, 43]. Rather, these 2D and 3D kinetic models typically suggest that fast reconnection can be mediated by electron inertia, and terms in the electron pressure tensor [63, 53, 64, 65, 66, 67]. These effects require the formation of intense electron current channels with widths characterized by either the electron inertial length $d_e = c/\omega_{pe}$ or the electron orbit scale [68].

To observationally address this issue, a primary goal of NASA's Magnetospheric Multiscale (MMS) Mission is to characterize the structures of EDRs for reconnection sites in the Earth's magnetosphere [1]. However, the *in situ* observations have not as yet provided conclusive insight to the role of anomalous resistivity. For example, the initial magnetotail observations are consistent with laminar kinetic reconnection [69, 52, 70, 71]. Meanwhile, for a magnetopause reconnection layer crossing [72], evidence for anomalous resistivity was identified near an EDR [73], but a separate analysis concluded the electron dynamics were in agreement with a 2D kinetic model (without anomalous resistivity) [74].

Dedicated laboratory experiments can provide complementary methods to study EDRs. Contrary to spacecraft measurements, laboratory experiments allow the controlled and reproducible study of reconnection layers with well understood upstream conditions and magnetic geometry. Results from the Magnetic Reconnection Experiment (MRX) at Princeton find that the current layer widths are much wider (by approximately a factor of four) compared to the predictions by kinetic models [75]. This disagreement [76] remains unresolved as it persists even when accounting for collisions [77], and 3D instabilities [68].

7.1.2 Ohm's Law

The physics that allows the electron fluid, with bulk velocity $\mathbf{v_e}$, to decouple from the motion of the magnetic field can be analyzed using the momentum equation of the electron fluid (the generalized Ohm's Law), which takes the form[1]:

$$\mathbf{E} = -\mathbf{v_e} \times \mathbf{B} + \eta \mathbf{J_e} - \frac{1}{ne} \boldsymbol{\nabla} \bullet \mathbf{P_e} - \frac{m_e}{e} \frac{\mathrm{d}\mathbf{v_e}}{\mathrm{d}t} \tag{7.1}$$

Here $\mathbf{P_e}$ is the electron pressure tensor, with elements $p_{ij} = m \int (u_i - v_{e,i})(u_j - v_{e,j}) f(u) \mathrm{d}^3 u$, $\mathbf{v_e}$ is the bulk electron fluid velocity, $f(u)$ is the velocity distribution function, and $\mathrm{d}/\mathrm{d}t$ is the total convective derivative, $\mathrm{d}/\mathrm{d}t = \partial/\partial t + \mathbf{v_e} \bullet \boldsymbol{\nabla}$.

In particular for the pressure tensor, we may split its contributions into its scalar and off-diagonal parts $\mathbf{P_e} = p_e \mathbf{I} + \boldsymbol{\Pi}$, where $\mathrm{trace}(\boldsymbol{\Pi}) = 0$. As discussed in Section 8.1.2, the reconnection rate E_{rec} is proportional to the $R_x(\phi)$-average of $\mathbf{E}$, and it becomes clear that while $-\nabla p_e$ contributions can be important to balance local electrostatic components of $\mathbf{E}$, the total contribution is 0 because $\oint \nabla p_e \bullet d\mathbf{l} = 0$. Thus, the $\boldsymbol{\nabla} \bullet \mathbf{P_e}$ term only contributes to reconnection through the off-diagonal stress in $\boldsymbol{\Pi}$.

7.1.3 Review: Properties of TREX

The applied TREX configuration is presented by the engineering schematic in Fig. 7.1(a). The vacuum vessel, provided by the Wisconsin Plasma Physics Laboratory (WiPPL) [22], is a 3 m diameter sphere that uses an array of permanent magnets embedded in the chamber wall to limit the plasma loss area to a very narrow fraction of the total surface area while keeping the bulk of the plasma unmagnetized. The setup includes a set of internal drive coils, as well as an exterior Helmholtz coil that provides near-uniform axial magnetic fields with magnitudes up to 100 mT [15, 17]. The current through the three internal drive coils (purple) ramps up to create a magnetic field that opposes and reconnects with the background

[1] This is equivalent to Eq 1.4 after canceling out the ion contributions.

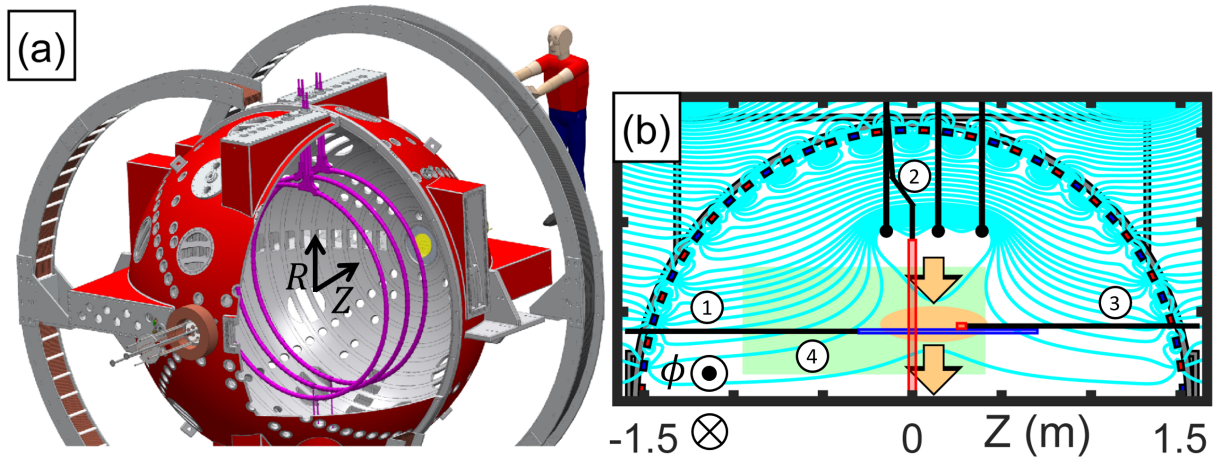

Figure 7.1: (a) Engineering sketch of TREX. The internal drive coils (purple) drive a magnetic field that opposes the external Helmholtz coil's field. The plasma source is a polar array of plasma guns (yellow). (b) A cross-section of the top half of the TREX vessel showing a theoretical example of the typical experimental geometry. The magnetic field lines are shown in cyan. The reconnection region (light orange) is driven down from the drive coils to the central axis, as indicated by the arrows. The layer is measured during this transit by the three probes shown: (1) the 3-axis linear $\dot{B}$ probe array (blue), (2) the speed probe (long red), and (3) the multi-tip Langmuir temperature/density probe, known as the T_e probe (short red). (4) The hook probe, another array of 3-axis $\dot{B}$ probes can be scanned through the shaded green area, allowing for the compilation of data from multiple experimental shots. These probes operate on sampling frequencies on the order of 10 MHz, while the elapsed time between the layer's generation and its arrival at the central axis is on the order of 20 µs. This is a repeated version of Fig. 5.5 with some slight modifications.

Helmholtz field, resulting in an anti-parallel magnetic configuration (e.g. no significant guide field). The plasma source is a set of plasma guns located at the machine's pole (shown in yellow). TREX can operate in hydrogen, deuterium and helium plasmas; experimental results presented in this paper will focus on hydrogen and deuterium.

In the planar cut of TREX shown in Fig. 7.1(b), the cyan lines are theoretically-derived magnetic flux contours meant to illustrate the typical magnetic geometry of an experimental run. As the current through the drive coils ramps up, the reconnection region is pushed from underneath the drive coils radially inward (orange arrows in Fig. 7.1(b)). During this transit, the reconnection layer "jogs" past the electrostatic and magnetic probes. Given the near constant speed of the reconnection layer, this facilitates high spatial resolution

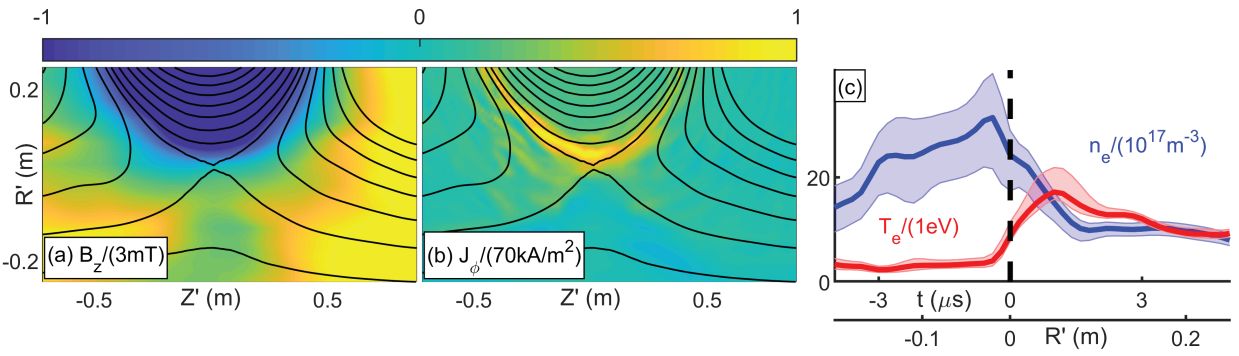

Figure 7.2: Example of experimental data. Plots (a) and (b) show the data from the hook probe recorded in a scan including 34 different probe positions covering the green region in Fig. 7.1(b). The black lines are contours of the flux function, Ψ, which map to the magnetic field lines. (a) shows the reconnecting magnetic fields, and (b) shows the out-of-plane current layer. (c) shows data from the T_e probe (short red in Fig. 7.1(b)); the shaded regions represent the 95% confidence interval for the values of density and temperature based on the fit of the probe's IV curve. The data in (c) is compiled using the jogging method to convert the time signal into a measurement of the R-coordinate. The lower R side of the layer is closer to the plasma sources and thus has a higher density than the other side of the layer. There is a jump in the plasma temperature when the layer passes the probe. The R' and Z' coordinates are versions of the regular machine R and Z coordinates but re-centered on the layer's location. This is a repeated version of Fig. 5.8.

measurements of the entire layer geometry over the course of a single experimental shot; this type of measurement is referred to as the jogging method. These probes and their locations are represented by the blue and red rectangles in Fig. 7.1(b). In addition to these jogging method probes, a third array of 3-axis $\dot{B}$ probes can be moved between shots, allowing for the creation of multi-shot datasets. The coverage area of this probe is given by the light green rectangle in Fig. 7.1(b) and is commonly known as the "hook" probe. By compiling data from multiple shots taken at different locations, this probe provides information about the reconnection geometry without relying on the jogging method.

An example of data collected from a typical set of experimental shots is provided in Fig. 7.2, where Fig. 7.2(a-b) shows data from 34 shots combined into one picture; for each shot, the hook probe is at a different position within the green region in Fig. 7.1(b). The black lines are contours of the flux function Ψ to illustrate the in-plane magnetic field lines. Fig. 7.2(c) shows the temperature and density data measured by the T_e probe. Note that in

Fig. 7.2(c), the time signals from the T_e probe are converted into position data using the jogging method described above. Typical plasma parameters include $T_i \ll T_e \simeq 5 - 20$ eV, $n_e \simeq 2 \bullet 10^{18}$ m^{-3}, $B_{rec} \simeq 4$ mT, yielding $\beta_e \simeq 0.4$ and $S \simeq 10^4$.

7.1.4 Review: Properties of TREX VPIC

TREX was simulated using VPIC, a kinetic particle-in-cell code [44, 46, 78]. The TREX boundary conditions were implemented in the new Cylindrical VPIC code with conducting walls at $R = 1.5$ m and $Z = \pm 1.5$ m, as well as an additional conducting wall at an adjustable minimum (nonzero) R near the central axis. Within the simulation domain, current sources with the same dimensions as the TREX drive coils were added at the drive coil locations. The current density at these locations is increased as a function of time to mimic the ramping current injection utilized in the experiment. Using density data from TREX, initial density and magnetic field profiles were set at the simulation start time to balance the magnetic and kinetic pressures for a given applied Helmholtz field. Electron-electron, electron-ion, and ion-ion collisions were implemented in some 2D runs with a Monte-Carlo collision operator for binary Coulomb collisions [51]. The collision frequencies were calculated from TREX data. Not all simulations implemented collisions; results from testing a range of 2D simulation collision parameters at relevant experimental levels showed very little difference between runs with and without collisions. The 3D run discussed in this paper did not include collisions.

The number of grid-points in the 2D simulation described here was 1512 by 3600 in the R and Z directions, respectively; in 3D, these decreased to 1024 and 2048 respectively with another 256 grid divisions in the ϕ direction. The system size in 2D was about 193 by 399 electron skin depths in the R and Z directions, respectively. In 3D, these values were 87 and 186 electron skin depths, respectively. The average number of super-particles per cell was 500 in 2D and 100 in 3D. In both simulations, the ratio of the electron cyclotron frequency to the electron plasma frequency was 1.

Both 2D (RZ) and 3D ($R\phi Z$) simulations of TREX can be compared to experimental

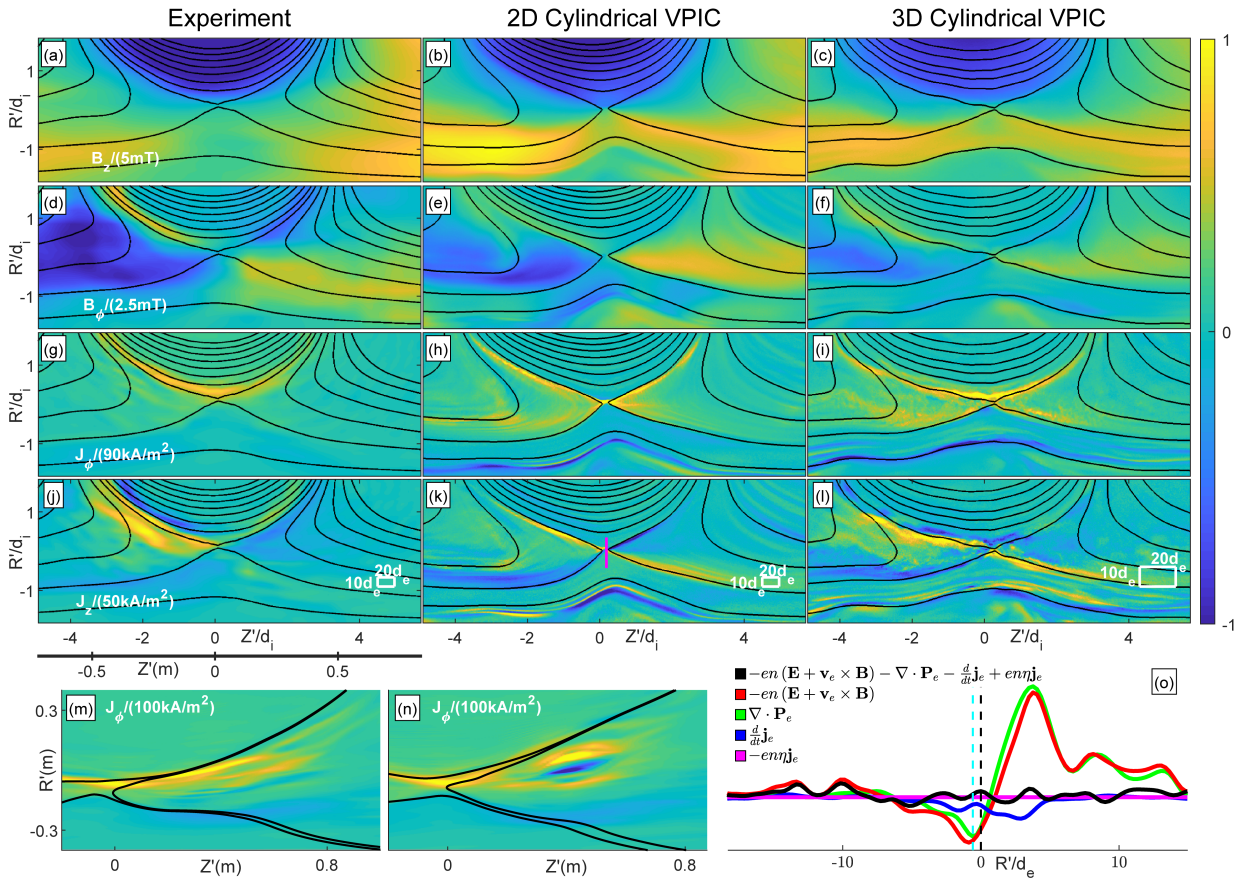

Figure 7.3: Comparison of TREX experimental data from a scan of the hook probe (green in Fig. 7.1(b)) with cylindrical VPIC runs in both 2 and 3 dimensions. The 2D run is at full mass ratio, and the 3D run is at a mass ratio of 400. The 3D run plots show data taken from a single value of ϕ. Each row of plots shows a different magnetic feature and each of these is over-plotted with contours of the magnetic flux function ψ in black. Each row has been scaled relative to the same magnitude, shown in the leftmost plot of each row. (a-c) compare the in-plane (B_z); (d-f) show out-of-plane (B_ϕ) magnetic fields. (g-i) show the out-of-plane current density (J_ϕ); (j-l) show the in-plane (J_z) current structures. Plots (m) and (n) show experimental data from the linear probe (blue in Fig. 7.1(b)) using the jogging method. The jogging method provides a high spatial resolution of ~ 0.4 cm in the R direction. Plot (m) shows a mostly laminar layer with some bifurcation, whereas plot (n) shows a plasmoid being ejected from the reconnection region. Plot (o) is a standard Ohm's Law analysis of the 2D VPIC simulation, along the path indicated by the magenta line in plot (k). The dashed cyan line is the location of the $B_z = 0$ point along the line; the dashed black line is the location of the maximum out-of-plane current density. Subplots (a) through (l) are reproduced from 6.8.

results; one such comparison is shown in Fig. 7.3. Experimental data in subplots (a,d,g,j) come from combining multiple shots worth of experimental data from the hook probe (green in Fig. 7.1(b)).

The 2D simulation (b,e,h,k) was obtained at full mass ratio while the 3D simulation (c,f,i,l) applies $m_i/m_e = 400$. For numerical tractability, the 3D simulation is limited to a 60° wedge with periodic boundaries in ϕ. Both the experimental and simulation profiles in Fig. 7.3(a-l) are displayed with the domains normalized by the local ion skin depths. Here the local ion skin depth is obtained from the value of n_e in the high-density inflow (e.g., the density value shown in Fig. 7.2(c) at $R' \sim -0.1$ m). The scaling of simulation variables relative to experimental ones was implemented using the technique described in Egedal et al. [52], where temperature and magnetic field profile matching occurred near the X-line during the reconnection process. Further similarities between TREX and 3D Cylindrical VPIC will be discussed later in this chapter.

7.2 Ohm's Law and the LHDI in TREX VPIC

7.2.1 Ohm's Law Analysis in 2D VPIC

An analysis of the generalized Ohm's Law for a 2D VPIC simulation of TREX is shown in Fig. 7.3(o), where the terms of Ohm's Law are evaluated along the path defined by the magenta line in Fig. 7.3(k). Given the boundary conditions of this simulation, this analysis does not include any form of spatial averaging, resulting in some fluctuation in the net Ohm's law term (the black line in Fig. 7.3(o)). Nonetheless, the pressure tensor divergence term (green) is clearly the dominant contributor to the reconnection electric field (red), consistent with prior 2D simulations of low-collisionality asymmetric reconnection, including Egedal et al. [74].

7.2.2 The Lower Hybrid Drift Instability in 3D VPIC

The full 3D simulation domain can be seen in Fig. 7.4(a). Taking a cut through the layer reveals the development of a toroidal instability which is inferred to be the lower hybrid drift instability (LHDI). Because the LHDI is driven by diamagnetic currents, it can be more vigorous within asymmetric reconnection layers which feature strong pressure gradients in the central portion [61, 79, 43], and several of the characteristics of the LHDI [80, 81] matched the numerical layer fluctuations. The fastest growing LHDI modes are short wavelength ($\rho_e k_\perp \sim 2.9$), primarily electrostatic, and are localized on the edge of the layer; these can be seen in Fig. 7.4(b). However, the LHDI features a rich spectrum [80], with longer wavelength $\sqrt{\rho_e \rho_i} k_\perp \sim 1.4$ electromagnetic modes that penetrate into the center, giving rise to a global rippling of the layer in the toroidal direction; this matches the characteristics of the kinking in the $B_z = 0$ and the current layer, as shown in Fig. 7.4(a)-(c). Further information on the properties of the LHDI are available in Appendix D.

7.2.3 Ohm's Law Analysis for 3D VPIC

Contrary to the Ohm's Law analysis for 2D VPIC, the choice of a path over which to integrate is nontrivial; prior publications analysing Ohm's Law in similar parameter regimes have returned different results based on different choices of how to spatially average the relevant variables [82, 43]. A simple average over a single dimension (usually one analogous to what is here defined as our ϕ (toroidal) dimension) may pick up data from outside the diffusion region, leading to dominant terms that do not appear when an average is made over a path that has been adapted to fit the shape of the layer and any constituent instabilities [58, 82, 43].

Keeping this in mind, we chose to integrate over a layer-specific path while showing the potential consequence of selecting a simple single-variable path. The simple path is shown in Fig. 7.4(c) as a white dashed straight line labeled SL. The black path represents the contour along which $B_z = 0$; this path was used as a starting point for an iterative process that determined the layer-specific contour C (solid white curve) by minimizing the contributions

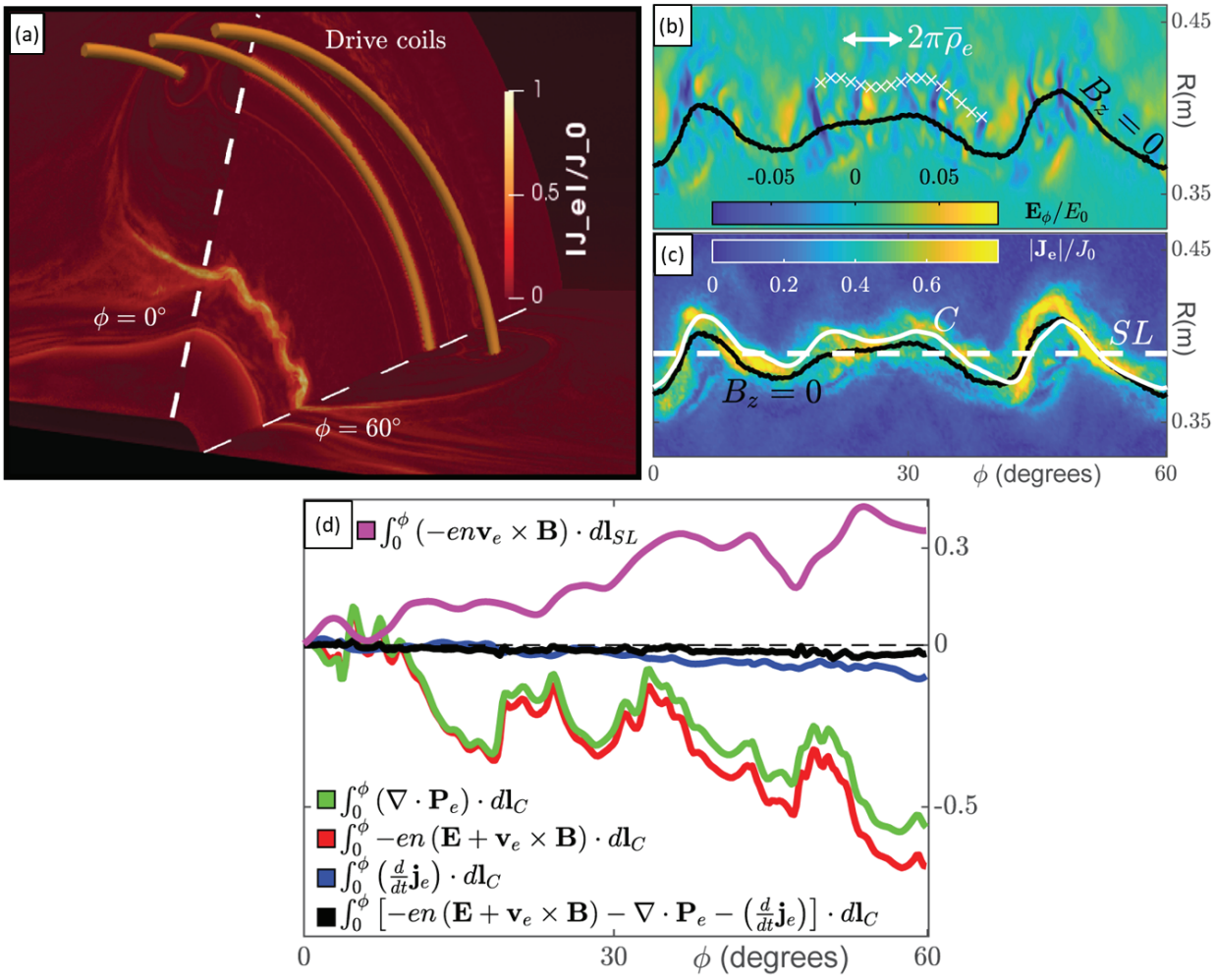

Figure 7.4: (a) Cuts of the current density, $|\boldsymbol{J}_e|$, in a 3D kinetic simulation of TREX implemented as a 60° wedge with periodic boundaries in ϕ. The drive coils are shown as gold surfaces. (b) Simulation profiles of $\boldsymbol{E}_\phi$ mapped onto the $R\phi$-plane at a single value of Z. The black line represents the $B_z = 0$ line. Fluctuations in $\boldsymbol{E}_\phi$ have the characteristics of the electrostatic LHDI; notably, they are stronger above the layer where the particle density is lower. The average electron cyclotron radius, $\overline{\rho}_e$, is calculated along the path marked by the small white Xs; this is one of the primary scale lengths used to describe the two modes of the LHDI. (c) Profile of $|\boldsymbol{J}_e|$ mapped onto the $R\phi$-plane at a single value of Z; the black line is still the $B_z = 0$ line. Also shown in white are two different paths of integration, a straight line (labeled SL) that simply cuts through the entire ϕ domain and the optimized integration curve C. The results of integrating the different terms of Ohm's Law along path C are shown in (d); the Lorentz term (red) is almost completely matched by the pressure divergence term (green), and the net Ohm's Law term (black) is consistently negligible. Also displayed are the results of integrating solely the $\mathbf{v_e} \times \mathbf{B}$ term over the straight path SL (shown in magenta).

of the $-en\mathbf{v_e} \times \mathbf{B}$ term to the path integral.

Integrating Eq. 7.1 along the path C produces the terms in Fig. 7.4(d). Note that collisionality was set to 0 in this simulation, so the resistivity term of Eq. 7.1 is also 0. The left side of Eq. 7.1 (the red line) is almost completely matched at every location by the pressure-tensor-divergence term (green line). The net Ohm's Law term (black) line remains near zero at every location. These two observations demonstrate that the pressure-tensor-divergence term is large enough to provide the frozen-flux-breaking electric field and that there are no significant contributions unaccounted for in Eq. 7.1.

Also shown in Fig. 7.4(d) is the $-en\mathbf{v_e} \times \mathbf{B}$ term for the SL result, given by the magenta line. The kinking in the layer results in SL including locations that are outside the diffusion region, resulting in large contributions of $-en\mathbf{v_e} \times \mathbf{B}$, the primary term for balancing E_ϕ outside the layer. By focusing on an average defined by C, we can minimize the $-en\mathbf{v_e} \times \mathbf{B}$ contributions and thus avoid drawing conclusions about the relevant terms of Ohm's Law in a manner that includes contributions from the non-reconnecting plasma regions. In previous analyses, contributions from the correlated fluctuations of the $-en\mathbf{v_e} \times \mathbf{B}$ term are combined with those from the pressure divergence to form the anomalous viscosity [43, 58]. These anomalous terms, when present, have been proposed as a mechanism that broaden the diffusion region and thus increase the reconnection rate [83]; however, more recent results from reconnection dominated by kinetic effects show that this can be achieved without these anomalous terms becoming significant [43]. While there has been some disagreement about whether or not these anomalous terms are dominant in 3D kinetic reconnection [58, 82, 43], our conclusion is that the answer will depend on the path used to define the spatial average. We find that the path that stays inside the diffusion region where $-en\mathbf{v_e} \times \mathbf{B}$ is small is the more physical choice. Furthermore, the dominant term breaking the electron frozen-in condition in the diffusion region is observed to be $\boldsymbol{\nabla} \bullet \mathbf{P_e}$ and is in agreement with recent spacecraft observations [52, 84].

7.3 Layer Width

In the above analysis of the kinetic simulation it was shown that the off-diagonal stress of $\nabla \bullet \mathbf{P_e}$ is mainly responsible for breaking the electron frozen-in condition. From theory, this off-diagonal stress scales roughly as $1/\delta_J^2$, where δ_J is the half-width of the reconnection current layer [85]. Prior simulation results have established that when the current layer half-width δ_J is on the order of a few electron scale lengths (here taken to be the electron skin depth, $d_e = c/\omega_{pe}$, which at electron β near unity is nearly equivalent to both the electron meandering width and the electron gyroradius), the pressure tensor divergence term will be sufficiently large to become the dominant term in Ohm's Law [68]. This characteristic defines the regime of collisionless reconnection; as such, the measurement of layer widths on the order of the several d_e can be used to establish the regime in which the reconnection is operating [53, 50].

To address whether $\nabla \bullet \mathbf{P_e}$ breaks the frozen-in condition in the experiment as it does in the simulation, we compare the widths of the current layers observed in TREX and the simulation. TREX is not yet able to measure the value of $\nabla \bullet \mathbf{P_e}$ directly, but as described above, the existence of thin current layers implies that the $\nabla \bullet \mathbf{P_e}$ contribution to Ohm's Law dominates the breaking of the frozen-in condition. The method of characterizing the layer half-width, δ_J, is illustrated in Fig. 7.5(a), where the current density is recorded by the linear $\dot{B}$ probe array (blue in Fig. 7.1(a)) at a set ϕ location for a range of Z values. In addition, a toroidally curved $\dot{B}$ probe array is used to characterize toroidal variations in the TREX current layers. An example dataset is shown in the top half of Fig. 7.5(b), documenting the intensity of the toroidal current density, with a range of different radial layer widths indicated below. This toroidal variation is similar to instability in the simulation, though the experimental observation is limited by the spatial resolution of the probe. More information about the construction and resolution limitations of this curved probe may be found in Section C.1.

Note that there is also some minor variation in the layer structure in the plane perpendic-

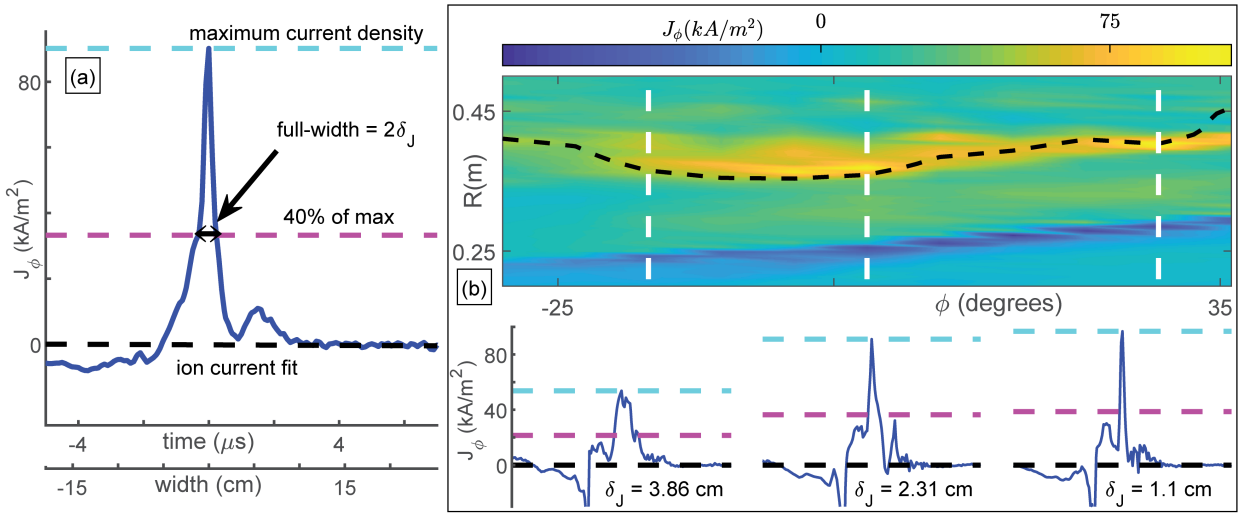

Figure 7.5: Measuring layer width. (a) method for inferring the current layer half-width, δ_J, defined as the half-width of the layer at 40% of the maximum. (b) shows an $R\phi$ contour plot of the current layer in TREX recorded by a curved $\dot{B}$ array sampling multiple toroidal angles. Three example slices at fixed ϕ are represented by the white dashed lines documenting variations in the layer widths.

ular to the toroidal direction; this can be seen in the existence of several smaller peaks in the current densities plotted in the bottom of Fig. 7.5(b). In this plane, the layer occasionally experiences some small amount of bifurcation or other minor irregularities. Examples of such behaviour are shown in Fig. 7.3(m) and (n). In this analysis, only the primary peaks in the electron current density cuts are taken into consideration.

Repeating the width measurement process for a range of experimental settings we obtain mean values for δ_J and d_e. The results are plotted in Fig. 7.6, where each data point represents the average result for δ_J and d_e for a given set of drive potential, Helmholtz field, gun number, and ion species. There are approximately ten different experimental shots averaged for each data point, which include estimates for the experimental uncertainties. Also plotted is the line corresponding to the previously reported experimental results in MRX [75]. The orange region represents the mean of the numerical layer widths from the 3D simulation in Fig. 7.4(b), ± a standard deviation. Similar to the experimental measurement process shown in Fig. 7.5(b), the numerical width results were obtained from radial cuts at

different ϕ values relative to the phase of the instability. Finally, the width recorded in a corresponding 2D simulation in the RZ-plane is given by the solid black line.

The width of the current layer is physically limited by the electron meandering scale, which is slightly larger than the electron inertial scale and has only a weak dependence on the precise β_e [76]; in the experiments that provided the data points for Fig. 7.6, this parameter is nearly constant ($\beta_e \sim 10^{-1}$). There is a clear divide between the blue (2 guns, lower density) and red (6 guns, higher density) datapoints, as expected from $d_e \propto n_e^{-1/2}$. Additionally, even though the lower density points have larger skin depths, they also have larger layer widths, keeping them on the same scaling as the higher density datapoints. There is no particular relationship between ion species and the experimental width scaling. Most notably, there is a general spread in measured layer widths, both relative to different parameter sets and within a given parameter set itself (demonstrated by the vertical uncertainties). This is consistent with the presence of the toroidal instability measured in TREX and demonstrated in the 3D simulations. Crucially, both the absolute values and spread of the measured current layer widths is in good agreement between the simulation and the experiment.

7.4 Conclusion

To summarize, reconnection in TREX is characterized by thin electron current layers, consistent with kinetic simulation results. The widths include a notable spread, $\delta_J \sim (1.5-3)d_e$, which can be attributed to the development of a toroidal instability in the current layer. Compared to previous experiments in MRX, the TREX temperature ratio $T_i/T_e \ll 1$ may be more favorable to this instability [61]. Nevertheless, the TREX current layers are in good agreement with those observed in a 3D kinetic simulation, and are much thinner than those observed previously in the MRX experiment.

The new Cylindrical VPIC code has allowed the TREX reconnection experiments to be modeled in a way that preserves its nominal cylindrical symmetry. Both 2D and 3D simulations reproduce the magnetic geometry measured in TREX, and 3D Cylindrical VPIC

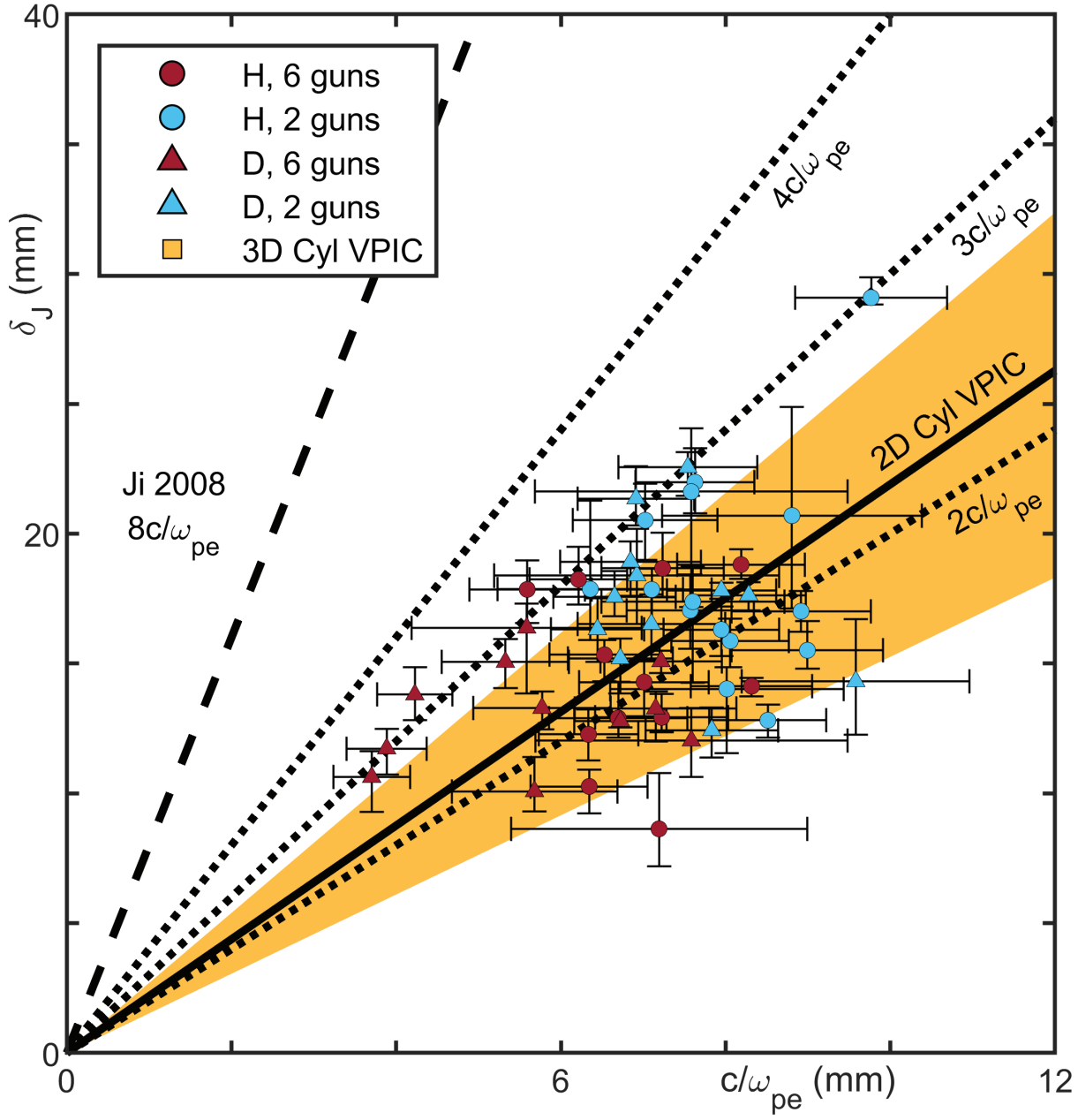

Figure 7.6: Results of measuring experimental layer width over several different parameter sets. The colors highlight the difference between "2 gun" (lower density) and a "6 gun" (higher density) plasmas. The orange region shows the range of current layer widths measured in the 3D simulation, and the solid black line shows the result from a 2D axisymmetric simulation (without the instability). The spread in the experimental and 3D Cylindrical VPIC layer widths is attributed to the toroidal instability described in Fig. 7.5.

also shows the development of a toroidal instability that produces the same spread in the layer width scaling. The narrow current layers observed in TREX and their match to 3D kinetic simulation results validates the numerical result that off-diagonal stress in the electron pressure tensor is responsible for breaking the frozen-in condition for low collisionality configurations relevant to reconnection in the Earth's magnetosphere.

Chapter 8

Simulated Reconnection Rate

8.1 Introduction and Background

The reconnection rate determines the speed at which plasma and magnetic field lines can move into and out of the reconnection region, effectively setting the timescale of the entire process [83, 4, 86]. Previous investigations from TREX have characterized the rate at which reconnection occurs in the experiment [17]. These TREX results showed the importance of magnetic flux pileup and the formation of a shock preceding the reconnection layer in maintaining force balance and setting the normalized reconnection rate. Furthermore, the experimental rate has a dependence on the size of the system relative to the ion scale; smaller scale size produces higher rates, indicative of the transition from ion-coupled toward electron-only reconnection [17, 87, 88].

This chapter's analysis applies fully kinetic simulations with the aim to confirm and reproduce the results of Olson et al. [17]. This is part of an ongoing effort to synchronize data collection between the experimental and simulated TREX environments, using the VPIC code developed at Los Alamos National Laboratory [16, 78, 46, 44]. Multiple simulations of TREX were analyzed to verify that pressure balance exists across the reconnection shock front. Further simulations of TREX were evaluated to check if the reconnection rate results match the values measured in TREX and their dependence on normalized experimental

system size.

The results and analyses in this chapter are mainly taken from Greess et al. [18], as well as some information about the reconnection rate in TREX which has been transferred from the paper detailed in the previous chapter. As with the prior chapter, several of the basic details of TREX and TREX VPIC have been repeated for clarity, and some of the figures will be partially or entirely repeated from earlier portions of this thesis.

8.1.1 Review: Properties of TREX

An engineering schematic of TREX is presented in Fig. 8.1(a). The vacuum vessel, provided by the Wisconsin Plasma Physics Laboratory (WiPPL) [22], is a 3 m diameter sphere that uses an array of permanent magnets embedded in the chamber wall to limit the plasma loss area to a very small fraction of the total surface area while keeping the bulk of the plasma unmagnetized. The setup includes a set of internal drive coils and an exterior Helmholtz coil that provides a near-uniform axial magnetic field with a magnitude up to 28 mT [15, 17]. The current through the three internal drive coils (purple) ramps up to create a magnetic field that opposes and reconnects with the background Helmholtz field, resulting in an anti-parallel magnetic configuration (e.g. no significant guide field). The plasma source is a set of plasma guns located at the machine's pole (shown in yellow). This setup mimics the asymmetric conditions of the dayside magnetopause; the high-density, low-field inflow at low R (analogous to the solar wind) is opposed by the low-density, high-field inflow at high R (analogous to the Earth's magnetic field). TREX is typically operated in either hydrogen, deuterium, or helium plasmas.

In the planar cut of TREX shown in Fig. 8.1(b), the cyan lines illustrate the typical magnetic geometry of an experimental run. As the current through the drive coils ramps up, the reconnection region is pushed from underneath the drive coils radially inward (orange arrows in Fig. 8.1(b)). With a typical reconnection layer speed of 50 km/s, the temporal resolution of our probes (10 MHz) translates to a high spatial resolution measurement of

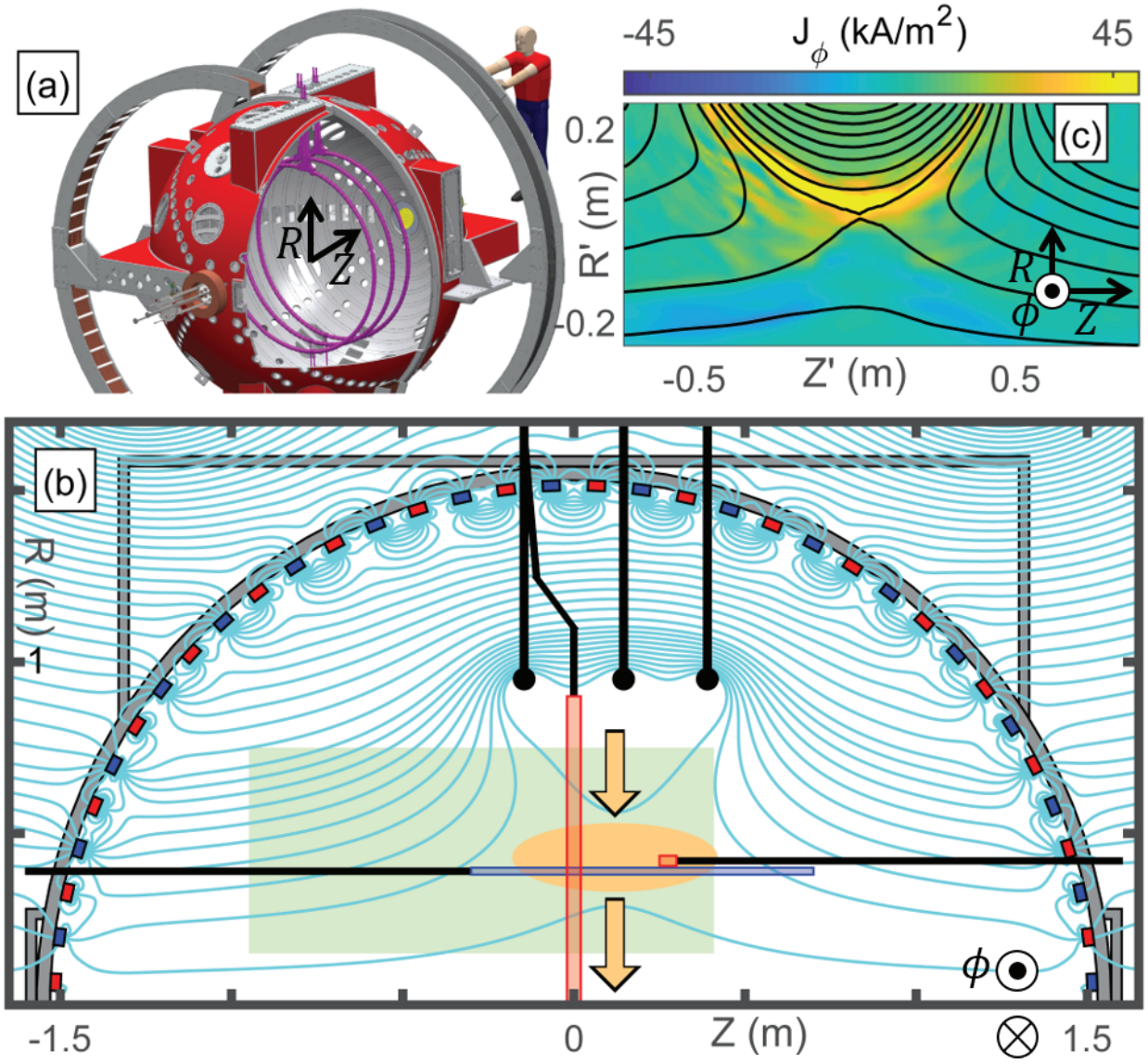

Figure 8.1: (a) Engineering sketch of TREX. The internal drive coils (purple) drive a magnetic field that opposes the external Helmholtz coil's field. The plasma source is a polar array of plasma guns (yellow). (b) A cross-section of the top half of the TREX vessel showing a theoretical example of the typical experimental geometry. The magnetic field lines are shown in cyan. The reconnection region (light orange) is driven down from the drive coils to the central axis, as indicated by the arrows. The layer is measured during this transit by our diagnostic suite. (c) shows a plot of an experimental out-of-plane reconnection current layer, created by collating data taken from a single probe as it is moved through the green shaded region in (b). The black lines are contours of the flux function, Ψ, which map to the magnetic field lines. The data has been re-centered around the x-point. This figure contains elements of both Fig. 5.5 and Fig. 5.8 with some slight modifications.

about 5 mm. This process, referred to as the "jogging method", permits the magnetic structure of the entire reconnection geometry to be characterized in a single experimental shot. The various magnetic and temperature probes and their locations are represented by the blue and red rectangles in Fig. 8.1(b). In addition to the jogging method probes, a different array of 3-axis $\dot{\mathbf{B}}$ probes can be moved between shots, allowing for the creation of multi-shot datasets. The coverage area of this probe is given by the light green rectangle in Fig. 8.1(b).

An example of data collected from a typical set of experimental shots is provided in Fig. 8.1(c), where data from 34 shots are combined into one picture; for each shot, the probe is at a different position within the green region in Fig. 8.1(b). The black lines are contours of the flux function Ψ to illustrate the in-plane magnetic field lines. Typical plasma parameters near the reconnection region include $T_i \ll T_e \simeq 5-20$ eV, $n_e \simeq 2\times10^{18}$ m^{-3}, $B_{rec} \simeq 4$ mT, yielding $\beta_e \simeq 0.4$ and $S \simeq 10^4$.

8.1.2 The Reconnection Electric Field

In 3D geometries the rate of reconnection is not always trivial to define [85]. However, given the nominal 2D experimental setup we can define the reconnection rate as the rate at which flux upstream of the reconnection region reconnects and moves downstream.

Fig. 8.2 shows the different "categories" of magnetic flux in the TREX cross-section. The red region contains field lines from the Helmholtz coil that go through the drive loop area and are upstream of the reconnection region. The blue lines are also upstream of the reconnection, but these represent the new magnetic flux injected into the system by the drive coils. Reconnection results in the downstream field lines, shown in green. The magenta field lines are those from the external Helmholtz coil that are initially above the internal drive coils and thus do not take part in the reconnection process. We can then define the remaining unreconnected flux, Ψ_B, as the (red) magnetic flux between $R = 0$ and the reconnection layer $\Psi_B = \int_0^{2\pi} \mathrm{d}\phi \int_0^{R_x(t,\phi)} RB_z dR$, where the integral is taken at a constant Z that matches the

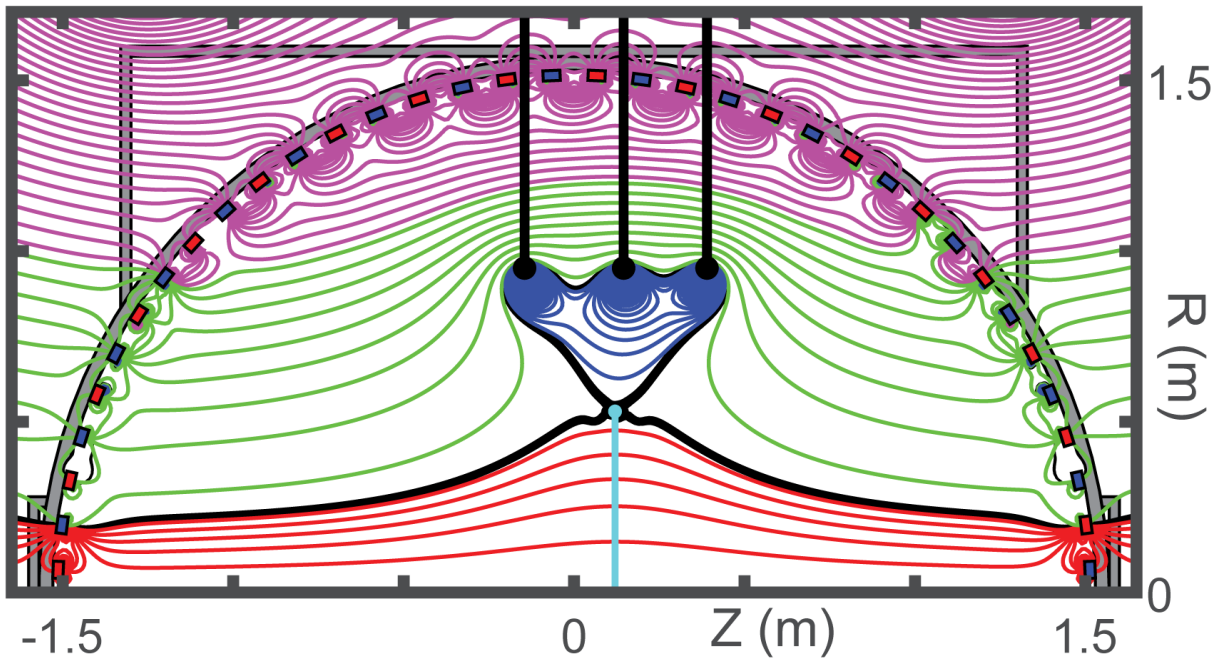

Figure 8.2: Block diagram of TREX's theoretical magnetic geometry, demonstrating the different regions of flux relative to the location of the reconnection layer. Blue and red are upstream of the reconnection region, starting from the drive coils and the Helmholtz coil, respectively. The green lines are downstream of the reconnection region, and the magenta lines are those that originate from the Helmholtz coil but are above the drive coils and thus do not impact the reconnection process. The cyan line represents the path of the integral used to define the flux function Ψ.

location of the X-line and from $R = 0$ to $R = R_x$. Here $R_x(t, \phi)$ is the radius of the center of the current layer which is moving radially inwards and which in the simulation is observed to be a function of ϕ. This path of this integral is represented by the cyan line in Fig. 8.2.

As Ψ_B is the remaining un-reconnected magnetic flux, it is clear that $-d\Psi_B/dt$ is the rate at which magnetic flux is being reconnected, i.e. the reconnection rate. There exists of course ambiguity in how to define the center of the reconnection layer $R_x(t, \phi)$, but as long as $R_x(t, \phi)$ correctly characterizes the inward motion of the reconnection layer it turns out that $-d\Psi_B/dt$ is largely unaffected by the differences between any reasonable choice of $R_x(t, \phi)$. By Faraday's law it is also clear that

$$-\frac{d\Psi_B}{dt} = \oint_{R_x} (\mathbf{E} + \mathbf{v}_{R_x} \times \mathbf{B}) \bullet d\mathbf{l} \simeq \oint_{R_x} \mathbf{E} \bullet d\mathbf{l} \quad . \tag{8.1}$$

Note that in 3D for a particular choice of $R_x(t,\phi)$ the value of $B_z(R_x(t,\phi))$ could be finite and oscillate along $R_x(t,\phi)$, but it is reasonable to impose that for a valid choice of $R_x(t,\phi)$, the average value of $B_z(R_x(t,\phi))$ must be small. Meanwhile $\mathbf{v}_{R_x}$ will be near constant and directed radially inward such that the average value of $(\mathbf{v}_{R_x} \times \mathbf{B}) \bullet d\mathbf{l}$ also becomes small and can be neglected, as expressed in Eq. 8.1.

In 3D configurations variations are permitted and likely present in $\mathbf{E}$ along $R_x(t,\phi)$. However, the local electric field may always be expressed on the form $\mathbf{E} = -\nabla\Phi - \partial\mathbf{A}/\partial t$, and because for any Φ we have $\oint_{R_x} \nabla\Phi \bullet d\mathbf{l} = 0$, it becomes clear that the reconnection electric field defined as

$$E_{rec} \equiv -\frac{1}{2\pi \langle R_x \rangle}\frac{d\Psi_B}{dt} = \frac{1}{2\pi \langle R_x \rangle}\oint_{R_x} -\frac{\partial \mathbf{A}}{\partial t} \bullet d\mathbf{l} \quad , \tag{8.2}$$

is a measure of the average toroidal inductive electric field, not directly dependent on any electrostatic electric fields $-\nabla\Phi$ which may be present in the reconnection region.

8.1.3 Review: Properties of TREX VPIC

TREX is simulated using VPIC, a kinetic particle-in-cell code [44, 46, 78]. VPIC has previously been used to mimic the TREX setup and produce results comparable to experimental data. More information on the general usage of VPIC to simulate TREX may be found in Chapter 6 and Appendix B. The number of grid-points in the 2D simulations described here is 756 by 1800, spanning a system size of about 4.5 by 9 ion skin depths (d_i) in the R and Z directions, respectively, in our standard density case. The low R boundary is set at $R \approx 0.155 d_i$ in the standard case and acts as a reflecting conductor; this is meant to replicate the effect of the cylindrical TREX current layer bouncing off of itself once it reaches $R = 0$ m in the experiment (cylindrical VPIC cannot operate at $R = 0$, so a relatively close value is chosen for the lower bound instead; the closer this value is to 0, the higher the computational load). The average number of macro-particles per cell is 500. In all simulations presented here, the ratio of the electron cyclotron frequency to the electron plasma frequency is 1 and

the mass ratio m_i/m_e is 400. Sub-realistic mass ratios are typical of PIC simulations for computational tractability; as a consequence, the experimental size measured in d_e is slightly larger than the simulation domain. However, Olson et al. [17] ran the TREX experiment at different ion masses and verified that the reconnection rate is tied to d_i rather than d_e. A typical experimental reconnection drive is modeled by injecting a linearly increasing current through the simulated drive coils. The strength of this current drive is given as a fraction of a typical experimental measurement of the time rate of change of the current in the drive coils, $\dot{I}_0 \approx 6.28 \times 10^8$ A s^{-1}.

8.2 Reconnection Regions and Pressure Balance

In TREX and TREX simulations during a reconnection discharge, the upstream plasma below the current layer can be divided into several distinct regions [17]. Working in the reference frame of the reconnection layer (r, red), the far upstream (u, blue) moves toward the layer at a speed faster than the local Alfvén speed. This necessitates the formation of a region of magnetic flux pileup (p, purple); this region is separated from the far upstream by a sub-critical shock (s, green). In the lab frame, the shock and the current layer move down with different speeds; generally speaking, the shock is faster. Pressure balance between these regions was verified using TREX data in the shock's reference frame in Olson et al. [17]; the assumptions and approximations involved with this calculation will be detailed below. An illustration of these regions is given in Fig. 8.3(a), where the velocities in the image are taken to be in the frame of the shock.

When combined with Ampère's Law, the MHD momentum balance equation for the plasma in regions u and p is

$$\rho \frac{\mathrm{d}\mathbf{v}}{\mathrm{d}t} = \frac{1}{\mu_0} (\boldsymbol{\nabla} \times \mathbf{B}) \times \mathbf{B} - \boldsymbol{\nabla} p \quad . \tag{8.3}$$

where ρ is the plasma density, $\mathbf{v}$ is the plasma flow speed, $\mathbf{B}$ is the magnetic field, p is the

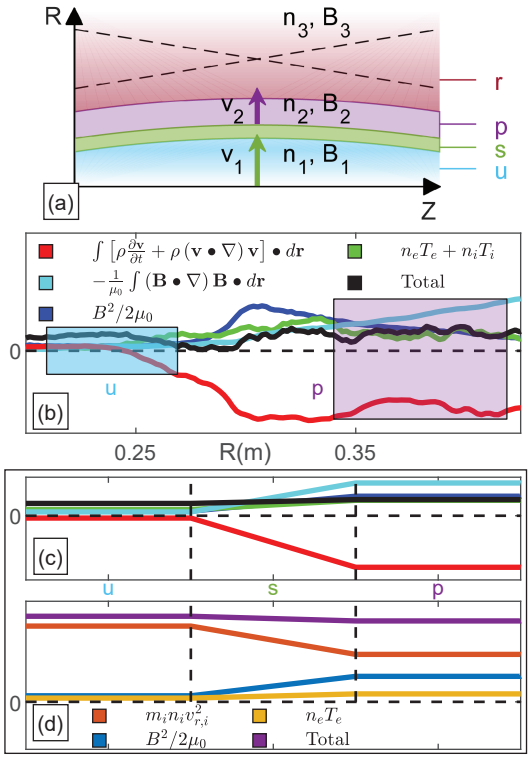

Figure 8.3: (a) Cartoon showing the regions that compose the area below a reconnection layer in the experiment, as described in Olson et al. [17]. At the lowest R values, we start in region u, below the shock (s) that precedes the reconnection layer. Following the shock, the pileup region (p) comes before the reconnection region (r). All labeled velocities are shown to be in the reference frame of the shock layer (s). (b) A plot of how the different terms of the momentum/pressure balance equation in simulation data vary across the shock. The net momentum remains roughly constant moving from region u (blue highlight) through the shock up to region p (purple highlight). (c) The same data as subplot (b), but averaged over the highlighted regions to give single values for each term in regions u and p. (d) A recreation of the momentum/pressure balance demonstration from Olson et al. [17]. This analysis of simulation data applies the assumptions that were necessary for the initial experimental data evaluation in Olson et al. [17], which are borne out by the fact that the pressure is still balanced in this application of the method to simulation data. Subplots (b)-(d) are all in arbitrary code units.

plasma kinetic pressure, and $\mathrm{d}/\mathrm{d}t$ is the total convective derivative, $\mathrm{d}/\mathrm{d}t = \partial/\partial t + \mathbf{v} \bullet \boldsymbol{\nabla}$. By expanding the convective derivative and using a vector identity, Eq. 8.3 can be rewritten as

$$\boldsymbol{\nabla}\left(p + \frac{B^2}{2\mu_0}\right) = \frac{1}{\mu_0}\left(\mathbf{B} \bullet \boldsymbol{\nabla}\right)\mathbf{B} - \rho\frac{\partial \mathbf{v}}{\partial t} - \rho\left(\mathbf{v} \bullet \boldsymbol{\nabla}\right)\mathbf{v} \quad . \tag{8.4}$$

Due to the toroidal symmetry of our experiment and the periodic boundary conditions in ϕ in our simulation, we assume that $\partial a/\partial\phi = 0$ for any quantity a. To evaluate the pressure balance between regions u and p, we will integrate Eq. 8.4 over a path $\mathrm{d}\mathbf{r}$ between arbitrary points g and h, where these points share the same value of the Z coordinate such that $\mathrm{d}\mathbf{r} = \mathrm{d}r\hat{\mathbf{r}}$. The resulting momentum/pressure balance relation is

$$\begin{aligned}\left[p + \frac{B^2}{2\mu_0}\right]_g - \left[p + \frac{B^2}{2\mu_0}\right]_h - \frac{1}{\mu_0}\int_h^g \left(\mathbf{B} \bullet \boldsymbol{\nabla}\right)\mathbf{B} \bullet \mathrm{d}\mathbf{r} \\ + \int_h^g \left[\rho\frac{\partial \mathbf{v}}{\partial t} + \rho\left(\mathbf{v} \bullet \boldsymbol{\nabla}\right)\mathbf{v}\right] \bullet \mathrm{d}\mathbf{r} = 0 \quad .\end{aligned} \tag{8.5}$$

By taking g and h to be in regions u and p respectively, we can evaluate the change in the different terms of this equation across the shock that separates the two regions; this analysis is shown in Fig. 8.3(b). Here, the equation has been split into distinct terms, where the magnetic pressure is in blue, the magnetic curvature is in cyan, the total convective acceleration is in red, the total kinetic pressure (given as the sum of the ion and electron pressures) is in green, with the total (the sum of all the terms) given in black. All terms are evaluated in the reference frame of the shock. The value for each term can be averaged over the points highlighted in regions u and p to give a single value for each, resulting in Fig. 8.3(c); in this plot, the values in s are simply the difference between the u and p regions. This averaging was done to mimic the limitations of the TREX experiment: the speeds of different regions cannot be measured simultaneously, so only a single value for each term can be calculated in each of regions u and p. Both u and p are taken to be outside the electron diffusion region, such that the electron contribution to the inertia term is neglected [17]. As expected, the total momentum/pressure is constant across the shock layer.

When evaluating the pressure balance across the shock layer in the experiment, several approximations are needed to account for the limitations of data collection (including the region speed limitation detailed above). Most notably, the analysis in Olson et al. [17] assumed that in regions u and p, changes in the plasma's velocity with respect to time or spatial coordinate are both minor relative to the ram pressure term, $m_i n_i v_{r,i}^2$, and balanced by the change in the magnetic tension term. The experimental analysis also assumed that $T_e \gg T_i$. Both of these assumptions are tested in Fig. 8.3(d), where the simulation data is used to recreate TREX's measurements. The total of the approximate pressure terms, shown in purple, is constant across the shock, as it is in the full momentum balance analysis detailed above and shown in Fig. 8.3(b) and (c). From this, we conclude that the assumptions that went into Olson et al. [17] are also consistent with the presented numerical results.

8.3 Reconnection Rate in TREX VPIC

As described previously, reconnection in TREX is asymmetric in plasma density and magnetic field on the opposing sides of the reconnection layer. As such, the reconnection rate is appropriately normalized by the method derived in Cassak and Shay [89]:

$$E_{rec} = \alpha B_{red} V_{A,hyb} \quad , \tag{8.6}$$

$$B_{red} = \frac{2B_2 B_3}{B_2 + B_3} \quad , \tag{8.7}$$

$$V_{a,hyb} = \left[\frac{1}{\mu_0 m_i} \frac{B_2 B_3 (B_2 + B_3)}{n_3 B_2 + n_2 B_3}\right]^{1/2} \quad . \tag{8.8}$$

where α is the normalized reconnection rate, E_{rec} is the reconnection electric field, B_{red} is the reduced magnetic field, $V_{a,hyb}$ is the hybrid Alfvén speed, and B and n are magnetic field and plasma density values at locations 2 and 3 as shown in Fig. 8.3(a). Experimental values of α were calculated in TREX, where the reconnection electric field was derived from the time rate of change of the magnetic flux function, Ψ [17]. Results from this evaluation are shown as the yellow points in Fig. 8.4(a); the normalized reconnection rate, α, is plotted against

the normalized system size, L/d_i, where d_i is the ion skin depth, $d_i = c/\omega_{pi}$. Similar to other analyses of simulated reconnection [90, 91], the rate increases as the normalized system size decreases. This is consistent with the transition toward electron-only reconnection, where the ions become less coupled to the field lines on the scale of the reconnection region, allowing reconnection to proceed without being constrained by the inertia of the ion fluid [87, 88]. The full analysis in Olson et al. [17] also showed that the effective reconnection rate is constant regardless of the applied current drive $\left(\dot{I}\right)$; this is due to the interplay between particle density and magnetic field strength upstream of the layer. Even if the layer is forced down with a stronger drive, producing a larger E_{rec} value, the shock structure and flux pileup will develop in such a way to produce a similar increase in the product of B_{red} and $V_{a,hyb}$, resulting in a constant value for the scaled rate α.

The TREX experiment is typically operated between two different density settings with three different ion species (hydrogen, deuterium, and helium), yielding six experimental points shown in Fig. 8.4(a). To compare these results to simulated TREX setups in VPIC, we instead vary the value of initial plasma density. Examples of applied initial density profiles are shown in Fig. 8.4(b). Our standard density profile vs R is shown in red and labeled as n. To reach a range of values for the scaled system size, this standard density was varied up and down by a single factor multiplying the entire profile; for example, a profile of twice the standard density ($2n$) is shown in yellow, while another profile of half the standard density ($0.5n$) is shown in blue. Note that the profiles shown here have had their density gradient decreased from the actual profiles used in the simulations for the sake of clarity. The real density profiles are based on measurements in the experiment and show a much stronger dependence on the value of the R coordinate.

Simulations were run for density values as low as $n/5$ and as high as $4n$, where n represents our standard density. Three runs of each density value with different random initialization seeds were compared to reduce the chances of an anomalous result skewing the conclusions. Within each individual run, multiple points in time corresponding to the reconnection region being in the range of R values most readily measured by the experiment ($R = 0.35 - 0.45$ m)

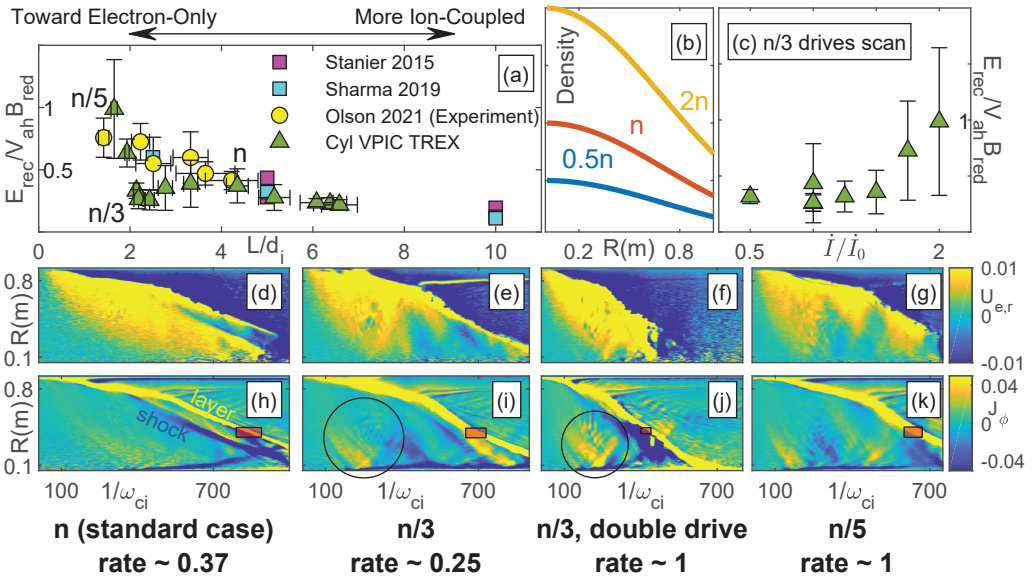

Figure 8.4: (a) The rate results of our density scan simulations, compared with prior simulation results and the TREX experimental results from Olson et al. [17]. The new rates (triangles) exhibit the same scaling as previous rate results, but with a slight dip around the $L/d_i \approx 2$ region. (b) A rough demonstration of how the densities of our simulations were varied to control the scaled system size. Our initial density profile (n) is scaled up or down by a variety of factors from 1/5 up to 4. (c) Variation of the rate for density $n/3$, the bottom of the dip in the simulation points in (a). The three points that are averaged together to get the $n/3$ in (a) are each shown here at the $\dot{I}/\dot{I}_0 = 1$ location. As the rate of current injection (i.e., the strength of the drive) increases, dip feature disappears. (d)-(k) are profiles in the R vs time plane (cuts of constant Z through the x-point) of different variables for four different simulations, showing how the reconnection features change with the rate. The first column is our standard density case, the second is an $n/3$ scan (in the dip of (a)), the third is an $n/3$ scan with twice the standard drive (rightmost point in (c)), and the last is an $n/5$ scan. The first row (d)-(g) shows the radial electron velocity, $U_{e,r}$. The second row (h)-(k) shows the current layer density J_ϕ; the layer and the preceding shock are labeled in the standard case (h) and visible with varying degrees of strength in the other cases. The black circles in (i) and (j) are showing the current due to the propagation and rebounding of the Alfvénic perturbation. The red rectangles represent the location of the x-point when the reconnection rate is measured, corresponding to our experimental measurement region of $R = 0.35 - 0.45$ m.

were selected and data from each of these points in time were sampled in regions p and r. This data was then used to calculate the reconnection rate (following Eq. 8.6-8.8) and the local ion skin depth. The results from all these time points from each of the three repeated simulations of a given initial density setup were averaged together to produce the green points in Fig. 8.4(a); the error bars represent the uncertainty estimate obtained by propagating the standard deviation of the distribution of selected density and magnetic fields through the rate equations. In general, these points follow the same trend as the experimental points (yellow), with increasing rate as the system size decreases.

One point of interest in Fig. 8.4(a) is the dip in the green simulation rate results localized around $L/d_i \approx 2.2$. This feature is a real aspect of the data trend, tied to subtle Alfvénic wave dynamics related to our cylindrical reconnection drive scenario. When the drive current begins to ramp up, the pressure balance of the initial configuration is suddenly violated, causing an Alfvénic perturbation to propagate from beneath the drive coils downward toward $R = 0$ m. Although this wavefront is propagating down, the wave itself corresponds to a radially-outward expansion of the plasma[1]. In the standard scenario with density scale n (Fig. 8.4(d) and (h)) this expansion persists throughout the reconnection layer formation and inward propagation, allowing the reconnection dynamics to adjust in a manner that keeps the effective rate consistent with expectation, as described earlier and in Olson et al. [17]. However, in the lower density scenario ($n/3$, Fig. 8.4(e) and (i)) the initial wavefront travels inward and then reflects off of the low R boundary while the reconnection layer is still evolving. On the tailing side of the reflected wave-front the plasma expansion is significantly reduced, corresponding to a transient reduction in the drive as the front reaches the reconnection layer. The upstream conditions of the reconnection layer cannot instantly adjust to these effects, resulting in normalized reconnection drives that can be either enhanced or reduced.

[1]The reasoning behind this is as follows: the initial density profile has larger plasma density at smaller values of R (see Eq 6.9). This profile is unstable unless balanced by magnetic pressure profile with field values increases with increasing R. When the TREX drive initiates, the magnetic fields near the coils suddenly decreases, disrupting the magnetic pressure profile that holds the plasma density in place. Once no longer balanced by the magnetic pressure, the dense plasma at small R begins to expand out into the rest of the domain.

So far, this feature has not been clearly observed in the experiment, as it exists in a parameter regime that is not reachable in TREX. TREX has reached values of $L/d_i \approx 2.2$, but this was done with helium and deuterium plasmas rather than by going to lower density values. Furthermore, the effect of this Alfvénic feature may be influenced by our simulation's reflecting boundary condition at low R, which approximates TREX's behaviour but may not be exactly analogous. This dip would not be expected in scenarios without some manner of reflection along one of the domain boundaries. Similarly, the results in Fig. 8.4(c) show variation relative to drive current ramp intensity due to the above feature's effect in extinguishing the upstream inflow. This feature only appears in the simulations, causing them to diverge from the results of Olson et al. [17] that showed experimentally that the drive intensity does not affect the scaled rate.

8.4 Conclusions

Experiments conducted in the Terrestrial Reconnection EXperiment (TREX) over a range of different scaled system sizes showed a range of reconnection rates which increased as the system size decreased. As part of an ongoing effort to model the TREX experimental setup in a particle-in-cell simulation, VPIC was used to replicate TREX runs at a range of densities, many of which were outside TREX's normal operating parameters. Within the range of the TREX parameters, the numerical simulations confirmed the experimentally observed rates of reconnection, weakly dependent on the normalized size of the experiment with higher rates at smaller system size indicative of the transition toward electron-only reconnection. Additionally, the high detail of simulation data allows the full pressure balance equation across the reconnection shock front to be calculated and pressure balance to be confirmed. This calculation also allowed us to verify the accuracy of some of the assumptions that were needed in TREX's experimental pressure balance calculation. Together with previous results [16], these conclusions continue to verify VPIC's ability to accurately capture the full shock formation and reconnection dynamics observed in TREX.

Chapter 9

Conclusions

This thesis has presented results from the Terrestrial Reconnection EXperiment (TREX) and from Vector Particle-In-Cell (VPIC) simulations designed to mimic the TREX experimental parameters. Work over the course of this graduate program entailed both experimental and computational components, with an eventual emphasis on using either method as a model or motivation for the other. On a more specific level, work in both of these areas was intended to provide evidence that TREX is operating in the parameter regime it is designed to reach, as referenced in the phase space diagram Fig. 1.8. All together, the essential points that have been presented in this thesis are as follows:

- **The Big Red Ball (BRB) is a versatile platform that can host a wide variety of plasma experiments.** The BRB's customizability is an essential feature that allows TREX (and other experiments) the freedom to modify its hardware and probe suite with minimal difficulty.
- **TREX is designed to access the collisionless reconnection regime.** This low-collisionality reconnection is the type that characterizes reconnection at the Earth's magnetopause. TREX has undergone several iterations to improve its ability to delve into this parameter space.
- **Cylindrical VPIC has been adapted to model the TREX experiment.** Cylin-

drical VPIC can simulate TREX efficiently without sacrificing TREX's cylindrical symmetry. Significant time was spent creating a general starting deck on which all TREX VPIC simulations are based; this included work devoted to understanding the intricacies of comparing code units with their real-life equivalents.

- **Results from early TREX iterations established the presence of plasmoids in the reconnection region, certifying that it was within the realm of multiple X-line reconnection.** This result was mainly found through the data collected by a custom, hand-built magnetic flux array.

- **Results from later TREX iterations proved that the widths of the reconnection layer are on the order of $2-3$ electron skin depths, indicating reconnection in the collisionless regime.** The presence of a two dimensional instability in the reconnection layer (thought to be the Lower Hybrid Drift Instability (LHDI)) artificially broadened the measured layer widths. $2D$ and $3D$ TREX VPIC simulations confirmed this layer width scaling, the fact that this scaling corresponded to a significant anisotropy in the plasma pressure, and the existence of the instability.

- **Ohm's Law analyses of 2D and 3D VPIC both showed that the majority of the reconnection electric field was supplied by the divergence of the electron pressure tensor.** The total reconnection electric field is well-modeled without the introduction of anomalous terms. Furthermore, while the LHDI did not introduce anomalous resistivity to the reconnection layer, it did alter the shape of the layer such that an imprudent selection of the spatial average over which Ohm's Law is evaluated could result in the inclusion of areas outside the electron diffusion region; contributions from these areas could be misinterpreted as anomalous terms within the reconnection layer.

- **TREX VPIC was able to successfully model and match the experimentally-derived reconnection rate scaling established by prior TREX investigations.**

These simulations were made to complement the work done in Olson [14] as well as providing data from scenarios beyond TREX's standard operational parameters.

9.1 Future Work

In the immediate future, there remains more work to be done regarding the suspected LHDI in the TREX 2018 configuration. While preliminary results have indicated the existence of a toroidal instability in the experiment, scheduling and hardware issues have prevented revisiting the complete TREX 2018 setup with the recently constructed high-spatial-resolution curved probe. A solid, quantify-able measurement of the instability and its properties (preferably in enough detail to conclusively establish that the instability is the LHDI) needs to be taken to solidify the comparison with TREX VPIC results presented in Chapter 7 and Appendix C.1. Furthermore, while the experimental and simulated results present here strongly suggest that TREX is operating in the collisionless reconnection regime, this conclusion may remain open to debate until such time as the expected anisotropy in the plasma's velocity distribution is directly measured. Several different iterations of the "anisotropy" probe have been built and tested concurrent with the work done in this thesis (and beyond), but a successful implementation of such a diagnostic has thus-far proved elusive. As of this writing, the work continues. Finally, and most generally, the geometry of TREX (and potential VPIC simulations of that geometry) is customizable to an almost limitless degree. Different types of TREX hardware (especially with respect to the geometry of the drive coils) have been and will be implemented to explore different reconnection parameters and dynamics; TREX VPIC will be available to model or test these new configurations. For example, while the results given in this thesis are confined to antiparallel reconnection, TREX has built and installed a toroidal field coil that can apply an out-of-plane ("guide") magnetic field in addition to the standard TREX drive field. Experimental data collected from these runs but they have not yet (as of this writing) been published. The few VPIC simulations of the guide field configuration that have been only briefly investigated.

References

[1] J. L. Burch, T. E. Moore, R. B. Torbert, and B. L. Giles. Magnetospheric Multiscale Overview and Science Objectives. *Space Science Reviews*, **199** (2016). doi:10.1007/s11214-015-0164-9.

[2] J. P. Freidberg. *Plasma Physics and Fusion Energy*. Cambridge University Press, (2007). doi:10.1017/CBO9780511755705.

[3] P. A. Sweet. The production of high energy particles in solar flares. *Nuovo Cimento Suppl.*, **8** (1958).

[4] E. G. Zweibel and M. Yamada. Perspectives on magnetic reconnection. *Proc. R. Soc. A*, **472** (2016). doi:10.1098/rspa.2016.0479.

[5] H. Ji, M. Yamada, S. Hsu, and R. Kulsrud. Experimental test of the sweet-parker model of magnetic reconnection. *Phys. Rev. Lett.*, **80** (1998). doi:10.1103/PhysRevLett.80.3256.

[6] H. Ji, M. Yamada, S. Hsu, R. Kulsrud, T. Carter, and S. Zaharia. Magnetic reconnection with sweet-parker characteristics in two-dimensional laboratory plasmas. *Physics of Plasmas*, **6** (1999). doi:10.1063/1.873432.

[7] H. Ji and W. Daughton. Phase diagram for magnetic reconnection in heliophysical, astrophysical, and laboratory plasmas. *Physics of Plasmas*, (2011). doi:10.1063/1.3647505.

[8] O. O. C. Ohia. *Two-fluid Simulations of Magnetic Reconnection with a Kinetic Closure for the Electron Pressure Anisotropy*. PhD thesis, Massachusetts Institute of Technology, (2014).

[9] M. Hesse, S. Zenitani, and A. Klimas. The structure of the electron outflow jet in collisionless magnetic reconnection. *Physics of Plasmas*, **15** (2008). doi:10.1063/1.3006341.

[10] J. Egedal, H. Gurram, S. Greess, W. Daughton, and A. Lê. The force balance of electrons during kinetic anti-parallel magnetic reconnection, (2022).

[11] J. Egedal, A. Le, and W. Daughton. A review of pressure anisotropy caused by electron trapping in collisionless plasma, and its implications for magnetic reconnection. *Phys. Plasmas*, **20** (2013). doi:10.1063/1.4811092.

[12] W. Daughton and V. Roytershteyn. Emerging parameter space map of magnetic reconnection in collisional and kinetic regimes. *Space Science Reviews - SPACE SCI REV*, **172** (2011). doi:10.1007/s11214-011-9766-z.

[13] A. Lê, J. Egedal, W. Daughton, V. Roytershteyn, H. Karimabadi, and C. Forest. Transition in electron physics of magnetic reconnection in weakly collisional plasma. *Journal of Plasma Physics*, **81** (2015). doi:10.1017/S0022377814000907.

[14] J. Olson. *Exploring Driven, High Lundquist Number Magnetic Reconnection In The Laboratory: Studies Of Sub-Ion Scale Plasmoids, And The Interplay Between Shocks And Magnetic Flux Pileup*. PhD thesis, University of Wisconsin-Madison, (2020).

[15] J. Olson, J. Egedal, S. Greess, R. Myers, M. Clark, D. Endrizzi, K. Flanagan, J. Milhone, E. Peterson, J. Wallace, D. Weisberg, and C. B. Forest. Experimental Demonstration of the Collisionless Plasmoid Instability below the Ion Kinetic Scale during Magnetic Reconnection. *Physical Review Letters*, (2016). doi:10.1103/PhysRevLett.116.255001.

[16] S. Greess, J. Egedal, A. Stanier, W. Daughton, J. Olson, A. Lê, R. Myers, A. Millet-Ayala, M. Clark, J. Wallace, D. Endrizzi, and C. Forest. Laboratory verification of electron-scale reconnection regions modulated by a three-dimensional instability. *Journal of Geophysical Research: Space Physics*, **126** (2021). doi:https://doi.org/10.1029/2021JA029316. e2021JA029316 2021JA029316.

[17] J. Olson, J. Egedal, M. Clark, D. A. Endrizzi, S. Greess, A. Millet-Ayala, R. Myers, E. E. Peterson, J. Wallace, C. B. Forest, and et al. Regulation of the normalized rate of driven magnetic reconnection through shocked flux pileup. *Journal of Plasma Physics*, **87** (2021). doi:10.1017/S0022377821000659.

[18] S. Greess, J. Egedal, A. Stanier, J. Olson, W. Daughton, A. Lê, A. Millet-Ayala, C. Kuchta, and C. B. Forest. Kinetic simulations verifying reconnection rates measured in the laboratory, spanning the ion-coupled to near electron-only regimes. *Physics of Plasmas*, **29** (2022). doi:10.1063/5.0101006.

[19] E. J. Spence, K. Reuter, and C. B. Forest. A SPHERICAL PLASMA DYNAMO EXPERIMENT. *Astrophys. J.*, **700** (2009). doi:10.1088/0004-637X/700/1/470.

[20] C. M. Cooper, J. Wallace, M. Brookhart, M. Clark, C. Collins, W. X. Ding, K. Flanagan, I. Khalzov, Y. Li, J. Milhone, M. Nornberg, P. Nonn, D. Weisberg, D. G. Whyte, E. Zweibel, and C. B. Forest. The Madison plasma dynamo experiment: A facility for studying laboratory plasma astrophysics. *Phys. Plasmas*, **21** (2014). doi:10.1063/1.4861609.

[21] D. B. Weisberg, E. Peterson, J. Milhone, D. Endrizzi, C. Cooper, V. Désangles, I. Khalzov, R. Siller, and C. B. Forest. Driving large magnetic Reynolds number flow in highly ionized, unmagnetized plasmas. *Phys. Plasmas*, **24** (2017). doi:10.1063/1.4978889.

[22] C. Forest, K. Flanagan, M. Brookhart, M. Clark, C. Cooper, V. Désangles, J. Egedal, D. Endrizzi, I. Khalzov, H. Li, M. Miesch, J. Milhone, M. Nornberg, J. Olson, E. Peterson, F. Roesler, A. Schekochihin, O. Schmitz, R. Siller, A. Spitkovsky, A. Stemo, J. Wallace, D. Weisberg, and E. Zweibel. The Wisconsin Plasma Astrophysics Laboratory. *Journal of Plasma Physics*, (2015). doi:10.1017/S0022377815000975.

[23] C. M. Cooper, D. B. Weisberg, I. Khalzov, J. Milhone, K. Flanagan, E. Peterson, C. Wahl, and C. B. Forest. Direct measurement of the plasma loss width in an optimized, high ionization fraction, magnetic multi-dipole ring cusp. *Phys. Plasmas*, **23** (2016). doi:10.1063/1.4963850.

[24] E. E. Peterson, D. A. Endrizzi, M. Beidler, K. J. Bunkers, M. Clark, J. Egedal, K. Flanagan, K. J. McCollam, J. Milhone, J. Olson, C. R. Sovinec, R. Waleffe, J. Wallace, and C. B. Forest. A laboratory model for the Parker spiral and magnetized stellar winds. *Nat. Phys.*, **15** (2019). doi:10.1038/s41567-019-0592-7.

[25] D. Endrizzi, J. Egedal, M. Clark, K. Flanagan, S. Greess, J. Milhone, A. Millet-Ayala, J. Olson, E. E. Peterson, J. Wallace, and C. B. Forest. Laboratory resolved structure of supercritical perpendicular shocks. *Phys. Rev. Lett.*, **126** (2021). doi:10.1103/PhysRevLett.126.145001.

[26] D. Weisberg. *Pursuing The Plasma Dynamo And MRI In The Laboratory: Hydrodynamic Studies Of Unmagnetized Plasmas At Large Magnetic Reynolds Number*. PhD thesis, University of Wisconsin-Madison, (2016).

[27] M. Brookhart. *Subcritical Onset of Plasma Fluctuations and Magnetic Self-Organization in a Line-Tied Screw Pinch*. PhD thesis, University of Wisconsin-Madison, (2015).

[28] G. Fiksel, A. F. Almagri, D. Craig, M. Iida, S. C. Prager, and J. S. Sarff. High current plasma electron emitter. *Plasma Sources Science & Technology*, **5** (1996).

[29] M. Bongard, G. Bodner, M. Burke, R. Fonck, J. Pachicano, J. Perry, C. Pierren, J. Reusch, A. Rhodes, N. Richner, C. Rodriguez Sanchez, C. Schaefer, and J. Weberski. Advancing local helicity injection for non-solenoidal tokamak startup. *Nucl. Fusion*, **59** (2019). doi:10.1088/1741-4326/ab17e3.

[30] D. Endrizzi. *The Formation of Parallel and Perpendicular Collisionless Shocks in the Big Red Ball*. PhD thesis, University of Wisconsin-Madison, (2021).

[31] D. Biskamp. Magnetic reconnection via current sheets. *The Physics of Fluids*, **29** (1986). doi:10.1063/1.865670.

[32] W. Daughton, J. Scudder, and K. Homa. Fully kinetic simulations of undriven magnetic reconnection with open boundary conditions. *Phys. Plasmas*, **13** (2006). doi:10.1063/1.2218817.

[33] N. F. Loureiro, A. A. Schekochihin, and S. C. Cowley. Instability of current sheets and formation of plasmoid chains. *Physics of Plasmas*, **14** (2007). doi:10.1063/1.2783986.

[34] W. Daughton, V. Roytershteyn, H. Karimabadi, L. Yin, B. J. Albright, B. Bergen, and K. J. Bowers. Role of electron physics in the development of turbulent magnetic reconnection in collisionless plasmas. *NATURE PHYSICS*, **7** (2011). doi:10.1038/NPHYS1965.

[35] S. Dorfman, H. Ji, M. Yamada, J. Yoo, E. Lawrence, C. Myers, and T. D. Tharp. Three-dimensional, impulsive magnetic reconnection in a laboratory plasma. *Geophysical Research Letters*, **40** (2013). doi:https://doi.org/10.1029/2012GL054574.

[36] W. Gekelman and H. Pfister. Experimental observations of the tearing of an electron current sheet. *The Physics of Fluids*, **31** (1988). doi:10.1063/1.866650.

[37] W. Gekelman, P. Pribyl, Z. Lucky, M. Drandell, D. Leneman, J. Maggs, S. Vincena, B. Van Compernolle, S. K. P. Tripathi, G. Morales, T. A. Carter, Y. Wang, and T. DeHaas. The upgraded large plasma device, a machine for studying frontier basic plasma physics. *Review of Scientific Instruments*, **87** (2016). doi:10.1063/1.4941079.

[38] G. I. Taylor. The spectrum of turbulence. *Proceedings of the Royal Society of London. Series A - Mathematical and Physical Sciences*, **164** (1938). doi:10.1098/rspa.1938.0032.

[39] J. Yoo and M. Yamada. Experimental evaluation of common spacecraft data analysis techniques for reconnection region analysis in a laboratory plasma. *Journal of Geophysical Research: Space Physics*, **117** (2012). doi:https://doi.org/10.1029/2012JA017742.

[40] A. Lê. *Electron Equations of State During Magnetic Reconnection*. PhD thesis, Massachusetts Institute of Technology, (2012).

[41] W. Daughton, T. Nakamura, H. Karimabadi, V. Roytershteyn, and B. Loring. Computing the reconnection rate in turbulent kinetic layers by using electron mixing to identify topology. *Phys. Plasmas*, **21** (2014).

[42] A. Lê, J. Egedal, O. Ohia, W. Daughton, H. Karimabadi, and V. S. Lukin. Regimes of the Electron Diffusion Region in Magnetic Reconnection. *Phys. Rev. Lett.*, **110** (2013). doi:10.1103/PhysRevLett.110.135004.

[43] A. Lê, W. Daughton, O. Ohia, L. J. Chen, Y. H. Liu, S. Wang, W. D. Nystrom, and R. Bird. Drift turbulence, particle transport, and anomalous dissipation at the reconnecting magnetopause. *Phys. Plasmas*, **25** (2018). doi:10.1063/1.5027086.

[44] K. Bowers, B. Albright, L. Yin, W. Daughton, V. Roytershteyn, B. Bergen, and T. Kwan. Advances in petascale kinetic plasma simulation with VPIC and Roadrunner. *Journal of Physics: Conference Series*, **180** (2009).

[45] W. Daughton, V. Roytershteyn, B. J. Albright, H. Karimabadi, L. Yin, and K. J. Bowers. Influence of coulomb collisions on the structure of reconnection layers. *Physics of Plasmas*, **16** (2009). doi:10.1063/1.3191718.

[46] W. Daughton, A. Stanier, A. Le, S. Greess, J. Egedal, J. Jara-Almonte, and H. Ji. High fidelity kinetic modeling of magnetic reconnection in laboratory plasmas. In *APS Meeting Abstracts*, page CP11.023, (2018).

[47] L. Yin, B. J. Albright, B. M. Hegelich, K. J. Bowers, K. A. Flippo, T. J. T. Kwan, and J. C. Fernández. Monoenergetic and gev ion acceleration from the laser breakout afterburner using ultrathin targets. *Physics of Plasmas*, **14** (2007). doi:10.1063/1.2436857.

[48] E. Lichko. *Magnetic pumping as a source of particle heating*. PhD thesis, University of Wisconsin-Madison, (2020).

[49] K. J. Bowers, B. J. Albright, L. Yin, B. Bergen, and T. J. T. Kwan. Ultrahigh performance three-dimensional electromagnetic relativistic kinetic plasma simulation. *Physics of Plasmas*, **15** (2008). doi:10.1063/1.2840133.

[50] P. Pritchett. Geospace environment modeling magnetic reconnection challenge: Simulations with a full particle electromagnetic code. *J. Geophys. Res.*, **106** (2001).

[51] T. Takizuka and H. Abe. A binary collision model for plasma simulation with a particle code. *Journal of computational physics*, **25** (1977).

[52] J. Egedal, J. Ng, A. Lê, W. Daughton, B. Wetherton, J. Dorelli, D. Gershman, and A. Rager. Pressure tensor elements breaking the frozen-in law during reconnection in earth's magnetotail. *Phys. Rev. Lett.*, **123** (2019). doi:10.1103/PhysRevLett.123.225101.

[53] V. M. Vasyliunas. Theoretical models of magnetic field line merging. *Reviews of Geophysics*, **13** (1975). doi:10.1029/RG013i001p00303.

[54] K. Papadopoulos. A review of anomalous resistivity for the ionosphere. *Reviews of Geophysics*, **15** (1977). doi:10.1029/RG015i001p00113.

[55] J. D. Huba, N. T. Gladd, and K. Papadopoulos. The lower-hybrid-drift instability as a source of anomalous resistivity for magnetic field line reconnection. *Geophysical Research Letters*, **4** (1977). doi:10.1029/GL004i003p00125.

[56] M. Hoshino. Forced magnetic reconnection in a plasma sheet with localized resistivity profile excited by lower hybrid drift type instability. *Journal of Geophysical Research: Space Physics*, **96** (1991). doi:10.1029/91JA00984.

[57] I. Silin, J. Büchner, and A. Vaivads. Anomalous resistivity due to nonlinear lower-hybrid drift waves. *Physics of Plasmas*, **12** (2005). doi:10.1063/1.1927096.

[58] H. Che, J. F. Drake, and M. Swisdak. A current filamentation mechanism for breaking magnetic field lines during reconnection. *Nature*, **474** (2011). doi:10.1038/nature10091.

[59] P. A. Muñoz, J. Büchner, and P. Kilian. Turbulent transport in 2d collisionless guide field reconnection. *Physics of Plasmas*, **24** (2017). doi:10.1063/1.4975086.

[60] Y.-H. Liu, W. Daughton, H. Karimabadi, H. Li, and V. Roytershteyn. Bifurcated structure of the electron diffusion region in three-dimensional magnetic reconnection. *Phys. Rev. Lett.*, **110** (2013). doi:10.1103/PhysRevLett.110.265004.

[61] V. Roytershteyn, W. Daughton, H. Karimabadi, and F. S. Mozer. Influence of the lower-hybrid drift instability on magnetic reconnection in asymmetric configurations. *Phys. Rev. Lett.*, **108** (2012).

[62] M. Hesse, Y.-H. Liu, L.-J. Chen, N. Bessho, S. Wang, J. L. Burch, T. Moretto, C. Norgren, K. J. Genestreti, T. D. Phan, and P. Tenfjord. The physical foundation of the reconnection electric field. *Physics of Plasmas*, **25** (2018). doi:10.1063/1.5021461.

[63] T. Speiser. Particle trajectories in model current sheets .i. analytical solutions. *J. Geophys. Res.*, **70** (1965).

[64] L. R. Lyons and D. C. Pridmore-Brown. Force balance near an x line in a collisionless plasma. *Journal of Geophysical Research: Space Physics*, **95** (1990). doi:10.1029/JA095iA12p20903.

[65] R. Horiuchi and T. Sato. Particle simulation study of driven magnetic reconnection in a collisionless plasma. *Physics of Plasmas*, **1** (1994).

[66] H.-J. Cai and L. Lee. The generalized ohm's law in collisionless magnetic reconnection. *Phys. Plasmas*, **4** (1997).

[67] M. M. Kuznetsova, M. Hesse, and D. Winske. Kinetic quasi-viscous and bulk flow inertia effects in collisionless magnetotail reconnection. *J. Geophys. Res.*, **103** (1998).

[68] V. Roytershteyn, S. Dorfman, W. Daughton, H. Ji, M. Yamada, and H. Karimabadi. Electromagnetic instability of thin reconnection layers: Comparison of three-dimensional simulations with MRX observations. *Physics of Plasmas*, (2013). doi:10.1063/1.4811371.

[69] R. B. Torbert, J. L. Burch, T. D. Phan, M. Hesse, M. R. Argall, J. Shuster, R. E. Ergun, L. Alm, R. Nakamura, K. J. Genestreti, D. J. Gershman, W. R. Paterson, D. L. Turner, I. Cohen, B. L. Giles, C. J. Pollock, S. Wang, L.-J. Chen, J. E. Stawarz, J. P. Eastwood, K. J. Hwang, C. Farrugia, I. Dors, H. Vaith, C. Mouikis, A. Ardakani, B. H. Mauk, S. A. Fuselier, C. T. Russell, R. J. Strangeway, T. E. Moore, J. F. Drake, M. A. Shay, Y. V. Khotyaintsev, P.-A. Lindqvist, W. Baumjohann, F. D. Wilder, N. Ahmadi, J. C. Dorelli, L. A. Avanov, M. Oka, D. N. Baker, J. F. Fennell, J. B. Blake, A. N. Jaynes, O. Le Contel, S. M. Petrinec, B. Lavraud, and Y. Saito. Electron-scale dynamics of the diffusion region during symmetric magnetic reconnection in space. *Science*, (2018). doi:10.1126/science.aat2998.

[70] K. J. Genestreti, T. K. M. Nakamura, R. Nakamura, R. E. Denton, R. B. Torbert, J. L. Burch, F. Plaschke, S. A. Fuselier, R. E. Ergun, B. L. Giles, and C. T. Russell. How accurately can we measure the reconnection rate em for the mms diffusion region event of 11 july 2017? *Journal of Geophysical Research: Space Physics*, **123** (2018). doi:https://doi.org/10.1029/2018JA025711.

[71] T. K. M. Nakamura, K. J. Genestreti, Y.-H. Liu, R. Nakamura, W.-L. Teh, H. Hasegawa, W. Daughton, M. Hesse, R. B. Torbert, J. L. Burch, and B. L. Giles. Measurement of the magnetic reconnection rate in the earth's magnetotail. *Journal of Geophysical Research: Space Physics*, **123** (2018). doi:https://doi.org/10.1029/2018JA025713.

[72] J. L. Burch, R. B. Torbert, T. D. Phan, L.-J. Chen, T. E. Moore, R. E. Ergun, J. P. Eastwood, D. J. Gershman, P. A. Cassak, M. R. Argall, S. Wang, M. Hesse, C. J. Pollock, B. L. Giles, R. Nakamura, B. H. Mauk, S. A. Fuselier, C. T. Russell, R. J. Strangeway, J. F. Drake, M. A. Shay, Y. V. Khotyaintsev, P.-A. Lindqvist, G. Marklund, F. D. Wilder, D. T. Young, K. Torkar, J. Goldstein, J. C. Dorelli, L. A. Avanov, M. Oka, D. N. Baker, A. N. Jaynes, K. A. Goodrich, I. J. Cohen, D. L. Turner, J. F. Fennell, J. B. Blake, J. Clemmons, M. Goldman, D. Newman, S. M. Petrinec, K. J. Trattner, B. Lavraud, P. H. Reiff, W. Baumjohann, W. Magnes, M. Steller, W. Lewis, Y. Saito, V. Coffey, and M. Chandler. Electron-scale measurements of magnetic reconnection in space. *Science*, **352** (2016). doi:10.1126/science.aaf2939.

[73] R. B. Torbert, J. L. Burch, B. L. Giles, D. Gershman, C. J. Pollock, J. Dorelli, L. Avanov, M. R. Argall, J. Shuster, R. J. Strangeway, C. T. Russell, R. E. Ergun, F. D. Wilder, K. Goodrich, H. A. Faith, C. J. Farrugia, P. A. Lindqvist, T. Phan, Y. Khotyaintsev, T. E. Moore, G. Marklund, W. Daughton, W. Magnes, C. A. Kletzing, and S. Bounds. Estimates of terms in Ohm's law during an encounter with an electron diffusion region. *Geophy. Res. Lett.*, **43** (2016). doi:10.1002/2016GL069553.

[74] J. Egedal, A. Lê, W. Daughton, B. Wetherton, P. A. Cassak, J. L. Burch, B. Lavraud, J. Dorelli, D. J. Gershman, and L. A. Avanov. Spacecraft Observations of Oblique Electron Beams Breaking the Frozen-In Law During Asymmetric Reconnection. *Phys. Rev. Lett.*, **120** (2018). doi:10.1103/PhysRevLett.120.055101.

[75] H. Ji, Y. Ren, M. Yamada, S. Dorfman, W. Daughton, and S. P. Gerhardt. New insights into dissipation in the electron layer during magnetic reconnection. *Geophysical Research Letters*, (2008). doi:10.1029/2008GL034538.

[76] S. Dorfman, W. Daughton, V. Roytershteyn, H. Ji, Y. Ren, and M. Yamada. Two-dimensional fully kinetic simulations of driven magnetic reconnection with boundary conditions relevant to the magnetic reconnection experiment. *Physics of Plasmas*, **15** (2008). doi:10.1063/1.2991361.

[77] V. Roytershteyn, W. Daughton, S. Dorfman, Y. Ren, H. Ji, M. Yamada, H. Karimabadi, L. Yin, B. Albright, and K. Bowers. Driven magnetic reconnection near the dreicer limit. *Physics of Plasmas*, **17** (2010). doi:10.1063/1.3399787.

[78] Bowers. Vpic source code - version 1.1, (2020).

[79] A. Lê, W. Daughton, L. J. Chen, and J. Egedal. Enhanced electron mixing and heating in 3-D asymmetric reconnection at the Earth's magnetopause. *Geophy. Res. Lett.*, **44** (2017). doi:10.1002/2017GL072522.

[80] W. Daughton. Electromagnetic properties of the lower-hybrid drift instability in a thin current sheet. *Phys. Plasmas*, **10** (2003). doi:10.1063/1.1594724.

[81] R. C. Davidson, N. T. Gladd, C. S. Wu, and J. D. Huba. Effects of finite plasma beta on the lower-hybrid-drift instability. *The Physics of Fluids*, **20** (1977). doi:10.1063/1.861867.

[82] L. Price, M. Swisdak, J. F. Drake, J. L. Burch, P. A. Cassak, and R. E. Ergun. Turbulence in Three-Dimensional Simulations of Magnetopause Reconnection. *Journal of Geophysical Research: Space Physics*, **122** (2017). doi:10.1002/2017JA024227.

[83] E. N. Parker. Sweet's mechanism for merging magnetic fields in conducting fluids. *J. Geophys. Res.*, **62** (1957).

[84] R. Nakamura, K. J. Genestreti, T. Nakamura, W. Baumjohann, A. Varsani, T. Nagai, N. Bessho, J. L. Burch, R. E. Denton, J. P. Eastwood, R. E. Ergun, D. J. Gershman, B. L. Giles, H. Hasegawa, M. Hesse, P.-A. Lindqvist, C. T. Russell, J. E. Stawarz, R. J. Strangeway, and R. B. Torbert. Structure of the current sheet in the 11 july 2017 electron diffusion region event. *Journal of Geophysical Research: Space Physics*, **124** (2019). doi:https://doi.org/10.1029/2018JA026028.

[85] M. Hesse and J. Birn. Parallel electric fields as acceleration mechanisms in three-dimensional magnetic reconnection. *Advances in Space Research*, **13** (1993). doi:https://doi.org/10.1016/0273-1177(93)90341-8.

[86] H. Ji, W. Daughton, J. Jara-Almonte, A. Le, A. Stanier, and J. Yoo. Magnetic reconnection in the era of exascale computing and multiscale experiments. *Nature Reviews Physics*, **4** (2022). doi:10.1038/s42254-021-00419-x.

[87] T. D. Phan, J. P. Eastwood, M. A. Shay, J. F. Drake, B. U. O. Sonnerup, M. Fujimoto, P. A. Cassak, M. Øieroset, J. L. Burch, R. B. Torbert, A. C. Rager, J. C. Dorelli, D. J. Gershman, C. Pollock, P. S. Pyakurel, C. C. Haggerty, Y. Khotyaintsev, B. Lavraud, Y. Saito, M. Oka, R. E. Ergun, A. Retino, O. Le Contel, M. R. Argall, B. L. Giles, T. E. Moore, F. D. Wilder, R. J. Strangeway, C. T. Russell, P. A. Lindqvist, and W. Magnes. Electron magnetic reconnection without ion coupling in earth's turbulent magnetosheath. *Nature (London)*, **557** (2018). doi:10.1038/s41586-018-0091-5.

[88] Y.-H. Liu, M. Hesse, F. Guo, W. Daughton, H. Li, P. A. Cassak, and M. A. Shay. Why does steady-state magnetic reconnection have a maximum local rate of order 0.1? *Phys. Rev. Lett.*, **118** (2017). doi:10.1103/PhysRevLett.118.085101.

[89] P. A. Cassak and M. A. Shay. Scaling of asymmetric magnetic reconnection: General theory and collisional simulations. *Phys. Plasmas*, **14** (2007). doi:10.1063/1.2795630.

[90] A. Stanier, W. Daughton, L. Chacón, H. Karimabadi, J. Ng, Y.-M. Huang, A. Hakim, and A. Bhattacharjee. Role of ion kinetic physics in the interaction of magnetic flux ropes. *Phys. Rev. Lett.*, **115** (2015). doi:10.1103/PhysRevLett.115.175004.

[91] P. Sharma Pyakurel, M. A. Shay, T. D. Phan, W. H. Matthaeus, J. F. Drake, J. M. TenBarge, C. C. Haggerty, K. G. Klein, P. A. Cassak, T. N. Parashar, M. Swisdak, and A. Chasapis. Transition from ion-coupled to electron-only reconnection: Basic physics and implications for plasma turbulence. *Physics of Plasmas*, **26** (2019). doi:10.1063/1.5090403.

[92] A. Kesich, J. Bonde, J. Egedal, et al. Magnetic flux array for spontaneous magnetic reconnection experiments. *Review of Scientific Instruments*, **79** (2008).

[93] N. A. Krall and P. C. Liewer. Low-frequency instabilities in magnetic pulses. *Phys. Rev. A*, **4** (1971). doi:10.1103/PhysRevA.4.2094.

[94] D. B. Graham, Y. V. Khotyaintsev, C. Norgren, A. Vaivads, M. André, S. Toledo-Redondo, P.-A. Lindqvist, G. T. Marklund, R. E. Ergun, W. R. Paterson, D. J. Gershman, B. L. Giles, C. J. Pollock, J. C. Dorelli, L. A. Avanov, B. Lavraud, Y. Saito, W. Magnes, C. T. Russell, R. J. Strangeway, R. B. Torbert, and J. L. Burch. Lower hybrid waves in the ion diffusion and magnetospheric inflow regions. *Journal of Geophysical Research: Space Physics*, **122** (2017). doi:https://doi.org/10.1002/2016JA023572.

[95] C. Norgren, A. Vaivads, Y. V. Khotyaintsev, and M. André. Lower hybrid drift waves: Space observations. *Phys. Rev. Lett.*, **109** (2012). doi:10.1103/PhysRevLett.109.055001.

[96] D. Biskamp. *Magnetic Reconnection in Plasmas*. Cambridge Monographs on Plasma Physics. Cambridge University Press, (2000). doi:10.1017/CBO9780511599958.

[97] D. G. Swanson. *Plasma waves.* Institute of Physics Publishing, second edition, (2003).

[98] T. H. Stix. *Waves in plasmas*. American Institute of Physics, (1992).

Appendix A

Additional TREX Probe Documentation

The purpose of this appendix is to hold information about various probes from the different TREX iterations that the author judges important enough to record but not strictly relevant to understanding the main results of this thesis. Much of this appendix, like Appendix B, is intended more as a tutorial/list of engineering notes for future graduate students who may find themselves in a similar position to the author, in the hopes that it will help inform future decisions regarding probe construction and implementation.

A.1 The Magnetic Flux Array

The main contribution to TREX 2015-2016 by the author was in the construction and maintenance of the magnetic flux array. The flux array was strongly based on the flux array design first implemented in the Versatile Toroidal Facility at MIT in the mid-2000s, as detailed in Kesich et al. [92]. Though the flux array was not a contributor to the data that forms the main work of this thesis (for reasons which will be explained in Section A.2.2), it represents a sizable amount of the author's time and was instrumental in conducting the measurements that resulted in the first TREX publication (Olson et al. [15]) and the first

TREX-based thesis (Olson [14]).

A.1.1 Motivation & Theory

In the earliest iteration of TREX, magnetic data was attained from a linear array of $\dot{B}$ pickup probes[1]. The data collected was confined to locations reachable by the probe while anchored on one of the BRB's sweep stages, and the construction of full data profiles necessitated combining data from multiple different experimental shots into a single picture. The flux array was envisioned as a method of collecting reconnection data through the entire time duration of the shot. Furthermore, its placement takes advantage of the motion of the reconnection layer down toward the central axis from underneath the drive coils. The array could sample data from the layer over (nearly) its entire transit time, rather than being limited to data collected at the layer's intersection with the linear probe array's sweep stage position. The basis of the flux array's functionality is the assumption that the TREX experimental domain is cylindrically symmetric (i.e., symmetric to rotations in the ϕ direction about the central axis). This leads to our main symmetry assumption about the magnetic field:

$$\mathbf{B_P}(R,Z) = \nabla \times A_\phi(R,Z)\hat{\phi} \tag{A.1}$$

where $\mathbf{B}$ is the magnetic field, $\mathbf{A}$ is the magnetic vector potential, the subscripts P and ϕ represent the poloidal and toroidal vector components, respectively[2], and $\hat{\phi}$ represents the unit vector in the toroidal direction. To be more specific about what is involved in reaching Eq A.1, it is assumed that the poloidal field contributions from the toroidally asymmetric poloidal currents is small, scaling as the toroidal field contributions from these same currents multiplied by the ratio of the poloidal and toroidal scale lengths [92].

[1] see Section 5.1 for more information on the theory of $\dot{B}$ pickup probes.
[2] The poloidal plane refers to the R, Z plane, as shown in Figure A.1.

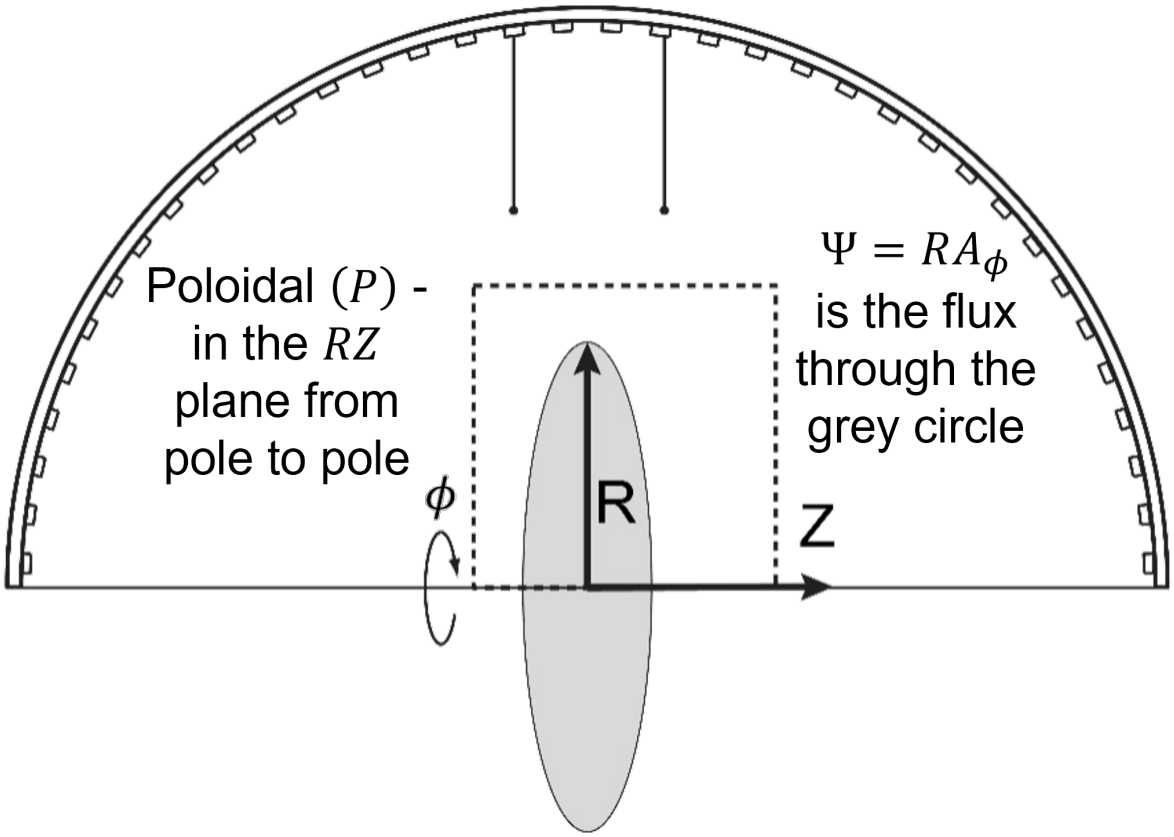

Figure A.1: The poloidal plane of the TREX experiment. The experiment is assumed to be symmetric to rotations in the ϕ (toroidal) direction about the central axis. The flux function Ψ is defined as the amount of magnetic flux through the grey circle with arbitrary radius R.

Following the establishment of Eq A.1, we can define the following relation:

$$\Psi = RA_\phi \tag{A.2}$$

where Ψ is the magnetic flux function[3]. The physical meaning of Ψ is shown in Figure A.1; it is the amount of flux through a circle coaxial with the experiment with some arbitrary radius. By plugging this into Eq A.1, the result is

$$R\mathbf{B_P} = (\nabla_{\mathbf{RZ}}\Psi) \times \hat{\phi} \tag{A.3}$$

[3]Readers may recognize this as the definition of the poloidal flux from the Grad-Shafranov Equation, save for a factor of $1/2\pi$ that varies by convention.

where $\nabla_{\mathbf{RZ}}$ represents the gradient operator without the ϕ component (e.g. only the R and Z components). Let us define the differential length in the R, Z plane between points (R_0, Z_0) and (R_1, Z_1) as $d\mathbf{l}_{\mathbf{RZ}}$. Noting the following vector identity,

$$\left([\nabla_{\mathbf{RZ}}\Psi] \times \hat{\phi}\right) \times d\mathbf{l}_{\mathbf{RZ}} = \hat{\phi}\left([\nabla_{\mathbf{RZ}}\Psi] \bullet d\mathbf{l}_{\mathbf{RZ}}\right)$$

and using the gradient theorem, we can rewrite the time derivative of Eq A.3 as the following integral:

$$\left[\dot{\Psi}(R_1, \phi_0, Z_1) - \dot{\Psi}(R_0, \phi_0, Z_0)\right]\hat{\phi} = \int_{R_0,Z_0}^{R_1,Z_1} R\dot{\mathbf{B}}_{\mathbf{P}} \times d\mathbf{l}_{\mathbf{RZ}} \tag{A.4}$$

We note that the left side was obtained by integrating over the gradient of the $\dot{\Psi}$ function. As the integrand was the gradient of a scalar function, the integral is path independent if that function is continuously differentiable over all space; this is the definition of a conservative field. Thus, if we take $\dot{\Psi}$ to be continuously differentiable over all values of R and Z, we can choose any arbitrary path between the points (R_0, Z_0) and (R_1, Z_1). Assume this to be true[4]; this allows us to select a path that goes from R_0 to R_1 and then from Z_0 to Z_1, such that the integral in Eq A.4 can be split into two separate integrals, one over R and another over Z:

$$\Delta_R\dot{\Psi} = \dot{\Psi}(R_1, Z_0) - \dot{\Psi}(R_0, Z_0) = \int_{R_0}^{R_1} R\dot{B}_Z dR \tag{A.5}$$

$$\Delta_Z\dot{\Psi} = \dot{\Psi}(R_0, Z_1) - \dot{\Psi}(R_0, Z_0) = -R\int_{Z_0}^{Z_1} \dot{B}_R dZ \tag{A.6}$$

Note that Eq A.5 can be re-written in terms of the change in flux $(\dot{\psi})$ through a loop in the $R\phi$ plane:

$$\dot{\psi} = \int_{R_0,\phi_0}^{R_1,\phi_1} R\dot{B}_Z dR d\phi = \Delta\phi\Delta_R\dot{\Psi}$$

$$\rightarrow \Delta_R\dot{\Psi} = \frac{\dot{\psi}}{\Delta\phi} \tag{A.7}$$

[4]This can be proved via Faraday's Law and knowing that the induced electric field is divergence-less.

where $\Delta\phi$ is the angular width of the loop. It is from Eqs A.5, A.6, and A.7 that the utility of the flux array becomes apparent; the spatial difference between the time change in the flux function Ψ between any two locations can be quickly constructed from a simple addition of the measured change in magnetic field through a set of properly-constructed Faraday pickup loops (e.g., $\dot{B}$ coils) with normal vectors in the $\hat{\mathbf{R}}$ and $\hat{\mathbf{Z}}$ directions. For a flux array that extends from the $R = 0$ line (where $\Psi = 0$ always) and begins taking measurements before the experiment begins, the entire flux function at any point covered by the flux array can be calculated [92]. These requirements motivated the design of the flux array, which is presented in Figure A.2. The array consists of 8 rows of 16 cells each; the cells are trapezoidal, saved for the lowest one (cell 1) which is triangular. This shape scheme allows each row of the array to narrow to a point; when all these endpoints are aligned, they can be placed along the $R = 0$ axis to guarantee that values for Ψ constructed from the bottom of the array always start from a point where $\Psi = 0$. Furthermore, each cell in the array has the same angular width, $\Delta\ \phi = 4.5°$. The array also included two horizontal rows of rectangular cells with normal vectors in the $\hat{\mathbf{R}}$ direction (not shown in Figure A.2), such that Eq A.6 can be utilized if any of the lower cells are broken; the flux from the cell in one row that is level with the horizontal cells is equivalent to the flux through the corresponding cell in the adjacent row added to the flux through the horizontal cell between them.

Once the signals from the array are collected, much of the electromagnetic information relevant to the reconnection process becomes readily available:

$$\Psi = \int_0^t \dot{\Psi} dt \qquad \mathbf{A} = A_\phi \hat{\phi} = \frac{\Psi}{R}\hat{\phi}$$

$$B_R = -\frac{1}{R}\frac{\partial \Psi}{\partial Z} \qquad B_Z = \frac{1}{R}\frac{\partial \Psi}{\partial R}$$

$$\mu_0 J_\phi = -\frac{1}{R}\frac{\partial^2 \Psi}{\partial Z^2} - \frac{\partial}{\partial R}\left[\frac{1}{R}\frac{\partial \Psi}{\partial R}\right]$$

$$E_{rec} = -\frac{\dot{\Psi}}{R} \qquad \mathbf{B}_P \bullet \nabla\Psi = 0$$

where E_{rec} is the reconnection electric field, otherwise known as the absolute reconnection

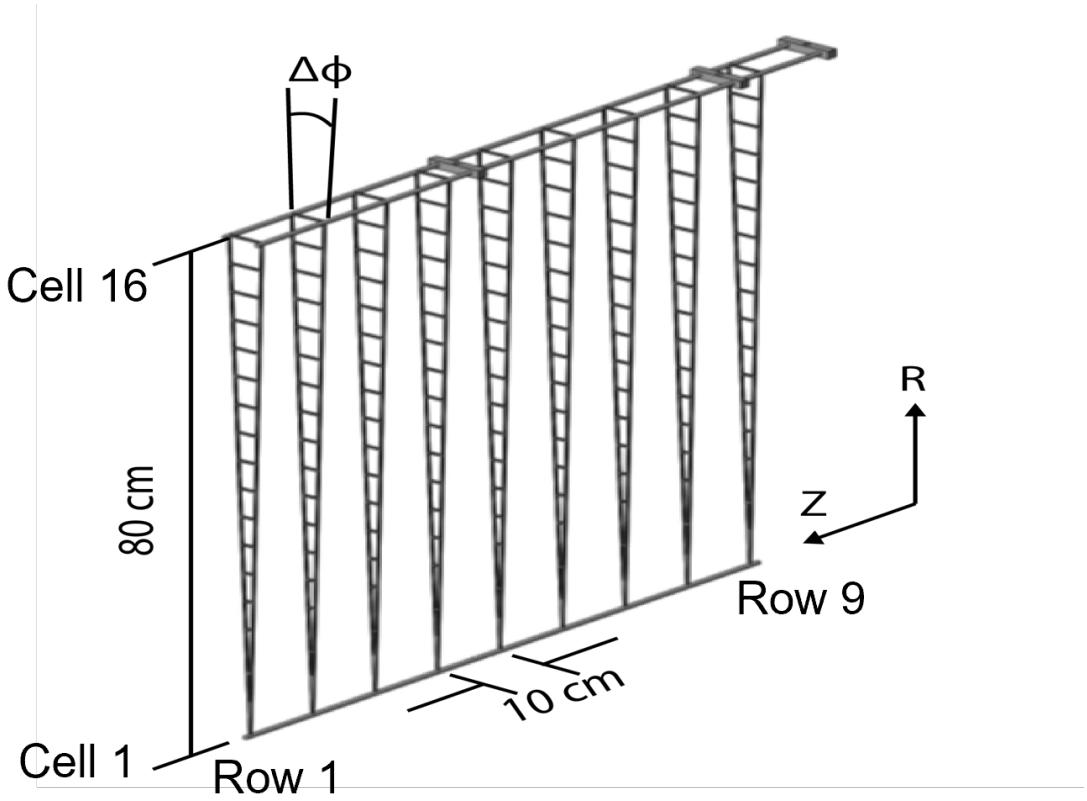

Figure A.2: Basic flux array design for the 2015-2016 runs. The two horizontal loop rows are not shown. Partially reproduced from Olson [14].

rate. The last equation in this group indicates that Ψ is constant along the direction of $\mathbf{B}_P$ at any given location, meaning that contours of Ψ will map to the poloidal magnetic field lines. Note that some authors use a different definition for Ψ that includes an additional factor of 2π ($\Psi = 2\pi R A_\phi$).

A.1.2 Construction

The 2015 flux array was hand-wound from 0.003 and 0.004 inch diameter HML-coated magnet wire. A sketch of an individual row of the flux array was used to create a frame made of pins stuck into a wooden plank; the wires were wound around these pins to form each of the cells. After an individual cell was wound, the wire leads (long enough to reach from the cell to the top of the array and then along the array's anchor to the BRB wall and out of the

vacuum to the breakout boards) was hand-twisted into a twisted pair. Cells had different numbers of windings based on the relative size of the cell; smaller cells (toward the bottom of the array) had more windings that larger cells (at the top). After winding was completed for a layer, the wires were coated in an ethanol-thinned Torr Seal[5] mixture, which acted as a vacuum-safe glue. Two photographs of the array are shown in Figure A.3.

After drying, the wire row was removed from the frame and tied to the ceramic rods that supported the full array. One ceramic rod at the bottom of the array kept all the rows weighted down and convergent to a single axis; two ceramic rods at the top kept the arrays fixed in place and were attached to a steel bar that anchored the array to the wall of the BRB. The two rectangular rows made to measure contributions from Eq A.6 were wound separately and eventually thread-ed through the regular array rows. The leads from each cell of the array were sealed into a feed-through with Torr Seal before exiting the vacuum vessel, where they were soldered into breakout boards and sent into the TREX digitizers. While the Torr Sealed feed-through was an effective way to get the wires out of the vacuum without causing a leak, it represented a potential single point of failure for the entire array system; a break in the (extremely brittle) Torr Sealed wires at this point would destroy the array's functionality. It also meant that if one row of the array failed, it could not be replaced individually- repairing the array would have to be an all-or-nothing process once the wire feed-through was sealed. These issues will be relevant in the next TREX iteration.

A.1.3 Raw Data

An example of raw data from three rows of the flux array is shown in Figure A.4. In the three rows shown, the signal spike corresponding to the reconnection layer is shown appearing in cells at lower values of R later in time than in cells are higher R values; this is indicative of the layer moving down the array from Cell 16 down toward Cell 1 as time passes. To see an example of data obtained from the flux array after processing, see Figure 3.4 in Section 3.2.1.

[5]Also known as Hysol-1C or Loctite 9492, depending on brand type or region of manufacture.

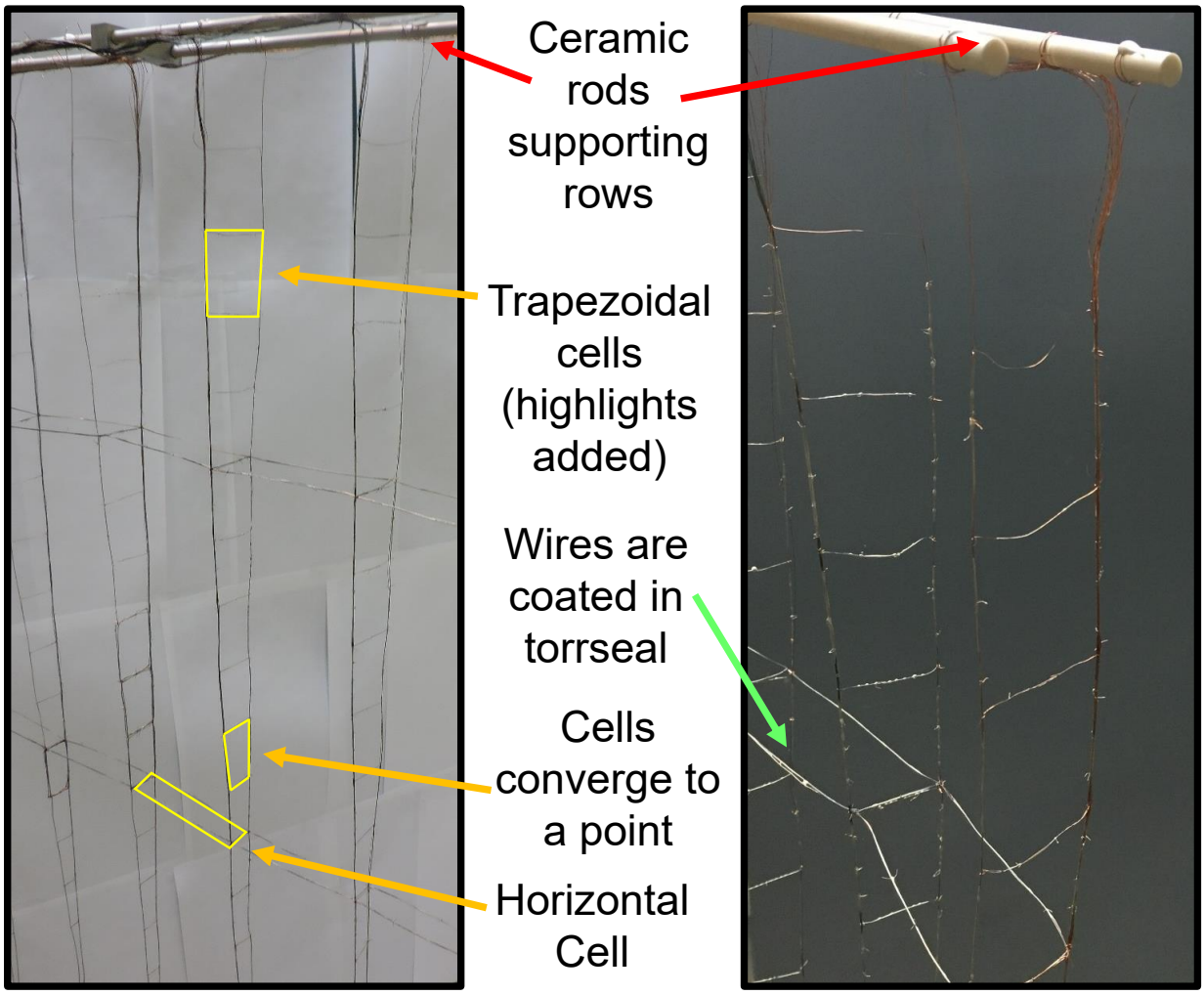

Figure A.3: Two pictures showing portions of the completed flux array from different angles. Because of the nature of the array's construction (e.g., it's wound from thin wires), the array can be difficult to see and photograph. Several cells have been highlighted to make the general cell shape clear. The wires are coated in a thinned Torr Seal and ethanol mixture, which acts as a vacuum-safe glue. The flux array was supported by two ceramic rods that were held at a fixed distance apart by a series of metal braces.

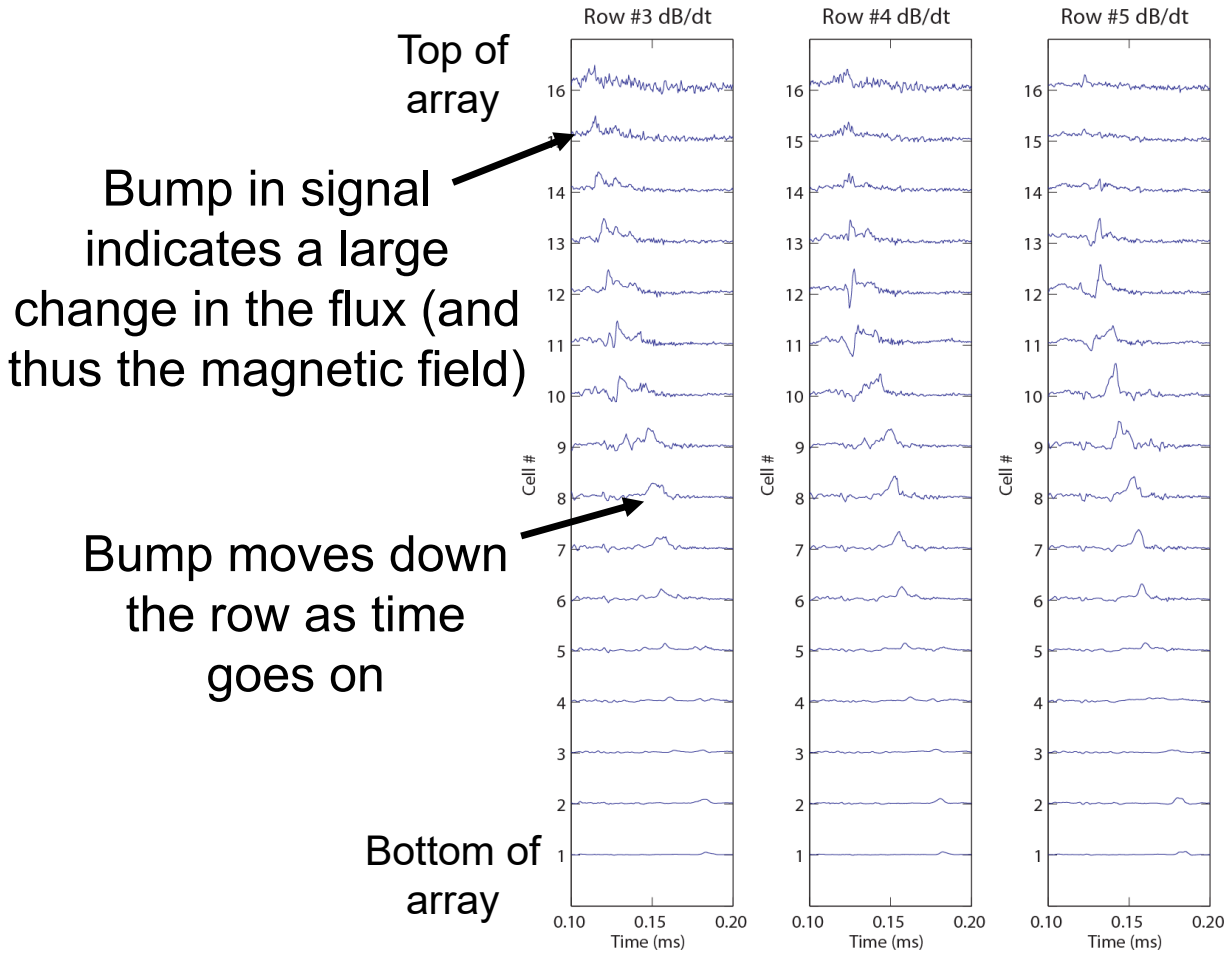

Figure A.4: Example of a reconnection pulse recorded by the flux array. Here, three adjacent rows of the array show how the reconnection layer moves down from the top of the array (Cell 16) to the bottom of the array (Cell 1). These are the raw $\dot{B}$ signals that the array sends into its digitizer channels.

A.1.4 Necessary Engineering Improvements

In addition to the plasmoid measurement considerations discussed in Section 3.3, there were several design and construction considerations that needed to be addressed when evaluating the utility of the flux array going forward. While the array was an extremely successful magnetic probe that showed clear evidence of plasmoid formation in the TREX current layers, it was ultimately a collection of thin, fragile wires that were repeatedly placed in

a high-temperature (though extremely fleeting) plasma environment; inevitably, different wires in the array broke or had their insulation burned away, putting them in electrical contact with the plasma and rendering any change in flux measurements unreadable. The Torr Seal used to bind the wires and seal them in the vacuum feedthrough rendered them both inseparable and brittle, making the cells both more vulnerable to physical damage and incapable of being replaced on an individual basis. As such, the next flux array would ideally be stronger, more completely insulated from the plasma, and repairable on a row-by-row or even a cell-by-cell basis.

A.2 Second Magnetic Flux Array

The second iteration of the magnetic flux array was redesigned with the aim of improving its hardiness and repairability. The main design upgrade was the addition of custom-manufactured stainless steel shields which were meant to enclose the array wires to protect them from the plasma and increase their durability. These shields (parts of which are viewable in Figure A.5) were fabricated in rows of 16 cells each, where each cell subtended a different toroidal angle (as opposed to the single angular value shared by all the cells in the first generation flux array) and included an additional set of 8 rectangular cells that were meant to be bent 60° from the rest of the array to pick up changes in the B_ϕ component of the field. The shields had small gaps in each cell, such that image currents would not be able to form in the shielding and screen out the changing fields from the plasma; these gaps would be covered with DuPont™ Kapton® tape[6] after the row was assembled to protect this small length of exposed wire.

These shields were cut by laser from thin stainless steel sheet metal in separate pieces that had to be spot-welded together before construction could proceed. Additionally, indentations had to be pressed into the shield metal to create channels that would hold the array's wires,

[6] DuPont™ and Kapton® are trademarks or registered trademarks of E.I. du Pont de Nemours and Company.

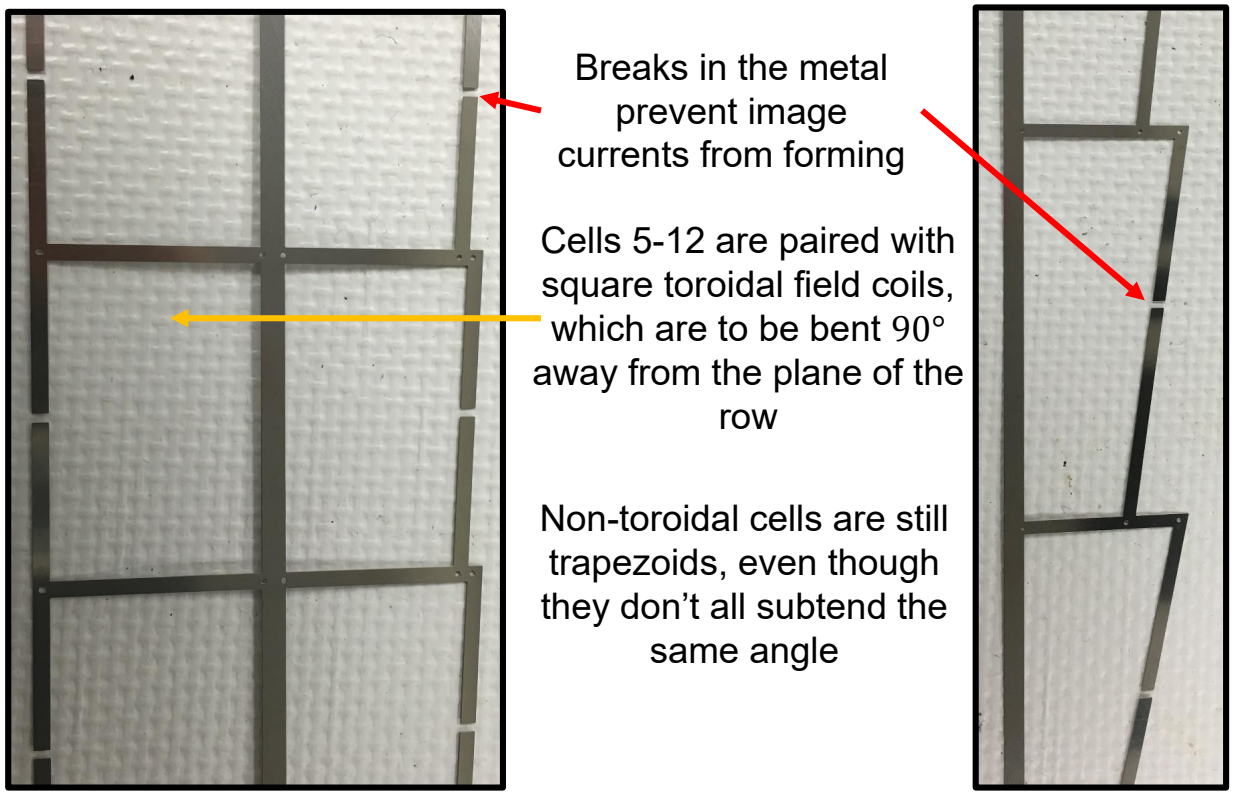

Figure A.5: The stainless steel shields manufactured for use on the second flux array. Ideally, the array wires would be wound on top of one shield (using pins inserted into the holes at the corner of each cell) and then a second shield would be placed on top to provide a barrier between the wires and the plasma. Gaps in the shields were used to prevent the formation of image currents that could screen out the signals from the plasma; the gaps were meant to be covered in small pieces of (insulating) Kapton® tape. The shields also include spaces for coils that were to be bent °90 after being wound to allow them to measure changes in the toroidal magnetic field. Note that while all the cells in a row no longer line up to form a single triangle, their shapes still point toward the central axis and the angles each cell subtends is known (clearly, different cells will have different angle values depending on their shape and how far away they are from the bottom of the row).

to ensure that they were completely enclosed inside the shielding. To do this, a custom steel mold was created that could be loaded with a single shield piece held in place using a series of alignment pins and then squeezed with a hydraulic press. This press is shown in Figure A.6. After the pressing and spot-welding processes, the shield pieces were anchored to a wooden board using pins placed through the pre-machined holes in the corners of each cell of the shield. These pins where then used to shape the wire as it was hand-wound into the cells, similar to the process with the first array. Finally, a second shield piece would be placed on top of the first shield and the now completed wires and the entire row was sealed shut. Several different sealing methods were attempted, including Torr Seal, solder, spot-welding, and sewing the shields together with wire.

A.2.1 Vacuum Interface

After the shields, the next biggest upgrade to the array was the design and creation of a custom multi-channel vacuum interface, which is shown in Figure A.7. In the first array, all the wires were Torr Seal-ed into a single vacuum feedthrough, which while effective acted as a potential single-point failure and precluded the array from being repaired on a row-by-row basis rather than having to be rebuilt completely from scratch. The new flange design was intended to address both of these issues by assigning each row of the array to its own separate individual feedthrough. These individual feedthroughs were able to be removed from the entire flange design independently of one another, and thus gave the same flexibility in movement to individual rows of the array relative to the entire probe.

A.2.2 Difficulties

The best laid plans of grads. and profs. often go awry[7]. Contrary to our intentions regarding the flux array upgrades, in practice the entire process was unsuccessful- every major upgrade

[7]With apologies to Robert Burns.

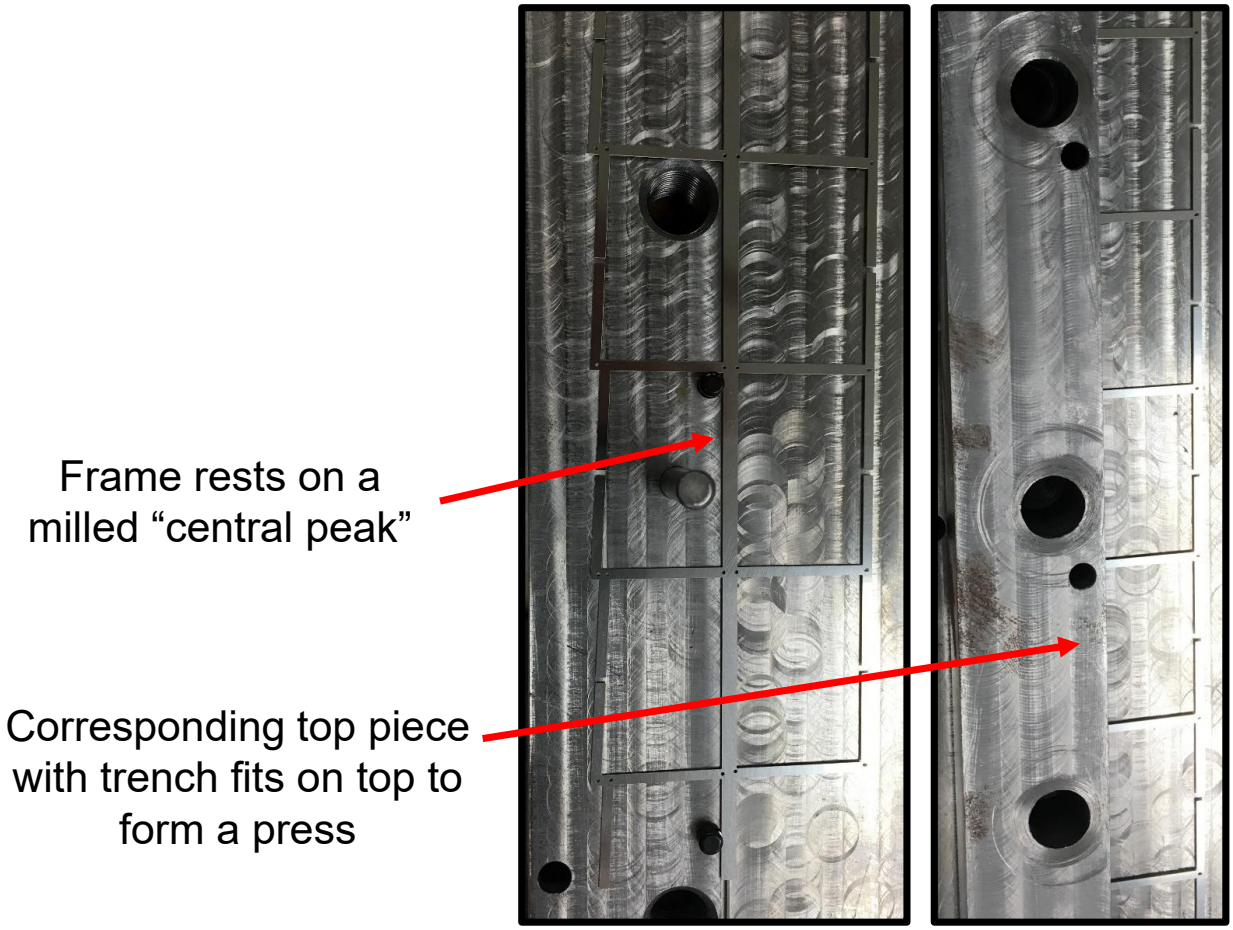

Figure A.6: Milled steel press used to bend channels into the stainless steel shields. These channels provided space for the wires to travel along each row's central shield piece. Each shield had to be aligned in the mold using alignment pins and then compressed in a hydraulic press. Half the shield pieces were pressed in one direction while the other half were pressed in the opposite direction to maximize the size of the central wire channel when the two opposing shield pieces were sealed together.

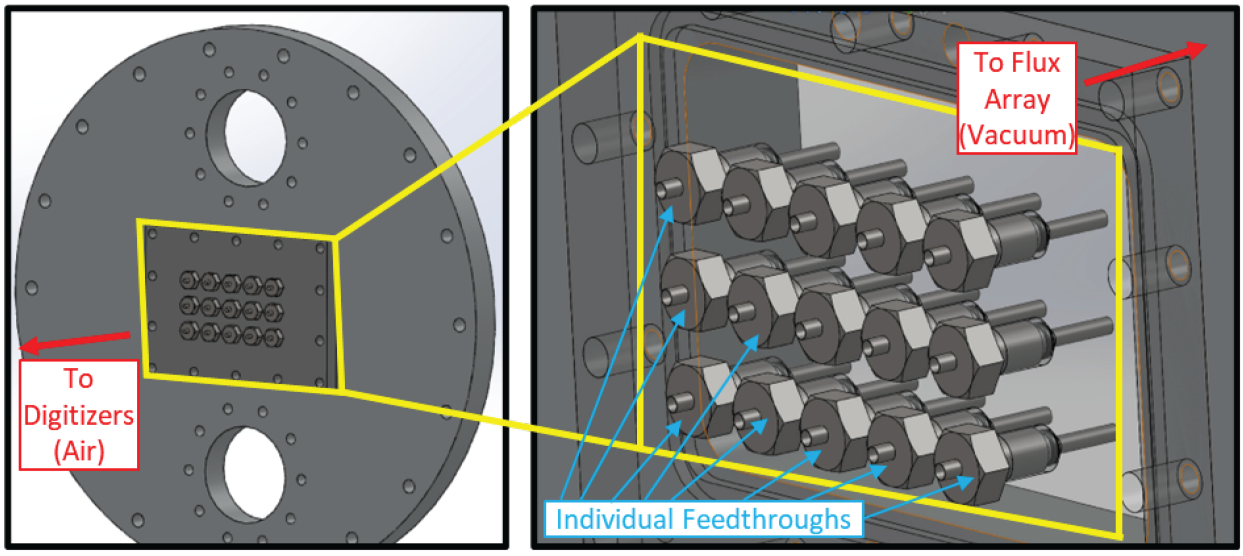

Figure A.7: The flange designed for the second flux array. Instead of one vacuum seal that contains all the wires, this flange had multiple separate vacuum seals for each row of the array, such that one array row could theoretically be removed and replaced without breaking the feedthroughs of the other rows.

change contributed to the second generation flux array being worse than its predecessor in basically every way[8].

First of all, while the stainless steel shields may have increased the durability of the array cells once they were constructed, the construction process itself was a significant danger to the integrity of the wires. Like the previous array, pins were used to provide a frame on which the coils were wound; in this case, the pins also functioned as anchors for the bottom shield layers and an alignment guide for the top shield layer when it was placed over the completed coils. These pins were supposed to be removed from each row after they were assembled, but the removal process was usually more difficult than anticipated and the wires were often broken in the act. Attempts to seal the shields together generally fell into two categories: ineffective and actively damaging. Soldering the shields together with the wires inside them produced a well-sealed array but could melt the insulation off the wires, shorting

[8]The reader may ask, "then why include it in this dissertation?". May the issues described here serve as a warning to any related future attempts at probe construction, especially those that take more than half a year and several thousand dollars to complete.

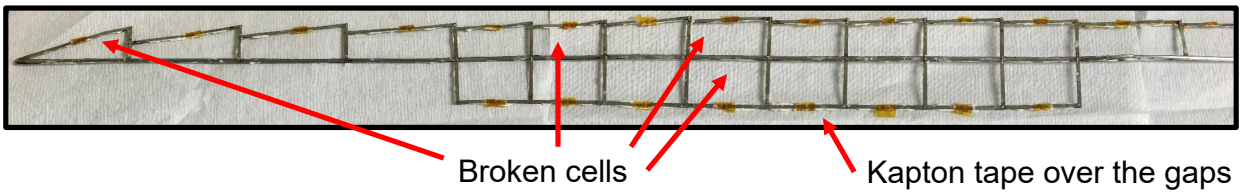

Figure A.8: The stainless steel shields for the second flux array proved to be extremely cumbersome. Shown here is one of the completed rows. In addition to the three broken cells in the main row, it was found to be impossible to bend the toroidal coils into their designated positions without breaking most if not all of the wires. Eventually all the toroidal cells had to be cut off of the shields. While the row shown in this picture has comparatively few broken cells compared to others in the construction process, the break in the bottom-most cell renders the utility of this row questionable at best. Also shown are the Kapton® tape pieces mentioned in Figure A.5.

them to the shielding and, when applicable, the ambient plasma- this was one of the main issues the shields were created to avoid. The shields themselves were made to be thin enough to cause minimal disruption to the plasma environment, but in practice this meant that they were easily warped by forces and torques applied in the construction process, which added another mechanism for creating wire breaks. Most egregiously, attempts to bend the toroidal coils into place after the row construction was finished often caused all them coils, if not the entire array row, to shatter. Eventually it was decided that the toroidal cells would need to be cut off the shielding before construction began. A "complete" row is shown in Figure A.8; this row has three broken cells, which is comparatively low but far worse than the success rate of row construction for the first array.

Even worse was the total failure of the new flux array flange. The original potential single point of failure was replaced with multiple independent points of failure. The flange, whether through incompetence on the part of the author or through damage after its initial successful vacuum testing[9], was completely incapable as acting as a vacuum-sealed interface. The separate feedthroughs were so closely spaced that it became impossible to identify individual leaks; the entire arrangement had to be treated as porous and an *ad hoc* miniature vacuum drum with its own set of permanently sealed feedthroughs had to be fitted over the faceplate

[9]Hopefully the latter.

Figure A.9: Two examples that came out of the extended prototyping and testing of $\dot{B}$ probes during TREX's 2017 run. Both examples are made from carved LEGO pieces and hand-wound with magnetic wire. The prototype in the top picture shows early attempts at impedance-matching the probes, in this case by connecting the probe leads to resistors that have been glued to a scrap piece of phenolic. Lessons learned from these probe construction experiments went into the development of the standardized $\dot{B}$ probes used in TREX 2018.

of the array flange[10]. To add insult to injury, the process of attempting to repair the leaks led to several of the feedthroughs and their wires breaking, rendering entire rows of the array inoperable.

A.3 2017 Bdot Probe Prototypes

Despite large time periods spent attempting first to repair the flux array and then to obtain meaningful data out of the functional parts of it, it was barely functional as a probe in its own right and an almost total failure as an improvement over the first. Use of the array was eventually abandoned in favor of the creation of linear $\dot{B}$ probe arrays. Two examples of these are shown in Figure A.9.

The 2017 $\dot{B}$ probes went through several iterations, starting with a single individually-wound triplet and eventually progressing to rows probes hand-wound around hand-carved

[10]It was extremely fortunate that this pre-made feedthrough was available after being salvaged from the VTF experiment at MIT.

LEGO® pieces[11]. These 2017 $\dot{B}$ probes were essentially prototypes of the final standardized probe design that was used all through TREX 2018[12]. For this reason, an extended discussion of the theory of $\dot{B}$ probes will be included in the next chapter, specifically in Section 5.1.

While design considerations for the TREX 2018 $\dot{B}$ probes were the main takeaways from the 2017 $\dot{B}$ probes, they also provided a preliminary picture of the reconnection geometry of the new TREX drive coil setup. One example of this is shown in Figure A.10, which displays processed 2017 $\dot{B}$ data from a Hydrogen plasma shot. This data verified the existence of the Hall fields, provided an initial estimation of the width of the reconnection current layers, and resulted in a good understanding of how fast the layer was preceding down from below the coils toward the BRB's central axis. Speeds in excess of 50 $\mathrm{km\,s^{-1}}$, in conjunction of the layer width estimates, provided a good starting point in understanding the spatial and temporal resolution requirements of the next $\dot{B}$ design. Again, these new designs are covered in detail in Section 5.1.

A.4 2018 Temperature Probe Raw Data Examples

As stated in Section 5.2, the process of operating the T_e probe during an experiment is nontrivial[13]. The data recorded by the probe must be monitored through the run to ensure that it is valid; in addition to a potential malfunction, it is entirely possible for the probe to report measurements that appear valid but are in fact unreliable due one or more aspects of the probe being run in a way that violates the assumptions necessary to complete the IV curve calculation. This can result in a significant loss of time if unnoticed[14]. To combat this possibility in future potential runs, Figures A.11 and A.12 have been included here. These figures represent some of the raw, uncleaned data outputs from the T_e probe as seen from the

[11]These were literally LEGO pieces that we carved grooves into and then wrapped in wires.

[12]The probes have been further redesigned several times as of this writing, but 2018 represented the start of a new paradigm of custom-designed probes and probe PCBs.

[13]Compare with the $\dot{B}$ probes which passively take measurements without the need for user input aside from their digitizer trigger.

[14]This is known from experience.

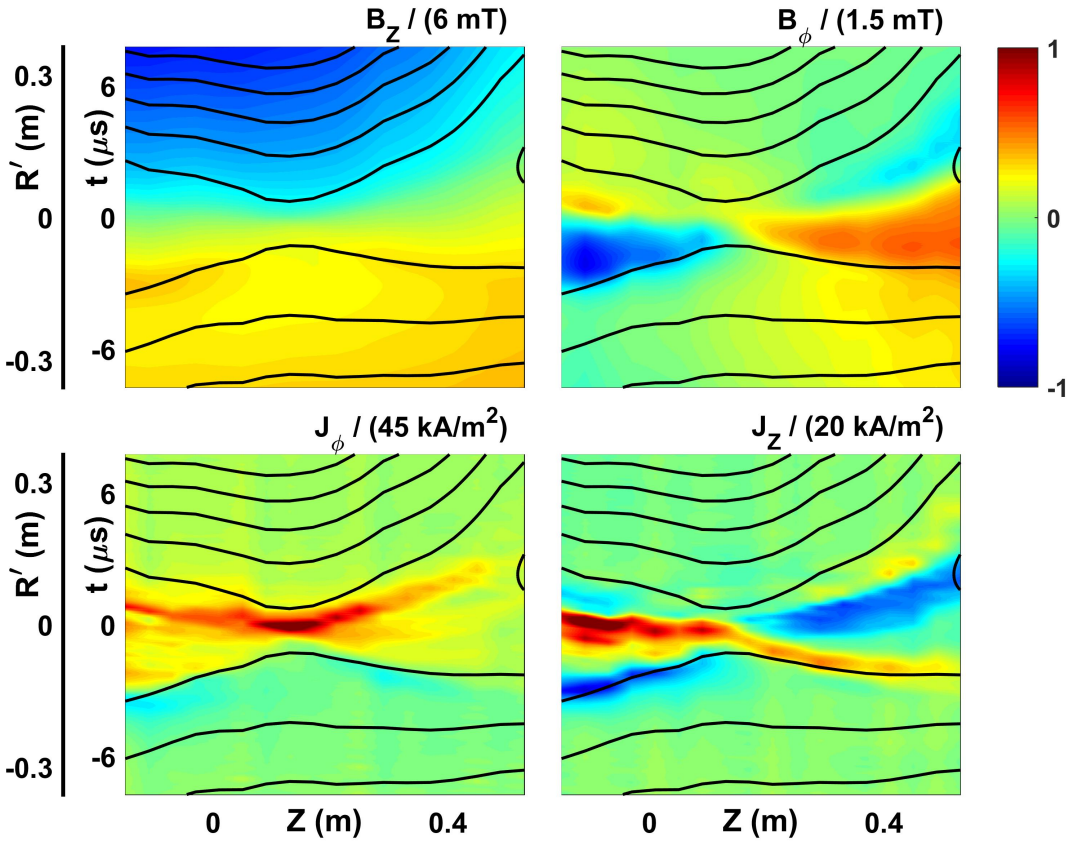

Figure A.10: Example data from some of the 2017 $\dot{B}$ probes. While it was concluded that the 2017 probes had a variety of limitations with respect to resolution (spatial and time) and irregularities in their construction process, they were able to provide helpful data from the TREX reconnection discharges. For example, this experimental shot in Hydrogen, with a 3 kV drive capacitor bank potential and a 30 G Helmholtz field, demonstrates the quadrupolar Hall magnetic field archetypical of two-fluid reconnection (see Section 1.2.3). This field is in the top-right plot of B_ϕ; note that the density asymmetry in TREX means that the two poles at lower values of R are stronger than the two poles at larger R.

BRB control room during regular experimental operation[15]. Fig. A.11 shows the raw probe tip bias potentials and the currents each tip draws; the current signals need to be checked for clipping, which can indicate the tip is being saturated, or for excessive jumpy noise, which can indicate a tip is dirty. Fig. A.12 shows examples of a potential IV curve fit and the associated values of T_e and n_e at different times relative to when the current layer passes the probe (plot (c)). The fits need to be evaluated by how well they model points on either side of the exponential's knee; a failure to adequately set the probe tip biases can result in too many points on one side or the other. Furthermore, different sides of the T_e probe (indicated by all-odd tip numbers on one side and all-even on the other side) may give different results depending on the probe's orientation relative to the reconnection features, and individual tips may fail while others function correctly. For these reasons, the tips used in the fit need to be approved on a case-by-case basis. For more information on the operation of this probe, please see Olson [14].

[15]Of course some of these plots, particularly the preliminary IV fitting do involve some data processing; both the full and scaled-down-for-use-in-the-control-room versions of the T_e probe processing code are originally courtesy of J. Olson.

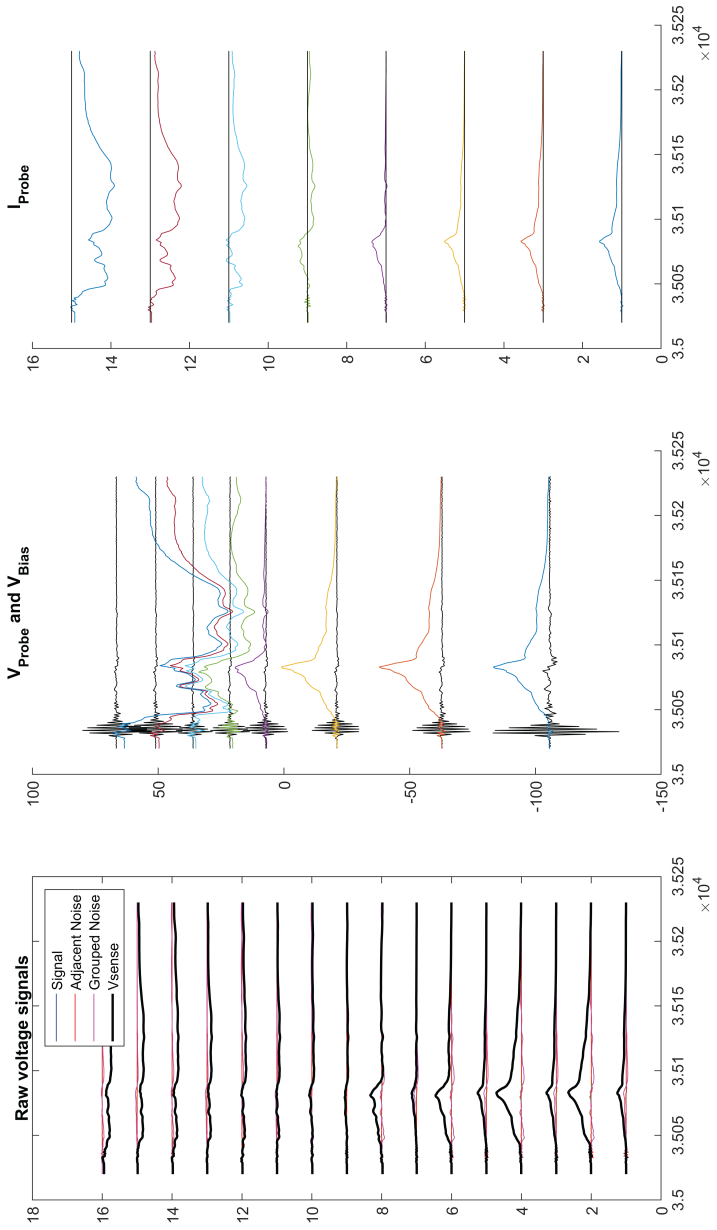

Figure A.11: Examples of the raw T_e probe data one would see in the control room while running. The biases, potentials, and currents measured at each probe tip are displayed through the relevant times of the experimental shot. Probe currents I_{probe} need to be checked for clipping (none shown here) to ensure the probe tip is not being saturated; saturated probes return unreliable data. If these current traces are excessively noisy, that usually indicates the probe is dirty and must be cleaned by subjecting it to multiple plasma shots until the noise recedes. These plots (in conjunction with Figure A.12) have been reproduced almost exactly from how they would appear in the control room so that they can provide an example of the features that should be checked for during a run to ensure the T_e is operating correctly.

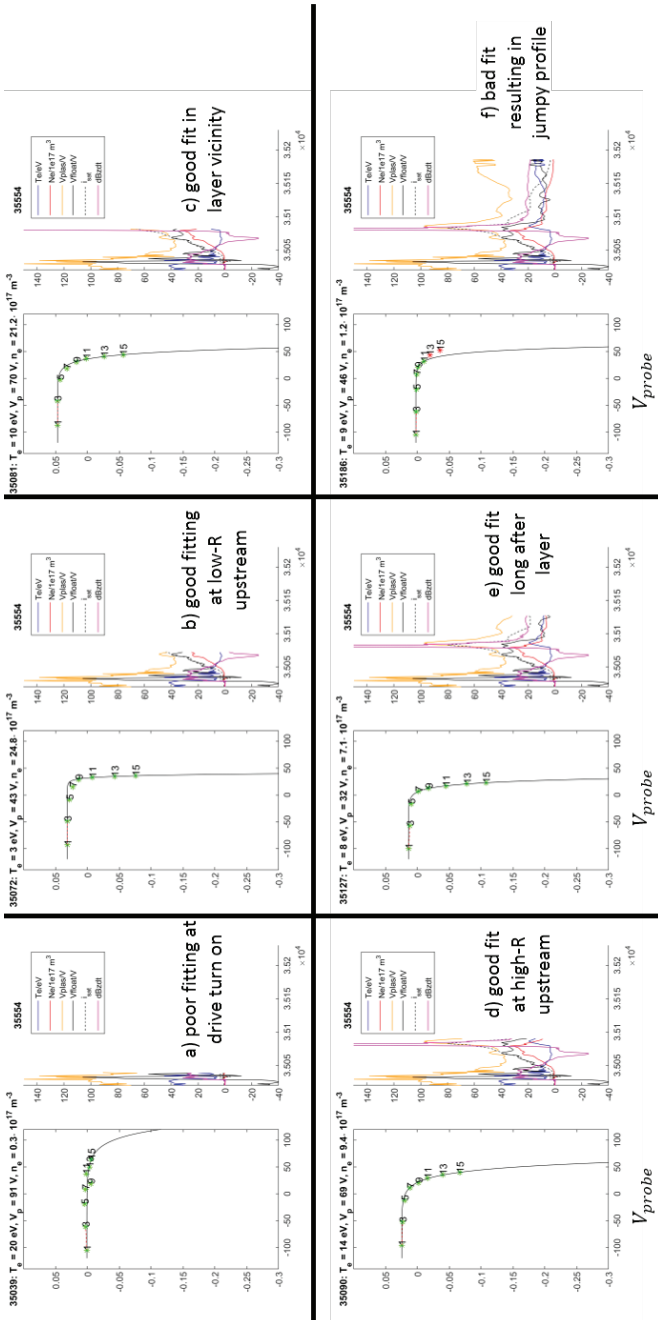

Figure A.12: Examples of the raw T_e probe data one would see in the control room while running. Confirming the existence of a decent fit during times relevant to measuring at and around the reconnection layer ((b)-(e)). A poor fit ((a) and (f)) can still give a data profile that seems reasonable in isolation, but cannot be taken as valid. A good fit includes points around the heel of the exponential and a few points on either side; it may be necessary to adjust the bias potentials of the different probe tips to ensure this. These plots (in conjunction with Figure A.11) have been reproduced almost exactly from how they would appear in the control room so that they can provide an example of the features that should be checked for during a run to ensure the T_e is operating correctly.

Appendix B

Additional VPIC Information

The purpose of this appendix is to provide additional information on the use of Cylindrical VPIC to simulate the TREX experiment. Aside from some unpublished TREX VPIC results shown at the end of this appendix, the content of this portion of my thesis will operate as a reference guide for any future graduate students who may find themselves in the position I found myself in at the start of 2018- namely, that of an experimentalist completely unfamiliar with the intricacies of simulation work and too anxious to make any edits to the basic TREX deck without triple-checking the definition of each affected variable. As such, this appendix is written in a manner that, in comparison to prior parts of this thesis or to the general tone of research publications, may be characterized as redundant or excessively verbose. This is entirely intentional, on the principle that too much information (when properly organized) does more to quench nervous self-doubt than too little.

B.1 General Initialization Parameters (Free and Otherwise)

The following variables are part of the construction of a given simulation; understanding them is necessary for setting up the simulation properly, understanding how to change the starting values of the simulated experiment, how to calculate the code time step, etc. Some

of these are free parameters that are specified in the simulation deck by the user; they are labeled below with some sample values given. These sample values are taken from typical 2D simulations of a standard TREX geometry; 3D cases will have variables associated with the ϕ coordinate set to numbers other than 1. In this and future section, code variable names and calculations will be presented `in this font`; in some cases, a LaTeX-equivalent variable name will be given in standard math script.

`x`, `y`, and `z` are the three spatial dimensions of the simulation. These represent CYLINDRICAL coordinates, not Cartesian ones. `x` maps to R, `y` maps to ϕ, and `z` maps to z. These are used on their own or as identifiers in different variable names to indicate which dimension that variable applies to. Henceforth, any variable that has three permutations with one for each of these coordinates will be written as `variable_i`, where `i` is an index standing in for `x`, `y`, or `z`.

`cfl_rec` or CFL_{rec} is the Courant–Friedrichs–Lewy condition (commonly just the Courant condition). It should be less than 1 to preserve causality. The Courant condition ensures that the timestep must be small enough to allow information to propagate over a single grid spacing. Free parameter; typical value: 0.98.

`mi_me` or m_i/m_e is the mass ratio. Larger mass ratios result in longer computation times (see Sections B.3.4 and B.3.3 below). The ion mass set to some multiple of the electron mass. Free parameter; typical values: $100 - 400 - 1836$.

`m_ion_electron` or $m_{ion}/m_{electron}$ is the reference mass ratio; as TREX simulations have not modeled any species aside from Hydrogen, this is kept at 1836.

`wpewce` or $\omega_{p,e}/\omega_{c,e}$ is the electron plasma to cyclotron frequency ratio. $\omega_{p,e}/\omega_{c,e}$ sets the

electron Alfvén speed relative to the speed of light:

$$\left(\frac{\omega_{p,e}}{\omega c, e}\right)^2 = \left(\frac{4\pi n_e e^2}{m_e}\right)\left(\frac{m_e^2 c^2}{e^2 B^2}\right) = \frac{c^2}{V_{A,e}^2}$$

where the above calculation is given in CGS units. In natural electron units (which the code uses), $c = 1$. As the value of $\omega_{p,e}/\omega_{c,e}$ gets larger, changes in the magnetic field propagate more slowly relative to the speed of light; this means that the time it takes for the magnetic field to change increases, and the simulation becomes more expensive. Free parameter; typical value: 1.

`dide` or d_i/d_e is the ratio of the ion to electron skin depths. This is set by the mass ratio `mi_me` and the ion charge Z (in units of elementary charge):

$$\frac{d_i}{d_e} = \frac{1}{Z}\sqrt{\frac{m_i}{m_e}}$$

`nppc` is the number of macro particles per cell of each species. Instead of simulating every particle in a given density distribution ($\mathcal{O}(10^{19})$), give or take an order of magnitude), VPIC simulates a smaller number of macro particles that are each representative of a number of real particles. These particles are more massive, but their relative charge is also scaled up by the same factor, keeping the charge-to-mass ratio constant. Free parameter; typical value: 500.

`topology_i` is the number of computational domains in each dimension of the simulation. This is how the simulation will be split up among different processors. The total number of processors that a simulation needs is equal to the product of all three of these values. These parameters should be selected such that each subdivision has a similar number of particles; otherwise, the computational load will be unbalanced between the different processors, making the total simulation less efficient in time. Free parameter; typical values

in `x,y,z` order are $1, 1, 360$ - this is because the standard TREX simulations have a starting density profile that is invariant in the Z direction, so multiple slices in Z each (initially) have equal numbers of particles.

`ni` or `n_i` are the number of grid cells in each of the three simulation dimensions. The ratio between `n_i` and its associated `topology_i` value must be an integer, because processors can only take whole divisions, not fractions. If these values are too small, then the grid size may be too large to properly resolve the Debye length, meaning that the recorded electric and magnetic fields along the grid lines will not be able see the effect of localized charge accumulations. This can be solved fairly easily by multiplying the offending `n_i` value(s) by some integer (2 is probably fine). Free parameter: typical values in `x,y,z` order are $756, 1, 1800$.

`Li` or L_i is the spatial extent of the domain in each of the three simulation dimensions, in code units of reference electron skin depths $d_{e,0}$, where $d_{e,0} = d_{i,0}/(d_i/d_e)i$ for the L_x and L_z values. The L_y value is given in radians.

`output_interval` is how often the code saves an output that can be accessed as a dataset, in terms of $1/\omega_{c,i}$ times. This is NOT the simulation timestep; this is merely how often data values from the simulation are saved into files that can be read after the simulation is finished. See Section B.3.4 below for more information. Free parameter; typical value: 0.1.

`n_e_si` or $n_{e,SI}$ is the reference electron density in SI units. Taken to be the density measured at $R = 0.5$m. See Section 6.2.2 for more information about the initial density profile. Free parameter; typical value: 5×10^{17}.

`t_e` and `t_i` or T_e and T_i are the reference electron and ion temperatures (respectively) in electron volts. These are taken to be the temperatures at $R = 0.5$m. Free parameter; typical

values: $T_e = 2.5 - 5$, $T_i = 1$.

`b0_trex` or B_{HH} is the reference magnetic field, set to the value of the Helmholtz field in a given run. Free parameter; typical values: $1 - 7 \times 10^{-3}$ [in SI units].

`wce_trex` or $\omega_{ce,0}$ is the reference electron cyclotron frequency in 1/s. This is set by the `b0_trex` value and the SI values of the electron charge q_e and electron mass m_e:

$$\omega_{ce,0} = \frac{q_e B_{HH}}{m_e}$$

`wci` or $\omega_{ci,0}$ is the reference ion cyclotron frequency in SI units. This is obtained by dividing the reference electron cyclotron frequency by the reference mass ratio `m_ion_electron`.

`vA` or $v_{A,0}$ is the reference Alfvén speed in SI based on the reference values for magnetic field, density, and ion mass ratio:

$$v_{A,0} = \frac{B_{HH}}{\sqrt{(m_{ion}/m_{electron})\, m_e \mu_0 n_{e,SI}}}$$

`di_trex` or $d_{i,0}$ is the reference ion skin depth in SI, derived from the other SI reference values:

$$d_{i,0} = \frac{v_{A,0}}{\omega_{ci,0}} = \frac{1}{q_e}\sqrt{\frac{(m_{ion}/m_{electron})\, m_e}{\mu_0 n_{e,SI}}}$$

`betae0` or $\beta_{e,0}$ is the reference electron β based on the other SI reference values:

$$\beta_{e,0} = \frac{2\mu_0 n_{e,SI} T_e q_e}{B_{HH}^2}$$

B.2 Initialization Unit Scale

As described in Section 6.3, the matching of a simulation's output code units to SI units is nontrivial. However, when considering the initialized simulation units, the matching is far easier: typically SI values that need to be converted to code units are simply divided by the initialized reference values. The following is a list of simple scalings that are useful when changing the starting point of the simulation:

- To convert an SI density into a code unit density, divide the SI density by the value `n_e_si`.
- To convert an SI magnetic field into a code unit field, divide the SI magnetic field by the factor `(b0_trex*wpewce)`.
- To convert an SI current into a code unit current, divide the SI current by the factor `(b0_trex*wpewce*(di_trex/dide)/mu_0)`.
- To convert an SI length into a code unit length, divide the SI length by the factor `(di_trex/dide)`.

B.3 Timestep Notes

The following timestep calculation assumes several example values, some of which are free parameters and some of which come from the `vpic.out` output file. These values have been chosen for ease-of-comprehension of the components of the calculation, rather than because they represent a specific simulation:

$$\frac{m_i}{m_e} = 100$$
$$\frac{\omega_{p,e}}{\omega_{c,e}} = 4$$
$$n_x = 1512$$

$$n_z = 3024$$

$$L_x = 45.0285$$

$$L_z = 93.1624$$

Assume that reading from the `vpic.out` file, we find that for 200 timesteps, about 90% of the time is spent advancing particles, and this process takes 1000 seconds of computing time. Then the size of a code time step $\mathrm{d}t$ is $1000/(0.9 \times 200) = 5.56$ seconds of computing time[1] Now, the code timestep in units of $1/\omega_{p,e}$ is calculated as follows:

$$\begin{aligned} \mathrm{d}t &= 0.98\sqrt{\frac{1}{\frac{1}{(L_x/n_x)^2} + \frac{1}{(L_z/n_z)^2} + \frac{1}{(L_y^*/n_y^*)^2}}} \\ &= 0.0214\left(\frac{1}{\omega_{p,e}}\right) \end{aligned} \tag{B.1}$$

where 0.98 is the courant condition `cfl_rec`. **Note the asterisks on the y component terms.** This is to indicate two properties specific to that term:

- This term is not included in the calculation if $n_y = 1$ (i.e., if the simulation is in 2D). The calculation would only include the L_x/n_x and L_z/n_z terms.

- The variable L_y^* is **NOT** equivalent to the L_y value used in the input deck and defined above. This value is the length of the arc subtended by the total angular width of the simulation at the minimum value for R, in reference electron skin depths. The value of L_y used in the deck is in radians. The formula for conversion between them is as follows, where R_{min} is in SI units and the d_i/d_e ratio is the `dide` variable defined above:

$$L_y^* = L_y\frac{R_{min}}{d_{e,0}} = L_y\frac{R_{min}}{d_{i,0}}\frac{d_i}{d_e}$$

[1]This will be used as a reference to convert between code timesteps and computing time timesteps, but in really this value will vary as the simulation runs depending on the code's efficiency.

B.3.1 Ramp Time

Now, the total time the simulation is told to run from the deck is given by the variable `tau`, also called `tauwci` in the `vpic.out` file. This time is set by the ramp time parameter (`ramptime_si`) in the deck, which is the time allotted for the current drive to be actively ramping up. In practice, this time allotment is set to longer than necessary for modeling a given experimental run[2], and is almost certainly longer that the amount of time that will be allotted to the simulation to run on a supercomputing cluster, so this parameter is generally ignored. Nonetheless, some of its relevant timing calculations will be included here for completeness. Take the value of `tauwci`[3] from the `vpic.out` file to be 26.823, which is in units of $1/\omega_{c,i}$. This can be converted to a value in units of $1/\omega_{p,e}$ by the following:

$$26.823 \times 100 \times 4 = 10729.2$$

where 100 is the mass ratio `mi_me` and 4 is the frequency ratio `wpewce`. Given the result of Eq B.1, we can find the total number of code timesteps allotted by the ramp time parameter:

$$\frac{10729.2}{0.0214} \approx 511308$$

The ramp time supplied by the input deck needs 511308 code timesteps (dts) to be fully realized. Based on our above calculation of the size of the computing time timestep, we find that a simulation of this many code timesteps would take $511308 \times 5.56 \approx 2.84 \times 10^6$ seconds or about 790 hours of computing time. As mentioned earlier, this is far more than we will actually need.

[2] See Section 6.2.4 for more detail about how the timescale of the actual reconnection experiment compares to the timescale of the drive current ramp.

[3] Assume, for the purpose of this analysis, that this corresponds to a total current ramp time on the order of 40µs, which is similar to the total time it takes in the experiment for the drive current to reach its maximum.

B.3.2 Quota Time

Another definable variable is `quota_sec`, which is the run quota in seconds of computer time. After this quota is used up, the simulation will shut itself down. Similar to the ramp time, this is again a parameter that is usually superseded by the time requested from the supercomputer cluster when the deck is submitted. Consider a quota of 11.5 hours. Based on our value for $\mathrm{d}t$ in computational time, this means the quota will provide roughly $11.5 \times 60 \times 60/5.56 \approx 7400$ total code timesteps. Note that this is lower than the 511308 timesteps needed to complete the ramp time, meaning that the quota parameter setting supersedes the ramp time parameter setting[4] Now let our `output_interval` value be the standard 0.01, meaning that data from the simulation will be saved at every $0.011/\omega_{c,i}$. If we ran through the full ramp time, this would generate $26.823/0.01 \approx 2682$ saved output time slices, or in other words, 2682 indices for a data matrix in the dimension corresponding to time. Since the quota parameter is the limiting parameter in this case, we can calculate the number of output time slices by taking the quota steps as a fraction of the ramp time steps and multiplying it by the total number of ramp time output time slices: $(7400/511308) \times 2682 \approx 39$ output time slices.

B.3.3 Computational Time Scaling

As a general rule for particle-in-cell codes, the amount of computer time a simulation will take to depends on both the mass ratio `mi_me` and the number of spatial dimensions being simulated; this will need to be kept in mind when designing a simulation and requesting supercomputer access.

$$computer\,time \propto (mass\,ratio)^{\#\,of\,dimensions+\frac{1}{2}}$$

[4]Though again, both are likely superseded by the computing cluster request.

B.3.4 Output Interval in Code Units

Often times when evaluating simulation output data it becomes important to understand the time difference between saved output time slices in code units. We will refer to this variable is Δt, to distinguish it from the internal code timestep $\mathrm{d}t$. The output interval is defined in terms of $1/\omega_{c,i}$, while the internal code timesteps are defined in terms of $1/\omega_{p,e}$. **Assuming an output interval of** 0.1, the calculation is as follows:

$$\begin{aligned} \omega_{c,i} &= \frac{Z q_e B}{(m_i/m_e) m_e} \qquad \omega_{c,e} = \frac{q_e B}{m_e} \\ \rightarrow \frac{\omega_{c,i}}{\omega_{c,e}} &= \frac{Z}{m_i/m_e} \end{aligned} \tag{B.2}$$

$$\begin{aligned} \frac{1/\omega_{p,e}}{1/\omega_{c,i}} &= \frac{\omega_{c,i}}{\omega_{p,e}} = \frac{\omega_{c,i}}{\omega_{c,e}} \frac{\omega_{c,e}}{\omega_{p,e}} \\ &= \frac{Z}{m_i/m_e} \frac{1}{\omega_{p,e}/\omega_{c,e}} \\ \rightarrow \frac{1}{\omega_{c,i}} &= \frac{m_i/m_e}{Z} \frac{\omega_{p,e}/\omega_{c,e}}{} \left(\frac{1}{\omega_{p,e}}\right) \\ \therefore \Delta t &= 0.1 \left(\frac{1}{\omega_{c,i}}\right) = 0.1 \left[\frac{m_i/m_e}{Z} \frac{\omega_{p,e}/\omega_{c,e}}{}\right] \left(\frac{1}{\omega_{p,e}}\right) \end{aligned} \tag{B.3}$$

where the mass ratio and the electron plasma to cyclotron frequency ratio are free parameters as defined above, and Z is the ion charge number. Most of our simulations run with $Z = \omega_{p,e}/\omega_{c,e} = 1$, which reduces Eq B.3 to $\Delta t = 0.1 m_i/m_e$ in code units of $1/\omega_{p,e}$.

B.4 Time Averaging Notes

Time-averaged data can be useful in simulations when evaluating variables that can be particularly noisy when viewed from a single time slice, like components of the electric field[5]. Time-averaging is distinct from simply averaging the regular output time slices of a simulation because the time-averaging process involves a rolling-average over some or all of the internal

[5]For example, the Ohm's Law analysis in Section 7.2 uses time-averaged data.

code timesteps, which in the regular case would not be sampled or saved once that code timestep is finished. Time-averaging involves three new free parameters:

- `AVG_SPACING` is the number of `output_intervals` at which the averaged data should be saved into an output file. This parameter behaves very similarly to how the `output_interval` parameter functions for regular data, except that the units of `AVG_SPACING` are (# of `output_intervals`), **NOT** units of $1/\omega_{c,i}$ times. If regular data is saved every `output_interval`$1/\omega_{c,i}$, then time-averaged data will be saved every `AVG_SPACING` $\times$ `output_interval`$1/\omega_{c,i}$.

- `AVG_SAMPLE` is the sampling frequency of the rolling average in number of code dts. For example, if `AVG_SAMPLE` $= 3$, then the code will use every 3^{rd} internal code timestep in its rolling average. This parameter should **ALWAYS** be an integer. `AVG_SAMPLE` $= 1$ is the most expensive possible setting.

- `AVG_TOTAL_STEPS` is the number of sampled code steps that will be used to compute an average. For example, if `AVG_TOTAL_STEPS` $= 4$, then the code will create an average from every 4 samples that have been taken from the simulation, on a rolling basis. This value is **ALWAYS** an integer as well.

These last two definitions can be combined to define the rolling average. Let `AVG_TOTAL_STEPS` $= n$ and `AVG_SAMPLE` $= m$, and let the average begin on some arbitrary code timestep with index i. The average value of some variable A is found as follows:

$$\bar{A} = \frac{A_i + A_{i+m} + A_{i+2m} + ... + A_{i+(n-1)m}}{n} = \frac{1}{n} \sum_{j=0}^{j=n-1} A_{i+jm} \tag{B.4}$$

While these are free parameters from a deck input perspective, there are two dependencies these three variables have on each other that limit their range of possible values. First, average data can only be dumped when an average has occurred, which puts a lower limit on `AVG_SPACING`. A naïve approach to finding this boundary would be to set it as the product of `AVG_SAMPLE` and `AVG_TOTAL_STEPS`; while this is correct in principle, `AVG_SPACING` is in

units of (# of `output_interval`s), not in units of (# of dts). The actual relation with the proper unit conversion is as follows:

$$\frac{\texttt{AVG\_SPACING} \times \texttt{output\_interval} \times \texttt{mi\_me} \times \texttt{wpewce}}{\mathrm{d}t} \geq \texttt{AVG\_SAMPLE} \times \texttt{AVG\_TOTAL\_STEPS} \tag{B.5}$$

Here, we have used Eq B.3 to convert `AVG_SPACING` to internal code units of $1/\omega_{p,e}$ and then converted that into dts. The second dependency relates the product of `AVG_SAMPLE` and `AVG_TOTAL_STEPS` to the internal physics of the simulation, ensuring that averages are taken over enough time for the simulation to evolve:

$$\texttt{AVG\_SAMPLE} \times \texttt{AVG\_TOTAL\_STEPS} \gtrsim 5 \times \mathcal{O}\left(max\left[\frac{1/\omega_{p,e}}{\mathrm{d}t}, \frac{1/\omega_{c,e}}{\mathrm{d}t}, \frac{1/\nu_{ei}}{\mathrm{d}t}\right]\right) \tag{B.6}$$

where 5 has been chosen as a decent value to ensure a reasonable difference in size between the total average interval and the largest physics process of the code (both in units of dts)[6]. If the simulation does not include collisions, then the $\frac{1/\nu_{ei}}{\mathrm{d}t}$ term is omitted. Together, Eqs B.5 and B.6 represent the high and low boundaries (respectively) on the possible choices of the size and resolution of the rolling average.

[6] If we consider the sample value of $\mathrm{d}t = 0.0214(1/\omega_{p,e})$ calculated in Eq B.1, then $1/\omega_{p,e} \approx 47\,\mathrm{d}t$ and $1/\omega_{c,e} \approx 188\,\mathrm{d}t$ using $\omega_{p,e}/\omega c, e = 4$.

B.5 Sample Info File

```
Computational Parameters:

Processors:                     0
Topology (x):                   1
Topology (y):                   1
Topology (z):                   360
Time step:                      0.0820256
Max time:                       35176.4
Num steps:                      428846
restart interval:               2000
quota (hours):                  15.5
Charge/macro electron:          -0.000254672
Charge/macro H:                 0.000254672
Average particles/processor:    7.56e+06
Average particles/cell:         500

Size Parameters:

Debye length:                   0.100333
di_trex (m):                    0.322018
Lx:                             192.941
Ly:                             0.0872665
Lz:                             399.188
nx:                             1512
ny:                             1
nz:                             3600
dx:                             0.127606
dy:                             0.0872665
dz:                             0.110885

Simulation Parameters:

mi/me:                          1836
denScale                        1
weightScale                     1
seed_mult                       4
seed_add                        26
num_emit                        20
output time (code units):       183.6
pos_si_to_code:                 133.063
b_si_to_code:                   200
wpewce:                         1
Fraction of courant limit:      0.98
vthe/c:                         0.100333
vthi/c                          0.00148094
cvar:                           5.2088e-06
sqrt(cvar*scale)                0.0359063

Collision Parameters:

ee_collisions:                  1
ei_collisions:                  1
ii_collisions:                  1
tstep_coll:                     20
nu/wce:                         0.00418034
coll. enhancement:              1
nu*dt_coll:                     0.0068579

TREX Initialization Parameters:

Vdrive_si:                      5000
b0_trex:                        0.005
I_tf_total (A)                  1500
Z:                              1
Plasma density:                 5e+17
T_e:                            2.5
T_i:                            1
vA0_trex:                       154241
wce_trex:                       8.7941e+08
wci_trex:                       478981
beta0 trex:                     0.0201335
```

Figure B.1: Sample Info file initialization output from a typical VPIC run.

B.6 Sample Mid-Run Timing Table

Operation	Since Last Update Pct	Time	Count	Per	Since Last Restore Pct	Time	Count	Per
clear_accumulators	0%	2.7e-02	2.0e+02	1.4e-04	0%	1.4e-01	1.0e+03	1.4e-04
sort_p	4%	8.2e-01	2.0e+01	4.1e-02	4%	4.2e+00	1.0e+02	4.2e-02
advance_p	67%	1.2e+01	4.0e+02	3.1e-02	64%	6.2e+01	2.0e+03	3.1e-02
reduce_accumulators	0%	2.9e-02	2.0e+02	1.4e-04	0%	1.4e-01	1.0e+03	1.4e-04
emission_model	0%	1.6e-04	2.0e+02	7.9e-07	0%	7.8e-04	1.0e+03	7.8e-07
boundary_p	15%	2.9e+00	6.0e+02	4.8e-03	13%	1.2e+01	3.0e+03	4.1e-03
clear_jf	0%	3.1e-02	2.0e+02	1.5e-04	0%	1.6e-01	1.0e+03	1.6e-04
unload_accumulator	0%	1.1e-02	2.0e+02	5.4e-05	0%	5.3e-02	1.0e+03	5.3e-05
synchronize_jf	2%	2.8e-01	2.0e+02	1.4e-03	1%	9.6e-01	1.0e+03	9.6e-04
advance_b	0%	2.4e-02	4.0e+02	6.1e-05	0%	1.3e-01	2.0e+03	6.3e-05
advance_e	4%	6.6e-01	2.0e+02	3.3e-03	2%	2.4e+00	1.0e+03	2.4e-03
clear_rhof	0%	7.0e-05	1.0e+00	7.0e-05	0%	2.8e-04	4.0e+00	7.1e-05
accumulate_rho_p	0%	2.9e-02	1.0e+00	2.9e-02	0%	2.1e-01	5.0e+00	4.2e-02
synchronize_rho	0%	1.6e-03	1.0e+00	1.6e-03	0%	7.6e-03	4.0e+00	1.9e-03
compute_div_e_err	0%	6.8e-04	2.0e+00	3.4e-04	0%	3.1e-03	7.0e+00	4.4e-04
compute_rms_div_e_err	1%	2.2e-01	2.0e+00	1.1e-01	1%	1.2e+00	7.0e+00	1.7e-01
compute_div_b_err	0%	1.6e-04	2.0e+00	8.2e-05	0%	1.8e-03	7.0e+00	2.6e-04
compute_rms_div_b_err	0%	1.8e-04	2.0e+00	8.9e-05	0%	5.3e-02	7.0e+00	7.6e-03
synchronize_tang_e_norm_b	0%	5.3e-04	1.0e+00	5.3e-04	0%	3.1e-01	7.0e+00	4.4e-02
load_interpolator	0%	6.3e-03	2.0e+02	3.1e-05	0%	3.3e-02	1.0e+03	3.3e-05
compute_rhob	0%	0.0e+00	0.0e+00	0.0e+00	0%	1.2e-03	1.0e+00	1.2e-03
uncenter_p	0%	0.0e+00	0.0e+00	0.0e+00	0%	2.6e-02	2.0e+00	1.3e-02
user_initialization	0%	0.0e+00	0.0e+00	0.0e+00	1%	7.1e-01	1.0e+00	7.1e-01
user_particle_collisions	6%	1.2e+00	2.0e+02	5.9e-03	6%	5.8e+00	1.0e+03	5.8e-03
user_particle_injection	0%	1.1e-04	2.0e+02	5.6e-07	0%	6.2e-04	1.0e+03	6.2e-07
user_current_injection	0%	4.8e-02	2.0e+02	2.4e-04	0%	2.4e-01	1.0e+03	2.4e-04
user_field_injection	0%	1.2e-04	2.0e+02	5.9e-07	0%	5.7e-04	1.0e+03	5.7e-07
user_diagnostics	0%	9.7e-04	2.0e+02	4.8e-06	7%	6.4e+00	1.0e+03	6.4e-03

Figure B.2: Sample computational timing output table from a `vpic.out` output file. The text contained in the blue box states that 67% of the simulation's computing time since the last update was spend advancing the particles to their new positions. The interval between updates is 200 code timesteps; this number can be changed by modifying the `status_interval` variable if desired, but should generally be left unchanged. The text outlined in blue also states that 12 seconds were spend advancing the particles, meaning that the total computational time for this interval is $12/0.67 \approx 18$ seconds. The text in the orange box states that 15% of the simulation's time was spent transferring particles between different processors; if this process takes too much time, the `topology_i` variables should be adjusted, either by making each topological subset of the simulation domain larger or changing the overall geometry of the topological divisions to discourage excessive transfers between different subsets. Note that the values given in this table are rounded, such that these computational time calculations are not exact.

Appendix C

Additional Layer Width Information

This appendix serves as a collection of supplementary material for Chapter 7, which itself is heavily based on Greess et al. [16]. These materials include engineering and programming details that may be relevant for future investigators.

C.1 Curved Probe and Toroidal Mode Measurements

A photograph of the curved probe used to evaluate the different widths measured at different values of the toroidal angle ϕ in Figure 7.5 is shown in Figure C.1. While this probe did demonstrate that there is some kind of toroidal developing in the TREX current layer, the resolution of the probe was not sufficient to allow us to quantitatively analyze its properties. This issue is shown in Figure C.2, where the experimental data plots (top three) are compared to the simulation data at its full resolution (bottom plot) and downsampled to match the resolution of the curved probe (plot second from the bottom). The downsampled simulation data bears some similarities with the experimental data, but going forward we would like to implement a curved probe array with a higher spatial resolution to allow for a quantitative comparison. Despite the resolution difficulties, it is clear that for the three experimental shots (which were all run at the exact same parameter set), there is both variation in the current layer relative to ϕ and variation in the phase of this current layer kinking from one

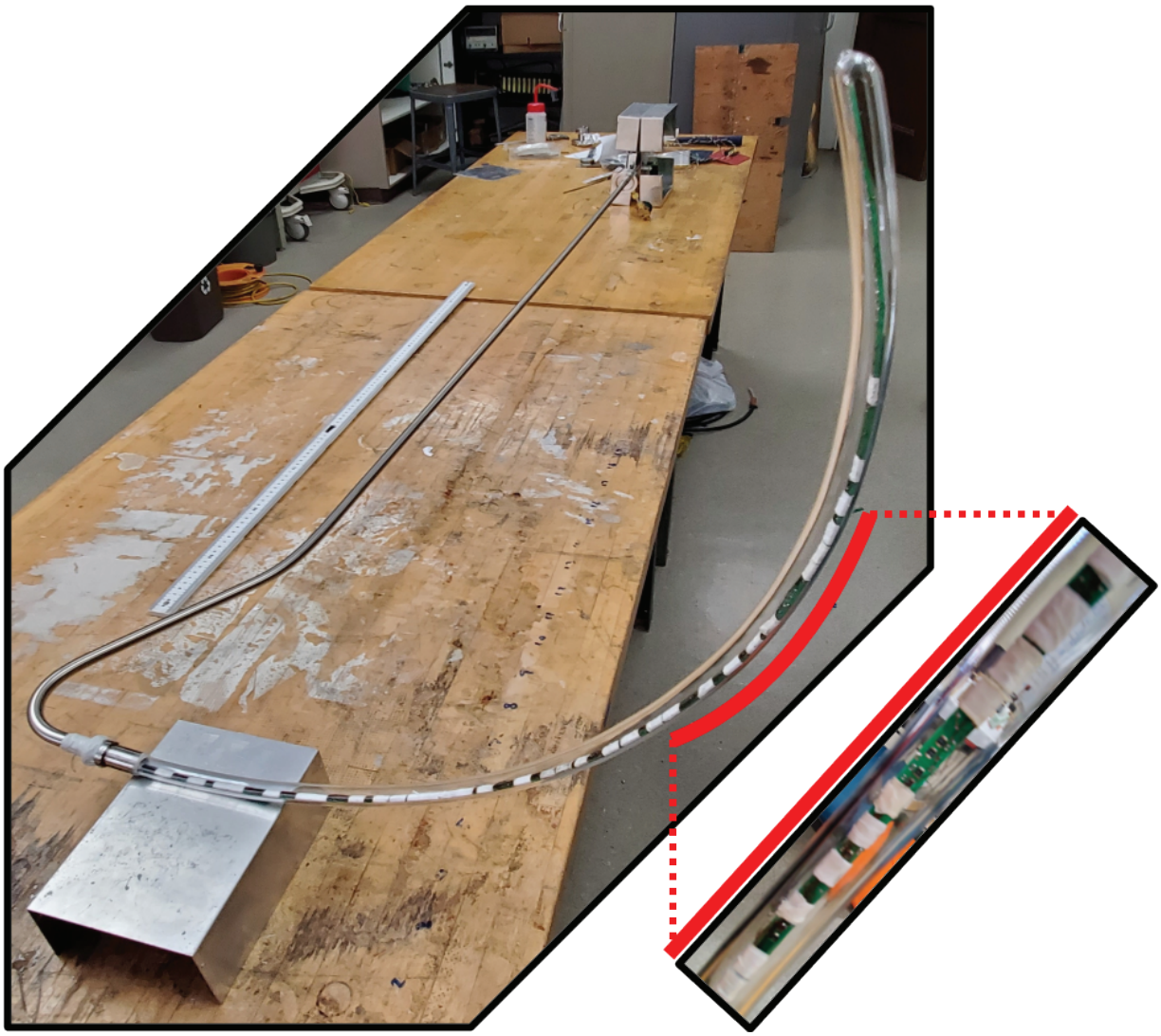

Figure C.1: The curved Bdot probe array used to measure the toroidal variation in the TREX current layer. The probe boards (shown in the insert photograph) are contained within the curved glass tube, which has been bent to keep the probes fixed at a single value of R and Z inside the BRB.

shot to another; both of these properties are necessary to explain the data spread displayed in Figure 7.6.

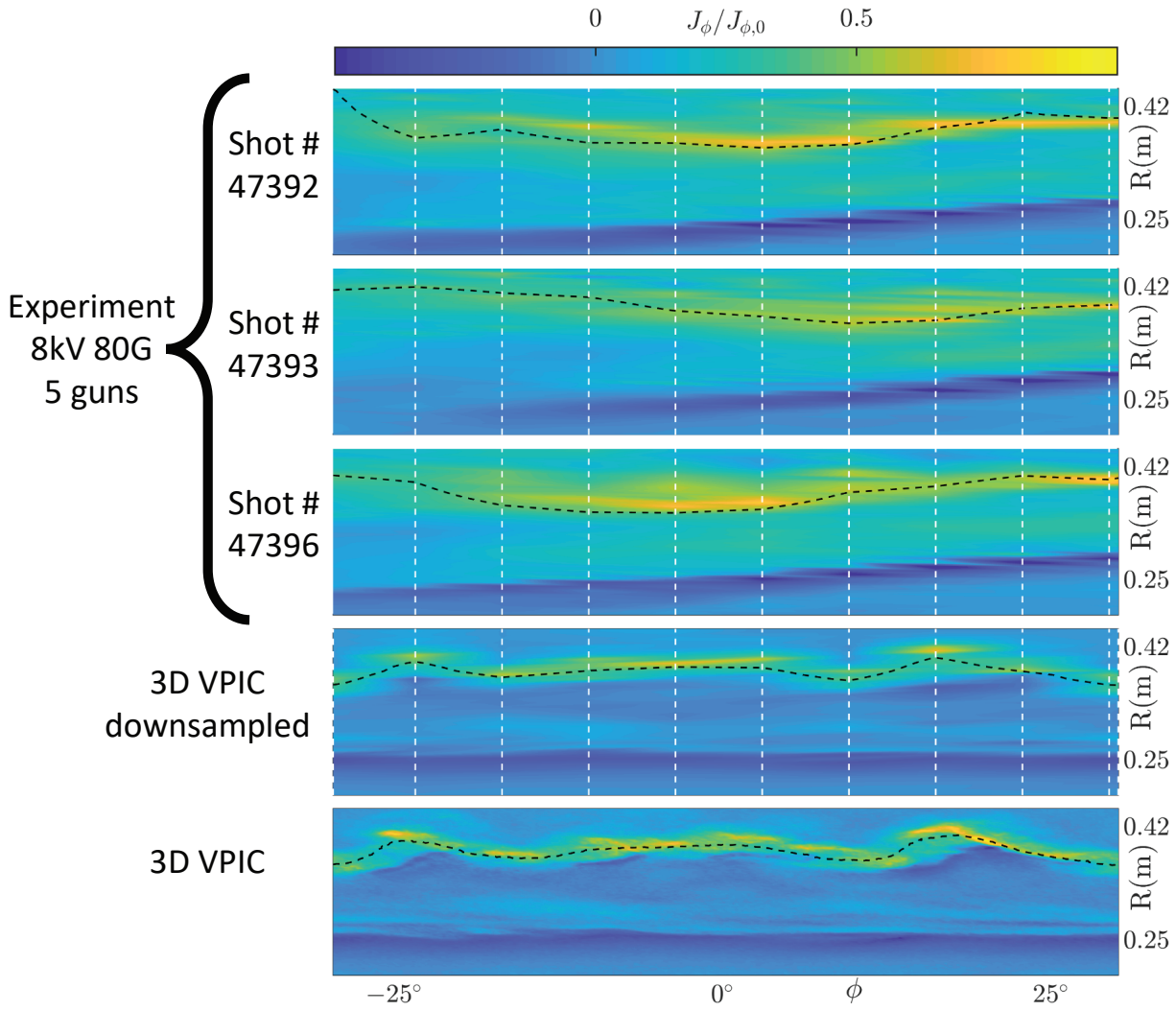

Figure C.2: (Top three) Curved probe data from three separate experimental shots, all at the same parameter set. There is clear variation with respect to toroidal angle and with respect to the phase of this variation from one shot to the next. The black dashed lines represent the $B_z = 0$ line. The dashed white lines are the locations of the individual Bdot probes that make up the curved probe array. The probe spacing is the main factor decreasing the spatial resolution of the curved probe data far below that of the full TREX-VPIC simulation (bottom plot). As a comparison, the TREX-VPIC simulation has been downsampled to the individual probe location (plot second from the bottom).

C.2 Density Selection for Skin Depth Measurement

As mentioned in Sections 5.2 and A.4, the temperature and density data fitting process is nontrivial, and the results of such a fit and the decisions made that lead to that fit (e.g., probe tip biases, number of tips to include, etc.) can include significant uncertainty. Indeed, it is not considered unreasonable to assume that any given calculated value of the density includes a systematic uncertainty of $\pm 50\%$ [14]. Keeping this uncertainty in mind, the process developed for selecting the density measurements used to define the local electron skin depth[1] is more of a guideline rather than a hard procedure leading to a single, definable answer. To help mitigate of the variability in a given selection as well as the experimental uncertainty, multiple blind[2] repeat density selection measurements were taken for each experimental shot dataset. Propagation of the systematic uncertainty through these processes resulted in the horizontal error bars on the data shown in Figure 7.6.

The density selection procedure is demonstrated by the two plots shown in Figure C.3. The densities used to calculate the electron skin depths are taken to be the average of densities on either side of the layer at a distance of approximately one ion skin depth from the center of the layer. To facilitate this process, we first use the calculated density profile to calculate a value for the ion skin depth at every timestep (red line in Figure C.3(a)). Using the jogging method described in Section 5.3, we then compare these skin depths to the distance between the probe and the peak current density of the layer at every timestep, plus or minus some arbitrary cutoff value (blue shaded 'V' in Figure C.3(a)). The timesteps where these two curves overlap are marked on the density profile (red) in Figure C.3(b) by the green and magenta 'X's. These points are NOT the only points selected for the electron skin depth calculation; they are merely used as a guideline for the person or persons making the selection by eye. Whether or not the selected points are themselves valid must be determined on a case-by-case basis; for example, the green 'X' at timestep ~ 10 is clearly an artifact of the

[1] A very similar process was also used for the ion skin depth measurements necessary for the analysis in Chapter 8, except with simulation data.

[2] "Blind" here means that the selections on multiple different data sets were repeated in random order without any identifiers that could indicate which parameter set the data belonged to.

breakdown in the density fit right as the experimental shot starts.

As stated earlier, these guidelines are used to inform selections by eye, and multiple blind repeated selections are made to try to minimize the variability associated with the final averaged density value. In this relatively straight-forward case, the selection by eye would most likely be all the non-erroneous green points and the unmarked density values between them as well as all the magenta points and the unmarked density values between them. Though this process is fairly subjective, the analysis of the final selections made over all the blind measurement processes found that the variance between different selections was not very large; this is reflected in the relatively small horizontal error bars on the datapoints in Figure 7.6.

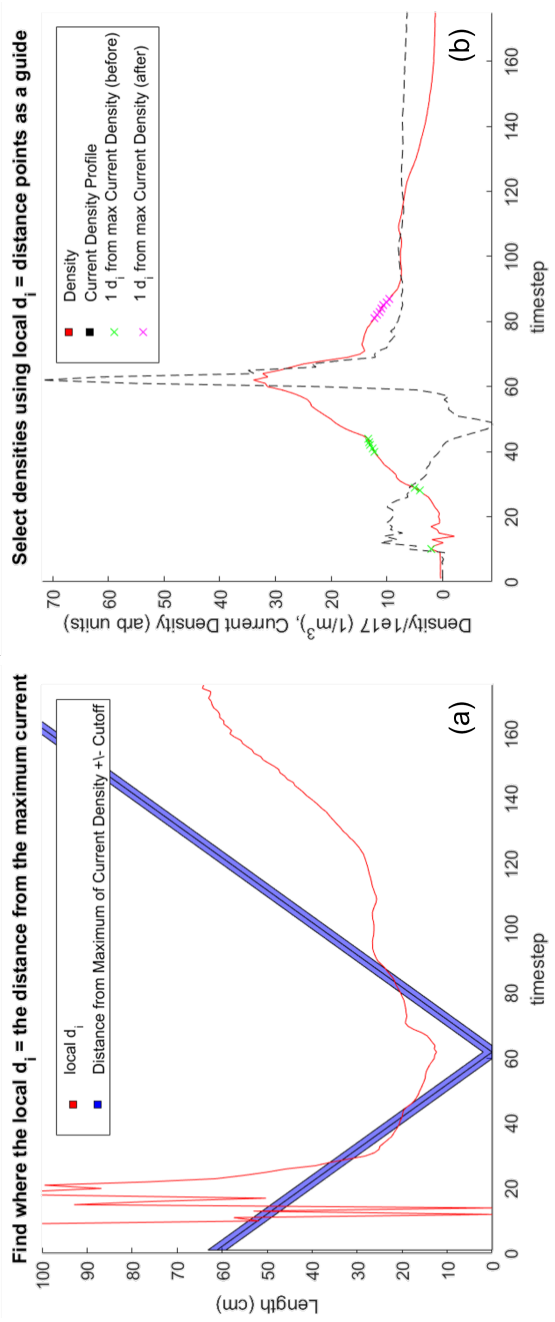

Figure C.3: An overview of the procedure used to select the densities that define the electron skin depth measurements in Figure 7.6. (a) The calculated local ion skin depth (red) compared with the distance from the peak of the current layer (blue). The distance from the layer includes an arbitrary cutoff value (in this case, ± 2 cm) to make the overlap between the red and blue curves easier to find. When these two curves overlap, the density measurement at that timestep can be said to be one ion skin depth from the center of the layer. These values are marked on the density curve (red) in (b) with 'X's, where the green marks come before the layer and the magenta marks come after. A scaled version of the current density profile is shown with a black dashed line, for context.

Appendix D

Lower Hybrid Drift Instability

The purpose of this appendix is to provide a brief overview of the Lower Hybrid Drift Instability (LHDI) due to its appearance in the TREX VPIC simulation described in Chapter 7. This appendix will not include a full derivation of the LHDI (that would be far beyond the scope of this thesis; see Krall and Liewer [93] for the full derivation of the dispersion relation), but a modest review of the LHDI's properties and physical meaning is useful in contextualizing the significance of our observation and conclusions, which are recapped below:

The LHDI has been observed by spacecrafts at both the magnetopause [94] and the magnetotail [95], as well as in a wide variety of previous numerical simulations [41, 96]. The LHDI has been considered as a source of "anomalous resistivity", a phrase which here describes a resistive component of Ohm's Law (Eq 7.1) that is necessary to break the frozen-in condition and allow reconnection to proceed, but is not described by the classical definition of electrical resistivity. Anomalous resistivity is of particular interest in kinetic (or "collisionless") reconnection, where the lack of particle collisions implies that the standard electrical resistivity value is 0; anomalous resistivity has been invoked in this parameter regime as a way to compensate for this term in Ohm's Law. As was explained in Chapter 7, it is our conclusion that anomalous resistivity is NOT necessary to break the frozen-in condition; the pressure-tensor-divergence term is sufficient to match the reconnection electric field. Furthermore, we contend that measurements of anomalous resistivity in prior analyses

may be due to the "kinking" induced in the reconnection current layer by the LHDI; if the spatial averaging involved in the calculation of the terms of Ohm's Law does not take this kinked geometry into account (e.g. by using an average that goes straight through the layer region rather than one that adapts to the kinked layer path), terms outside of the diffusion region can be included, thereby giving the illusion of a necessary additional resistivity component.

The following sections of this appendix will detail the coupling between drift waves and lower hybrid waves that establishes the LHDI and give a brief summary of the LHDI parameters most relevant to the instability identification process in Chapter 7.

D.1 LHDI Wave Physics

D.1.1 Drift Waves

Drift waves are a near-ubiquitous form of wave because all that they require to exist are a spatial gradient in the plasma in the direction perpendicular to the magnetic field. Drift waves are driven by diamagnetic electron and ion currents, which in turn depend on the total drift velocity perpendicular to the background magnetic field. The choice of reference frame will change the apparent contribution of different drift effects to the total perpendicular drift velocity. These effects can include the standard picture of a diamagnetic drift due to a pressure gradient perpendicular to $\mathbf{B}$, the $\mathbf{E} \times \mathbf{B}$ drift, and the $\nabla \mathbf{B}$ drifts [11]. For the initial Krall and Liewer [93] LHDI derivation detailed below, the reference frame used is the rest frame of the ions, such that $v_i = 0$ and $\mathbf{E} \neq \mathbf{0}$. Combined with their assumption of a weak $\nabla \mathbf{B}$ drift, this leads to the perpendicular drift velocity being defined completely by the $\mathbf{E} \times \mathbf{B}$ drift velocity:

$$\mathbf{v}_E = c\frac{\mathbf{E} \times \mathbf{B}}{B^2}$$

where c is the speed of light[1]. Many more recent Harris-sheet-based analyses of the LHDI, including all the Daughton *et al.* papers cited in this appendix and Chapter 7, choose a frame where the background electric field is 0. This is taken to be the case in Section D.2.

D.1.2 Lower Hybrid Waves

The Lower Hybrid Wave is one of the two solutions for the extraordinary (X) wave in a cold plasma (the other solution is the Upper Hybrid Wave). The X wave and its counterpart, the ordinary (O) wave, constitute the two solutions to the cold plasma dispersion relation for waves propagating perpendicularly to a magnetic field. The dispersion relation for X waves is fairly complicated, as far as cold plasma waves go, so it will not be reproduced here; interested parties are encouraged to consult Equation (2.38) in Section 2.2.2.2 of Swanson [97] (pg 31).

Finding the lower hybrid resonance dispersion relation (after eliminating the relatively easier-to-solve upper hybrid resonance and removing terms of order m_e/m_i) results in the following frequency relation:

$$\omega_{LH}^2 = \omega_{ce}\omega_{ci}\left(\frac{\omega_{pe}^2 + \omega_{ce}\omega_{ci}}{\omega_{pe}^2 + \omega_{ce}^2}\right) \tag{D.1}$$

where $\omega_{cj} = |q_j|B/m_j$ is the cyclotron frequency of species j and $\omega_{pj} = \sqrt{n_j q_j^2/m_j\epsilon_0}$ is the plasma frequency of species j (both defined here in SI units). We can simplify this result further by considering the ratio of these two standard frequencies:

$$\frac{\omega_{pj}^2}{\omega_{cj}^2} = \frac{n_j m_j}{B^2\ \epsilon_0}$$

Considering some standard TREX scale values ($B \approx 10^{-2}$ T and $n \approx 10^{18}$ 1/m^3) and using

[1]This equation and others in this section are in Gaussian units; this should be assumed to be the case unless otherwise specified. This is the unit scheme that seems to have been adapted by the main sources cited in this section, and it is preserved here in the hopes of avoiding any potentially erroneous changes to the well-established formulae. Sorry Jan.

$\epsilon_0 = 8.854 \times 10^{-12}$ F m^{-1} and $m_e = 9.11 \times 10^{-31}$ kg, we find that

$$\frac{\omega_{pe}^2}{\omega_{ce}^2} \approx 1030 >> 1$$

where the fraction for the ions is clearly even larger (assuming quasineutrality of a singly-ionized plasma). In this limit[2], the lower hybrid resonance can be simplified to the much more convenient form:

$$\omega_{LH} \approx \sqrt{\omega_{ce}\omega_{ci}} \tag{D.2}$$

where ω_{LH} is now the geometric mean of the two cyclotron frequencies.

This new definition also gives us insight into the physical meaning of the lower hybrid wave in this limit. As the geometric mean of the electron and ion cyclotron frequencies, the lower hybrid frequency will be between them both (larger than ω_{ci} and smaller than ω_{ce}). This means that on the timescale of the wave fluctuations, the ions are essentially unmagnetized, as they are not seen as undergoing cyclotron motion; however, the electrons are still undergoing several cyclotron orbits by the time the lower hybrid wave completes one period. This in turn means that while the ions oscillate in the same direction as the wave electric field (perpendicular to the magnetic field[3]), the electrons move in both the direction of $-\mathbf{E}$ and in the $\mathbf{E} \times \mathbf{B}$ direction. By evaluating the single particle orbits of the electrons and ions, it can be shown that the displacement of both the electrons and ions in the electric field direction are equal and in phase with each other when the frequency of their oscillation is exactly equal to the geometric mean of the two cyclotron frequencies[4]. Thus, when we oscillate at the lower hybrid frequency in this $\omega_{pe}^2 >> \omega_{ce}^2$ limit, there is essentially no net charge displacement along the electric field, but there is a net migration of charge in the direction of $\mathbf{E} \times \mathbf{B}$, due to the electron motion in that plane that is not canceled by equal

[2]Rather confusingly with respect to the reconnection phase diagram explained in Section 1.3, Swanson [97] and Stix [98] both refer to this as the "high density limit". The name in this context refers to the rest mass energy density of the plasma being much greater than the magnetic energy density.

[3]As opposed to in the ordinary wave, where $\mathbf{E}||\mathbf{B}$.

[4]For more information on this process, see Section 2.1.1.1 in Swanson [97] (pgs 23-24) and Problem #6 in Stix [98] (pg 43).

ion motion. This charge migration is the lower hybrid wave in the "high-density" limit (Stix [98], pg 36).

D.1.3 Lower Hybrid Drift Instability

As previously stated, the full derivation of the LHDI's dispersion relation is far beyond the scope of this thesis. The full derivation may be found in the original LHDI paper by Krall and Liewer [93] from 1971. This short summary of the LHDI's relation to the two waves described in the prior sections will begin with that paper's Equation (7), the dispersion relation for the LHDI after some simplifying assumptions and Bessel function expansion:

$$(\omega - k_y v_E)\left[\frac{\omega^2}{\omega_{pi}^2}\left(1 + \frac{4\pi n m c^2}{B^2}\right) - 1\right] = -\frac{k_y v_\Delta}{k^2 \lambda_D^2}\frac{\omega^2}{\omega_{pi}^2} \tag{D.3}$$

where v_E is the $\mathbf{E} \times \mathbf{B}$ drift velocity, λ_D is the Debeye length, and all the terms are given in CGS units. v_Δ is a velocity driven by gradients in various plasma quantities:

$$v_\Delta = -\frac{T_e}{m\omega_{ce}}\left[\frac{1}{n_e}\frac{\mathrm{d}n_e}{\mathrm{d}x} - \frac{1}{B}\frac{\mathrm{d}B}{\mathrm{d}x} - \frac{k^2\rho_e^2}{2}\frac{1}{T_e}\frac{\mathrm{d}T_{\perp\ e}}{\mathrm{d}x}\right] \tag{D.4}$$

where ρ_e is the electron gyroradius. If the plasma were completely homogeneous such that v_Δ were 0, the right hand side of Eq D.3 would be 0, leading to two resonances:

$$\omega = k_y v_E \tag{D.5}$$

$$\omega^2 = \omega_{pi}^2\left(1 + \frac{4\pi n m c^2}{B^2}\right)^{-1} \approx \omega_{ce}\omega_{ci} \tag{D.6}$$

where the last approximation is true in the "high density limit", where $B^2 << 4\pi n m c^2$. These two waves are the $\mathbf{E} \times \mathbf{B}$ drift wave (top) and the lower hybrid wave (bottom) in the high density limit (Eq D.2). This means that the LHDI is a phenomenon brought about by the coupling of these two waves; the strength of the coupling is dependent on how much inhomogeneity there is in the plasma [93].

A note about the directional conventions used in the Krall and Liewer [93] derivation; the gradients in the x direction and the wave propagation in the y direction are defined only in terms of their orthogonality to the magnetic field. These values are not related to the direction of the electric field assumed by the derivation; the directions of any or all of these features can be altered, as long as they all remain perpendicular to the magnetic field. Keep in mind as well that the Krall and Liewer [93] derivation uses a Cartesian geometry, as opposed to TREX and TREX VPIC's cylindrical configuration. The slab geometry used by Krall and Liewer [93] is reproduced in Figure D.1.

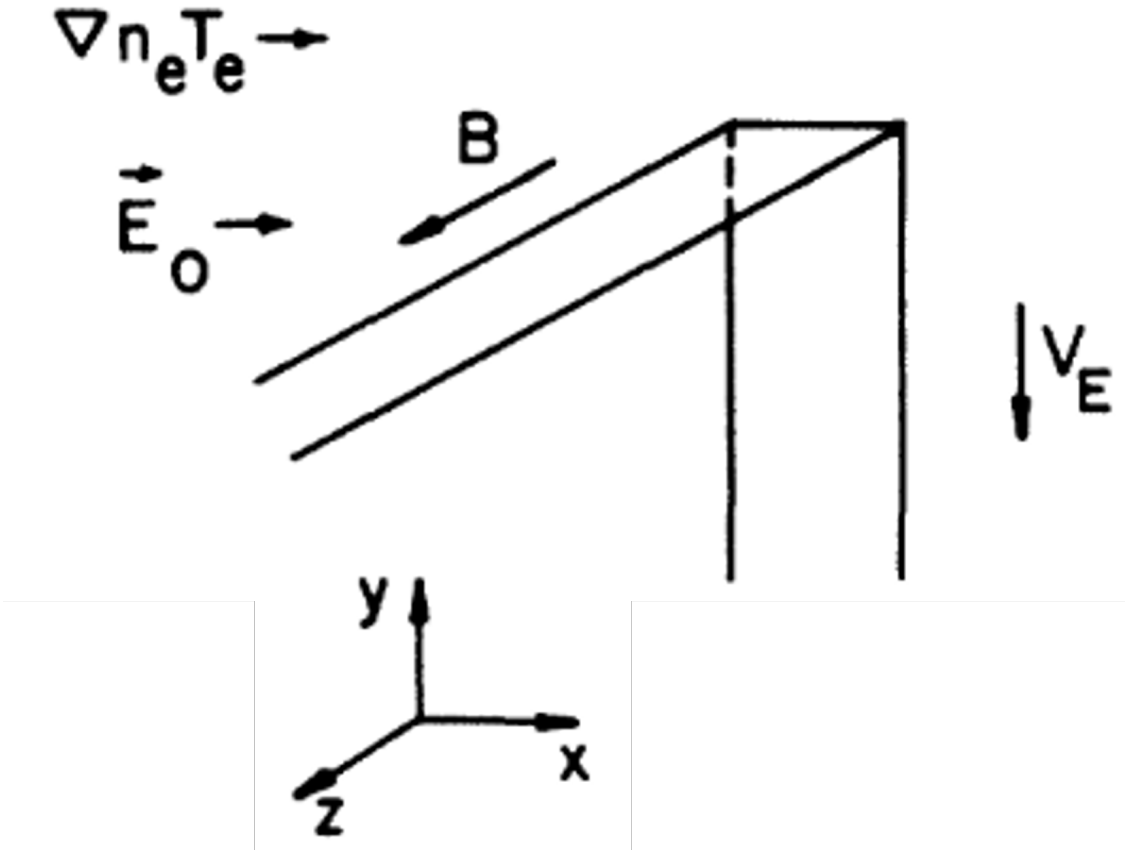

Figure D.1: The slab geometry used by Krall and Liewer [93] to describe the background plasma that gives rise to the LHDI. Reproduced from Krall and Liewer [93] with minor alterations. Note that this is in Cartesian coordinates.

D.2 LHDI Properties

The various attributes of the LHDI have been established through years of work, both analytically through mathematical analysis and empirically through simulations [96, 80]. What follows is a list of these attributes, several of which were used to identify the LHDI in the 3D TREX VPIC simulations described in the main body of this thesis. For more information on how this identification occurred, see Section 7.2.2. For convenience, two views of the instability in 3D TREX VPIC are shown in Figure D.2. In this section, ω_{LH} is taken to be that of Equation D.2.

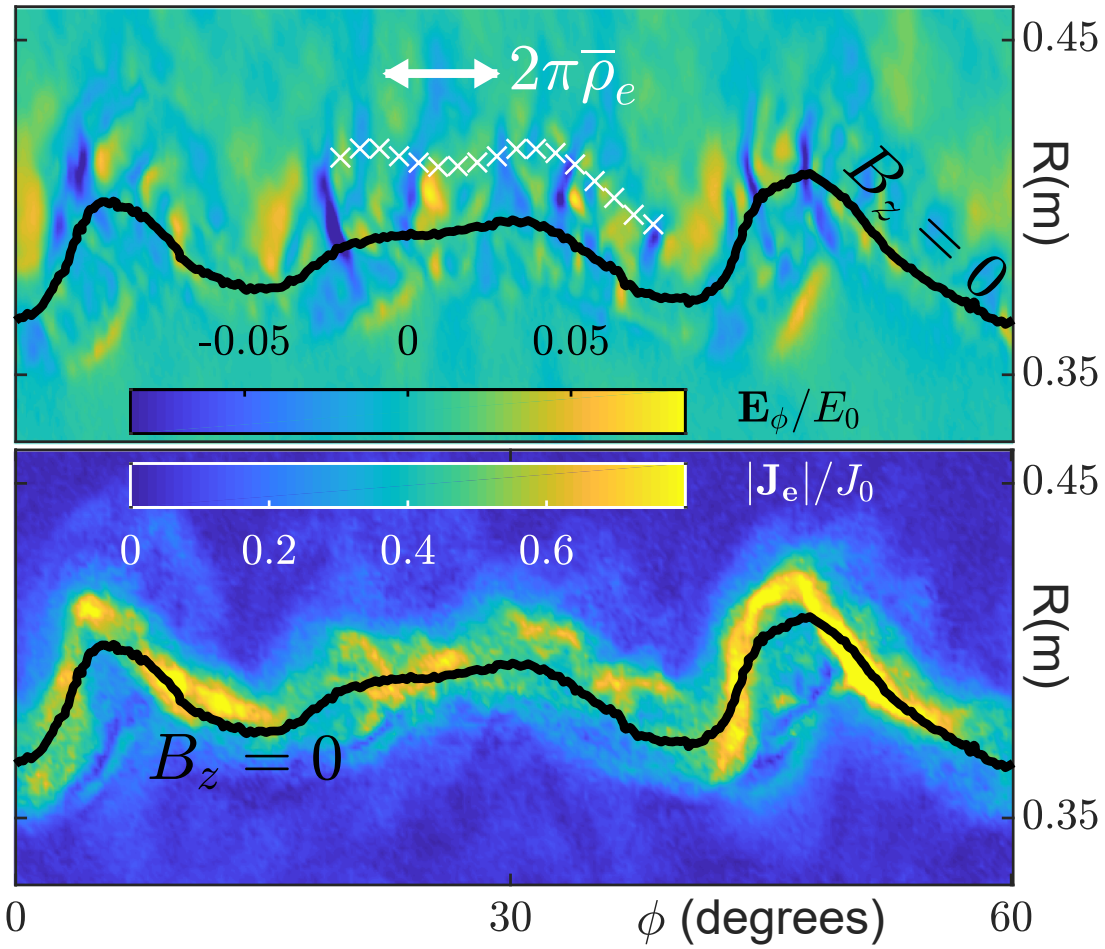

Figure D.2: The toroidal electric field (top) and total current density magnitude (below) of the reconnection layer in the 3D TREX VPIC simulation described in Chapters 6 and 7. A partial reproduction of Figure 7.4 in Section 7.2.2.

The LHDI has two components: a fast, primarily electrostatic component and a slow, primarily electromagnetic component. The latter of these two is responsible for the kinking of the reconnection layer, while the former is visible in the top plot of Figure D.2.

D.2.1 Electrostatic

Properties of the fast, electrostatic component, which dominates in regions of low plasma β:

- $\mathbf{k} \bullet \mathbf{B} = 0$ (electrostatic) [80].
- $k_y \rho_e \sim 1$ [80].
- $\omega \sim k_y U_i \lesssim \omega_{LH}$, where $U_i = -\frac{\nabla p \times \mathbf{B}}{qnB^2}$ is the diamagnetic drift velocity [80].
- $\gamma \lesssim \omega_{LH}$, where γ is the growth rate of the instability [80].
- The electrostatic mode cannot be excited directly within a reconnection current layer, only along its edges (Biskamp [96] pg 291). The low-β limit where the LHDI is dominated by its electrostatic component breaks down in this region.
- The magnitude of the electrostatic mode grows in conjunction with growth in the magnitude of the density gradient [43]; for example, the reconnection layer in TREX VPIC (Figure D.2) has higher density at lower R values and lower density at higher R values. On the high-density side, the plasma compression due to the layer's movement keeps the density relatively constant, while on the low-density side of the layer, the density rapidly approaches 0 from it's peak inside the current layer. As expected based on this description of the TREX VPIC density gradient, the electrostatic fluctuations are stronger on the larger R flank of the layer.

D.2.2 Electromagnetic

Properties of the slow, electromagnetic component:

- $k_y \sqrt{\rho_e \rho_i} \approx 0.85$ [80].

- Longer wavelength LHDI modes are dominantly (but not completely) electromagnetic. These modes are responsible for altering the geometry of the current layer [80].

D.2.3 Ion Beta Modifications

One aspect of both of these modes that must be noted: the empirical relations are derived from analyses that assume extremely small ion betas ($\beta_i \approx 0$). As the plasma moves to larger ion beta values, the wavenumber k_y increases in size. This effect was established by Davidson et al. [81] and is presented in Figure D.3, which is partially reproduced from that paper. This means that any relation involving k_y will also be scaled up; for example, the electrostatic property given above as $k_y\rho_e \sim 1$ will become $k_y\rho_e \gtrsim 1$ for plasmas with realistic (nonzero) ion betas. This behaviour was taken into account when the properties of the instability introduced in Section 7.2.2 were compared with the general LHDI properties described above.

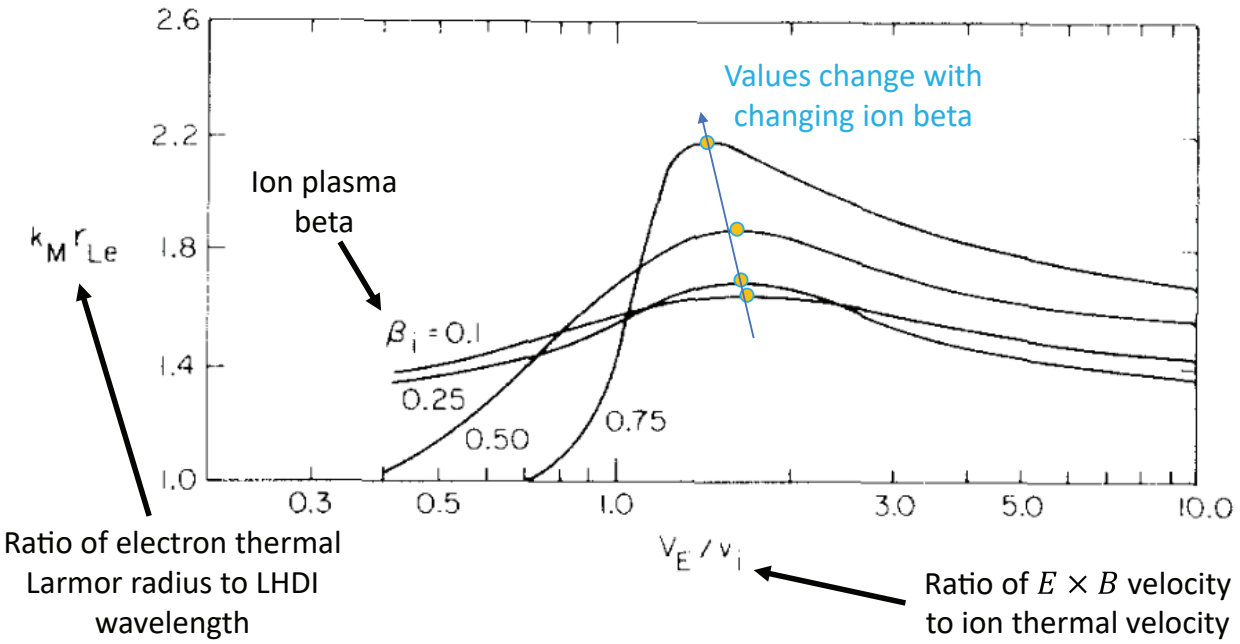

Figure D.3: The dependence of the LHDI wavelength relative to different values of the ion beta parameter. Reproduced from Davidson et al. [81] with some alterations.